Unlocking the sulphur chemistry in a protostellar environment
physical and chemical conditions

A dissertation presented by

Manar el Akel

to

Niels Bohr Institute & Centre for Star and Planet Formation

And

LERMA & Observatoire de Paris

in partial fulfillment of the requirements
for the degree of

PHILOSOPHIÆ DOCTOR

February 11th, 2022

Title	Unlocking the sulphur chemistry in a protostellar environment: physical and chemical conditions
Author	ir. Manar el Akel
Department	Niels Bohr Institute
	Centre for Star and Planet Formation (Starplan)
	Faculty of Science, University of Copenhagen
	AND
	LERMA
	Observatoire de Paris
	Faculty of Science, University of Cergy-Paris
Academic Advisors	Dr. Lars E. Kristensen
	Dr. Francois Dulieu
Assessment Committee	Dr. Darach J. Watson (chair)
	Dr. Brunella Nisini
	Dr. Asuncion Fuente
	Dr. Timea Csengeri

A MES PARENTS,

Abstract

The origin of our solar system hosting the only habitable planet, the Earth, has been, for centuries, the source of human interest for space. Several studies have been conducted to better understand the universe, from the study of our solar system to the Milky Way and other galaxies. A main focus over the years has been how the stars evolve from their birth. In this study, we focus on the early stage of the star, from a chemical and physical point of view. The protostellar environment is governed by the interaction of the gas and dust grains, leading to rich gas and surface chemistries. It is through the evolution of such processes that it will be possible to understand how the star evolves, to ultimately form a protostellar system. The chemistry occurring in protostars is vast, therefore, our attention is focused on one specific family of species: the sulphur-bearing molecules. These have been detected in several regions of the protostar, displaying different physical conditions. However, it is unclear the extent of the role this family plays in the protostellar evolution and how.

To unveil the importance of this molecular family in the protostellar environment, I conducted several studies on the sulphur chemistries based on millimeter and submillimiter observations, combined with in-situ laboratory experiments and modeling. Through observation, different regions of different protostars could be analysed, from the cold part (T~10 K) to the warm region (T≥100 K) of the protostar, including the strong outflow region. In such a way, the sulphur chemistry could be analysed. Although the observational approach has been the common thread of all the previous studies, these were complemented with laboratory experiments simulating the ISM conditions and studying the reactivity of H_2S, the initial product of atomic sulphur with one of the most abundant elements in the ISM, atomic hydrogen. Moreover, the modeling aspect was used in parallel with the observations for the study of an outflow, as together with the observations, they provided physical constraints on the region and understanding on the physical processes occurring there. By combining such three methods, it was possible to gain a more extensive understanding of the studied region. All the selected sources for this research are famous class 0 protostars, located in the star forming region at proximity of our solar system.

In this research, we studied the protostellar environment in two stages. On one side, we investigated the sulphur chemistry in the cold and hot environments of the protostar. We pointed out the high reactivity of H_2S in a cold surface to produce the organo-sulphur, OCS. We could determine which sulphur bearing molecules trace the cold envelope and the hot core of a protostar, by comparing several sources of the Cygnus-X complex. In this way, these molecules were quantified towards the different environments and possible chemical paths could be identified. The combination of laboratory and observational methods have shown the importance of H_2S in the sulphur chemistry, as a key element for the production of organo-sulphurs on the icy dust grains. We highlighted the early production of H_2S in a protostellar environment. *The study of the sulphur chemistry in the cold envelope and hot core of the protostar is an essential springboard for future work on the sulphur chemistry, and for understanding how it has evolved during the protostar evolution.*

On the other side, we discussed the chemistry and physical characteristics of a well-known strong outflow, with a focus on S-bearing molecules. The combination of high-resolution observations with shock models allowed us to pinpoint the physical conditions of the outflow and provided us insights on the effects of the shock history on the chemical evolution of the region. This work demonstrated the efficient combination of both methods to interpret such regions. It therefore constitutes a reliable path for future work on outflows.

Dansk resumé

Vores solsystems oprindelse, der førte til den eneste beboelige planet, Jorden, har i århundreder været kilden til menneskers interesse for rummet. Adskillige undersøgelser er blevet gennemført for bedre at forstå universet, fra studiet af vores solsystem til Mælkevejen og andre galakser. Et hovedfokus gennem årene har været, hvordan stjernerne udvikler sig fra deres fødsel. I denne undersøgelse fokuserer vi på den tidlige fase af stjernen, set fra et kemisk og fysisk synspunkt. Det protostellare miljø er styret af interaktionen mellem gas- og støvkorn, hvilket fører til rige gas- og overflade kemier. Det er gennem udviklingen af sådanne processer, at det vil være muligt at forstå, hvordan stjernen udvikler sig for i sidste ende at danne et protostellart system. Den kemi, der forekommer i protostjerner, er enorm, og derfor er vores opmærksomhed fokuseret på en specifik familie af molekyler: de svovlholdige molekyler. Disse er blevet påvist i flere regioner af protostjernen, der udviser forskellige fysiske forhold. Ikke desto mindre, er det uklart, hvilken rolle denne familie spiller i protostjernernes udvikling og hvordan.

For at afdække betydningen af denne molekylære familie i det protostellare miljø, har jeg gennemført flere undersøgelser af svovlkemien baseret på millimeter- og submillimeter observationer kombineret med in-situ laboratorieeksperimenter og modellering. Gennem observationer kunne forskellige regioner i forskellige protostjerner analyseres, fra den kolde del (T~10 K) til den varme region (T≥100 K) af protostjernen, inklusiv den stærke outflow-region. På denne måde kunne svovlkemien analyseres. Selv om den observationelle tilgang har været den røde tråd i alle de tidligere undersøgelser, er disse blevet suppleret med laboratorieeksperimenter, der simulerer ISM betingelser og undersøgelse af reaktiviteten af H_2S, det første produkt af atomart svovl med et af de hyppigst forekommende grundstoffer i ISM, nemlig atomar brint. Desuden, blev modelleringsaspektet anvendt parallelt med observationerne til undersøgelse af et outflow, da de sammen med observationerne gav fysiske begrænsninger på regionen og forståelse for de fysiske processer, der finder sted der. Ved at kombinere disse tre metoder var det muligt at opnå en mere omfattende forståelse af den undersøgte region. Alle de kilder, der er udvalgt til denne undersøgelse, er berømte protostjerner af klasse 0, der befinder sig i stjernedannende regioner i nærheden af vores solsystem.

I denne forskning har vi undersøgt det protostellare miljø i to faser. På den ene side undersøgte vi svovlkemien i de kolde og varme miljøer af protostjernen. Vi påpegede den høje reaktivitet af H_2S i de kolde skyer omkring de unge stjerner for at producere organosvovl-forbindelsen, OCS. Vi kunne bestemme, hvilke svovlbærende molekyler der sporer de kolde omkringliggende skyer og den varme kerne af protostjernen, ved at sammenligne flere kilder i Cygnus-X-komplekset. På denne måde blev disse molekyler kvantificeret mod de forskellige miljøer, og mulige kemiske veje kunne identificeres. Kombinationen af laboratorie- og observationsmetoder har vist H_2S's betydning i den svovlkemi, som et potentielt S-reservoir og som et nøgleelement for produktionen af organisk svovl på de isdækkede støvkorn. Vi fremhævede den tidlige produktion af H_2S i et protostellart miljø. *Undersøgelsen af svovlkemien i protostjernens kolde omkringliggende skyer og varme kerne er et vigtigt springbræt for fremtidigt arbejde med svovlkemien og for at forstå, hvordan den har udviklet sig i løbet af protostjernens udvikling.*

På den anden side diskuterede vi kemien og de fysiske egenskaber ved et velkendt stærkt outflow med fokus på S-bærende molekyler. Kombinationen af højopløsningsobservationer med chokmodeller gjorde det muligt for os at indkredse de fysiske forhold i outflowet og gav os indsigt i chokhistoriens indvirkning på regionens kemiske udvikling. Dette arbejde demonstrerede den effektive kombination af begge metoder til at fortolke sådanne regioner. Det udgør derfor en pålidelig vej for fremtidigt arbejde med outflows.

Résumé Français

L'origine de notre système solaire habritant la seule planète habitable connue à ce jour a été pendant des siècles pour les Hommes, une des sources d'interêt principale pour l'espace. Plusieurs études ont été menées afin de mieux comprendre l'univers, se focalisant à la fois sur notre système solaire, mais également tant sur notre galaxie, la Voie Lactée, que sur d'autres galaxies. A travers le temps, un des centres d'intérêt principal de ce désir de connaissances sur l'univers a été l'évolution des étoiles depuis leur naissance.

A travers cette étude, nous nous focalisons sur les premiers cycles de vie d'une étoile, d'un point de vue chimique et physique. L'environnement protostellaire est régi par les intéractions des particules dans le gas et sur les graines des poussières interstellaires, résultant en une chimie riche en phase gazeuse et solide. Ce n'est principalement que via l'évolution de tels procédés qu'il est possible de comprendre comment les étoiles évoluent, mais également comment se forme un système protostellaire. La chimie présente dans les protoétoiles est vaste et par conséquent, notre attention ne se porte que sur une famille de molécules: les molécules soufrées. Ces dernières ont été détectées dans différentes régions protostellaires, caracterisées par diverses conditions physiques. Cependant, l'étendu du rôle que cette famille soufrée joue dans l'évolution protostellaire ainsi que ses fonctions, ne sont pas clairement connus à ce jour.

Afin de dévoiler l'importance de cette famille moléculaire dans un environnement protostellaire, nous avons réalisé plusieures études sur la chimie du soufre basées sur des observations millimétriques et submillimétriques, combinées avec des expériences en laboratoire et des simulations. A travers ces observations, différentes régions de différentes protoétoiles ont pu être analysées. Ces zones d'étude consistent en des régions régies par des températures dites froides (T~10 K), chaudes (T≥100 K) mais également des régions perturbées par le passage d'un choc.

Bien qu'une approche observationnelle ait été réalisée précédemment par plusieurs, nous combinons ici cette approche observationnelle avec des expériences en laboratoire reproduisant les conditions interstellaires tout en étudiant la réactivité de la molécule H_2S, qui est le produit initial du soufre atomique avec une des molécules les plus abondantes du milieu interstellaire, à savoir l'hydrogène atomique.

De plus, des simulations d'une région de choc ont été utilisées en parallèle avec les observations afin d'étudier ces régions protostellaires. Ce couplage d'observations et de modèles permet de définir et de comprendre les conditions physiques de ces régions.

En combinant ces trois méthodes, il a été possible d'acquérir une meilleure compréhension des régions étudiées. Toutes les sources sélectionnées dans cette étude font partie de la classe 0, situées dans des régions de formation d'étoiles à proximité de notre système solaire.

Durant cette recherche, nous avons étudié l'environnement protostellaire en deux phases. D'une part, nous avons investigué la chimie du soufre dans les régions dites chaudes et froides d'une protoétoile. Nous avons démontré une grande réactivité de H_2S sur une surface froide produisant la molécule OCS. De plus, nous avons déterminé l'éventail de molécules soufrées traçant l'environnement froid de l'enveloppe protostellaire ainsi que celui traçant la région centrale chaude d'une protoétoile. Ceci en comparant différentes sources du complexe Cygnus-X. De cette manière, les molécules soufrées dans ces régions ont pu être quantifiées et les possibles différentes réactions chimiques ont pu être identifiées. La combinaison des observations et des expériences en laboratoire a souligné la place centrale de H_2S dans la chimie du soufre comme un élément-clé de la production des molécules soufrées sur les particules de poussières gelées. Nous avons également souligné la production précoce d'H_2S dans le milieu interstellaire.

L'étude de la chimie du soufre dans l'enveloppe froide et l'intérieur chaud d'une protoétoile est un tremplin essentiel pour la continuation du travail sur la chimie soufrée ainsi que pour la compréhension de comment celle-ci a évolué durant la formation d'une protoétoile.

D'autre part, nous avons discuté les caractéristiques chimiques et physiques d'une région de choc, avec une attention particulière sur les molécules soufrées. La combinaison des observations de haute-résolution et des modèles de chocs ont permis de mettre en avant les conditions du choc étudié ainsi que les effets de l'historique d'un choc sur l'évolution chimique de la région. Ce travail démontre la combinaison efficace de ces méthodes afin d'interpréter ces régions. Cela constitue, par conséquent, un moyen fiable pour la continuation des études sur les régions de chocs.

Acknowledgments

Nothing great ever came that easy. This PhD has been an incredibly journey, personally and professionally. I had the occasion to acquire a huge amount of knowledge and to discover that my limits can always be pushed further. But most at all, I learned that we are the only masters of our life who define what our future will be.

I would like to express my deep gratitude towards my main collaborators Antoine Gusdorf and Romane LeGal who guided me throughout the science and always had time for me. It was an invaluable experience working with you, you were incredible mentors to me.

I also want to thank Marianne Vestergaard and Mariam Mellouli who were there when I needed it and supported me throughout the hardest part of my Ph.D.

I would also like to thank Frank Morgese who has been there since my master journey and never said no when I asked for help.

The journey would have not been what it was without the presence of the incredible team at Starplan, especially with Kasia Dutkowska, Charl van der Walt, Giulia Perotti, Martine Lützen, Will Rocha, Sébastien Manigand, Mafalda Costa, Nikitha Saji, Georgy Makhatadze, Lu Pan, Zhengbing Deng, Jean Bollard and Martin Bizzarro. I will definitely miss my time at Starplan, especially the social events, the badminton games and the Julefrokost.

Last but not least, I would like to thank my parents, sister and brother who have been incredible during these last three years. You made me laugh when it was not easy and gave me the force to continue whatever the difficulties I faced. This entire Ph.D would have not be possible without you, you were my fuel. Finally, a special thank you to my grandparents and uncles as well as to Camilla and Sofia, who have been cheering me on in the backstage. I realize how fortunate I have been to have you on my side.

Contents

1

Introduction

Exploring the universe has triggered mankind for millennia. From navigation, time-keeping purposes to agricultural planning and religious practices, astronomy has always had an impact on human life.

Over the years, the sky has been observed with the human eye, by Nicolaus Kopernikus, Galileo Galilei, Johannes Kepler, Charles Messier, etc., up to extremely sophisticated ground-based and in space telescopes, allowing us to unravel the greatness of the universe.

From the biggest scale to the smallest, the scientists have deployed significant effort throughout the years to understand the origin of the solar system and ultimately the universe. Retracing the origin of life has become the question of the century.

Among all the extensive studies for understanding the universe, a special attention has been given to the formation of stars and their evolution until potentially evolving into a planetary system. One main aspect of this research is on the molecular scale. The distance of the stars made them unavailable for physical research unlike meteorites and the planets of our solar system. Telescopes are therefore a primary source of information for these objects, allowing scientists to study them at the molecular level.

Although the universe is still holding its secrets, researchers are discovering new aspects of it from a chemical and physical perspective.

An important question that often arises in astronomical studies is *how the chemical and physical processes are interlinked in stars?*, in other words, how the chemical aspects of an environment have led to its evolution. This question has been a key driver of this study. Throughout this thesis, we looked at the earliest phases of a forming star, with a focus on the chemistry and physics.

In this thesis, we built our analysis on a step-per-step basis, which consists of six main parts.

First, the mandatory concepts necessary for fully understanding this study are displayed, in Chapter 1. In this Chapter, we will explain how an early star (i.e., protostar) forms in the interstellar medium (ISM) and, we will give a closer look at the different structures of a protostar, as well as the various classification systems for interstellar objects. Then, we will discuss the physical and chemical processes occurring in the ISM. Finally, we will focus our attention on a specific molecular family, i.e., the sulphur-bearing species, that will a key element of this study. To perform any study, data are required. In our case, we obtain them from various ways. The most famous way to study a star is by observations, but experiments and modelling are also reliable ways to quantify scientific projects. In Chapter 2, we will describe all the methods used in this study, from a technical and physical point of view. in this Chapter, the reader will acquire knowledge on what can be detected, how we deal with the data, and how these are interpreted.

For carrying out this study on protostars, sources to be studied have to be selected. Therefore, the next Chapter describes our regions of interest. It will provide to the user an overview of these sources: where they are and what are their main characteristics.

Before diving into this research subject, displayed in Chapters 5–7, we will first explain in detail our research description and the context, in Chapter 4.

Chapters 5–7 are the core of this thesis, as they represent the studies performed. These are in the form of articles, which are published, submitted to a journal or in preparation.

Finally, in Chapter 8, the main conclusions of this thesis are summarized. This chapter also includes the outlook for future work, as the science should always be moving forward.

1.1 THE PROTOSTELLAR SYSTEM: FROM THE ORIGIN TO THE FORMATION

Let's us begin our journey with the origin : *How is a protostar formed ?* The interstellar medium (ISM) which is the material among the galaxies consists of 99% of gas and 1% of dust by mass, and is constantly replenished by the remains of dead stars in a previous star cycle (Krumholz, 2017).

This gas part of the ISM is primarily constituted of Hydrogen (~90% by number of particles) and the remaining 10% by number is distributed over principally Helium (~9%) and the remaining 1% consists principally of other heavy elements such as Carbon, Oxygen, Nitrogen, Silicate and Iron (Draine, 2003).

The solid-state particles representing 1% of the ISM mass are also called dust grains, and have a typical size of ~0.1–1 μm. We will see later that this 1% of material in the ISM plays a primordial role in the protostar formation, as they constitute the surface on which chemistry and physics can occur. Although their exact composition are not yet fully understood, several elements, such as silicate, graphite, carbon have been discovered in dust grains. These particles are usually covered by ice in cold environments ($T \lesssim 20$ K), due to feeze-out of several atoms and molecules, such as atomic oxygen on the grains, which efficiently reacts with hydrogen to produce water (Min *et al.*, 2008; Henning, 2010; Schmalzl *et al.*, 2014; Boogert *et al.*, 2015).

This ISM is not uniformly distributed over space and can be denser at some locations. In such a way, several environments can be differentiated. Four main environments are listed in Table 1.1, varying from each other by their density, temperature and size (Krumholz, 2017; Herbst and van Dishoeck, 2009).

Giant Molecular Clouds (GMC's) are at the origin of star formation. These are the largest aggregation of material in the ISM. Several physical phenomena occur in these molecular clouds (MC) such as gravity, magnetic field, thermodynamics, turbulence and stellar feedback (i.e.supernova and stellar winds effects) which lead to the gas compression and ultimately to star formation (Ballesteros-Paredes *et al.*, 1999; Crutcher, 1999; André *et al.*, 2014; Ibáñez-Mejıa *et al.*, 2021).

After being subjected to the physical phenomena described above for tens of millions of years, the evolution of the molecular cloud leads to the formation of clumps of mass (10-50 M$_\odot$[1]) within it. These last clumps formed when the mass of the molecular cloud exceeds its Jeans mass, which is the mass above which gravity dominates. The cloud core, of typically 10^4 M$_\odot$, collapses under its own gravity. The star formation process is started and these clumps form into protostellar cores over millions of years. The properties of the different stages of the molecular clouds are shown in Table 1.1 from Krumholz (2017).

[1] M$_\odot$ represents 1 solar mass.

TABLE 1.1: Properties of the different interstellar clouds of the ISM based on their density, temperature range and size.

Region	Characteristics		
	Density [cm^{-3}]	Temperature [K]	Size [pc]
Giant Molecular Cloud (GMC)	1-3 10^2	7-15	10-60
Molecular Cloud (MC)	10^3-10^4	10-30	2-10
Stellar mass clumps	10^4-10^5	10-30	0.1
Protostar core	$\geqslant 10^5$	7-15	$\leqslant 0.1$

The protostar is formed from the collapsing material of molecular clouds (Shu, 1977; Terebey *et al.*, 1984; Shu, 1985). However, the formation path from the collapsing gas to what is defined by the astronomical community as a protostar, is not instantaneous and several physical and chemical processes take place.

When the gas collapses, the primary source of energy is the adiabatic compression of the gas. The increase in temperature by the collapsing gas is counteracted by the cooling, principally the thermal emission of the dust grains. This generates the so-called first hydrostatic core, which is a hydrostatic object, meaning that the external forces on this object are balanced by its own pressure gradient. At this stage, a protostar is born. This first core is a relatively small sphere with a size of few AU and a mass of hundredths of solar masses (Krumholz, 2017). However, this stage is temporary, as the compression from the accumulation of material within the center is efficiently raising the temperature at the center to thousands of K. This change in thermodynamics also affects the chemical aspect of the gas. For the case of molecular hydrogen, its binding energy (4.5 eV) and kinetic energy are too high for effective dissociation. However, the tail of the Maxwellian distribution[2] of a hot gas is moving fast enough for generating collisions. Therefore, the collisional rate of molecular hydrogen is extremely sensitive to an increase of temperature at the center. Due to this rise of temperature at the center, the system is not in hydrostatic conditions, and the first core is subject again to a free-fall collapse, marking the second collapse of the protostar (Krumholz, 2017). During this collapse, all the molecular hydrogen dissociates and ionizes, until reaching $\sim 10^4$ K at its center. This new hydrostatic object is now what can be called a conventional protostar.

[2]It defines the velocity distribution of a gas at a defined temperature.
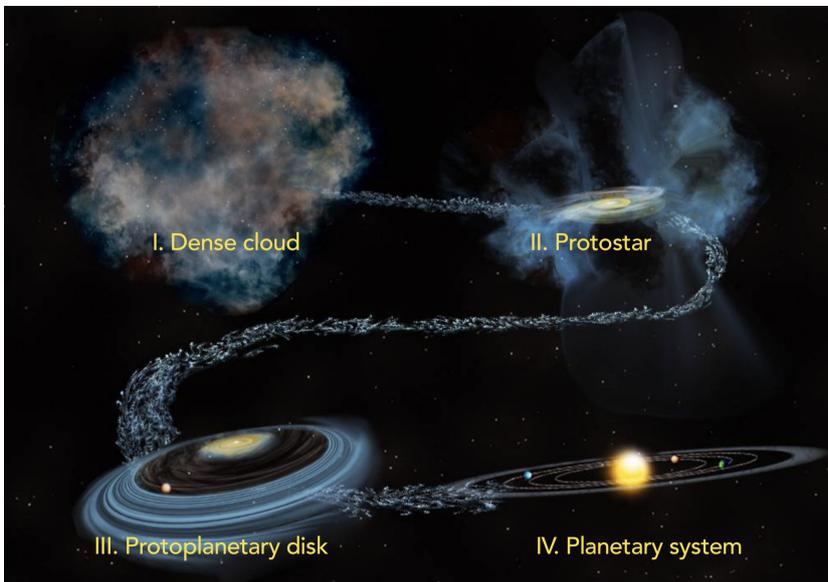
FIGURE 1.1: General steps of star Formation from the dense cloud to the planetary system. Credit: DSS

Eventually, the protostar will evolve to form a protoplanetary disk and planetary system, as our solar system, as shown in Figure 1.1. Nonetheless, the further evolution of the protostar is shortly discussed in Section 1.4. However, as this is beyond the scope of this Ph.D research, it will not be further detailed.

1.2 MORPHOLOGY OF STAR-FORMING REGIONS, A CLOSER LOOK

Different structures can be observed in the protostar, from its internal structure to the surrounding material enveloping it, each of them are defined by a set of the characteristics (pressure, temperature, size, etc.) and have distinct dynamical behaviour. In Figure 1.2, a figure of a protostar is shown. This study focuses on several parts of the protostar and, more specifically on which chemistry and physical processes are present in the protostellar regions. Therefore, it is primordial to understand the structure of the protostar.
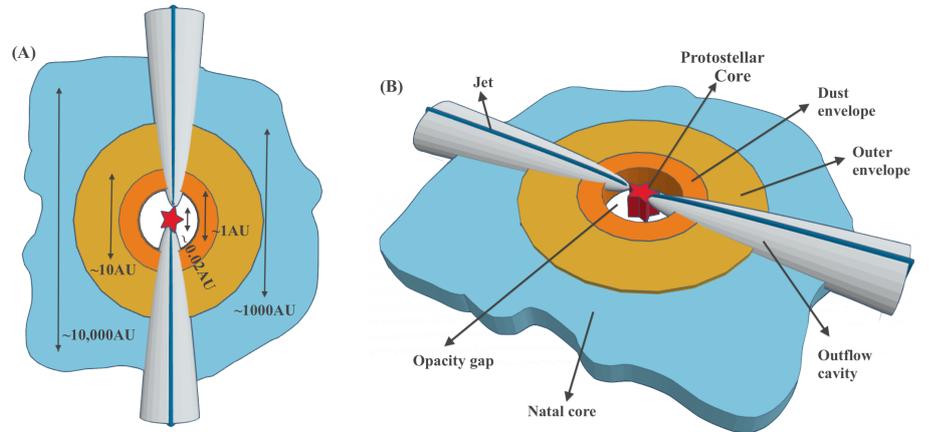
FIGURE 1.2: Figure of the different structures of the protostar: (A) shows the top view with the size (for $1M_\odot$ protostar) of each components described in Section 1.2. (B) displays the different components of the protostar.

1.2.1 Protostellar Core

The core is the central region of the protostar, namely the center of the hydrostatic object described earlier a size of ~0.02 AU (for $1M_\odot$ protostar, Krumholz, 2017). The infalling gas generates an accretion shock at the center of the protostar, generating energy radiating away from the center. The post-shock gas is thus heated such that it emits UV and x-rays. Moreover, at temperatures greater than ~1000 K, the dust made primarily of silicate and graphite will vaporize. Surrounding the center of the protostar, a dust free region, also called the opacity gap, is found and has a radius of ~1 AU from the center (Stahler and Palla, 2005). At this early stage of the star, the gravity of the center is the only source of energy and there is no nuclear burning yet and no fusion of the hydrogen atoms to form helium atoms in the core, unlike the Sun.

1.2.2 Envelope

As the temperature decreases with the distance with respect to the accreting star, the dust destruction barrier is overcome and dust grains are present in the surrounding. This colder environment is called the protostellar envelope, as the first layer after the opacity gap.

As mentioned earlier, the protostar is subject to gravity, thus the material within the envelope is collapsing onto the center.

This envelope can extend up to thousands of AU from the center. It therefore englobes several parts which need to be further clarified as they differ in temperature and density, which in turn greatly influence the chemistry: (a) the dust envelope, (b) the outer envelope. The dust envelope is the first layer after the opacity gap which is optically thick. This region expands up to ~10 AU and includes temperatures in the order of hundreds up to thousands of K, with respect to the distance from the center. The second layer, i.e., the outer envelope, starts at the end of the dust photosphere. Beyond the dust photosphere, the gas is optically thin and thus, in this region, the radiation emitted from the center of the protostar will be absorbed and, emitting at longer wavelengths. This outer envelope can extend up to thousands of AU from the center and displays a temperature range from hundreds of K down to ~10–30 K (Stahler and Palla, 2005).

In the following study (cf. Chapter 5), we will refer to hot core and the cold envelope, which are the innermost and outermost regions of the outer envelope, respectively. The outermost region has typical temperature range of 10 K–100 K, for display a density of 10^4–10^5 cm^{-3}, while the hot core is closer to the protostellar core, and thus has higher temperature range of hundreds of Kelvin and a denser environmental density of 10^6–10^7 cm^{-3} (Ziurys, 2006; Minh *et al.*, 2010). We will later discuss that differentiating the these two environments are essential for understanding the envelope, as they are affected by different processes acting on their chemical aspects and, ultimately on the physics.

1.2.3 *Outflow and Jet*

The rotation of the parental cloud causes the center of the protostar to spiral inward, causing this free fall material from the envelope which adds mass to the core. Although the angular momentum is conserved, due to this rotation and the collapse towards the center of the protostar, which is a smaller region, an increase of rotational speed is observed. This flattens the protostar. To release some of this energy from the protostellar center and thus reduce the rotational speed, the excess of angular momentum in the central region ejects material from its center. These are the so-called outflows and more specifically jet if the gas velocity exceeds ~50 km s^{-1} (Bachiller, 1996; Reipurth and Raga, 1999).

This material is ejected from the center in different physical conditions than the ambient material. This phenomenon generates shocks, which are caused by a propagating disturbance moving faster than the local speed of sound in the medium. In such a way, changes in pressure, density, temperature up to thousands of Kelvins are observed. These shock regions are easily traced by H$_2$ emission, which require a warm environment for emitting and SiO emission, which are a reliable indicator of the dust grains emission. However, the H$_2$ emission is detectable only if the outflow is at at least ~1000 AU of the protostars, as its wavelengths (2–28μm) coincide with the optically thick part of the envelope (Maret *et al.*, 2009). Moreover, the presence of an outflow and jet is confirmed with reliable shock tracers such as SO, CO, etc. The post-shock gas of these regions are often rich chemical reservoirs as they include the molecules expelled from the center to the apex of the protostar. But also, the extreme environmental conditions lead to a rich chemistry, e.g., reactions with high activation energies may happen due to the extreme temperatures reached (i.e., above ~100 K), the grain-to-grain collision is likely to occur to the velocity of the outflow/jet, etc. (Arce *et al.*, 2007).

Outflow and jets are characteristics of a forming star, as they eject the excess of angular momentum of the protostellar center such as it can further evolve to a star. Moreover, these ejections of material have an unalterable effect on the chemistry and thus on the post-shock gas. It is therefore essential to understand the effect of the outflow on the protostellar environment to understand its evolution. These have been deeply studied over the years with models and observations by, e.g., Gusdorf *et al.* (2011) used observations of SiO and H$_2$ emission of an outflow and compared them with shock model to constrain the pre-shock distribution of silicon on the dust grains. From this comparison, the main characteristics of this shock, that will be discussed in the next Section, could be determined. While in Gusdorf *et al.* (2015), combination of the CO, SiO and H$_2$ observations and shock models, allowed them to constrain the mass of the targeted outflow. Pineau des Forêts *et al.* (1993) investigated the sulphur chemistry with shock models and, found the enhancement of H$_2$S within a shock and these of SO and SO$_2$ during the shock and in the post-gas. While, it was pointed that CS is a sulphur bearing species not influenced by a shock. These represent only few examples of the work performed on outflows up to now, e.g., Arce *et al.* (2007) and Bally (2016).

1.3 A SHOCK REGION: WHAT ARE THE CHARACTERISTICS ?

We previously explained how important the shock is in the protostellar evolution. Proceeding inwards, in this Section, we will provide to the reader a deeper overview of the fundamentals of shocks physics.

A shock can be stationary (i.e., steady-state) or non-stationary. In the later case, its physical conditions are evolving throughout the shock propagation. This can be caused by the environmental conditions varying over smaller scales than the length of the shock, or due to an internal instability of the shock. Another reason might be the shock itself. A shock can be seen as piston moving forward, as shown in Figure 1.3. In a stationary type, the piston will move at a constant speed, while in a non-stationary case, the piston might accelerate or decelerate compared to its initial speed.
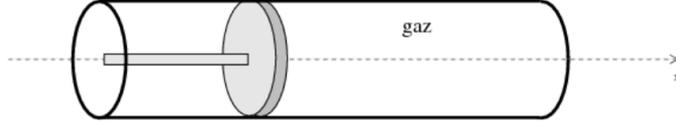
FIGURE 1.3: Schematic drawing of a piston representing a shock, in 1D plane. The movement of the piston generates a shock wave acting on the gas.

In the case studied in this thesis, in Chapter 6, only stationary models are considered. We follow Draine (1980) and define that a "steady state shock wave is any pressure-driven disturbance which is time-independent (in a comoving reference frame) and which effects an irreversible change in the state of the medium."

To understand how a stationary shock behaves, let's first consider this piston in a 1D plane, defining the shock frame as the reference frame. In this, the flow travels towards the shock at a certain speed. This flow is composed of neutral and ionized fluids, which are travelling at similar speeds but do not collide with each other, when there is no external forces acting on the system. We add to the system the presence of a transverse magnetic field, which is perpendicular to the shock propagation.

During a shock, there is a propagation of a shock wave. Depending on the direction of the magnetic field, we differentiate two types of magnetohydrodynamic waves: the Alfven and the magnetosonic waves. The Alfven waves are due to the propagation of the magnetic field in the same direction as the fluids, these are non compression waves and propagate at the so-called Alfven velocity, defined as follows:

$$V_\mathrm{A} = \frac{B}{\sqrt{4\pi\rho}} \tag{1.1}$$

in which, B is the magnetic field strength and ρ is the gas density. On the contrary, the magnetosonic waves travel perpendicular to the fluids propagation and, are compression waves. Their corresponding velocity is depending on the Alfven speed and the speed of sound, c, as follows:

$$V_\mathrm{ims} = \sqrt{c^2 + V_\mathrm{A}^2} \tag{1.2}$$

In the shocks described here (i.e., stationary shocks), we are dealing with magnetosonic waves, as we consider a transverse magnetic field. The velocity of the neutral and charged fluids (i.e., the shock speed) can therefore be quantified with the magnetosonic velocity, V_ims. Moreover, this assumption of 90 deg between the magnetic field and the fluids propagation means that the magnetic field resistance to the flow compression is the highest.

When the flow is subjected to a shock, the neutral and ions of the flow can be coupled or decoupled, thus the flow can be considered as a single fluid or as multi-fluids, respectively. The reason of this differentiation is later explained when we will discuss the two main types of shock and physical origins. However, let's consider now that the flow can act as single or multi fluid(s), in order to understand how the density, pressure and temperature vary across the shock.

When the fluids within the shock act as multi fluids, due to the presence of a strong magnetic field, then relations describing the conservation of particles number, mass, momentum and energy should be used to quantify the physical changes, e.g., the pressure, density, temperature, occurring prior and ante the shock.

In order to reduce the numerical complexity, we assume here a stationary state, i.e., $\delta/\delta t = 0$, therefore, we study the shock wave only in one spatial dimension. Here, we consider that the flow, u, is parallel to the x-plane, i.e., $\frac{d}{dt} = u \frac{d}{dx}$.

The corresponding particle number conservation for any species, is

$$\frac{d}{dx}(n_s V_s) = N_s \tag{1.3}$$

where n_s represents the number of particles, s, per unit volume, V_s is the particle velocity and N_s is the source term[3].

The mass conservation of the neutral, n, and charged, i, fluids is described as follows:

$$\frac{d}{dx}\rho_n V_n = S_n \tag{1.4a}$$

$$\frac{d}{dx}\rho_i V_i = S_i = -S_n \tag{1.4b}$$

where ρ is the mass density and S_n is the source term, displaying the change of mass in the fluids.

The conversion of momentum is shown by the following relationships, for the neutral and the charged fluids. In the case of charged fluid, the compression of the magnetic field is taken into account, contrary to the equation for the neutral fluid which is not directly influenced by the magnetic field.

$$\frac{d}{dx}\left(\rho_n V_n^2 + \frac{\rho_n k_b T_n}{\mu_n}\right) = A_n \tag{1.5a}$$

$$\frac{d}{dx}\left[\rho_i V_i^2 + \frac{\rho_i k_b (T_i + T_e)}{\mu_i} + \frac{B_0^2}{8\pi}\left(\frac{V_s}{V_i}\right)^2\right] = A_i = -A_n \tag{1.5b}$$

where, the subscript n, i, e and s refer for the neutrals, ions, electrons and shock, respectively. k_b is the Boltzmann factor, μ is the mean molecular weight, B_0 is the initial magnetic field strength and A_n is the source term of the momentum conservation.

While the conservation of energy for the neutral and charged particles is defined as follows :

$$\frac{d}{dx}\left(\rho_n V_n^3 + \frac{5}{2}\frac{\rho_n V_n k_b T_n}{\mu_n} + \frac{\rho_n V_n U_n}{\mu_n}\right) = B_n \tag{1.6a}$$

$$\frac{d}{dx}\left[\rho V_i^3 + \frac{5}{2}\frac{\rho_i V_i k_b (T_i + T_e)}{\mu_i} + \frac{B_0^2}{4\pi}\frac{V_s^2}{V_i}\right] = B_i + B_e \tag{1.6b}$$

in which U is the mean internal energy per neutral particle. In the case of charged fluid, the internal energy is neglected in the code. The corresponding energy source term for each fluid is denoted by B.

In the case of a single fluid, we refer to an infinitely thin shock, that we will later call a jump-type shock. This jump is a discontinuity in the physical parameters of the shock. In the later, the four laws of flux conservation described above can be simplified, for an infinitely thin shock, into the so-called Rankine-Hugoniot jump conditions. We will therefore here not differentiate the neutral and ionized fluid parameters but consider one single flow parameters.

The compression factor, C, which is the compression ratio in density, $\frac{\rho}{\rho_0}$, observed throughout the shock, is quantified as follows:

$$2(2 - \gamma)b\left(\frac{\rho}{\rho_0}\right)^2 + \left[(\gamma - 1)M^2 + 2\gamma(1 + b)\right]\frac{\rho}{\rho_0} - (\gamma + 1)M^2 = 0 \tag{1.7}$$

where γ is the adiabatic index, M the mach number which represents the ratio of shock speed over the speed of sound. $b = B_0^2/(8\pi p_0)$, where $B_0^2/(8\pi)$ and p_0 are the magnetic are gas pressures, respectively. In the absence of a magnetic field, i.e., $b = 0$, the compression factor can be simplified as followed:

$$C = \frac{\gamma + 1}{\gamma - 1}\frac{M^2}{M^2 + 2} \tag{1.8}$$

The compression of the flow affects the downstream pressure and, the shock also heats the flow due to its kinetic energy. The pressure, p, and temperature, T, downstream of the shock is described with the following relations.

$$p = p_0 \left(1 + \frac{2\gamma(M^2 - 1)}{\gamma + 1} \right) \tag{1.9}$$

$$T = T_0 \frac{p}{p_0} \frac{p + h^2 p_0}{p_0 + h^2 p} \tag{1.10}$$

in which, k is Boltzmann constant, M_s is the Mach number from the shock speed and P_0 and T_0 are the pre-shock pressure and temperature, respectively, and h^2 equals $(\gamma + 1)$ over $(\gamma - 1)$.

From these Equations, we can see that the pressure and density of the gas increases across the discontinuity. Moreover, considering a monoatomic gas, i.e., $\gamma = 5/4$, the limit of pressure difference $(p \gg p_0)$ leads to a maximum compression factor of 4. Following the Rankine-Hugoniot conditions, the density ratio is inversely proportional to the speed ratio. Therefore, the minimum shock speed at the end of the discontinuity will be a fourth of its initial value at front.

So far, we have analysed what happens upstream and downstream of the shock. Let's now have a closer look at the shock itself. Different main types of stationary shocks can be differentiated: jump (J-) and continuous (C-) type.

1.3.1 *J-type vs. C-type shock*

The transverse magnetic field plays a major role in the type of the shock. In the absence of a transverse magnetic field, the neutral and charged particles are coupled, i.e., they travel under similar conditions such as temperature and velocity. Moreover, the magnetosonic velocity (i.e., the charged fluids), is inferior to the shock velocity. In this case, the charged fluid does not receive the information downstream that there is a shock wave. When the fluids hit the shock wave, a jump (i.e., a discontinuity) in temperature and density is observed (Draine, 1980; Garcia and Ferreira, 2010).

However, the J-type shocks do not strictly include a zero magnetic field. Even weak magnetic fields are characteristic of J-type shock, as can be seen in panels a–d of Figure 1.4.

The presence of a magnetic field decouples the neutral and charged particles downstream and upstream. The flow is then constituted of multi-fluids: the neutral particles are not affected by the magnetic field, contrarily to the charged particles, which will couple with the magnetic field. The magnetic field acts a precursor, transitioning progressively the external physical parameters such as the velocity and temperature. The stronger the magnetic field, the stronger the effect of this precursor on the charged fluid. This precursor progressively compresses and slows down the charged fluid. The charged and neutral particles travel therefore at different velocities due to the magnetic field which lead to collisions among the charged and neutral particles. These collisions heat considerably the charged fluid but not much the neutral fluid. Although, the magnetic field is strong enough for $V_{ims} \geq V_s$, it does not have time to recouple with the neutral fluid before the discontinuity, thus the charged fluid does not experience any discontinuity at the shock front, contrary to the neutrals (cf. panels c and d in Figure 1.4). The intensity of the magnetic field affects the shock size, L (Garcia and Ferreira, 2010).

A C-type shock is observed when there is a strong magnetic field ($V_{ims} \geq V_s$) which leads to a large shock size. The interaction between the neutral and charged particles are thus stronger and over a larger distance L. Consequently, due to the collisions, the neutral fluid slows down, is compressed and heated. The transition throughout the shock is thus also continuous now for the neutral particles. This case is possible when the strength of the magnetic field is higher than the critical value, B_{crit}. This case is represented by panel e of Figure 1.4 from Draine (1980).

As mentioned previously, the shock size, *L*, also described as the distance is much larger for C-type shock than J-type. This demonstrates that the mechanical energy in C-type shock is scaled with the distance at which the neutrals and ions coupled, contrary to J-type shock where the mechanical energy is directly observed at the shock front. The temperature profiles of both shock types are also relatively different, as shown in Figure 1.5. This is explained by the coupling of the fluids in J-type shocks; at the arrival of the piston, a jump of the physical conditions is seen, generating this sharp temperature increase of the flow. While, the decoupling of the

fluids observed in C-type shocks generates a velocity differential, where the charged fluid is accelerated due to the magnetic precursor. Due to this velocity differential, the friction between the ionized and neutral fluids heats up principally the charged fluid and, accelerates the neutral fluid, which also is heated up.
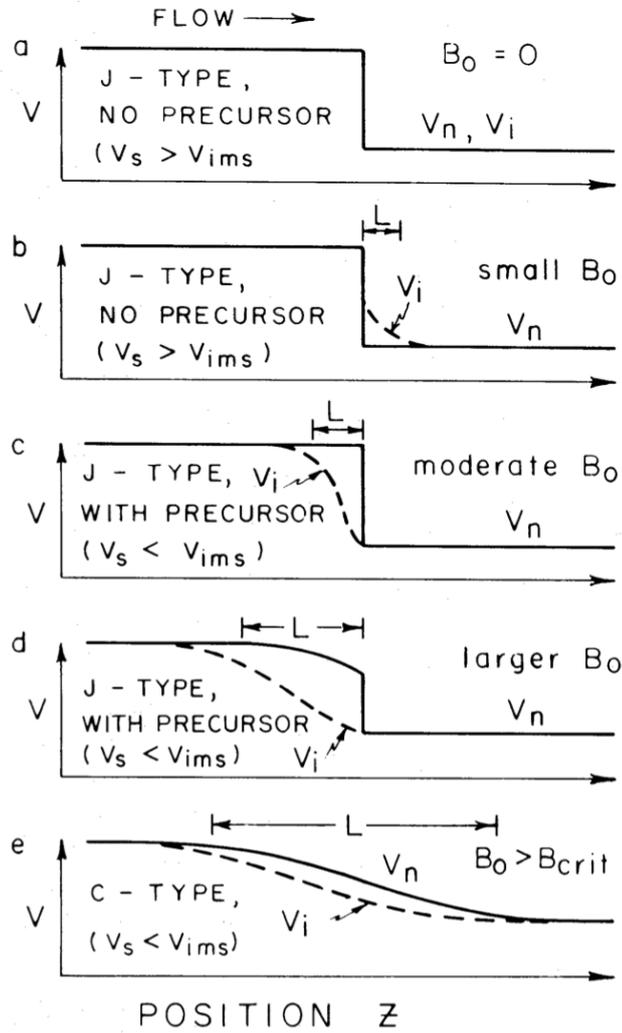
FIGURE 1.4: Flow velocity of the neutral and charged fluids throughout the shock, when the shock of length, L, is subject to different intensities of the magnetic field, B_0. V_i and V_n represent the ionized (i.e., charged) and neutral fluid velocity, respectively. While, V_{ims} is the ion magnetosonic velocity and V_s, the shock velocity. The reference system is the shock plane, the pre-shock environment is located on the left-side and the post-shock on the extreme right-side. Figure from Draine (1980).
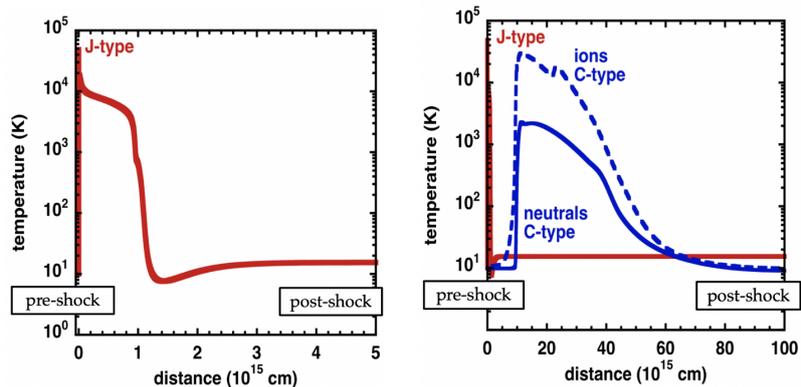
FIGURE 1.5: Temperature profiles of C-type (blue) and J-type (red) shocks over time in years. In the case of C-type shock, the temperature profile of the neutral and charged fluids have been shown separately. Figures from Gusdorf (2019).

1.4 STELLAR CLASSIFICATION

Up to now, we explained in detail how a protostar is born as well as its structure. However, the ISM is made of more than billions of objects, therefore classifications among them are necessary for differentiating and studying them. Over the years, astronomers have developed several classification categories for stars based on the dynamical properties of the object and on the spectral characteristics. Here, we point out two classification systems, the young stellar object classification, as it names indicates, categorized the young objects, such the protostars but also the sources which just left the protostellar stage. The second classification is the Morgan-Keenan, which deals with stars on the main sequence in a Hertzsprung-Russel diagram.

1.4.1 *Young stellar object classification*

The star formation process lasts millions of years and therefore, distinction has been made among the different stages of the young stellar object (YSO), into four classes (cf. Figure 1.6).

The early formation of YSO's is characterised by two main phases: the protostars (i.e. Class 0, I) and the pre-main sequence (PMS) (i.e. Class II, III). Protostars are highly embedded in ISM and can only be observed at the infrared and (sub-) millimiter ranges. How the objects are observed will be explained in detail later in Section 2.1.2. During the first phase, the star is acquiring an important mass by the accretion of the protostellar disk formed from the envelope, as discussed above. The accretion process generates strong molecular jets and outflows onto its surroundings. The end of the protostellar phase is characterized by the "birthline" of the pre-main sequence star. These are low mass stars, and are still at their early evolution therefore nuclear burning within their core has not happened yet. At the early stage of the PMS, remnants of the envelope are still present and finish completing the protostellar disk, in which the planetary system will be formed later.

The categorization among classes strongly depends on the physical characteristics which are described as follows:

Protostellar Phase:

– *Class 0:* Just after the collapse of the molecular cloud, the protostar core is not fully formed yet, the mass of its envelope is higher than the one of its core and has a bolometric temperature, T_{bol}[4] lower than 70 K.

– *Class I:* The envelope starts forming the protostellar disk. Its mass is now lower than the one of the core and its T_{bol} is between 70 K and 650 K.

Pre-Main Sequence Phase :

[4]This temperature is used for describing the evolution of a YSO. It represents the temperature of a black body having the same frequency as the one observed (Myers and Ladd, 1993; Chen *et al.*, 1995).

   – *Class II:* This class includes the classical type of stars called the T-tauri
     Stars. The remaining part of the envelope collapses into the protostellar
     disk, the bolometric temperature is now between 650 K and 2280 K and
     the mass of the disk is ~0.01 $M_\odot$.

   – *Class III:* This category englobes stars without a protostellar disk, as the
     resulting planets are already formed or in-formation (i.e., debris). Its
     bolometric temperature is thus higher than 2880 K.

1.4.2 *Morgan–Keenan classification*

The second type of classification called the Morgan–Keenan (MK) classification, is
based on the spectral features. The stars are ranked using the letters O, B, A, F, G, K,
and M. Each class is further subdivided into 0 to 9, from the hottest to the coolest
star, respectively. The physical parameters characterizing the different classes are
displayed in Table 1.2 and, the relative mass and chromaticity of the different classes
are shown in Figure 1.7.

TABLE 1.2: Physical parameters for the MK classification.

Class	Fractional part	Chromaticity	Temperature[a] 10^3 K	Mass	Main-Sequence Radius	L_{bol}[b]
O	~ 0.00003%	blue	≥ 30.0	≥ 16 $M_\odot$	≥ 6.6 $R_\odot$	≥ 30,000 $L_\odot$
B	~ 0.125%	blue white	10.00–30.0	2.1–16 $M_\odot$	1.8–6.6 $R_\odot$	25–30,000 $L_\odot$
A	~ 0.625%	white	7.5–10.0	1.4–2.1 $M_\odot$	1.4–1.8 $R_\odot$	5–25 $L_\odot$
F	~ 3.03%	yellow white	6.0–7.5	1.04–1.4 $M_\odot$	1.15–1.4 $R_\odot$	1.5–5 $L_\odot$
G	~ 7.5%	yellow	5.2–6.0	0.8–1.04 $M_\odot$	0.96–1.15 $R_\odot$	0.6–1.5 $L_\odot$
K	~ 12%	light orange	3.7–5.2	0.45–0.8 $M_\odot$	0.7–0.96 $R_\odot$	0.08–0.6 $L_\odot$
M	~ 76%	dark orange	2.4–3.7	0.08–0.45 $M_\odot$	≤ 0.7 $R_\odot$	≤ 0.08 $L_\odot$

[a] It represents the surface temperature of the object.

[a] Bolometric luminosity

- *Class O:* regroups highly luminous stars, which radiate in the UV range. These
  stars are extremely massive (≥ 16 $M_\odot$), which translates in highly hot cores
  (≥30.000K). They correspond to ~0.00003% of the stars from the main-
  sequence.

- *Class B:* stars are also very luminous blue stars and are differentiated from the
  Class O by the intensity of the [He I] violet spectrum or of [Si III] and [Si IV]
  spectrum, which are indicative of B-type stars. They correspond to ~0.125%
  of the stars from the main-sequence.

- *Class A:* stars are white objects observable at the visible spectrum. They are
  characterized by strong H lines and ionized metals ([Fe II], [Mg II] and [Si II]
  emission). They make up about 0.625% of the main-sequence stars.

- *Class F:* stars display strong lines of [Ca II] but weak H and ionized metals
  lines. They correspond to ~3.03% of the main-sequence stars.

- *Class G:* regroups the Sun-like category. These have strong [Ca II] and weaker
  H and ionized metals lines than for class F objects. Moreover, the presence of
  neutral metals and CN molecules are detected towards this star's type. They
  represent ~7.5% of the main-sequence stars.

- *Class K:* stars are the observed orange stars, which correspond to ~12% of the
  main-sequence stars. They have mostly neutral metals ([Mn I], [Fe I], [Si I]
  lines) and display weak hydrogen lines.

- *Class M:* are the most common star, as ~76% of main-sequence stars, but,
  display the lowest luminosity from all the above star classes. The spectrum of
  class M stars contains all neutral metals and oxide molecules, and does not
  contain any hydrogen lines.
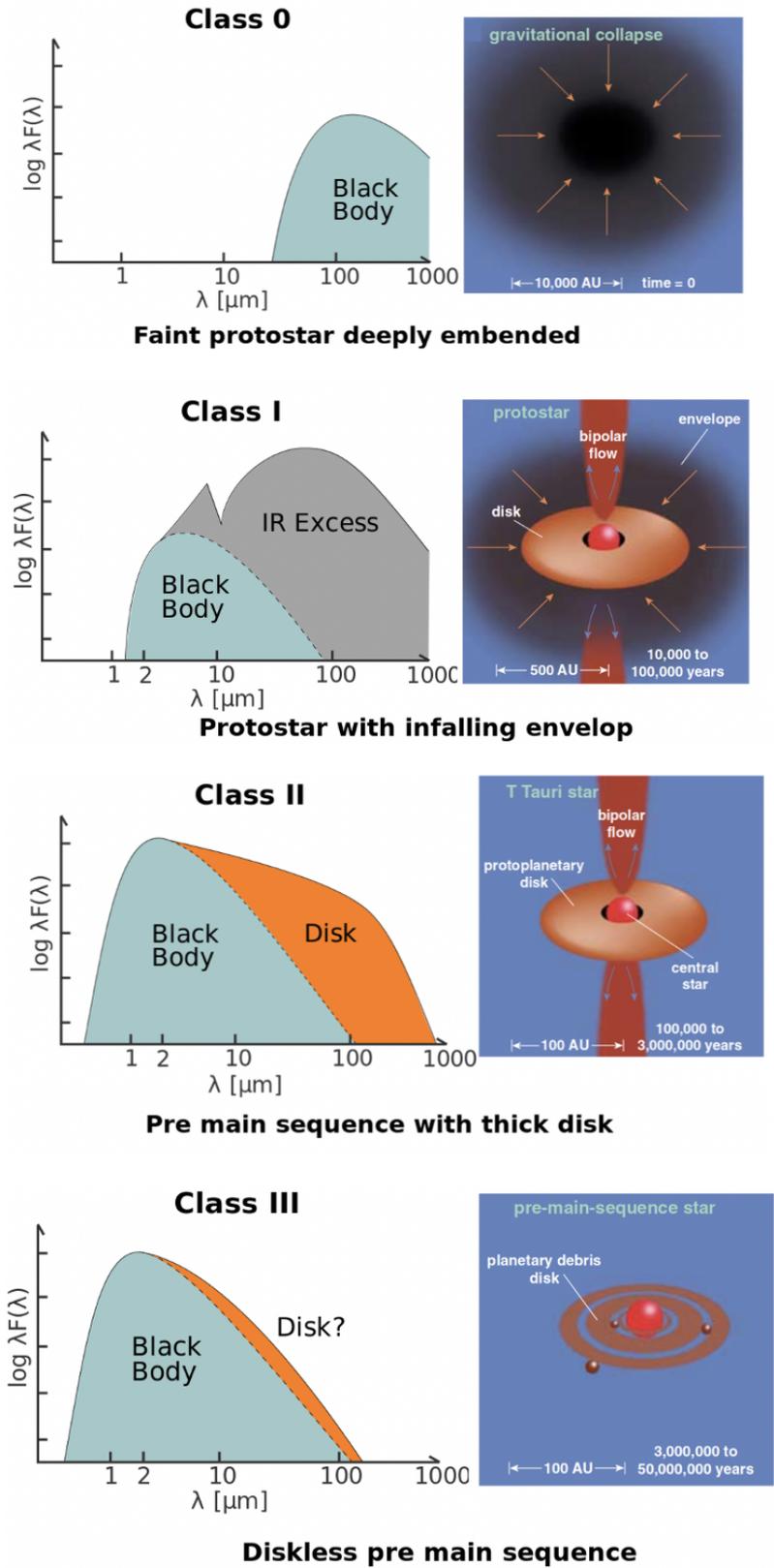
FIGURE 1.6: Young Stellar Objects classification. Each class is described, on the right, by an illustrative image of the (proto)star phase and, on the left by the spectral energy distribution. Figure taken from Cornu (2018).
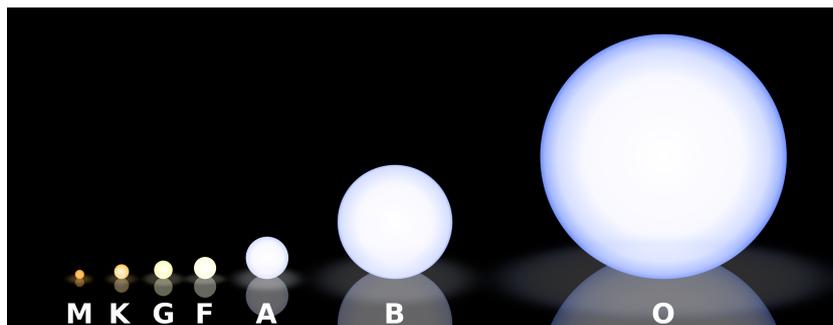
FIGURE 1.7: Morgan–Keenan classification. Credit: Wikipedia Commons

1.5 CHEMICAL AND PHYSICAL PROCESSES IN THE STAR-FORMING REGIONS

Understanding the star-forming regions is closely related to the understanding of the physics and chemistry occurring in such regions. Here, we have previously discussed the different regions around the centre of the protostars and how the densities and temperatures vary there, as well as the physical process of the outflows which strongly alter the gas composition. Over the years, numerous molecules have been observed in space, from simple di- and tri-atomic molecules to the complex organic molecules[5] (CH_3OCH_3, etc.) by, e.g., Thompson and Macdonald (2003), Bottinelli *et al.* (2012), Belloche, A. *et al.* (2014), Jørgensen *et al.* (2016), and van der Walt *et al.* (2021).

[5]They correspond to molecules with number of atoms exceeding 6 and containing at least one atom of carbon.

The detection of these molecules provide us insights on the chemistry and physics of the star-forming region. Indeed, how the molecules and atoms react in a specific environment affects its chemical evolution, which is in turn related to the physical physical conditions near the forming star. A lot of molecules are present in the gas phase, due to chemical reaction in the gas phase or due to physical processes, that will be discussed later in this Section. However, not all species do form in the gas phase, some of them are produced from the reactions of other species on a surface. In the ISM, this surface is the dust grains, which, as mentioned in Section 1.1, represent 1% of the total ISM mass. In the following, the reader will understand how this small fraction of the ISM plays a crucial role in the chemical environment of the protostars and how the physical processes connect the gas phase chemistry the surface chemistry. For associating the presence of a molecule to a specific environment, it is important to have an overview of the different chemical and physical processes occurring in the ISM.

In the following section, we will focus on two aspects (a) the solid-state phase, which is the process related to the dust grains present in the envelope. We will discuss their physical and chemical processes that can alter the gas composition. (b) the chemical reactions in the gas phase, which include several reaction processes also altering the gas composition.

1.5.1 *Solid-state phase*

(I) Surface physics

The atoms and molecules present in the ISM might react differently with a solid matter, the dust grain, depending on their molecules properties, i.e. mass, polarization, particle's energy but also, on the properties of the grain such as the structure and temperature.

Three main processes are possible on dust surfaces: (I.I) The accretion or absorption is the process in which the molecules/atoms in the gas phase adhere to a solid surface. (I.II) During the surface diffusion, the molecules/atoms stay on the surface. (I.III) The desorption describes the physical process where the molecules/atoms are released in the gas phase from the solid state.

(I.I) ACCRETION/ADSORPTION
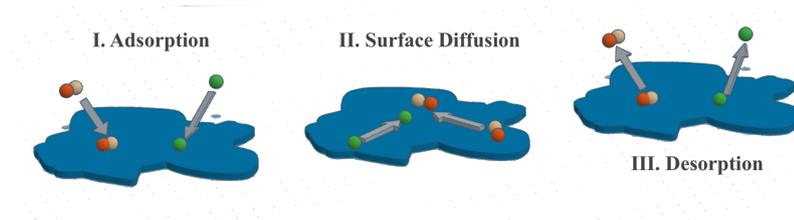
FIGURE 1.8: Physical processes of the molecules on the solid dust grain. It includes the adsorption, the surface diffusion and desorption processes.

The accretion of the gas elements onto the surface leads to collision of the particles with the surface. This physical process is seen during for example freeze out of the molecules. The molecules collide with the surface either with forces from the physical interaction (i.e., physisorption) or from the chemical crossing of their orbitals with the ones of the substrate (i.e., chemisorption).

The PHYSISORPTION involves intermolecular forces, in which the electronic structure of the molecules is not modified. It is a reversible process proportionally dependent on pressure and temperature. It does not require a high activation energy for this process to occur.

The CHEMISORPTION, contrary to physisorption, includes a chemical bonding, requiring high activation energy and is irreversible by nature. It is strongly dependent on the surface area, temperature and absorbate nature. For chemimsorption to occur three conditions should be met: (a) there are remaining active site on the surface (b) the colliding molecules are not saturated (c) the colliding molecules can achieve higher energy than activation barriers for reaction.

After collision of an atom/molecule on the surface, the probability that it stays on it is determined by the sticking coefficient. It measures the energy probability of the atoms in the gas phase to stick on the surface, and depends on not only the substrate temperature, coverage and properties but also, on the mass and kinetic energy of the colliding species. The inverse proportionality of the temperature on the sticking coefficient has been demonstrated by Wang and Gomer (1979) for high temperatures ($\sim$ 600-650K). Therefore, in this work the sticking coefficient, S_{coef}, is considered independent of temperature as the range considered in this study (i.e., observations and experiments) does not exceed 350 K and can, thus, be approximated by Equation (1.11).

$$S_{\text{coef}} \sim \frac{E_s}{E_k + E_b} \tag{1.11}$$

in which, E_s is the sticking energy, E_b is the binding energy and E_k is the gas particle energy.

When the particle is absorbed on the surface, the energy gain by this physical reaction is dissipated either through diffusion of the species on the surface or decomposition of the species. The decomposition leads to desorption or to the formation of new species on the substrate, that will be discussed later.

(I.II) SURFACE DIFFUSION

Once absorbed on the surface, the species are in the minimum potential and can move along it but with restrictions, this is called surface diffusion. Diffusion occurs when the diffusion energy, E_{diff}, is smaller than the desorption energy, E_{desor}. Diffusion can happen through four main mechanisms (cf. Figure 1.9):

- THERMAL HOPPING: The atoms, located on an absorption site, move from one site to another by jumping

- QUANTUM TUNNELING: The atoms, located on an absorption site, move from one site to another by crossing the diffusion barriers and thus in straight movement. This is the case for particles with low mass and E_{diff}.

- VACANCY: The atoms on the surface jump in a free position, creating a new free position on the surface.
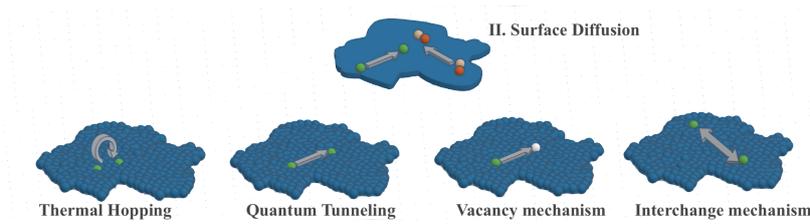
FIGURE 1.9: Diffusion mechanisms: thermal hopping, quantum tunneling, vacancy and interchange mechanisms.

- INTERCHANGE: The atoms exchange their positions with ones of the surface.

(I.III) DESORPTION

Desorption, contrary to adsorption, is the physical principle in which the molecules overcome the activation barrier and sublimate. Two desorption states can be distinguished: the thermal and the non-thermal state , which vary from each other from the thermodynamic conditions of the system.

The thermal desorption occurs when the system is in thermo-equilibrium. The species has thus to acquire a certain amount of energy to desorb from the change of temperature. Its desorption rate, r_{Tdesor} is described as follows:

$$r_{\text{Tdesor}} = f_n \cdot \theta_n \cdot exp\left(\frac{-E_{\text{b}}}{k_{\text{b}}T}\right) \tag{1.12}$$

in which, f is the frequency factor, θ is the surface coverage, k_{b} is the Boltzmann constant and, T is the temperature of state.

We point out that this desorption is strongly dependent on the type of substrate and on the adsorbate.

In this case, the frequency factor can be used as the frequency of vibration as it represents the bond between the molecule and the substrate. This frequency characterizes the state when the molecule attempts to detach from the substrate, in other words, when it attempts to desorb.

Contrarily to the thermal desorption, the non-thermal desorption refers to the resulting desorption from a local increase of energy (i.e., heat, kinetic energy, etc.) of the grain rather than an energy increase on the entire system.

The non-thermal desorption occurs when the system is subjected to a variation of energy from other bodies and/or chemical reactions (Markwick *et al.*, 2000; Dickens *et al.*, 2000; Bergin *et al.*, 1997; Willacy *et al.*, 1998). This can come from several sources: (a) the heating from an external source of energy, such as high energy photons (i.e., VUV, EUV, X-Ray) and particles (i.e., electrons and high energy particles). This process refers to the so-called photodesorption. This process does not inclusively lead to non-thermal desorption but also to photodissociation. (b) the sputtering which is the mechanical desorption of species on the grains due to collisions with neutral particles from the gas-phase (Flower and Pineau des Forêts, 1995). This process is common in outflows and more specifically in C-type shocks. (c) The chemical desorption which is a local heating of the grain due to exothermic reactions.

(II) Surface chemistry

So far, the possible physical processes going on the surface have been described, but the chemistry of the species can also play a role once on the surface. In the ISM, the dust constitutes the elementary surface for chemical reactions to occur, acting as a catalyst. Three processes can happen on the surface leading to molecular reactions: the Eley-Rideal mechanism, the Langmuir-Hinshelwood mechanism and the hot atoms mechanism also referred as the Kasemo-Harris mechanism. The most common mechanism modeled for the ISM chemistry is the Langmuir-Hinshelwood mechanism. The three are as shown in Figure 1.10.
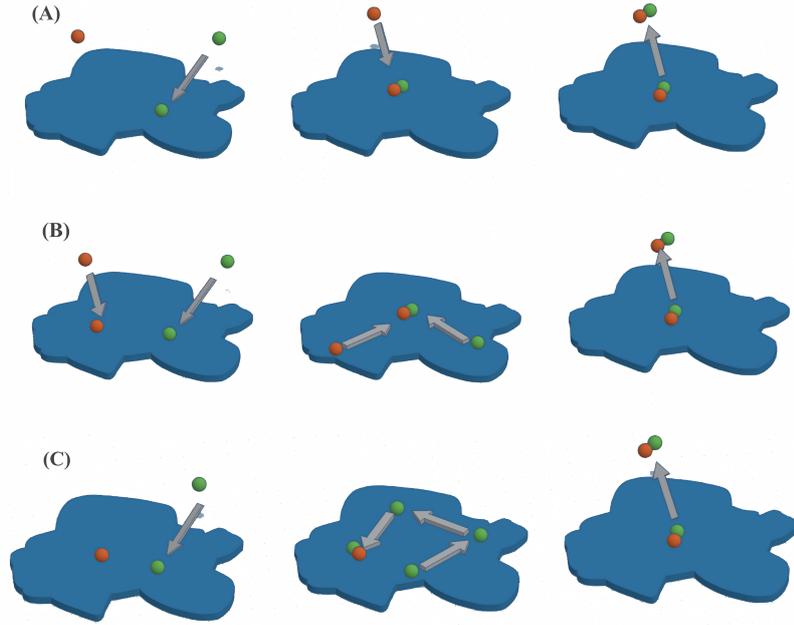
FIGURE 1.10: Surface Chemistry of species X and Y on dust grain (g) (a) Eley-Rideal mechanism (b) Langmuir-Hinshelwood mechanism (c) Kasemo-Harris mechanism.

(II.A) ELEY-RIDEAL MECHANISM (DIRECT MECHANISM)

The Eley-Rideal mechanism describes when a species, X, is adsorbed on the surface, while the other, Y, is still in a gaseous form. The species in the gas phase collides with the molecule on the surface and reacts with it. Their product is then desorbed in the gas phase. This is translated by Equation (1.15), in which the first arrow describes the adsorption process of species X on the grain (g) while, the second arrow describes the desorption of their product (Le Bourlot *et al.*, 2012; Ruaud *et al.*, 2015).

$$X + Y \quad \rightarrow \quad X : g + Y \quad \rightarrow \quad XY \qquad (1.13)$$

(II.B) LANGMUIR-HINSHELWOOD MECHANISM (DIFFUSIVE MECHANISM)

In the second mechanism, the species are both adsorbed on the substrate. At least one of the species is mobile, therefore, a diffusion process is observed. The adsorbed species meet and react with each other on the surface, and are potentially desorbed (Le Bourlot *et al.*, 2012). The adsorbed species react with each other if at least one of the molecules is mobile (i.e. diffusion process).

$$X + Y \quad \rightarrow \quad X : g + Y : g \quad \rightarrow \quad XY \qquad (1.14)$$
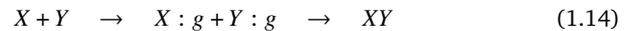
The corresponding analytical expression is shown in Equation (1.14), in which the first arrow points out the adsorption, while the second arrow describes the desorption after a diffusion process.

(II.C) KASEMO-HARRIS MECHANISM

This mechanism refers to a species adsorbed on the surface with an excess of energy as proposed by Harris and Kasemo (1981). With this extra energy, the species can move on the surface and react with other species already on the surface. This excess of energy is temporary, i.e., before its thermal equilibrium is reached. The product of their reaction, XY, is eventually desorbed later. The Kasemo-Harris mechanism on the species X and Y, is translated into equations as follows:

$$X : g + Y \quad \rightarrow \quad X : g + Y : g + Energy \quad \rightarrow \quad XY \qquad (1.15)$$
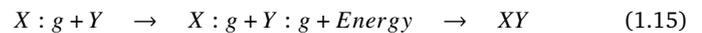
1.5.2   *Gas phase chemistry*

The gas phase chemistry in star-forming regions plays a major role in the environment of the protostars, especially when the temperatures are such that most of the species are in the gas phase (i.e., desorbed from the icy grains).

This chemistry is sensitive to the environmental conditions, i.e., temperatures, densities, etc. This influence of the physical conditions induces that the gas-phase chemistry in protostars is different than the chemistry observed in planetary systems. Moreover, within the protostar itself, we observe high differences in the gas phase throughout the envelope where the temperatures varies from 10 K to hundreds of K.

Two types of reactions might happen in the gas phase, the endothermic and exothermic reactions (Herbst and Klemperer, 1973). Both reflect how enthalpy varies from the initial state to the final. The endothermic reaction describes the system when the energy absorbed translates into heat. The enthalpy, Δh, is then positive. The exothermic reaction is the opposite and thus has negative enthalpy. In this case, the system releases the energy in the form of heat.

The molecular species are made of bonds among their different constituents. Due to chemical reactions, these bonds can be destroyed, rearranged and/or new bonds can be formed (Herbst and Klemperer, 1973; Smith, 2011).

The *bond formation* is mostly seen in radiative association, where collisions of species in the gas phase, cause the particles associate to form other species with the emission of a photon. This reaction is principally seen with hydrogen, as it is the most abundant atom in the ISM and thus has the highest probability of collision with other species (Herbst and Klemperer, 1973; Herbst and Klemperer, 1976).

The *bond destruction* is observed when an external form of energy is introduced in the system. In the protostellar environment, the external energy can be the UV radiation, cosmic rays, etc. Another source of energy can be the collisions with electrons, we will refer to dissociative recombination (Herbst and Klemperer, 1976; Wakelam *et al.*, 2017).

The last process describes the rearrangement of the bonds within a molecule. The species can be ions, molecule or neutrals, leading to the ion-molecules and the neutral-neutral reactions. This requires overcoming their activation barriers, contrary to ions-molecules reactions, which explains why such reactions occur in a high temperature environment, i.e., hot core.

1.6   HEATING AND COOLING PROCESSES, KEY DRIVERS OF THE DYNAMICS

Armed with an understanding of the chemical and physical processes discussed earlier, we can now approach another important aspect of the dynamics within clouds: the cooling and heating processes.

1.6.1   *Heating processes*

The heat is by definition an energy produced by a thermodynamic system. In the ISM, the sources of heat are various. Two main heating processes are identified, cosmic rays and interstellar irradiation.

Cosmic rays are mostly made of protons, heavy elements and electrons. Their interaction with the cloud ultimately leads to heat transfer, through several steps. First, the impact of the protons with the most abundant element of the ISM, H_2, generates ionization (Prasad and Tarafdar, 1983):

$$p^+ + H_2 \rightarrow H_2^+ + e^- + p^+ \tag{1.16}$$

There is no heat transfer at this stage, this later is related to the produced electron. This can take several routes, such as a further ionization of H_2 or dissociation of H_2, which heats the flow, as follows:

$$e^- + H_2 \rightarrow H + H + e^- \tag{1.17}$$

The local heating of the gas due to dissociation, leads to the desorption of nearby molecules, which was discussed earlier as a non-thermal desorption process. In this case, we refer to the cosmic-ray induced photodesorption. The presence of the photons is from recombination. For example, in the case of Eq. (1.16), the

recombination of H_2^+ and the electron will form H_2 and photons. It is also possible to witness desorption of molecules from cosmic ray impacts on the dust grain, which generates heat. This later case refers to the so-called direct cosmic ray heating (Roberts *et al.*, 2007).

The second important heating source is the interstellar radiation field, typically lower in energy than cosmic rays. The origin of this emission is from O- and B- stars. As it is the case for the cosmic rays, the UV radiation field might lead to the one of the previously discussed non-thermal desorption processes: the UV photodesorption. This second heating source acts on several aspects (Stahler and Palla, 2005):

- Carbon ionization UV: the UV component from the radiation field is too weak to ionize the hydrogen, thus molecules with lower ionization potential are affected by this UV component. The principal one is the atomic carbon, from which an electron will be ejected. This collides with the surrounding elements, leading to efficient heating mechanism.

- Photoelectric heating results from the interaction of UV photons with the dust grains, assuming that the grain is electrically neutral. This energy separates electrons from the surface. Two possibilities occur from this interaction, as shown in Figure 1.11. (a) the electrons escape from the surface. (b) the electrons' energy is transferred to the grain lattice by collision. This (b) option refers to the later discussed dust irradiation.

- Dust irradiation: This transfer of energy to the lattice leads to the radiation of infrared photons by the grain. In this case, the increase of temperature is on the grain and not to the gas. A heat energy transfer between these two components would be possible for high cloud densities as such collisions are efficient.
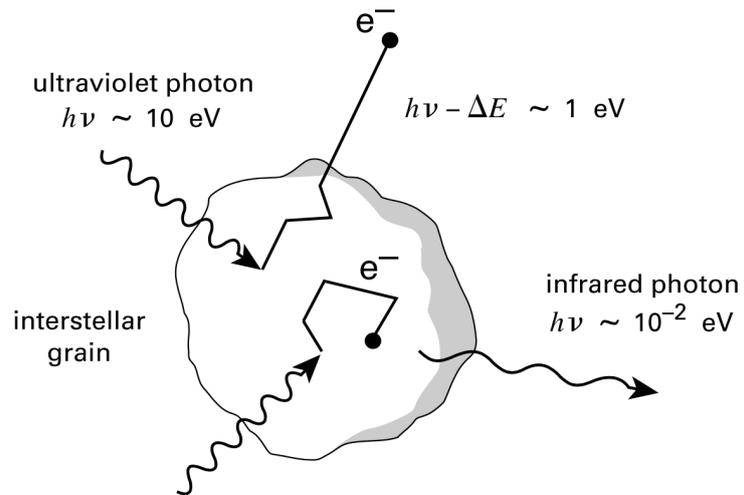
FIGURE 1.11: UV photons interaction with dust grain. Two mechanisms are represented: (a) the photoelectric heating (b) the dust irradiation. Figure taken from Stahler and Palla (2005).

1.6.2 *Cooling processes*

Proceeding inwards, we now consider the cooling mechanisms and thus when the clouds loose energy. Cooling in the ISM is induced by atoms, molecules or dust grains.

The primary source of cooling is the radiation emitted from the gaseous species. Species can be excited by collisions with hydrogen atoms, in a non-dense environment (hydrogen density (n_H)« species critical density(n_{crit})[6]. Under such conditions, the collisional excitation is followed by radiative decay. In the opposite case, it is followed by a collisional de-excitation rather than the radiative decay.

Although hydrogen and helium are the most abundant elements in the ISM, these are not effective coolants. Instead, other abundant species such the neutral atomic

[6]This concept will further elaborated in Section 2.1.6

oxygen [O I] and carbon, which have similar elemental abundances, are prone to collisions with hydrogen. As we explained previously, atomic carbon is efficiently ionized by UV radiation, therefore it is [C II] emission, which is the main actor of the cooling.

Collisions do not happen only with atoms but also with the other ISM constituents: molecular species and the dust grains. Radiative emission of infrared photons is obtained from collisions of several molecular species with hydrogen particles; in particular, from H_2O and O_2, which are so-called cooling agents. However, the most efficient cooling agent is CO.

As the reader might have noticed, the grains are important heating agents of the gas, through the adsorption of UV photons. However, energy can also be transferred to the dust grains through collisions, from which the dust grains radiate.

1.7   THE SULPHUR CHEMISTRY, WHERE DO WE CURRENTLY STAND?

Astrochemistry is a complex matter. Over the years, scientists have tried to determine whether the chemical legacy of a planet forming system is determined by the inheritance or reset scenario from the molecular cloud. In the case of inheritance, the chemical characteristics are preserved from the parent cloud, while in the case of reset, strong physical processes as, for example, strong dissociative shock in a dense media, would entirely initialise the chemical environment, where the chemistry would start again from atomic abundance (Pontoppidan and Blevins, 2014).

To tackle these questions, the molecular chemistry of several species have been studied in-depth. A very well known and understood chemistry is the one associated to CO. However, some other families are poorly understood, as is the case for sulphur chemistry. Currently, sulphur chemistry is not well constrained and only understood at a superficial level.

From the pre-collapse to the disk, the density varies by $\sim 10^4$ cm^{-3} and the temperature varies from 10 K to 300 K. The molecular species have therefore time to undergo freeze-out and desorption throughout the different parts.

In the cold part of the envelope (T$\sim$10 K), the species are adsorbed on the icy dust grains, where they react with each other to produce simple molecules but also complex ones. At this part of the envelope, desorption is possible by non-thermal processes only, as the dust temperature is too low to efficiently desorb the molecules on the grain surface. The formed molecules at this stage are referred as of the 0th-generation by Herbst and van Dishoeck (2009). At this stage, CO was adsorbed on the grains and has led to products such as H_2CO, HCO, CH_3OH, CH_2CH_3OH, etc. The collapsing envelope is associated to an increase of temperature, leading to the thermal desorption process. During this warm-up, the species of the 1st generation are created. These are formed by the produced species from the photo-dissociation of the 0th generation molecules.

Moving further to the center, when reaching the hot core region, temperature easily rises to hundreds of kelvins. At this location, all the molecules have desorbed from the grains and are in the gas phase. The high temperatures reached allow to overcome energy barriers and thus new chemical reactions in the gas-phase can take place (Jørgensen *et al.*, 2016). The molecules resulting from these reactions are the so-called 2nd generation molecules. The described path of CO throughout the different stages of the protostar is shown in Figure 1.12 from Herbst and van Dishoeck (2009).

Most of the observational studies point towards an inheritance scenario. Jørgensen *et al.* (2020) suggested from the chemical complexity (i.e., first and second generations) that the forming stars have inherited the chemistry from the protostellar phase.

We turn now our attention to the sulphur chemistry. As mentioned earlier, our current knowledge on this chemistry is limited. The first unknown arises from the origin of the S-reservoir in the pre-collapse phase. Atomic sulphur, is one of the most abundant species in the ISM (S/H $\sim 1.3{\times}10^{-5}$, Asplund *et al.*, 2009).

However, in the pre-collapse, it is unknown whether the atomic sulphur remains in its atomic form while on the grain, or if it reacts efficiently with the other compounds. Moreover, the extent of its reactions is unknown. It is believed that the
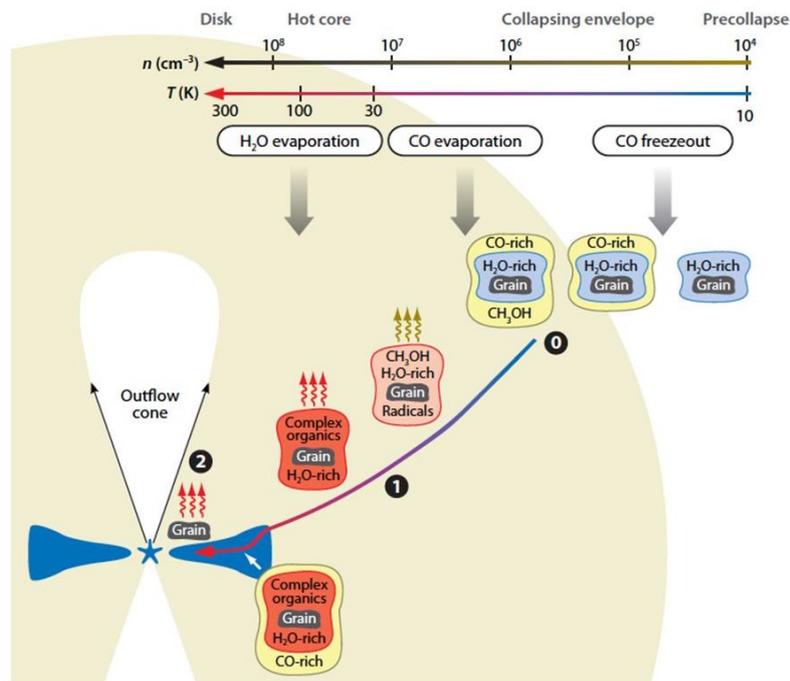
FIGURE 1.12: Schematic representation of the molecular evolution from the pre-collapse stage until the protoplanetary disk. The temperature and density scales of the different parts are shown on top of the figure. The indexes 0, 1, and 2 are placed in the locations where are formed the 0th, 1th and 2nd generation molecules, respectively. Figure from Herbst and van Dishoeck (2009).

some S-reservoirs such as H_2S and OCS are present on the grains and generate further 0th generation molecules but it has not been quantified (Laas and Caselli, 2019; Vidal et al., 2017). During the warm-up phase, we expect to see the desorbed 0th generation S-species in the gas-phase, and their further reaction might lead to 1st generation of molecules. Still, there is atomic sulphur which might be ionized in the form of S^+, which strongly impacts the degree of ionization of the gas. At this stage, several S-species have already been detected towards several protostellar environments and several formation paths have been suggested in the literature by e.g., Vidal and Wakelam (2018), Neufeld et al. (2015), and Wakelam et al. (2011). It was demonstrated that some sulphur molecules, such as SO and SO_2, are reliable tracers of the warm chemistry, i.e., under typical temperature condition of hot cores and outflows, and thus form efficiently in the gas phase (e.g., Pineau des Forêts et al., 1993; Tabone et al., 2017; Artur de la Villarmois et al., 2018). Moreover, the main abundant organosulphurs, i.e., OCS, H_2CS and CS, which are principally formed on the icy dust grains under low temperatures, are tracers of this region. At this stage, it is unclear whether the main sulphur reservoir in the cold envelope (T~10 K) is H_2S as suggested by Minh et al. (1990), Charnley (1997), and Vidal and Wakelam (2018) or in the form of organosulphurs (Laas and Caselli, 2019; van der Tak et al., 2003).

Furthermore, with our current knowledge, it is still not possible to reconcile the models predicting the sulphur abundances with the observations, as there is a discrepancy between the elemental S-abundance and the one derived from the S-species (Le Gal et al., 2019; Holdship et al., 2016).

The sulphur chemistry is therefore a so-called hot topic, and understanding how its chemistry has evolved throughout the protostar is a key aspect. It will provide insights on the possible inheritance or reset scenario, which is essential to understand the origin of sulphur species in planets, and ultimately on Earth, as these are prebiotic species.

Bibliography

1. P. André *et al.*, presented at the The Labyrinth of Star Formation, vol. 36, p. 225.

2. H. Arce *et al.*, presented at the Protostars and Planets V, ed. by B. Reipurth, D. Jewitt, K. Keil, p. 245, arXiv: `astro-ph/0603071 [astro-ph]`.

3. E. Artur de la Villarmois *et al.*, *A&A* **614**, A26, (`https://doi.org/10.1051/0004-6361/201731603`) (2018).

4. M. Asplund *et al.*, *ARA&A* **47**, 481–522, eprint: `https://doi.org/10.1146/annurev.astro.46.060407.145222`, (`https://doi.org/10.1146/annurev.astro.46.060407.145222`) (2009).

5. R. Bachiller, *ARA&A* **34**, 111–154 (Jan. 1996).

6. J. Ballesteros-Paredes, L. Hartmann, E. Vázquez-Semadeni, *ApJ* **527**, 285–297, arXiv: `astro-ph/9907053 [astro-ph]` (Dec. 1999).

7. J. Bally, *Annual Review of Astronomy and Astrophysics* **54**, 491–528, eprint: `https://doi.org/10.1146/annurev-astro-081915-023341`, (`https://doi.org/10.1146/annurev-astro-081915-023341`) (2016).

8. Belloche, A. *et al.*, *A&A* **561**, C1, (`https://doi.org/10.1051/0004-6361/201321096e`) (2014).

9. E. A. Bergin *et al.*, *ApJ* **482**, 285–297 (June 1997).

10. A. A. Boogert, P. A. Gerakines, D. C. Whittet, *Annual Review of Astronomy and Astrophysics* **53**, 541–581, eprint: `https://doi.org/10.1146/annurev-astro-082214-122348`, (`https://doi.org/10.1146/annurev-astro-082214-122348`) (2015).

11. S. Bottinelli *et al.*, presented at the From Atoms to Pebbles: Herschel's view of Star and Planet Formation, 19, p. 19.

12. S. Charnley, *ApJ* **481**, 396–405 (May 1997).

13. H. Chen *et al.*, *ApJ* **445**, 377 (May 1995).

14. D. Cornu, *Selection of Spitzer YSO candidates using Deep Learning classifiers*, 2018.

15. R. M. Crutcher, *ApJ* **520**, 706–713 (Aug. 1999).

16. J. Dickens *et al.*, *ApJ* **542**, 870–889 (Oct. 2000).

17. B. Draine, *ApJ* **241**, 1021–1038 (Nov. 1980).

18. B. Draine, *ARA&A* **41**, 241–289, arXiv: `astro-ph/0304489 [astro-ph]` (Jan. 2003).

19. D. Flower, G. Pineau des Forêts, *MNRAS* **275**, 1049–1056 (Aug. 1995).

20. P. J. V. Garcia, J. M. Ferreira, *Jets from Young Stars IV*, vol. 793.

21. A. Gusdorf, *Lecture notes on Studies of interstellar shocks*, Dec. 2019.

22. A. Gusdorf *et al.*, *Astronomy Astrophysics* **532**, A53, ISSN: 1432-0746, (`http://dx.doi.org/10.1051/0004-6361/201116758`) (July 2011).

23. A. Gusdorf *et al.*, *A&A* **575**, A98, (`https://doi.org/10.1051/0004-6361/201425142`) (2015).

24. J. Harris, B. Kasemo, *Vacuum* **31**, 511 (Oct. 1981).

25. T. Henning, *Annual Review of Astronomy and Astrophysics* **48**, 21–46, eprint: `https://doi.org/10.1146/annurev-astro-081309-130815`, (`https://doi.org/10.1146/annurev-astro-081309-130815`) (2010).

26. E. Herbst, W. Klemperer, *Physics Today* **29**, 32–39 (June 1976).

27. E. Herbst, W. Klemperer, *ApJ* **185**, 505–534 (Oct. 1973).

28. E. Herbst, E. F. van Dishoeck, *ARA&A* **47**, 427–480 (Sept. 2009).

29. J. Holdship *et al.*, *Monthly Notices of the Royal Astronomical Society* **463**, 802–810, ISSN: 0035-8711, eprint: https://academic.oup.com/mnras/article-pdf/463/1/802/18471485/stw1977.pdf, (https://doi.org/10.1093/mnras/stw1977) (Aug. 2016).

30. J. C. Ibáñez-Mejıa, M.-M. Mac Low, R. S. Klessen, *arXiv e-prints*, arXiv:2108.04967, arXiv: 2108.04967 [astro-ph.GA] (Aug. 2021).

31. J. Jørgensen, A. Belloche, R. Garrod, *ARA&A* **58**, 727–778, arXiv: 2006.07071 [astro-ph.SR] (Aug. 2020).

32. J. Jørgensen *et al.*, *A&A* **595**, A117, arXiv: 1607.08733 [astro-ph.SR] (Nov. 2016).

33. M. R. Krumholz, *Star Formation*.

34. J. C. Laas, P. Caselli, *A&A* **624**, A108, (https://doi.org/10.1051/0004-6361/201834446) (2019).

35. J. Le Bourlot *et al.*, *Astronomy Astrophysics* **541**, A76, ISSN: 1432-0746, (http://dx.doi.org/10.1051/0004-6361/201118126) (May 2012).

36. R. Le Gal *et al.*, *ApJ* **876**, 72, (%5Curl%7Bhttps://doi.org/10.3847%2F1538-4357%2Fab1416%7D) (May 2019).

37. S. Maret *et al.*, *ApJ* **698**, 1244–1260, arXiv: 0904.0603 [astro-ph.SR] (June 2009).

38. A. Markwick, T. Millar, S. Charnley, *ApJ* **535**, 256–265 (May 2000).

39. M. Min *et al.*, *A&A* **486**, 779–780, (https://doi.org/10.1051/0004-6361:20065436e) (2008).

40. Y. Minh *et al.*, *ApJ* **360**, 136 (Sept. 1990).

41. Y. Minh *et al.*, *ApJ* **723**, 1231–1240 (Nov. 2010).

42. P. Myers, E. Ladd, *ApJ* **413**, L47 (Aug. 1993).

43. D. Neufeld *et al.*, *A&A* **577**, A49, arXiv: 1502.05710 [astro-ph.GA] (May 2015).

44. G. Pineau des Forêts *et al.*, *MNRAS* **262**, 915–928 (June 1993).

45. K. Pontoppidan, S. Blevins, *Faraday Discussions* **168**, 49–60, arXiv: 1406.1457 [astro-ph.EP] (May 2014).

46. S. Prasad, S. Tarafdar, *ApJ* **267**, 603–609 (Apr. 1983).

47. B. Reipurth, A. Raga, presented at the The Origin of Stars and Planetary Systems, ed. by C. J. Lada, N. D. Kylafis, vol. 540, p. 267.

48. J. F. Roberts *et al.*, *Monthly Notices of the Royal Astronomical Society* **382**, 733–742, ISSN: 0035-8711, eprint: https://academic.oup.com/mnras/article-pdf/382/2/733/3428774/mnras0382-0733.pdf, (https://doi.org/10.1111/j.1365-2966.2007.12402.x) (Nov. 2007).

49. M. Ruaud *et al.*, *Monthly Notices of the Royal Astronomical Society* **447**, 4004–4017, ISSN: 0035-8711, eprint: https://academic.oup.com/mnras/article-pdf/447/4/4004/5811190/stu2709.pdf, (https://doi.org/10.1093/mnras/stu2709) (Jan. 2015).

50. M. Schmalzl *et al.*, *A&A* **572**, A81, (https://doi.org/10.1051/0004-6361/201424236) (2014).

51. F. Shu, *ApJ* **214**, 488–497 (June 1977).

52. F. Shu, presented at the The Milky Way Galaxy, ed. by H. van Woerden, R. Allen, W. Burton, vol. 106, pp. 561–566.

53. I. W. Smith, presented at the The Molecular Universe, ed. by J. Cernicharo, R. Bachiller, vol. 280, pp. 361–371.

54. S. Stahler, F. Palla, *The Formation of Stars, by Steven W. Stahler, Francesco Palla, pp. 865. ISBN 3-527-40559-3. Wiley-VCH , January 2005.* (Jan. 2005).

55. B. Tabone *et al.*, *A&A* **607**, L6, arXiv: 1710.01401 [astro-ph.SR] (Nov. 2017).

56. S. Terebey, F. Shu, P. Cassen, *ApJ* **286**, 529–551 (Nov. 1984).

57. M. A. Thompson, G. H. Macdonald, *Astron. Astrophys.* **407**, 237–248, arXiv: astro-ph/0305504 (2003).

58. F. F. S. van der Tak *et al.*, *A&A* **412**, 133–145, ISSN: 1432-0746, (http://dx.doi.org/10.1051/0004-6361:20031409) (Nov. 2003).

59. S. J. van der Walt *et al.*, *Astronomy Astrophysics* **655**, A86, ISSN: 1432-0746, (http://dx.doi.org/10.1051/0004-6361/202039950) (Nov. 2021).

60. T. H. G. Vidal, V. Wakelam, *MNRAS* **474**, 5575–5587, ISSN: 1365-2966, (http://dx.doi.org/10.1093/mnras/stx3113) (Jan. 2018).

61. T. H. G. Vidal *et al.*, *MNRAS* **469**, 435–447, ISSN: 1365-2966, (http://dx.doi.org/10.1093/mnras/stx828) (Apr. 2017).

62. V. Wakelam, F. Hersant, F. Herpin, *A&A* **529**, A112, arXiv: 1103.2860 [astro-ph.GA] (May 2011).

63. V. Wakelam *et al.*, *Molecular Astrophysics* **9**, 1–36, ISSN: 2405-6758, (https://www.sciencedirect.com/science/article/pii/S2405675817300271) (2017).

64. C. Wang, R. Gomer, *Surface Science* **90**, 10–36 (Dec. 1979).

65. K. Willacy *et al.*, *A&A* **338**, 995–1005 (Oct. 1998).

66. L. M. Ziurys, *Proceedings of the National Academy of Sciences* **103**, 12274–12279, ISSN: 0027-8424, eprint: https://www.pnas.org/content/103/33/12274.full.pdf, (https://www.pnas.org/content/103/33/12274) (2006).

2

Methods

In the first chapter, we described the protostellar system from the macro to microscopic scales. On the macroscopic side, the birth of the protostar was explained from a physical point of view, as well as an overview of the different regions of the protostellar environment which are studied in the thesis. On the other side, we described our current knowledge of the physical and chemical processes occurring in the protostar on the microscopic scale, which are extremely relevant for understanding the chemistry in these regions.

The star-forming regions, which are outside our solar system, are challenging for the types of space missions possible in our solar system, such as rovers, spectrometers aboard spacecraft, etc. due to the limitations of the current technology and the farness of the regions of interest. Thus, different methods are used to understand these regions. In this research, the three currently available methods are considered: modeling, observation by means of telescopes and in-situ laboratory experiments, each described by a section of this Chapter.

Characterizing the star-forming regions is not part of a cook-book, as each region is different and none of the three methods are sufficient to fully understand the regions independently, as each process has its limitations. Therefore, these three methods provide us insights of some aspects of the SFR and should be used in a complementary way.

2.1 OBSERVATIONS

Invaluable information is made accessible by telescopes. These provide us observations of molecular spectra and maps at different wavelengths of the observed regions. In this Section, we will explain what exactly is observable, which tools are used for the observations and finally how are the data reduced before being ready for the analysis.

2.1.1 *What can we detect?*

Molecules and atoms have unique emission line spectrum, which allow us to identity them in a band spectrum. Moreover, each line of a species corresponds to a specific energy state. Therefore, we should first explain what are the different energy levels of a species. Each species has a total energy, which is composed of its electronic, vibrational and rotational energies.

An atom or molecule is made of the nuclei and a certain amount of electrons. When there is a source of energy (i.e., photon at the right frequency), the electrons can jump to an excited state of the molecule/atom. We differentiate the ground state which is the lowest energy level, to the excited states, which are higher energy states than the ground state. The electrons within the molecule/atom can therefore transition within the different energy levels, i.e., the different orbitals, of the species. These changes of energy levels are characteristic of the so-called electronic excitation.

Unlike atoms, molecules undergo two other energies, due to the motion of the molecule. Both energies are related to the discrete energy levels of the Morse potential curve[1].

[1] This represents the potential energy surface of a molecular electronic state.

The vibrational energy is from the movement of the molecules along the bonds principal axes. It refers to the oscillations of the bonds, and thus to the modification the internuclear distance.

The rotational energy is from the movement of the molecule in three dimensions (Tielens, 2005). Each electronic state is composed of a set of vibrational states, which are themselves each associated to a set of rotational levels, as can be seen in Figure 2.1. Consequently, the rotational level has lower energy levels than the vibrational levels, which are lower than the electronic ones.

To illustrate the different energy states, let's take the example of the diatomic molecule H_2, which is made of two protons and 2 electrons. A differentiation is made between the ortho- and para-H_2. The ortho-H_2 means that both nuclei (nuclei of each atom) spin in the same direction, while the para-H_2 refers to the case where the nuclei spin in opposite directions. Moreover, para-H_2 will occupy the even rotational levels and the ortho-H_2, in the odd rotational levels. Quantum notation is used for pointing the different energy states. The letters v and J are used for referring to the vibrational and rotational states, respectively. In the case of H_2, letter S, Q and O are used in the quantum notation and refers to a change of J levels from the upper to lower level, corresponding to 2, 0 and -2, respectively. Moreover, for jumping from v=0 to v=1, a level energy of 6000 K is required, while from J=0 to J=2, and from J=1 to J=3, the system would require an energy of 510 K and 845 K, respectively (Field *et al.*, 1966). We will therefore see rotational excitation of H_2 starting at temperatures much lower than the vibrational excitation, i.e., T≥100 K vs. T≥1000 K.

It is clear now to the reader that molecules display more degree of freedom than atoms. As each energy state has its specific emission line, molecular spectral lines will be spread over more frequency space than atoms, in a spectral band.
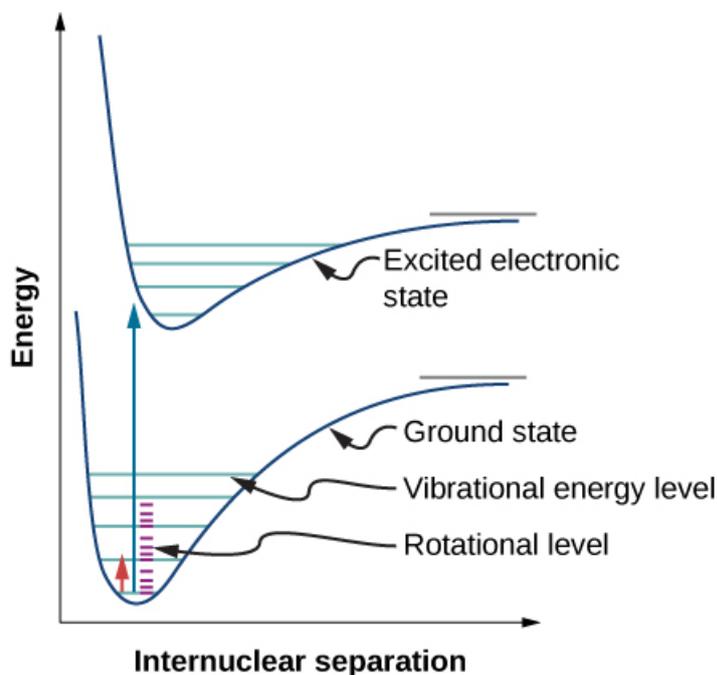
FIGURE 2.1: Representation of the Morse potential curve (blue curve), displaying the different energy levels. Two Morse potential curves correspond to different electronic levels, here the ground state and excited state. Within each electronic state, the different vibrational and rotational levels are shown. Credit: Ling *et al.* (2016)

This is translated by the molecular transitions observed at different wavelengths: the rotational transitions are observed at (far-)infrared range, the vibrational levels and ro–vibrational levels are detected at the infrared range. While, the electronic states are observed at the ultraviolet-visible spectra. The infrared range ($\sim 0.8 \mu$m up to $\sim 100 \mu$m is composed of the near-, mid- and far-infrared (their respective frequency range is shown in Figure 2.2).
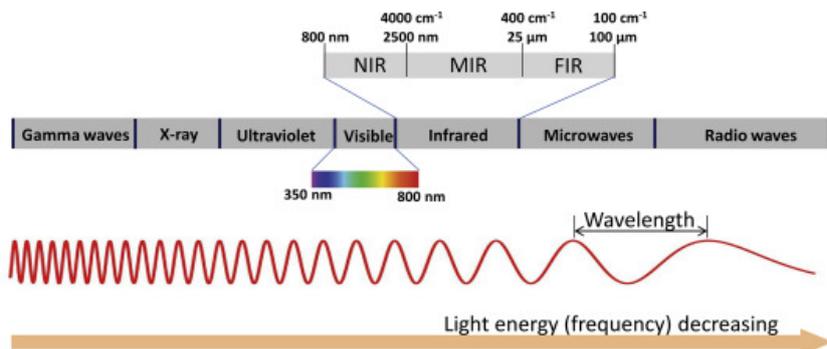
FIGURE 2.2: Spectrum displaying the frequency waves from the Gamma waves to the Radio waves. The infrared spectrum is categorized into the Near-, mid- and far-infrared (NIR, MIR, FIR), as a function the wavelength. Figure taken from Pu *et al.* (2020)

The spectral features in the infrared domain provide insights on the gas-phase and solid-state in different astronomical environments. In this way, the rotational and vibrational levels of the species are observed. A spectrum can show features such as emission lines, characteristic of the gas-phase and, absorption lines, characteristic of solid-state(van Dishoeck and Blake, 1998; Stahler and Palla, 2005; Jørgensen *et al.*, 2020).

2.1.2 *How can we detect the species?*

Observations are carried by telescopes. We find several of them on Earth, at strategic locations, such as IRAM-30m (Institut de radioastronomie millimetrique) in the Spanish Sierra Nevada, ALMA (Atacama large (sub)millimeter array) in Chile, etc. These ground telescopes are built at high altitude, where the weather is dryer, in order to reduce the atmospheric contamination, from which they are not entirely free. We therefore have access to several observable windows, at the mm and submm range, with the ground telescopes, but at other wavelengths are limited. These (sub)mm windows give access to most of the rotational transitions, allowing us to observe numerous species. Unfortunately, some of them, i.e., H_2 and several atomic lines can not be traced by ground-based telescopes as, most of the pure rotational transitions are located in the NIR/MIR window. At these infrared wavelengths, the Earth's atmosphere is opaque, meaning that the infrared light is absorbed by the atmosphere, mainly due to water vapour, O_2 and CO_2. Observations at strong absorption bands around 6–8 μm (H_2O), 9.5 μm (O_2), 14–16 μm(CO_2) are not possible. Moreover, the Earth's atmosphere radiates at 10 μm, narrowing even further the observable window from the ground (Kratz and Cess, 1985; Solomon *et al.*, 1998).

The alternative for carrying out observations are the telescopes located in orbit. In space, the entire infrared spectrum can be observed, as the observations do not suffer from the Earth's atmospheric effects. However, the space facilities for observations are limited due to their expensive building costs and the lack of accessibility during their operational time. These telescopes have also a limited operational life (e.g., 4 years for *Herschel space observatory* and 17 years for *Spitzer space telescope*, observing the frequency range 60–670 μm and 3–40 μm, respectively). Currently, there is no operational space telescope for infrared ranges and new hopes are projected towards the James Webb Space Telescope (JWST), which was launched in December 2021.

In this thesis, we used principally observations from ground-based telescopes.Two types of ground-based telescopes exist which operate at the mm and sub-mm wavelengths: (a) the single dish telescopes and (b) the interferometry, which consists of an array of several telescopes. In the following sections, we will explain in details the working principles of these ground-based telescopes and provide an overview of the facilities used.

2.1.3 *Single-dish observations*

As it name indicates, single-dish observations are carried out from one antenna, with a diameter, D. The resolution of observations, θ, at specific wavelength, λ, depends

on the wavelength and the antenna diameter, as follows (Rayleigh, 1879):

$$\theta = \frac{\lambda}{D} \tag{2.1}$$

This relation highlights that for increasing the spatial resolution (θ value), either a larger telescope is needed or, shorter wavelengths should be observed. If specific lines (i.e., wavelength) are targeted, for achieving a low resolution, a large telescope diameter is necessary, which is unfortunately limited in size due to technical aspects (i.e., structure and stability of the telescope). However, the current size of single-dish telescopes range between tens and hundreds of meters, which allow us to already achieve a high level of detail.

Out of the two types of telescopes, the single-dish telescope is the less complex system. It can be a prime focus or a Cassegrain system. In the following, only the Cassegrain will be explained, as it is charateristic of the telescope used for the observations of this thesis. It consists of a main parabolic reflector surface (i.e., dish) which is placed in the direction of the celestial object of interest. The emitted wavelengths from the source are collected by the dish which reflects them towards a subreflector, located in the focal point of the main reflector. There, the energy from the electromagnetic waves is focused and reflected to the feed horn, which is a flared waveguide, connecting the radiated to the conductive emission (Oberheuser, 1979; Liu *et al.*, 2020). The conductive emission finally proceeds into the receiver, where the signal is coupled, polarised and amplified. The signal is then digitized and processed, as shown in Figure 2.3. Single-dish telescopes such as the Atacama Pathfinder EXperiment (APEX) in Chile and IRAM-30m in Spain, shown in Figure 2.4, are used in this thesis. The APEX has a main diameter of 12 m and reaches an angular resolution of ~27″ at 1.3 mm (Güsten *et al.*, 2006) while the IRAM-30m has a diameter of 30 m and a resolution ~27″ at 3 mm (Greve *et al.*, 1996).
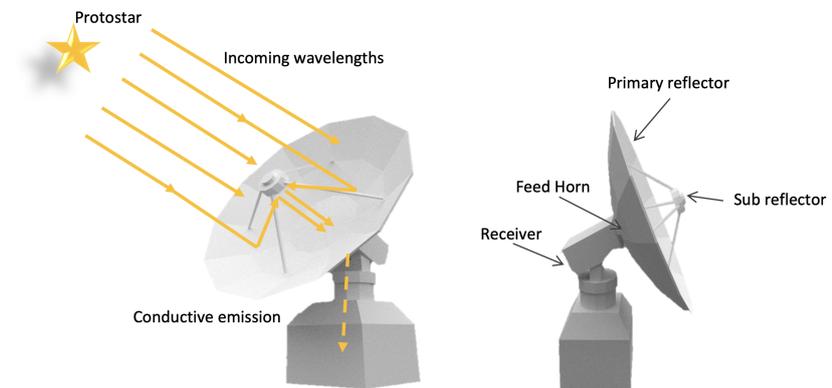
FIGURE 2.3: Schematic overview of the single-dish antenna- Cassegrain system

FIGURE 2.4: Single-dish telescopes. *left:* the Atacama Pathfinder EXperiment (APEX) in the Chajnantor plateau Chile. *right:* the IRAM-30m in Pico Veleta, Spain. Credits: *left:* APEX *right:* O'Sullivan, E.

IRAM-30m

The 30-meter telescope is a single-dish parabolic antenna of the IRAM facility and, is located in Pico Veleta, the Spanish Sierra Nevada, at ~2850 m altitude. It is currently one of the most sensitive radio telescope tracing millimeter wavelengths, allowing to explore the nearby galaxies and interstellar clouds (Baars *et al.*, 1987).

This telescope is equipped of three main instruments: EMIR (Eight MIxer receiver), HERA (HEterodyne Receiver Array) and NIKA2, which is dual-band camera. In the following, we will further discuss the EMIR instrument as it is the one used for data collected in the first article (cf., Chapter 5). An in-depth explanations of the other instruments can be found in Carsten and Sanchez Portal (2017). The EMIR receiver operates at 3, 2, 1.3, and 0.9 mm, covering a wide range of frequencies from ~75 GHz to ~375 GHz. This receiver is coupled with a FFTS (Fast Fourier Transform Spectrometer), working at 200 kHz or 50 kHz resolution. (Carsten and Sanchez Portal, 2017) The FFTS is a tool analysing the signal, its principle consists of two steps: the sampling through a ADC (analogue to digital converter) and the Field Programmable Gate Array (FPGA), which is the part performing the FFT calculation (Müller *et al.*, 2006; Klein *et al.*, 2009).

Once the data are collected, these are calibrated by the GILDAS software (Gildas Team, 2013).

2.1.4 *Interferometric observations*

For observing at low resolution with smaller wavelengths, the inteferometry method is used. This consists of combining the observations of several telescopes observing simultaneously, such that a baseline is created and the emission is superimposed to create a final output. In this way, all the antennas combined work as one large single-dish, reaching a collecting area up to ~6000 m^2 (with ALMA, Wootten, 2002). The individual antenna has the same technical system as the single-dish antenna, as shown in Fig. 2.3. However, once collected, the signals from all the telescopes are combined by the means of a correlator. The angular resolution of the observations is also determine by Equation (2.1), however, the diameter, D, is now equal to the longest baseline. This combination of arrays allows to reach an angular resolution up to ~0.01″ for band 6 and 7[2], by ALMA in its most extended configuration, i.e., C43-9 and C43-10 configurations which have a maximum baselines of 13.8 km and 16.1 km, respectively (Remijan *et al.*, 2019). This telescope is one of the largest telescopes providing interferometric observations on Earth. In a single dish antenna, the diameter is proportional to the angular resolution, while in the interferometers, the maximum separation among the antennas is proportional to the resolution. For both, the sensitivity is driven by the collecting area. When the source is not a point source, a good sensitivity is required for identifying the small-scale structure of an object, as it is the case for the observations discussed in Chapter 6. Such high resolution is essential to differentiate the different components of a structure, in this case, i.e., the inner structure of a shock region. Selecting the best telescope for the observations is a trade-off based on the scientific goal. Some case studies do not require having the highest possible angular resolution, as they aim at recovering the extended emission. This is not possible with high angular resolution as part of the emission is filtered. When aiming at high angular resolution observations, the ALMA facility is preferred if the target is in the line of sight of this telescope. However, when a lower angular resolution and lower line sensitivity is suitable for the science goal, then the submillimeter array in Mauna Kea (SMA) is used, which has a smaller maximum baseline and thus a lower achievable angular resolution (~3-4″, Ho *et al.*, 2004; Blundell, 2005) while having a large field of view. Moreover, the technical features of the SMA gives access to a wide coverage of frequencies during one round of observations. Some of the observations described in Chapters 5 and 7 are carried by the SMA as they provided suitable resolution for studying the sulphur emissions from the objects of interest. Both telescopes are illustrated in Figure 2.5.

[2]These bands correspond to the spectral range: 211 to 275 GHz for band 6 and, 275 to 373 GHz for band 7

FIGURE 2.5: Interferometric telescopes. *left:* the submillimeter array (SMA) in Mauna Kea, Hawaii. *right:* the Atacama Large Millimeter/submillimeter Array in the Chajnantor plateau Chile. Credit: *left and right:* ESO

(I) ALMA

The ALMA complex is made up of 66 antennas (54 antennas with 12 m diameter, known as the 12-m array, and 12 antennas with 7 m diameter, also known as the Atacama compact array, ACA) in the Atacama desert in Chile at 5000 m altitude, considerably reducing the atmospheric effects. These antennas operate at 3.6 up to 0.32 mm (~84–950 GHz) and have angular resolutions from 0.01″ to 12.5″, depending on the configurations and the observed band (i.e., frequencies). Eleven main configurations can be done (ten for 12 m arrays, one for the ACA) and the maximum baseline reaches up to 16 km and down to a resolution of 0.0122″ for band 7. Seven receivers are available for the different configurations, covering the so-called band 3 to band 10, corresponding to the spectral ranges, 84–116 GHz, 125–163 GHz, 158–211 GHz, 211–275 GHz, 275–373 GHz, 385–500 GHz, 602–720 GHz, 787–950 GHz, respectively (Remijan *et al.*, 2019).

The specificity of interferometers is the correlator which connects the signals among all the antennas. Two correlators are available for ALMA, the baseline correlator (BLC) for the 12 m array and the ACA correlator for the compact array (Escoffier *et al.*, 2007; Remijan *et al.*, 2019). However, as the observations used in Chapter 6 are from the 12 m array, only its corresponding correlator will be detailed. The reader can refer to the ALMA technical handbook of cycle 8[3] for further details on both correlators.

The BLC has two modes: the time division mode (TDM), which is used for continuum observations and the frequency division mode (FDM), used for spectral-lines observations. Differentiation is made between the two types of observations as the spectral lines require a higher spectral resolution than continuum observations (Escoffier *et al.*, 2007).

The data from the receiver is sent to a tunable filter bank card (TFB) which finds the change/delay in positions and selects bandwidth, and then the station card, which finds the time delays, re-orders and packetizes samples. Once ordered, the signals of all the selected antennas are sent to the correlator which connects them inside a matrix. The difference between the TDM and FDM is that the data in the TDM do not go through the TFB but directly through the station card (Escoffier *et al.*, 2007).

(II) SMA

In Chapters 5 and 7, observations are carried with the SMA, located in Mauna Kea, Hawaii, at 4100 m altitude. This interferometer is relatively smaller than the previously discussed ALMA telescope. It is composed of eight antennas of 6 m diameter with a maximum baseline of 509 m with a resolution up to 0.3″ (Peck and Schinckel, 2007). It is operating at 1.6 up to 0.7 mm (~180–418 GHz) and each telescope is equipped of two receivers which can work simultaneously. The SWARM (SMA Wideband Astronomical ROACH2 Machine) correlator is the central part of the SMA connecting all the output from the antenna receivers, providing a uniform 140 kHz resolution. As is the case for the ALMA correlator, the correlated signals are first corrected for the fine delay, phase control, etc. and then sent to a so-called crossbar switch which combines all the signals. Details explanations on the architecture of the SWARM correlator can be found in (Primiani *et al.*, 2016).

[3] https://almascience.eso.org/ documents-and-tools/cycle8/ alma-technical-handbook

2.1.5 *Data calibration and imaging*

To gain a more quantitative understanding of the observational data, let us now consider the process when the observations are collected by the telescopes. The telescope response, which corresponds to the correlated data, is integrated over time to produce a quantity called complex visibility, $V(u, v)$. This telescope response represents the intensity distribution of the source in the sky, $I(x, y)$. The operation to achieve the complex visibility is a Fourier transform of the intensity distribution, where (u,v) are the plane coordinates of the observer (i.e., the baseline) and (x,y) is the plane coordinates of the observed source. The later is located at a distance, L, from the observer and parallel to the (u,v) plane. The complex visibility is described as follows:

$$V(u, v) = \int \int A(x, y) I(x, y) e^{-2\pi i(ux+vy)} dx dy \qquad (2.2)$$

where, $A(x, y)$ is the beam shape of each antenna. The data are considered as complex visibilities, because the observational spectrum is affected by sine and cosine fringes. These are caused by the optic's design and by observational constraints such as, for example, the weather. The visibilities are therefore collected during each observational run for each baseline, when integration of the telescope response is integrated over time. This process is carried out over and over, until reaching a pre-defined sensitivity or uv coverage.

However, at this stage, the measurement sets are still not ready to use. Several calibrations steps, which are essential for having a reliable data set, have to be applied. Depending on the telescope, the calibrations have to be done by the user or have already been done at the telescope facility. Here, we will discuss the calibration steps performed by the users, they concern interferometric data and are applied with the tool CASA[4](McMullin *et al.*, 2007). For single dish observations, calibration steps are also required, however, they consist of the bandpass and flux calibrator only.

- *Bandpass calibrator:* It is the first step of the calibration. It corrects the signal for variations in the frequency domain (for each frequency interval). These variations might be caused by observational conditions (atmospheric effects) but also, by technical aspects, such as delays, etc. This step considerably improves the signal-to-noise ratio of the data. To ensure a signal over the entire frequency range, the bandpass calibrator will likely be a bright and line-free source, e.g., quasars.

- *Gain calibrator:* It corrects for the amplitude and phase variations over time caused by an environmental change, i.e., sky conditions (atmospheric properties, weather conditions, etc.). The gain calibrator, usually a bright quasar, is selected to be close to the object of interest so that the same sky conditions apply to it.

- *Flux calibrator:* This calibration adjusts the observations of the targeted source to an appropriate flux scale. This step consists of comparing the flux of another planet or satellite. The ratio of the modeled and observed amplitudes is then multiplied to the observations of the targeted source. The flux calibration is a multiplication factor, which can be applied before or after the gain calibrator, as this order does not drastically modify the final output. This calibration is usually applied after the gain calibration, as the atmospheric effect is already corrected from the gain calibration. The later leads to a better signal-to-noise ratio (SNR), when applying the flux calibrators. Typical sources used for calibration are planets or moons (Uranus, Titan, etc.), moons or quasars, depending of what is nearby the observed source at the time of observation.

Once the data are calibrated, they are in the form of a measurement set. To visualize the data, a conversion step from the measurement to a datacube needs to be performed. Again, this can be done directly at the telescope facility (e.g., dataset from ALMA) or by the user (e.g., SMA data). The datacube contains the observed intensity distribution over the observed region, i.e., for each pixel, covering the field of view. This conversion is done with the *CLEAN* algorithm, which is a widely-studied method for imaging interferometer data (Högbom, 1974; Remijan *et al.*, 2019). It constructs the final image by removing iteratively part of the flux, which is considered as the dirty image. This is performed in several steps:

- We previously discussed that visibilities are derived from the telescope response. An image can then be obtained from the visibility by inverting it to obtain the sky brightness distribution map (van Cittert, 1934; Zernike, 1938), as follows:

$$I'(x, y) = A(x, y)I(x, y) = \int \int V(u, v)e^{-2\pi i(ux+vy)} du dv \qquad (2.3)$$

The I' is in theory achieved with the inverse Fourier transform of the visibility. This method requires that the uv plane is entirely covered. However, in reality, this is often not the case. Therefore, the concept of weighting is frequently applied to the visibility and consists of the initial step of this *CLEAN* algorithm. The visibility is weighted with a function $g(u, v)$ to generate a so-called dirty image, I^D, by applying a discrete Fourier transform, as defined in the following:

$$I^D(x, y) = \int \int g(u, v)V(u, v)e^{-2\pi i(ux+vy)} \qquad (2.4)$$

Different types of weighting are possible, the most widely used are the uniform, natural and Briggs. In a natural weighting, the visibilities are given weight according to the SNR. While, in a uniform weighting, all the visibilities are considered irrespective of their SNR. The natural and uniform weightings are therefore on the opposite sides: the natural weighting privileges a better sensitivity, in cost of the angular resolution. While, with a uniform weighting, a better resolution will be achieved at the expense of the sensitivity.

The third weighting method, called Briggs, is a compromise between the two extremes (Briggs, 1995). It uses a *robust* parameter, to be defined by the user, which varies from -2 to 2, close to the uniform and natural weighting, respectively (Briggs *et al.*, 1999).

We can now related this dirty image, I^D, to the initial intensity, $I(x, y)$, by convolution, $\star$, with the dirty beam $B(x, y)$, which is a point spread function[5], with the following relation:

$$I^D(x, y) = B(x, y) \star I(x, y) \qquad (2.5)$$

- The *CLEAN* algorithm consists of examining the dirty image and selecting the point with the maximum intensity, from this image. Then, the dirty beam is scaled by a factor (defined in the *CLEAN* command), and is subtracted from the dirty image at the location of this emission peak. From this process, a clean component and a residual image is produced. This iteration is performed until the noise (the residual) reached a defined threshold, usually defined as three times the theoretical rms noise. Once this threshold is achieved, a clean image is created, from the summation of the residual and the convolution of the clean component and the clean beam.

Now that the calibrations and cleaning have been performed, the observer has a final product ready to use for analysis, in the format of a clean cube made of measurement sets.

2.1.6 *Line analysis tools*

At this point, we have explained what is detected, how the observations are carried out, what are the calibration steps required and how an image from the measurement set is created. The last step for the observational method is thus how to analyse the data. In this section, we will develop on the different methods and tools used in this thesis.

We have previously discussed that we can observe, with telescopes, excited molecules, which emit photons. However, we need tools to quantify the amount of the detected species in a certain energy level. To gain a more quantitative understanding of what we observe, let us first assume that we receive all the emitted photons from the excited species. In reality, it is not necessarily the case, as the photons can be absorbed by dust or other molecules and, therefore they are not all escaping the

[5]It represents the response of an imaging system to a point source.

cloud. We will refer to this last case as an optically thick emission. While, when each emitted photon is assumed to escape the cloud, this refers to an optically thin emission. This concept is physically translated by the optical depth, τ_ν, which correlates the brightness temperature[6] (T_B) and the excitation temperature, T_{ex}, as follows:

$$\tau_\nu >> 1 : T_B = T_{ex} \tag{2.6a}$$

$$\tau_\nu << 1 : T_B = \tau_\nu T_{ex} \tag{2.6b}$$

The relation of an optically thin emission implies that, for a homogeneous cloud, the line strength is proportional to the total quantity of the observed species, which we will call the total column density. To determine the τ value, we use the RADEX[7] tool (van der Tak *et al.*, 2007). This tool is one-dimensional non-local thermodynamic equilibrium (LTE) radiative transfer code, which calculates the radiative transfer parameters based on the spectral range and excitation conditions (i.e., kinetic temperature, H_2 density). In this way, it is possible to determine the limit of the total column density, for which the optically thin condition is valid, thus for $\tau_\nu < 1$.

The second assumption is related to the excitation and de-excitation of the molecules. We now consider a regime where the change of the energy state, cf. Section 2.1.1, is dominated by collisions. With this assumption, we refer to the, so-called, local thermodynamic equilibrium (LTE) condition.

To determine whether the change of the energy level of a specific species in a specific environment is driven by collisions, the density of the principal collider has to be above the critical density of the species of interest. In this way, the probability of a species to collide with H_2 molecules is high. In the ISM, H_2 is by few orders of magnitude one of the most abundant species and therefore the principal collider. The critical density of the species is the quantitative value describing the balance between the radiative and collisional de-excitation. The critical density, n_{crit}, is calculated as follows:

$$n_{crit} = A_{ji}/C_{ji} \tag{2.7}$$

where, A_{ji} is the radiative de-excitation rate and C_{ji} is the collisional rate coefficient. Both de-excitation parameters are from the upper energy level j to the lower energy level i. In the case of non-LTE ($n_{crit} >> n_{H_2}$), each energy level may be characterized by a different temperature than the one of the ground state. While under LTE condition ($n_{crit} << n_{H_2}$), all the excitation temperatures are the same, irrespective of the energy level. The relation between the population levels is shown by the following equation (Goldsmith and Langer, 1999):

$$\frac{n_j}{n_i} = \frac{g_j}{g_i} e^{-\Delta E_{ji}/kT_{ex}} \tag{2.8}$$

where, g is the degeneracy, ΔE_{ji} is the difference in energy of the two states, j and i and, k is the Boltzmann constant. These relationships are important for the derivation of the total column density, that will be described later.

As explained previously, depending on the telescope, the data format varies. However, the final output is a datacube from which is extracted a line spectrum, displaying the intensity in Jansky per beam or in Kelvin (i.e., the main beam temperature) over frequency or velocity. Now that we have stated our main assumptions, let's dive into the first step of the analysis, which is to determine which molecules are detected (cf. Section 2.1.1), based on spectroscopic and molecular databases (e.g., JPL[8], CDMS[9], LAMDA[10], etc.).

This can be done with visual identification and/or with the use of interactive tools such as CASSIS[11], and GILDAS[12], using the CLASS package, which are spectrum analysers. These tools are made of several packages which contain several functions, from the line analysis to the mapping.

Once the spectral lines, characteristic of a molecule/atom, have been detected, the second part of the analysis can start, which is strongly dependent on both assumptions we made earlier. This analysis can be performed in a classical way, with a Gaussian fit of each emission line of a species. This Gaussian fit provides information such as the full-width at half maximum (FWHM), the intensity observed and shift from the source velocity. These characteristics are important for gaining

[6]It corresponds to a blackbody temperature, which reproduces a given flux density at a specific frequency.

[7]https://home.strw.leidenuniv.nl/~moldata/radex.html

[8]Jet propulsion laboratory, https://spec.jpl.nasa.gov/ftp/pub/catalog/catform.html

[9]The Cologne Database for Molecular Spectroscopy, https://cdms.astro.uni-koeln.de

[10]Leiden Atomic and Molecular Database, https://home.strw.leidenuniv.nl/~moldata/

[11]Centre d'Analyse Scientifique de Spectres Instrumentaux et Synthétiques, http://cassis.irap.omp.eu

[12]Grenoble Image and Line Data Analysis Software, https://www.iram.fr/IRAMFR/GILDAS/

physical insights of the observed species: the FWHM provides information on the gas observed: a faster gas seen in, for example, outflows will display a higher FWHM than a slower gas. While, a possible shift of the peak intensity with respect to the source velocity, v_{lsr}, will point to whether the species is in a gas moving faster, slower or at the same speed than the source velocity.

As discussed above, under the conditions of LTE and optically thin emission, the line strength is directly proportional to the total column density, which allows us to quantify the amount of a detected species. The total column density, N_{tot}, is determined from the molecular line strength as follows (Goldsmith and Langer, 1999):

$$N_{\text{tot}} = \frac{N_{\text{i}}}{g_{\text{i}}} \frac{Q(T_{\text{ex}})}{e^{-E_{\text{i}}/(kT_{\text{ex}})}} \qquad (2.9)$$

such as (under the sole condition of optically thin emission),

$$N_i = \frac{8\pi k v \int T_B dv}{hc^3 A_{ij}} \qquad (2.10)$$

where $Q(T_{ex})$ is the partition function for a given excitation temperature, T_{ex}, E_i is the upper level energy, k is the Boltzmann constant, v is the frequency, $\int T_B dv$ is the integrated intensity, h is the Planck's constant, c is the speed of light and A_{ij} is the Einstein A-coefficient from the upper level i to the lower level j.

When several transitions of a same species are detected, a common technique to determine the column density of the species is by the use of rotation diagrams, also called Boltzmann plots or population diagrams. It displays the logarithmic value of the upper-level column density per sub-level as a function of the upper-level energy. This yields estimate of the total column density of a species and the excitation temperature (if conditions of LTE and optically thin emission are fulfilled, Blake *et al.*, 1987; Goldsmith and Langer, 1999; van der Tak *et al.*, 2007). The excitation temperature is a physical parameter under which a specific ratio of particles of two energy states (i.e., level populations) is expected. The rotational diagram method uses the spectroscopic characteristics and integrated intensity from the Gaussian fit of the emitted spectrum line. This diagram therefore displays the relationship between $\ln(\frac{N_i}{g_i})$ over $\frac{E_i}{k_b}$. Where, N_i is column density, g_i is the degeneracy and E_i is the energy of the upper level i; while k_b is the Boltzmann's constant. Moreover, it assumes similar beam size, optically thin emission and LTE condition.

Earlier in this section, we mentioned the non-interactive way to analyse the data. However, several tools have been made available to simplify the analysis of the observers, such as CASSIS and GILDAS (*CLASS* module). With these tools, the entire given spectrum is analysed, and for a defined telescope, an aperture size, a column density, excitation temperature and FWHM are derived. However, the user should always keep a critical mind and, verify analytically that the inferred values by the interactive tools are producing the expected output.

In the case of line modeling with an interactive tool, the best line fit is performed based on a minimum χ^2 analysis over all the molecular transitions found in the spectrum. This line fitting allows us to quantify the molecular column density and other physical characteristics such as the FWHM, the line shift with respect to the object velocity and the excitation temperature. If there is a non-detection, there are too many free parameters to perform a χ^2 analysis. Therefore, the excitation temperature is set to be equal to the excitation temperature of a species within the same molecular family[13], and the integrated intensity is taken as three times the rms, of the region where emission was expected, resulting in a so-called 3σ upper limit. These assumptions are taken in order to determine the upper limit of its column density. In the case of one molecular line detected, the same issue as for the non-detection occurs, namely there are too many free parameters for the χ^2 analysis. Although the gas temperature is not always the same as the excitation temperature, the assumption of both being equal is considered as reasonable, assuming LTE conditions.

So far, we have discussed the data analysis considering two main assumptions (i.e., LTE and optically thin emission). However, the reader might wonder how are the data analysed if these conditions are not met. In the case of non-LTE, the use of RADEX is made (van der Tak *et al.*, 2007). This tool uses the theory of radiative transfer, considering a homogeneous cloud, to determine the column density and

[13]A molecular family are molecules sharing at least two similar atoms, e.g. OCS and CS.

physical conditions. It provides a line strength based on the kinetic temperature, column density and H_2 number density. This line strength can be directly compared to the detected line. The radiation transfer relationship indicates how the intensity varies along a certain distance, if the absorption and the emission throughout the medium is considered. While in the case of optically thick emission, the use of isotopologues ratio, which depends on the observed region, is made, considering that the detected isotopologue has an optically thin emission (Wilson and Rood, 1994).

Hitherto, we explained how we analysed the line spectrum and modeled the emission for determining the molecular column densities in the observed region. These observational methods described here are the key modi operandi used in Chapters 5–**??** for analysing the observational data.

2.2   LABORATORY EXPERIMENTS

The second method used in this thesis is in-situ laboratory experiments. These are performed with the apparatus VENUS (Vers de nouvelles synthèses), in the LERMA (Laboratoire d'etudes du rayonnement et de la matière en astrophysique et atmosphères) laboratory, part of the observatory of Paris (Congiu *et al.*, 2020).

The VENUS apparatus consists of injecting molecules simultaneously or not, under specific conditions such as a controlled temperature, and low pressure (10^{-10}–10^{-11} mbar); on the sample during a specific lapse of time, and study the reactivity process occurring. This machine allows us to reproduce similar ISM conditions and to study the molecular behaviour in such an environment. Nevertheless, the environment in the ISM is more complex than what can be reproduced in the laboratory. Therefore, processes which require an external source of energy leading to non-thermal desorption (e.g., photodesorption, etc.) are not reproduced by this experimental setup. In this section, first the structural architecture of the machine will be explained, then how the experiments are performed will be discussed.

2.2.1   *Structural Architecture*

This apparatus consists of several structural parts, as described by Figures 2.6 and the schematic Figure 2.7:

(I)   Four injections entries allow to inject the molecules into the chambers, and thus to perform experiments with different molecules, simultaneously or/and in a chain process.

(II)   The Ultra High Vacuum (UHV) main chamber is where the ISM conditions are reproduced and the chemical reactions occur and are recorded.

(III)   Primary and Secondary Chambers are the transition chambers where the molecules are injected and the pressure is lowered progressively until reaching the ISM conditions.

(IV)   The Quadrupole Mass Spectrometer (QMS) records the different masses desorbed from the surface. The QMS is used when increasing the temperature in the main chamber. In such way, the recorded data provides a so-called temperature desorption profile (TPD), which is the mass intensity spectrum over temperature. With these data, it will be possible with a further analysis to determine the reactions occurring on the surface.

(V)   The Fourier Transform Reflection Absorption Infrared Spectrometer (FT-RAIRS) allows to determine the components present in the gas and therefore deposited on the surface. If a gas chemistry occurs before being adsorbed on the surface, it will be recorded by the FT-RAIRS.

(I) Injection Entries

Four injection entries are connected to the chambers such that it is possible to inject four different species for the experiments. Having independent injection pipes allows to inject the species simultaneously or following a certain chain process. It increases the manoeuvrability of the machine and therefore the diversity of the
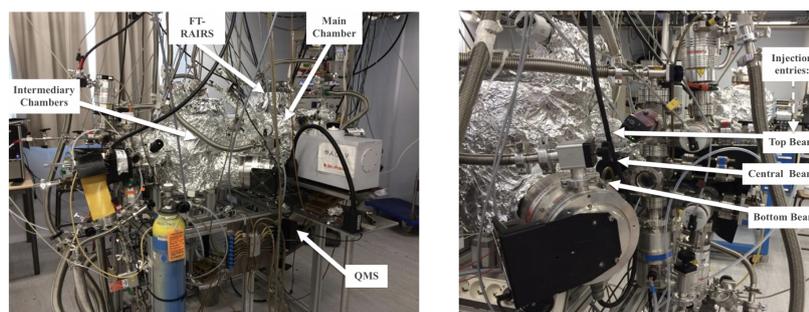
FIGURE 2.6: VENUS apparatus. *left:* front view of VENUS, displaying the intermediary chambers, main chamber, FT-RAIRS and QMS. *right:* Side view of VENUS showing the different three molecular injection entries (i.e., top, central and bottom beams) (atomic hydrogen entry not included).

possible experiments. Each beam-line is equipped with a standard cubic centimeters per minute (sccm) flow regulator. The gas is injected in a long tube passing through the different chambers via diaphragms before being injected into the sample in the main chamber via respective nozzle of 3 mm diameter. One of the injection entries is used for the injection of atomic hydrogen. However, as only the di-hydrogen is available in a gas bottle compatible to the apparatus, a dissociation microwave of 2.45 GHz has been installed within this injection tube, which dissociates the molecular di-hydrogen.

(II) Primary and Secondary Chambers

The intermediary chambers consist of two chambers, each equipped with a turbo molecular pumping system, before the main one, connected together through diaphragms allowing the creation of differential pumping. The pressure in these chambers is gradually decreased (10^{-8} and 10^{-9} mbar for the first and second chambers, respectively) until reaching the final pressure of 10^{-10}–10^{-11} mbar in the main chamber. This multi-chamber system emphasizes the difficulty to reach such final pressure, because the pressure achieved is considerably lower than the one experienced on Earth. One might notice that the lowest pressure achieved with this apparatus corresponds still to dense regions of the ISM.

(III) Main Chamber

The main Ultra High Vacuum (UHV) chamber is a stainless steel chamber in which the pressure reaches the order of 10^{-10}–10^{-11} mbar, and is connected to turbo molecular and titanium sublimation pumps. This UHV environment maintains a non polluted surface for performing the experiments and therefore, controlling the physical and chemical reactions occurring. Four main elements are present in this main chamber. (1) Within the main chamber, a circular (radius=4.5 mm) gold coated sample is placed (playing the role of the dust grain), attached to the cold head part of a Helium cryostat. The cryostat varies the sample temperature from 7 K to 350 K, with a regulated resistive heater attached on the back of the sample holder. (2) The end of the calibrated gas injection pipes, present in the main chamber, spread their contained gas into the substrate surface. These are located in front of the gold sample.(3) Also located on the top of the chamber is the FT-RAIRS. (4) Finally, the movable QMS is placed at the bottom of the main chamber, such that when in up-position, it is located in front of the sample, and in down-position, it does not block the injected molecules towards the gold coated sample.

(IV) Quadrupole Mass Spectrometer

The apparatus is also equipped with a quadrupole mass spectrometer (QMS), measuring the flux intensity and composition. This can be placed in front of the injection entries or in front of the sample when performing a Temperature Programmed Desorption (TPD). In this case, the QMS measures the composition of the gas injected,
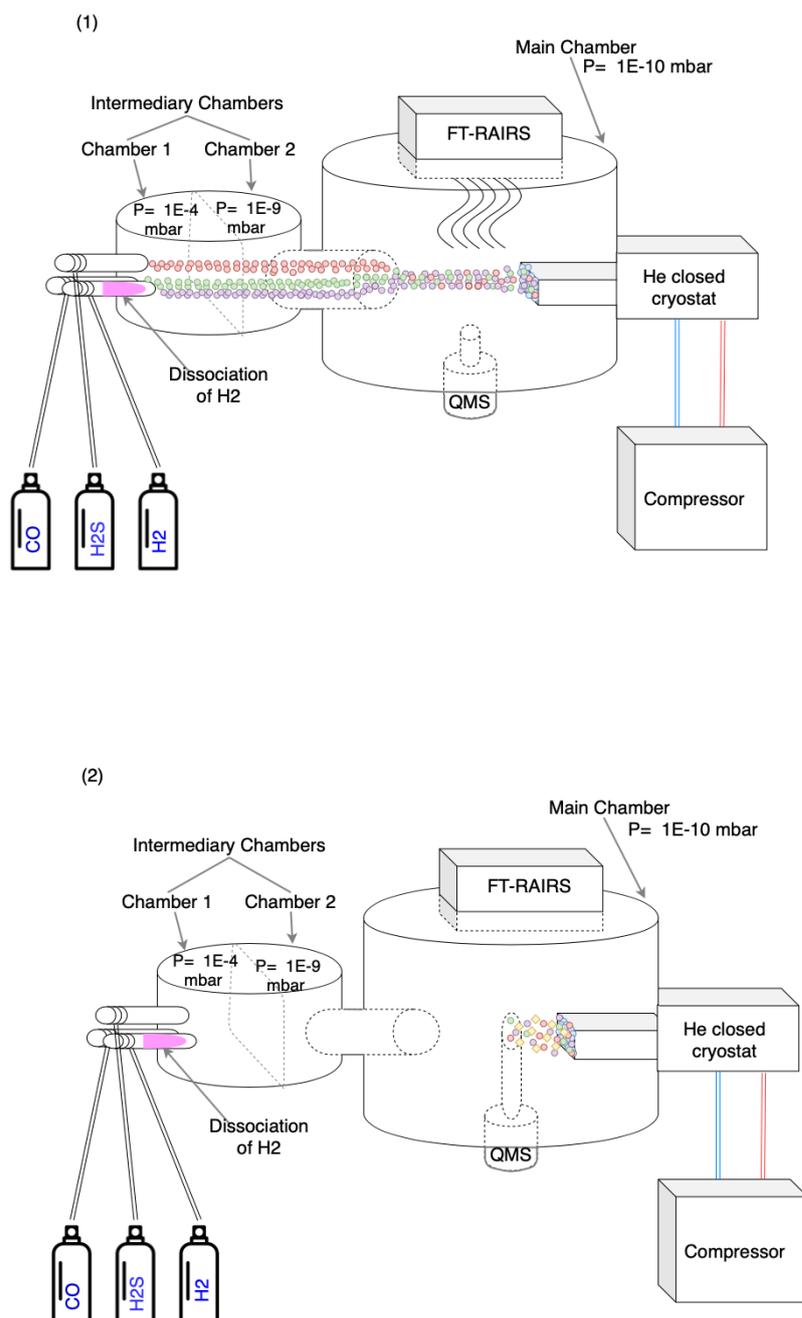
FIGURE 2.7: Schematic of the VENUS apparatus: (1) the molecules (H_2S and CO) and H atoms (dissociated hydrogen) are injected into the first chamber through the different injection pipes under a pressure of 10^{-4} mbar. After passing through the second chamber, with a pressure closer to the one of the main chamber, the molecules enter the main chamber and are focused onto the gold-coated substrate. While injecting the molecules, the FT-RAIRS records the infrared spectrum of the molecules arriving at the surface of the substrate. This graphical representation of the molecules displays a co-deposition of CO, H_2S and H. (2) The FT-RAIRS is stopped and the main chamber is heated while the QMS placed in front of the substrate is on. In this way, all the molecules which sublimate can be recorded by the QMS. Picture taken from **elAkel2021**

it is usually used for checking the composition of volatile species such as e.g., H_2S, CH_3OH. While in the second up-configuration, it measures the sublimated species from the surface.

(V) Fourier Transform Reflection Absorption Infrared Spectrometer

The experimentation process can be controlled by a Fourier Transform Reflection Absorption Infrared Spectroscopy, which shows the proportion of each molecule throughout time via their infrared spectrum. The FT-RAIRS records spectral range region between 3000–1000 cm^{-1} with a resolution of 4 cm^{-1}. However, the FT-RAIRS has a highly noise affected wavelength range, from which the origin is currently unknown and thus not corrected. Therefore, species with spectral range 500–1300 cm^{-1} could not be detected.

2.2.2   *Experimental methods*

In the previous section, the architecture of the VENUS apparatus has been described. In this Section, we will dive into the practical aspect of the experiments, namely *how* the experiments are conducted.

An important physical parameter is the quantity of molecules used in these experiments. This is expressed in monolayer (1 ML = 10^{15} molecules cm^{-2}), which corresponds to a full coverage of the substrate by one layer of molecules. For the case of a solid substrate, e.g., amorphous H_2O substrate, it corresponds to the number of absorption sites. However, when the substrate is porous, e.g., porous H_2O, the number of sites is not constant and 1 ML is not sufficient for entirely covering the substrate, consequently few ML would be required. For this reason, for all experiments, few ML were used.

Experimental Process

The experimentation conducted through the apparatus is a straightforward process, as described by Figure 2.9. It consists of three main work packages (WP): the preliminary work for performing the experiments, the experimental work itself and the data analysis.

WP1: The vacuum is created by "steaming" the main chamber for several weeks. Once it is operational, the experiments can take place. The preliminary step is to perform the temperature desorption profile of each reactant for setting the physical conditions (i.e., flow rate, pressure, time) such as 1 ML is achieved. For determining the kinetics behaviour of the species over the surface, the species is injected with constant conditions over a varying time lapse and then a TPD is performed. A TPD profile consists of gradually increasing the temperature to the system as described by Equation (2.11).

$$T = T_0 + \beta t \tag{2.11}$$

in which, T is the temperature in Kelvin at time, t, T_0 is the initial temperature and β is the temperature ramp rate in units of K sec^{-1}.

The QMS then records the molecules desorbed from the surface. Depending on the species, three type of TPD profiles might be observed, as shown in Figure 2.8. The 0th order describes a desorption profile independent of the coverage; in this case, determining the ML is not possible. The 1st order reflects the amount of adsorbed molecules on the surface, this order is characterized by a non varying peak positions with the deposition time and a symmetrical shape. The second order describes the proportional reaction rate with the amount of reactants. This case is observed when reactants are both adsorbed on the surface, diffuse and react with each other on the surface before desorbing (cf. Langmuir-Hinshelwood Mechanism, Section 1.5.1). This order is characterised by a symmetrical shape which peak is shifted to the left with increasing coverage.
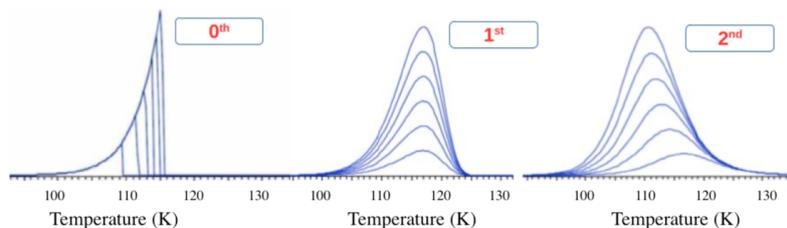
FIGURE 2.8: Different TPD profiles depending on the kinetics.

WP2: The second work package describes the experimental part itself. The first step consists of injecting the molecules independently in order to check that the species are pure and no leakage is present. The molecules and the dissociated hydrogen are then injected to the main chamber through the different injection pipes under a pressure of 10^{-4} mbar passing through the intermediary chambers. If an icy substrate is required, then the H_2O is injected by background; once the pressure in the main chamber is in the order of 10^{-8} mbar, then the number of ML starts being formed uniformly. While injecting the molecules, the FT-RAIRS is operational and records the infrared spectrum of the molecules reaching the surface of the substrate. Once the injection process is finished, the FT-RAIRS is stopped and the QMS, placed in front of the substrate for maximising the signal, is turned on. In this way, all the molecules which sublimate can be recorded by the QMS. Then, the main chamber is heated with a constant ramp rate of $12 \, K \, min^{-1}$,

WP3: Once the experiments are performed, the analysis part starts. This consists of two main data types: the infrared spectra and the mass spectra. Based on the spectroscopic data of the species, the detection of a molecule can be confirmed or not with the infrared spectra. In the mass spectrum, which is the output from a TPD, the detection of a species is determined for its mass decomposition. Each species is defined by a molecular mass (m/z), but it is composed of other masses at a lower fractional level. Therefore, when all the different masses at the right fractional level are observed in the mass spectrum, then a detection of a species is confirmed. The mass composition of a species are taken from the NIST[14] chemistry webbook. For example, in the case of the molecule H_2S, the main molecular mass $m/z = 34$ is expected at 100% of the signal, while the masses $m/z = 32$, $m/z = 33$, $m/z = 35$, $m/z = 36$, are expected to have an intensity of $\sim$ 45, 42, 5 and 7% of the main mass signal. The mass composition is an indicator of the detected molecule, but the exact composition as shown is not likely to be present in our experiments, as the QMS voltage is not used. Our instrument displays a lower voltage, therefore, the mass decomposition profile will be less dominant than the one listed in NIST, and most of the detection will be seen towards the main molecular mass, in this case, $m/z = 34$.

[14]National institute of standards and technology, https://webbook.nist.gov/chemistry/
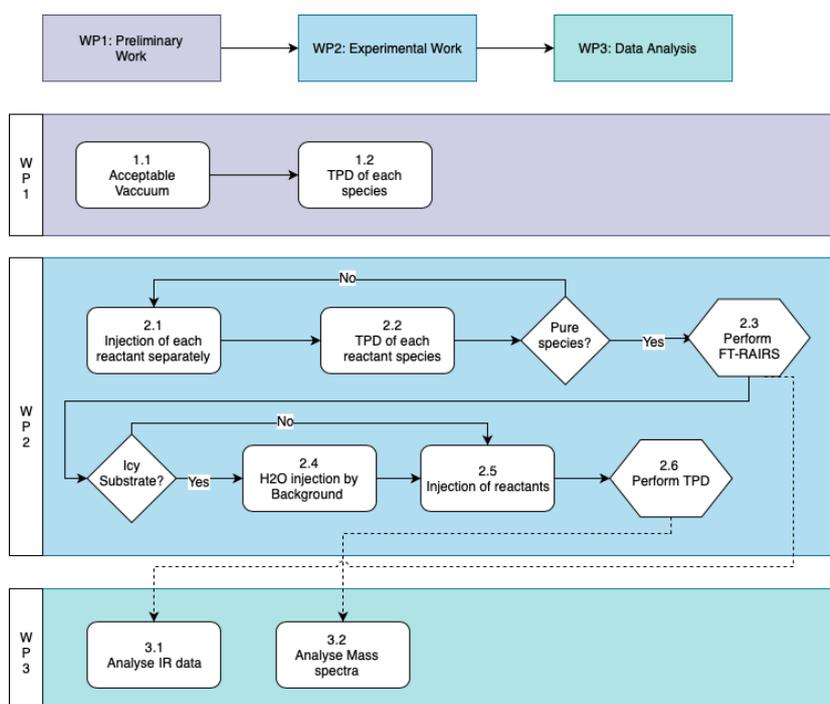
FIGURE 2.9: Flow Chart of the VENUS Experimental process. Three main work packages are identified: preliminary work, experimental work and data analysis. Each of the work packages is further detailed in each corresponding block.

2.3 SHOCK MODELS

The last method considered in the thesis is the modeling. This method is used only in Chapter 6, when discussing the outflow region of BHR71. In this, the described model is the Paris-Durham shock code[15] (Godard *et al.*, 2019). In the following, this method will be discussed in two steps: first, the software principles of the code will be explained, then the software architecture will be detailed.

2.3.1 *Software principles*

This numerical code simulates interstellar shocks generated by jet and outflows from forming stars, asymptotic giant branch (AGB) winds, cloud collisions or remnant shells from old supernovas. The simulation is in the form of a 1D plane-parallel shock wave propagating at a shock speed with respect to the ambient medium and perpendicular to a magnetic field. The molecular medium in which the wave propagates is considered homogeneous and affected by a uniform magnetic field which is, if specified by the user, irradiated upstream by an external FUV field. It considers the standard C- and J-type shocks, but also, the C^* and CJ shock types (Godard *et al.*, 2019; The ISM team, 2020).

This code solves for the shock physical conditions in parallel with the chemical and thermal conditions. These last are strongly correlated to each other during the shock propagation, for example, the ionization (chemical aspects) balances the neutral-ions coupling (dynamical aspect).

The Paris-Durham code works around four main aspects (The ISM team, 2020):

- *The dynamics* which consider the dynamical properties of the flow (i.e., velocity, density, temperature along the 1D flow and H_2 level populations).

- *The heating* & *cooling mechanisms*. As it name indicates, this aspect englobes all the heating and cooling mechanisms used in the code.

- *The chemical species* & *the grains* which include all the species in their neutral or ionized form, in the gas phase, on grain icy mantles, or inside grain refractory cores.

[15]Available online: https://ism.obspm.fr/shock.html

- *The chemical network* which is a list with all the chemical reactions. The standard version includes ∼ 1000 reactions. This parameter is free to be modified by the user (cf. Section *Input parameters*).

2.3.2 *Software architecture*

The software is composed of three main parts: the input parameters, the main algorithm and the output files. An overview of the architecture is displayed in Figure 2.10

(I) Input parameters

The input parameters of this numerical code consists of three main parts: the user input (*input_mhd.in*), the species file (*species.in*) and the chemistry file (*chemistry.in*).

(I.I) INPUT_MHD.IN

The code displays a large panel of customized parameters by the user. It covers the following categories:

- *File parameters:* it summarizes all the files to be used, such as the files with
  - the initial H_2 level populations,
  - the FUV radiation field at each point (if applicable),
  - the species list and their initial abundances,
  - all the chemical reactions considered.

- *Shock parameters:* In this section, the user specifies the shock characteristics with
  - the shock type (C or J),
  - the number of fluids, which defines if the neutrals and ions are coupled or not, in accordance with the later defined magnetic field. If the magnetic field is strong enough for decoupling to occur, then the defined number of fluids is overruled.
  - the magnetic field parameter, b, which is determined from the transverse magnetic field strength, B, as follows:

$$B(\mu G) = b\sqrt{n_{\mathrm{H}}(\mathrm{cm}^{-3})} \qquad (2.12)$$

    where, n_{H} is the atomic hydrogen density.
  - The shock speed,
  - the initial ion-neutral drift speed,
  - the initial proton density,
  - the initial temperature of the neutrals,

- *Environmental parameters:* the shock propagation is not only dependent on the shock parameters alone, but also, on the the environmental parameters. These include
  - the cosmic ray ionization rate per H atoms,
  - the shape of the incident FUV field, it can be a Draine from Draine (1978) or Mathis methods from Mathis *et al.* (1983), which are two different interpolation methods for determining the radiation field.
  - the mean intensity of the FUV field,
  - the visual extinction in front of the shock,
  - the FUV radiative transfer, necessary to compute the photodissociation and desorption rates,
  - the integration and conversion parameters of the visual extinction.

– The column density of H_2 and CO buffer[16], which provides insight on the H_2 and CO self-shielding; as well as the turbulent velocity used for H_2 self-shielding.

- *Grain properties:* these correspond to the grain temperature, size, core density, the grain size distribution and the ice layer density recovering the grain.

- *Excitation and cooling:* Setting the excitation cooling parameters is essential for the chemistry occurring in such an environment. These can be categorized into three: the gas temperature, the CO and H_2O cooling parameters and the full H_2 treatment. At each step of the code, all the level populations are calculated, which means that for each step of the code, the contribution of the H_2 is determined. This last step includes the number of H_2 levels, the H-H_2 collisional rates, etc.

- *Numerical parameters:* in this section, the integration steps, duration of the models, the precision parameter for the numerical integrator and the shock age (if non-stationary C-type shock) are required.

- *Output specifications:* The last step of the user input consists of specifying the format of the output files as well as the level of detail required in the output data.

(I.II) SPECIES.IN

The species file is the second file necessary for running the model. It provides a complete list of chemical species and their initial abundances at the beginning of the shock and their enthalpy of formation.

(I.III) CHEMISTRY.IN

The chemistry file summarizes all the chemical reactions considered in the shock model, and their corresponding reaction rates. It considers (1) the gas-phase reactions, (2) the dissociation and ionization from cosmic rays, impact and attenuated external FUV field. (3) the adsorption onto grains (4) the non-thermal desorption processes such as the sputtering, photodesorption, etc. (5) The thermal desorption.

(II) Main algorithm

The main algorithm calculates the coupled evolution of the dynamical, thermal and chemical structure of a 1D plane parallel shock wave, assuming steady-state, as specified in the previous Section 2.3.1. These computations are made by integrating a complex system of differential equations, more specifically, describing the conservation of the particles number, mass, momentum and, energy. These sets of Equations were already described in Section 1.3 (Equations 1.7-1.10).

They are resulting from the physical and chemical shock parameters and are resolved with the DVODE package, which solves the stiff kinetics ordinary differential equations (ODEs).

(II) Output

Two formats for output files are available, the ASCII and the hdf5 files. Four main files are provided by the code after running:

- *Information files:* they contain a summary of the parameters defined in the input files as well as a predicted H_2 excitation diagram.

- *Physical and chemical structure of the shock:* This file summarizes the physical variables (e.g., temperature, velocity, etc.), the chemical abundances and the species column densities.

- *H_2 excitation and cooling:* It regroups the H_2 data, namely the H_2 level populations and the line intensities.

- *Emissivities and cooling:* It includes the cooling and heating rates, the local level population and the flux of atoms and ions (Fe^+ included).

In this Chapter, we discussed in detail all the methods used in this thesis. They include the observations, laboratory experiments and the use of the Paris-Durham shock model. At this stage, the reader has not only gain a general insight of the different methods used but has also gained a deep understanding of how these are carried, what are the intermediate steps before having reliable data and how the results can be analysed.
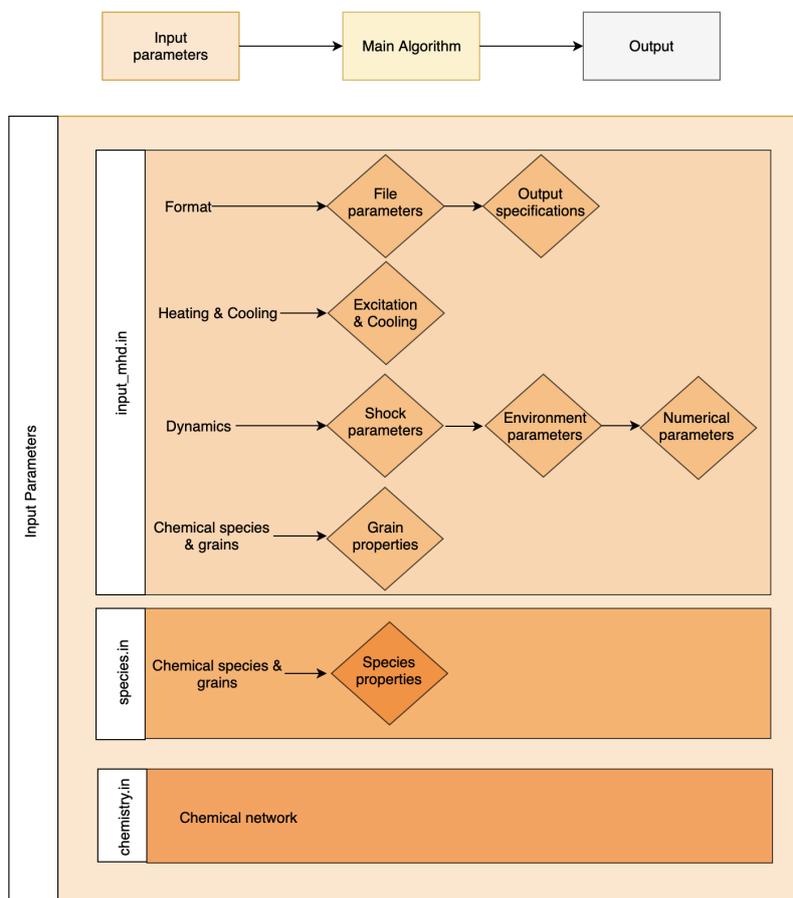
FIGURE 2.10: Flow Chart of the architecture of the Paris-Durham shock code. Three main work parts are differentiated: the input parameters, the main algorithm and the output.

Bibliography

1. J. Baars *et al.*, *A&A* **175**, 319–326 (Mar. 1987).

2. G. A. Blake *et al.*, *ApJ* **315**, 621 (Apr. 1987).

3. R. Blundell, *arXiv e-prints*, astro–ph/0508492, arXiv: `astro-ph/0508492 [astro-ph]` (Aug. 2005).

4. D. Briggs, presented at the American Astronomical Society Meeting Abstracts, vol. 187, 112.02, p. 112.02.

5. D. Briggs, F. Schwab, R. Sramek, presented at the Synthesis Imaging in Radio Astronomy II, ed. by G. Taylor, C. Carilli, R. Perley, vol. 180, p. 127.

6. K. Carsten, M. Sanchez Portal, *IRAM 30-meter Telescope Observing Capabilities and Organisation*, 2017, (`%5Curl%7Bhttps://www.iram.fr/GENERAL/calls/ s19/30mCapabilities.pdf%7D`).

7. E. Congiu *et al.*, *arXiv e-prints*, arXiv:2004.10668, arXiv: `2004.10668 [astro-ph.IM]` (Apr. 2020).

8. B. Draine, *ApJS* **36**, 595–619 (Apr. 1978).

9. R. P. Escoffier *et al.*, *A&A* **462**, 801–810, (`https://doi.org/10.1051/0004- 6361:20054519`) (2007).

10. G. Field, W. Somerville, K. Dressler, *ARA&A* **4**, 207 (Jan. 1966).

11. Gildas Team, *GILDAS: Grenoble Image and Line Data Analysis Software*, May 2013, ascl: `1305.010`.

12. B. Godard *et al.*, *A&A* **622**, A100, arXiv: `1901.04273 [astro-ph.GA]` (Feb. 2019).

13. P. F. Goldsmith, W. D. Langer, *ApJ* **517**, 209–225 (May 1999).

14. A. Greve, J. .-. Panis, C. Thum, *A&AS* **115**, 379 (Feb. 1996).

15. R. Güsten *et al.*, *A&A* **454**, L13–L16 (Aug. 2006).

16. P. T. Ho, J. M. Moran, K. Y. Lo, *ApJ* **616**, L1–L6, arXiv: `astro-ph/0406352 [astro-ph]` (Nov. 2004).

17. J. Högbom, *A&AS* **15**, 417 (June 1974).

18. J. Jørgensen, A. Belloche, R. Garrod, *ARA&A* **58**, 727–778, arXiv: `2006.07071 [astro-ph.SR]` (Aug. 2020).

19. B. Klein *et al.*, presented at the, pp. 199–201.

20. D. P. Kratz, R. D. Cess, *Tellus B: Chemical and Physical Meteorology* **37**, 53–63, eprint: `https://doi.org/10.3402/tellusb.v37i2.14995`, (`https://doi.org/10.3402/tellusb.v37i2.14995`) (1985).

21. S. Ling, J. Sanny, W. Moebs, *University Physics Volume 3* (OpenStax CNX, 2016), (`http://cnx.org/contents/af275420-6050-4707-995c-57b9cc13c358@ 12.2`).

22. X. Liu *et al.*, *Nanophotonics* **9**, 3263–3269, (`https://doi.org/10.1515/ nanoph-2020-0012`) (2020).

23. J. Mathis, P. Mezger, N. Panagia, *A&A* **500**, 259–276 (Nov. 1983).

24. J. McMullin *et al.*, presented at the Astronomical Data Analysis Software and Systems XVI, ed. by R. Shaw, F. Hill, D. Bell, vol. 376, p. 127.

25. S. Müller *et al.* (Jan. 2006).

26. J. H. Oberheuser, presented at the Optical Systems in Engineering I, vol. 0193, pp. 27–33.

27. A. Peck, S. Schinckel A.and team, presented at the Exploring the Cosmic Frontier, ed. by A. P. Lobanov *et al.*, pp. 49–50.

28. R. Primiani *et al.*, *SWARM: A 32 GHz Correlator and VLBI Beamformer for the Submillimeter Array*, 2016, arXiv: 1611.02596 [astro-ph.IM].

29. Y.-Y. Pu *et al.*, *International Dairy Journal* **103**, 104623, ISSN: 0958-6946, (https://www.sciencedirect.com/science/article/pii/S0958694619302602) (2020).

30. F. Rayleigh, *The London, Edinburgh, and Dublin Philosophical Magazine and Journal of Science* **8**, 261–274, eprint: https://doi.org/10.1080/14786447908639684, (https://doi.org/10.1080/14786447908639684) (1879).

31. A. Remijan *et al.*, *ALMA Cycle 7 Technical Handbook*, Additional contributors to this edition: Tim Bastian, Crystal Brogan, John Carpenter, Chinshin Chang, Geoff Crew, Daniel Espada, Paul Fisher, Misato Fukagawa, Melissa Hoffman, Todd Hunter, Ruediger Kneissl, Andy Lipnicky, Ryan Loomis, Sergio Martin, Lynn Matthews, Luke Maud, Rie Miura, Yusuke Miyamoto, Hiroshi Nagai, Kouichiro Nakanishi, Masumi Shimojo, Richard Simon, Jeremy Thorley, MCarmen Toribio, Catarina Ubach, Catherine Vlahakis, Martin Zwaan, (https://doi.org/10.5281/zenodo.4511522).

32. S. Solomon *et al.*, *Journal of Geophysical Research: Atmospheres* **103**, 3847–3858, eprint: https://agupubs.onlinelibrary.wiley.com/doi/pdf/10.1029/97JD03285, (https://agupubs.onlinelibrary.wiley.com/doi/abs/10.1029/97JD03285) (1998).

33. S. Stahler, F. Palla, *The Formation of Stars, by Steven W. Stahler, Francesco Palla, pp. 865. ISBN 3-527-40559-3. Wiley-VCH , January 2005.* (Jan. 2005).

34. The ISM team, *Documentation - shock code*, (http://ism.obspm.fr/shock.html).

35. A. G. G. M. Tielens, *The Physics and Chemistry of the Interstellar Medium* (Cambridge University Press, 2005).

36. P. van Cittert, *Physica* **1**, 201–210 (Jan. 1934).

37. F. F. S. van der Tak *et al.*, *A&A* **468**, 627–635, (https://doi.org/10.1051/0004-6361:20066820) (2007).

38. E. F. van Dishoeck, G. A. Blake, *ARA&A* **36**, 317–368 (Jan. 1998).

39. T. Wilson, R. Rood, *ARA&A* **32**, 191–226 (Jan. 1994).

40. A. Wootten, *Proc. SPIE* **4837** (Sept. 2002).

41. F. Zernike, *Physica* **5**, 785–795 (Aug. 1938).

3

The star-forming regions

At this stage, the reader has gained insights on the origin of the protostar, its structure as well as on the different physical and chemical aspects playing a role in the protostellar environment. Chapter 2 provided further knowledge to the reader on the different techniques used to study the different regions of a protostars. Now that the theoretical aspects have been explained, let us finally consider the sources studied in this thesis. As will be explained in Chapter 4, this thesis focuses on different parts of the protostars, more specifically the cold and warm envelope and the shock region. Therefore, we selected sources which are the most suitable to our scientific goals. Targeting two different environments was essential for this study: one source subject to strong jet and outflow, i.e., BHR71, and the other in an active and rich star forming region complex, i.e., Cygnus X complex.

"Science literacy is the artery through which the solutions of tomorrow's problems flow."
—N. deGrasse Tyson

3.1 CYGNUS-X COMPLEX

The Cygnus-X complex is located in the northern Cygnus constellation, at 1.4 kpc from the Sun and is of size $\sim$ 200 pc diameter (Bontemps *et al.*, 2010), shown in Figure 3.1. The Cygnus (derived from the Greek for swan) constellation is characterized by a line going from the tail to the beak of the swan, and another line connecting the wing extremities. There are five main stars laying on these two lines, also called the northern cross: the tail is the house of Deneb, the brightest class A star of Cygnus. Albireo, located on the beak, is a binary star. The center is where Sadr, a class F star, stands. While, the two other stars are Aljanah and Fawaris, located on the wing line, on either sides of the center. These are class K and B stars, respectively (Figure 3.1).

The Cygnus-X complex is a box of 5 deg.side, englobing Sadr (cf. Figures 3.1 and 3.2). This region is one of the richest regions in massive and highly luminous (luminosity up to 2×10^6 L$_\odot$) protostars close to the Sun (within 2 kpc radius). It also englobes several stellar associations of class O and B, including the largest OB association (M= $\sim 10^5$ M$_\odot$), Cygnus OB2, at such proximity of the Sun (Reddish *et al.*, 1966; Massey and Thompson, 1991). Cygnus OB2 contains around 2600 OB-stars and 100 O-stars, located near the complex's center (Knödlseder, 2000; Comerón *et al.*, 2002; Hanson, 2003).

The largest molecular clouds (total M = 3×10^6 M$_\odot$) within 2 kpc radius from the sun are also found in this complex (Schneider *et al.*, 2006). Schneider *et al.* (2006) pointed that the molecular clouds are connected and heated by the stellar associations, Cygnus OB2 and Cygnus OB1/OB9, found in this complex.

The presence of 40 massive protostars found in Cygnus X, as CygX-N44, CygX-N63, W75N(CygX-N30), etc. defines this complex as not only the richest region in protostars but also, the most active one close to the Sun.

This Cygnus X complex was divided into two main regions, Cygnus North and Cygnus South. Each region is delimited by the sources, DR17–DR23 for the northern part, and DR4–DR15, for the southern region, as shown in Figure 3.2 . The studied sources in this thesis are located in the northern region, N12 and N30.

The northern region hosts several H II regions, which can be embedded, as it is the case for DR21, DR20 and the YSO W75N (Cygnus X-N30), or distinct molecular clouds, e.g., DR17, DR23 and DR22. The Southern region contains less molecular
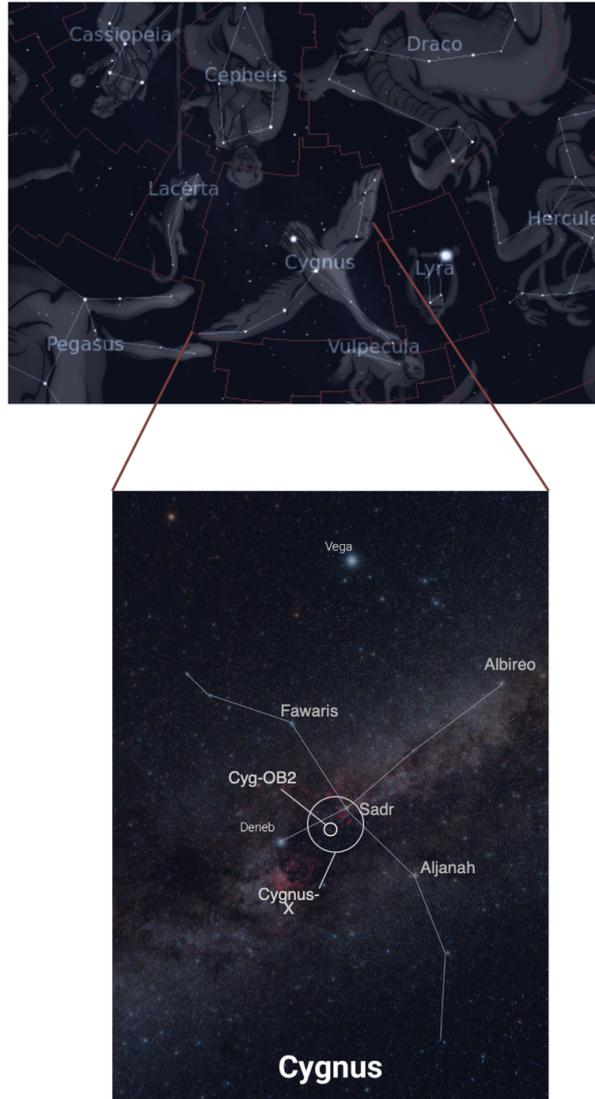
FIGURE 3.1: Cygnus map. *top:* schematic map of the constellations surrounding the Cygnus constellation. Credit: D. Ford *bottom:* Cygnus constellation highlighted by the Northern cross and five main stars: Deneb, Albireo, Sadr, Aljanah and Fawaris. Adapted Figures. Credit: astrobackyard

clouds than the northern one. We identified here the main H II clouds DR15, DR5, DR4 and AFGL2591.

Chapters 5 and 7 are centered on the northern part of the Cygnus-X complex, as shown by the right part of Figure 3.2. On Figure 3.2 adapted from Motte *et al.* (2007), the entire Cygnus X complex (cf. upper right panel) is shown as well as the distinction between the north and south regions. The upper left and bottom panels are zoom of the discussed north and south regions, respectively. The main molecular clouds and sources are displayed on these figures. In this thesis, we focused on CygX-N30 (α = 20^{h}38^{m}36.6^s, δ = 42°37′32″0 [J2000]) and CygX-N12 (α= 20^{h}36^{m}57.6^s, δ = 42°11′30″0 [J2000]). CygX-N30 is the most luminous source of the sample with a luminosity of 1.5×10^4 L$_\odot$, while CygX-N12 is the fourth most luminous protostar with a luminosity of 3.3–4.9×10^2 L$_\odot$ (Pitts *et al.*, 2021).
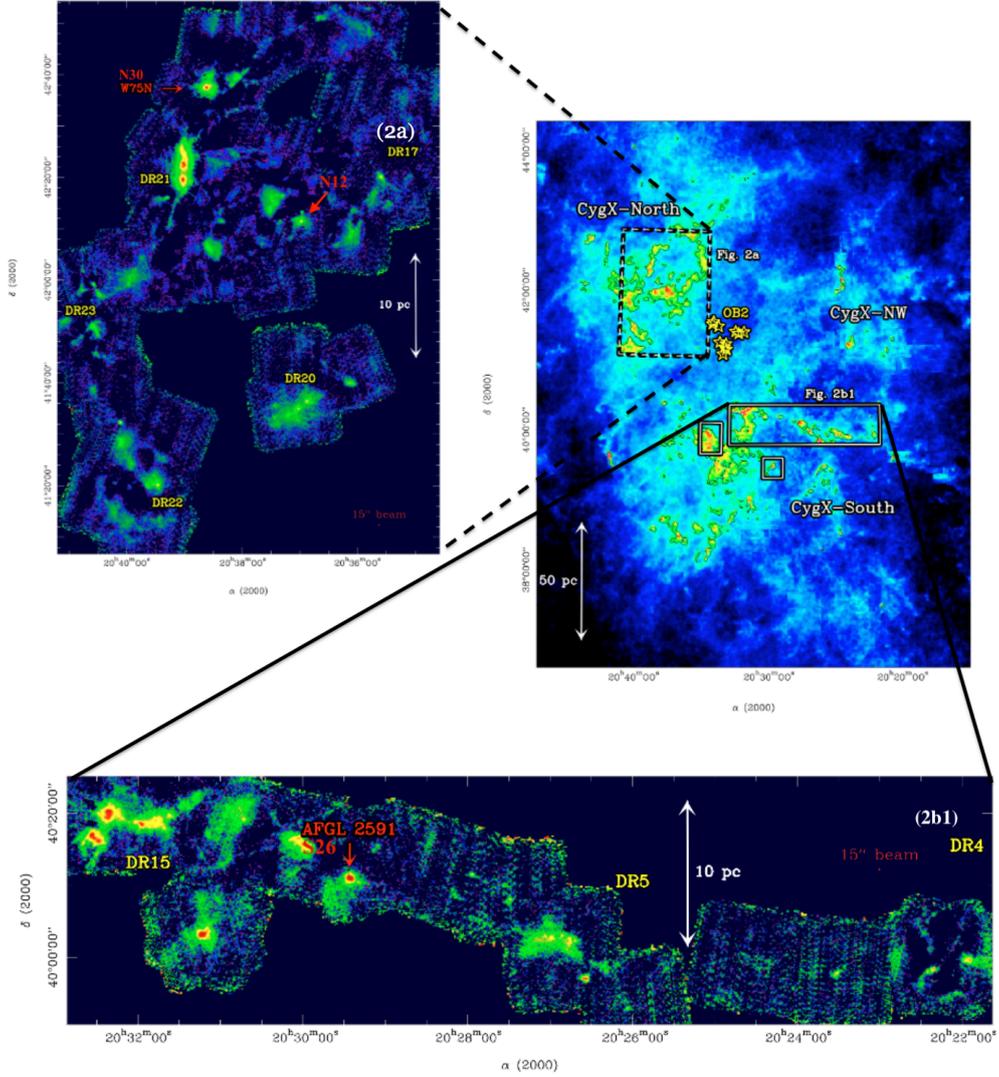
FIGURE 3.2: Cygnus-X map. *Top right:* extinction map of the Cygnus-X, displaying the Cygnus OB2 and the three main molecular clouds identified by (Schneider *et al.*, 2006). The color scale from dark blue to yellow corresponds to the lower extinction to the highest, while the contour displays 15 mag contour level. *Top left:* Millimeter continuum (1.2 mm) map of Northern (*Top left Fig.*) and Southern (*Bottom Fig.*) region of Cygnus-X, from IRAM-30m observations. The angular resolution is indicated on the lower left corner. The color scale is in units of mJy beam^{-1} (max. flux 8500 mJy beam^{-1}). Several sources within this region are indicated in yellow. The sources of interest for this study (N30, N12) are shown in red in Fig. (2a). Figures are adapted from Motte *et al.* (2007).

3.1.1   *CygX-N30*

CygX-N30 also called W75N(B) is a high mass class 0 protostar (M=340–480 $M_\odot$, Pitts *et al.*, 2021), formed in an hyper compact HII region (Motte *et al.*, 2007). This source hosts three continuum cores, MM1, MM2 and MM3, located at 0.5^s in R.A. from each other, as discussed in Shepherd (2001) and Minh *et al.* (2010). The brightest core MM1 is itself composed of two parts MM1a and MM1b, and three radio continuum sources VLA1, VLA2 and VLA3, as shown in Figure 3.3 from van der Walt *et al.* (2021). The VLA1, VLA2 and VLA3 detected with the very large telescope (VLA) are radio sources emitting continuum radiation, which are in this case generated by non-thermal emission, from ionized interstellar gases (i.e., HII region) or thermal jets (Shepherd *et al.*, 2003; Carrasco-Gonzalez *et al.*, 2010; Rodríguez-Kamenetzky *et al.*, 2020; van der Walt *et al.*, 2021).

Previous spectral observations by Minh *et al.* (2010) have pointed out that the hot core is located at MM1b and thermal jet is emitted from VLA1, while Hutawarakorn *et al.* (2002) pointed VLA2 as the outflow center. This VLA2 is believed to be a shock region from the star forming site at VLA1. Moreover, chemical differences have been observed by Minh *et al.* (2010) towards MM1a and MM1b suggesting an evolving star-forming core. These chemical differences have been later confirmed with an interferometric line survey by van der Walt *et al.* (2021).

3.1.2   *CygX-N12*

The Cygnus X–N12 is located in a comet-shaped cloud and, is isolated from the other protostars, as shown on the right panel of Figure 3.2. This source is also a class 0 protostar. High resolution observations at 1.3 mm by Bontemps *et al.* (2010) pointed that CygX-N12 contains four spherical, compact and aligned continuum sources, MM1/2/3/4 (cf. Figure 3.3). However, the central two cores MM1 and MM2, are the brightest ones and contain 28% of the CygX-N12 total mass. Motte *et al.* (2007) estimated its mass from 1.3 mm observations, to be 86 $M\odot$. This last was later adjusted by Pitts *et al.* (2021), finding a mass of 122–214 $M\odot$, from SED fitting and Transphere modelling. In this study, with the used sensitivity, only the main continuum cores are observed. Moreover, no strong radio continuum source was detected towards CygX-N12 (Bontemps *et al.*, 2010). This source in associated with outflows, observed with ^{12}CO and SiO emission by Csengeri *et al.* (2011), emphasizing that it is an actively forming star. These outflows are aligned with the continuum sources and believed to be emitted from the two most massive cores (Duarte-Cabral *et al.*, 2013).
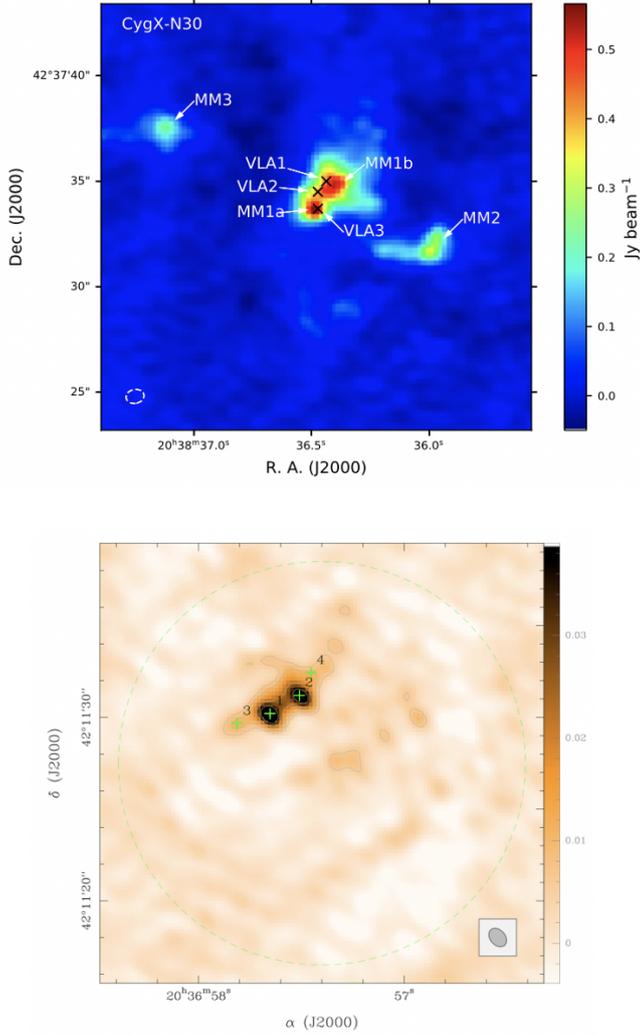
FIGURE 3.3: Map displaying the continuum cores. *top:* CygnusX-N30 continuum cores MM1, MM2 and MM3, and the radio continuum sources towards the central core MM1 (VLA1, VLA2 and VLA3), pointed with black crosses. The units are in Jy beam^{-1}. Figure taken from van der Walt *et al.* (2021). *Bottom:* CygnusX-N12 continuum cores from Bontemps *et al.* (2010). The units are in Jy beam^{-1} and the four continuum sources are indicated with green crosses. The contours correspond to levels: 3σ, 4.8σ, 7.5σ, 12σ, 19σ, 30σ, 75σ, and 120σ (σ corresponds to 1.9 mJy beam^{-1}).

3.2 BHR71

BHR71 is located in the southern constellation Musca ("the fly") also known as the Api constellation from the latin meaning bee. Musca is 184 pc from our solar system (Corradi *et al.*, 1997; Knude and Hog, 1998). It contains stars, star clusters and also nebulae. The main stars characteristic of this constellation are located along the fly or bee. These are named after the greek letters: α Muscae, β Muscae, ϵ Muscae, λ Muscae, γ Muscae and δ Muscae, as shown in Figure 3.4. The brightest star of this constellation is the α Muscae, located at the center of the constellation. As can be seen on the right side of Figure 3.4, ϵ Muscae is a red giant star, δ Muscae is an orange Giant and closest star to our solar system from this complex. β, α and γ Muscae are blue-white stars, while λ is a white star (cf. Stellar classification, Section 1.4). The Musca constellation englobes several stars clusters such as NGC4372, NGC4463, NGC4815 and NGC4833, and several nebulae. Amongst these nebulae, we find the famous dark doodad nebulae, also known as BHR80 and Sandqvist 149 (Wenger *et al.*, 2000). As its name indicates, it is a dark nebulae, which is dense molecular cloud not observable at the visible wavelength due to the dust opacity.

Another famous nebulae within this constellation is the BHR71, which is our source of interest in this thesis.
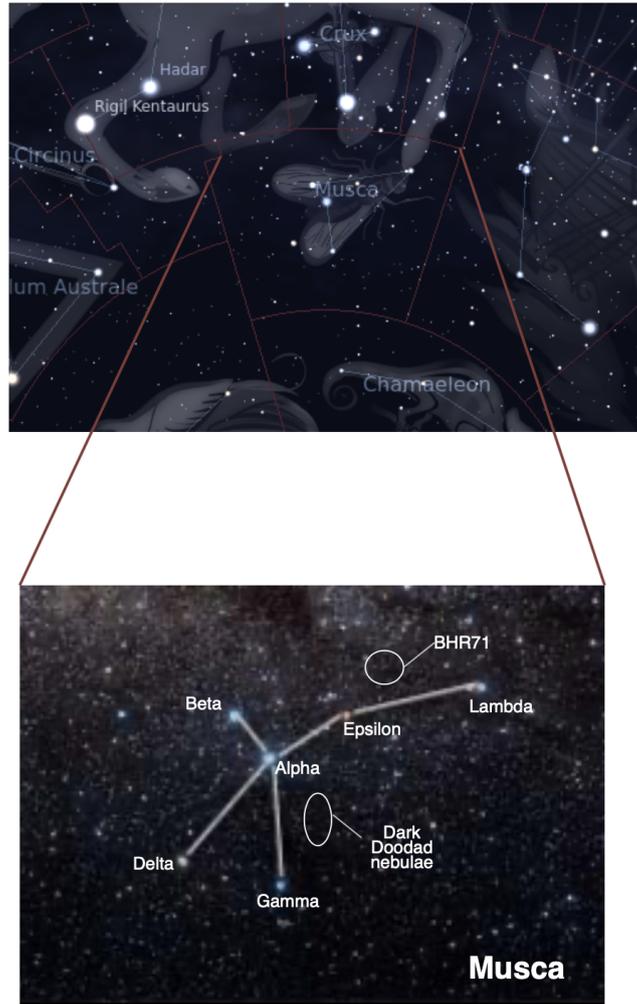
FIGURE 3.4: Musca map. *left:* schematic map of the constellations surrounding the Musca constellation. *right:* Musca constellation highlighted by the six main stars: α Muscae, β Muscae, ϵ Muscae, λ Muscae, γ Muscae and δ Muscae. The Dark Doodad nebulae (BHR80) is also highlighted as well as the BHR71 region. Adapted Figures. Credit: D. Ford and B. Simpson.

BHR71, located at 175 pc, is well-known isolated star forming region observable from the southern hemisphere (T. Bourke *et al.*, 1995a). This region is a small dark nebula of a diameter of ~0.32 pc (T. Bourke *et al.*, 1995b; T. Bourke *et al.*, 1995a). BHR71 is also referred as a Bok globule, which is an isolated small dark nebula. This source contains two class 0 protostars, IRS1 and IRS2, separated to each other each by 3400 AU (T. L. Bourke, 2001). IRS1, is the most luminous one with a luminosity of 13.5 L$_\odot$ and is located at $\alpha = 12^h01^m36.6^s$, $\delta = $ -65°08′48″5 [J2000]. While, IRS 2 has a luminosity of 0.5 L$_\odot$ and, located at $\alpha = 12^h01^m34.0^s$, $\delta = $ -65°08′44″5 [J2000] (Chen *et al.*, 2008; Gusdorf *et al.*, 2015). Both sources each drive a molecular outflow, shown in Figure 3.5. However, only the outflow driven by IRS1 contains significant amount of circumstellar material (T. L. Bourke *et al.*, 1997), and its outflow extents considerably compared to the outflow from IRS2 (cf. Figure 3.5) Moreover, two bright HH objects, HH320 and HH321, are associated with each outflow in their blueshifted lobes (Corporon and Reipurth, 1997). For the study of Chapter 6, a region of the shock has been targeted, shown by the green box in Figure 3.5. This region is centered around the so-called SiO-knot, defined by Gusdorf *et al.* (2011), in the northern outflow of the IRS1. This region located in the inner outflow cavity was selected as it is free from potentially contaminating envelope emission

(Gusdorf *et al.*, 2011), making it an ideal laboratory for understanding the chemistry in this shock region of BHR71.
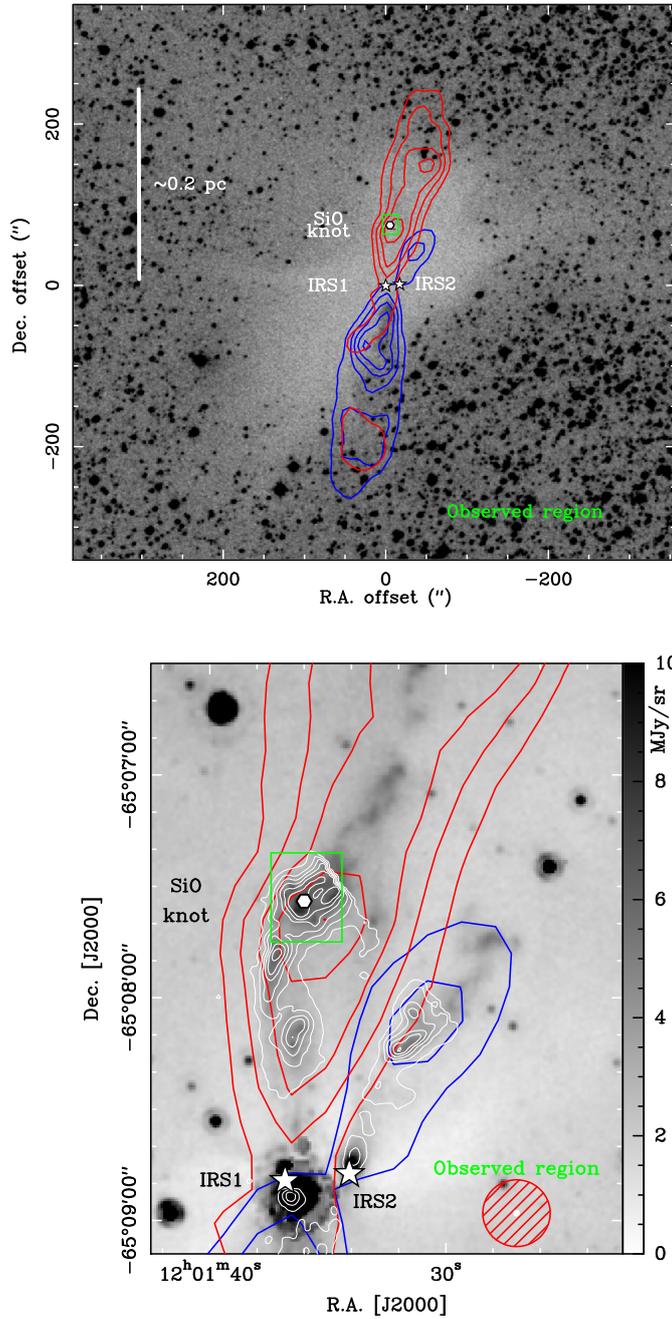
FIGURE 3.5: Map of the BHR71 region. *Top panel:* the entire region of BHR71 is shown, with the protostars IRS1 and IRS2. The extent of the outflows from both sources are shown with the red and blue contours from the APEX dataset presented in Gusdorf *et al.* (2015). The region of interest for this thesis around the SiO-knot is shown with the green square. *Bottom panel:* Zoom of the region of interest. The white contours represent the H_2 0–0S(5) emission presented in Neufeld *et al.* (2009). This Figure is adapted from el Akel et al., 2021 [subm.]

Bibliography

1. S. Bontemps *et al.*, *A&A* **524**, A18, (https://doi.org/10.1051/0004-6361/200913286) (2010).

2. T. Bourke, A. Hyland, G. Robinson, *MNRAS* **276**, 1052–1066 (Oct. 1995).

3. T. Bourke *et al.*, *MNRAS* **276**, 1067–1084 (Oct. 1995).

4. T. L. Bourke, *ApJ* **554**, L91–L94, arXiv: astro-ph/0105204 [astro-ph] (June 2001).

5. T. L. Bourke *et al.*, *ApJ* **476**, 781–800 (Feb. 1997).

6. C. Carrasco-Gonzalez *et al.*, *Science* **330**, 1209–12 (Nov. 2010).

7. X. Chen *et al.*, *ApJ* **683**, 862–875, arXiv: 0805.1533 [astro-ph] (Aug. 2008).

8. F. Comerón *et al.*, *A&A* **389**, 874–888 (July 2002).

9. P. Corporon, B. Reipurth, presented at the Herbig-Haro Flows and the Birth of Stars, ed. by B. Reipurth, C. Bertout, vol. 182, p. 85.

10. W. Corradi, G. Franco, J. Knude, *A&A* **326**, 1215–1227 (Oct. 1997).

11. T. Csengeri *et al.*, *A&A* **527**, A135, (https://doi.org/10.1051/0004-6361/201014984) (2011).

12. A. Duarte-Cabral *et al.*, *A&A* **558**, A125, (https://doi.org/10.1051/0004-6361/201321393) (2013).

13. A. Gusdorf *et al.*, *Astronomy Astrophysics* **532**, A53, ISSN: 1432-0746, (http://dx.doi.org/10.1051/0004-6361/201116758) (July 2011).

14. A. Gusdorf *et al.*, *A&A* **575**, A98, (https://doi.org/10.1051/0004-6361/201425142) (2015).

15. M. Hanson, *ApJ* **597**, 957–969, arXiv: astro-ph/0307540 [astro-ph] (Nov. 2003).

16. B. Hutawarakorn, R. Cohen, G. Brebner, *Monthly Notices of the Royal Astronomical Society* **330**, 349–364, eprint: https://onlinelibrary.wiley.com/doi/pdf/10.1046/j.1365-8711.2002.05068.x, (https://onlinelibrary.wiley.com/doi/abs/10.1046/j.1365-8711.2002.05068.x) (2002).

17. J. Knödlseder, *A&A* **360**, 539–548, arXiv: astro-ph/0007442 [astro-ph] (Aug. 2000).

18. J. Knude, E. Hog, *A&A* **338**, 897–904 (Oct. 1998).

19. P. Massey, A. Thompson, *AJ* **101**, 1408 (Apr. 1991).

20. Y. Minh *et al.*, *ApJ* **723**, 1231–1240 (Nov. 2010).

21. F. Motte *et al.*, *A&A* **476**, 1243–1260, (https://doi.org/10.1051/0004-6361:20077843) (2007).

22. D. A. Neufeld *et al.*, *The Astrophysical Journal* **706**, 170–183, (https://doi.org/10.1088/0004-637x/706/1/170) (Oct. 2009).

23. R. Pitts *et al.*, *arXiv e-prints*, arXiv:2110.11132, arXiv: 2110.11132 [astro-ph.GA] (Oct. 2021).

24. V. C. Reddish, L. Lawrence, N. M. Pratt, *Publications of the Royal Observatory of Edinburgh* **5**, 111–180 (Jan. 1966).

25. A. Rodríguez-Kamenetzky *et al.*, *Monthly Notices of the Royal Astronomical Society* **496**, 3128–3141, ISSN: 0035-8711, eprint: https://academic.oup.com/mnras/article-pdf/496/3/3128/33484821/staa1742.pdf, (https://doi.org/10.1093/mnras/staa1742) (June 2020).

26. N. Schneider *et al.*, *A&A* **458**, 855–871, (https://doi.org/10.1051/0004-6361:20065088) (2006).

27. D. Shepherd, *ApJ* **546**, 345–351 (Jan. 2001).

28. D. Shepherd, S. Kurtz, L. Testi, presented at the American Astronomical Society Meeting Abstracts, vol. 203, 94.10, p. 94.10.

29. S. J. van der Walt *et al.*, *Astronomy Astrophysics* **655**, A86, ISSN: 1432-0746, (http://dx.doi.org/10.1051/0004-6361/202039950) (Nov. 2021).

30. M. Wenger *et al.*, *A&AS* **143**, 9–22, arXiv: astro-ph/0002110 [astro-ph] (Apr. 2000).

4

Thesis Preamble

This Chapter consists of a preamble of the work performed during this thesis and consists of two parts. The first part explains the main research question to the reader, which is the motivation behind each study performed during this Ph.D. In this section, we will also introduce each subject of this thesis, covered in Chapters 5–7. The second part lists the scientific articles published, submitted or in preparation, which are part of this Ph.D and the implication for each author is detailed for each article.

4.1 RESEARCH CONTEXT AND DESCRIPTION

The dense and warm interstellar medium, associated with star formation, is a reservoir of an incredibly rich chemistry. From our current understanding, the most complex molecules form on ice-covered dust grains (Herbst and van Dishoeck, 2009). The different environmental conditions that include a protostar lead to a certain chemical complexity for understanding this region. In the cold part of the protostar (i.e., outermost envelope), the conditions are such that most the molecules freeze-out and surface chemistry and physics is possible on these icy dust grains. While in warmer environments (i.e., hot core), the environmental conditions in these star-forming regions enable the sublimation of the molecules formed on the surfaces of icy dust grains, making them directly observable at sub-mm wavelengths. Moreover, shocks and outflows from young stars are known to be unique chemical laboratories. When they impact the surrounding cloud material, the gas is heated and compressed by orders of magnitude, and ice from dust grains might be sputtered and released into the gas phase where they can be observed directly. These observations towards the different regions of a protostar in turn allows us to understand the chemical processes happening in these regions, and ultimately to understand the connection between the star formation and the chemistry.

One of the main goals of astrochemistry is understanding complex organic molecules by quantifying how, where and when they form in the star-formation process. For the last decade, special attention has been given to the complex organic molecules consisting of H, C, and O, and to some extent N, but little work has been done on the impact of the S chemistry, in spite of S being one of the more abundant species in the ISM (Asplund *et al.*, 2009; Goicoechea *et al.*, 2006; Neufeld *et al.*, 2015). Determining the abundances of these species allows us to understand the dominating chemical processes and the formed physical structures, which in turn broadens our knowledge of the physics of star-forming cores. At this stage, despite on-going efforts, the chemistry in star-forming regions is still not fully understood,

This family of sulphur species is one of the most intriguing in star-forming regions, as these seem to play a specific role in all the different regions of star formation (Jenkins, 2009). Indeed, the sulphur species are primarily known for tracing the warm gas, particularly toward low-mass protostars (Tabone *et al.*, 2017; Artur de la Villarmois *et al.*, 2018; Jiménez-Escobar and Muñoz Caro, 2011; Drozdovskaya *et al.*, 2018; van der Tak *et al.*, 2003). The S-bearing species are also often used as shock tracers, and more specifically the S-species such as SO, SO_2, OCS (Tabone *et al.*, 2017; Artur de la Villarmois *et al.*, 2018; Oya *et al.*, 2016). While in the cold envelope, the sulphur chemistry was found to be active on the icy dust grains,

leading to a large network of S-bearing molecules formed on the surface of dust grains (Wakelam *et al.*, 2005; Mitchell, 1984; Pineau des Forêts *et al.*, 1993).

Currently, several points of interest remain unknown. We do not know what their local concentrations are, how they interact with other molecules in these dense and warm regions to form a second generation of S-bearing molecules. It is also unknown why sulphur-bearing species are good shock tracers, under which shock conditions emission dominates, and what the local concentrations are. These questions are especially important if we want to use sulphur-bearing species to understand the chemistry occurring in star-forming regions, and to understand the amount of material involved in the different environments.

The cornerstone molecule from this family is H_2S, as this molecule is highly active in these types of environments and might play a bigger role in the astrochemistry than expected. This molecule is believed to be formed from atomic sulphur from hydrogenation of grains and therefore is associated with a possible reservoir of atomic sulphur(Smith, 1991; van der Tak *et al.*, 2003; Boogert *et al.*, 2015). Nevertheless, no detection of this hybrid on icy dust grains has been confirmed yet (Dagdigian, 2020).

To start addressing these questions, we conducted three studies, reported in Chapters 5 to 7:

1. We started our analysis with the observational study of hot-core (inner part of the envelope) and the cold envelope towards Cygnus X-N12 and observations solely of the hot core towards CygX-N30. Both targeted sources are protostars of the highly active star forming region, Cygnus-X. For understanding the effect of the different environments on the sulphur chemistry, we did a full line survey over 43 GHz for the cold envelope of CygX-N12, from 72 GHz to 115 GHz. For targeting the hot cores of both regions, we used data from the SMA survey PILS-Cygnus (van der Walt *et al.*, 2021). These consist of 32 GHz bandwidth observations from 329 to 361 GHz. Fifty-five and fifty-three sulphur molecular transitions were detected towards N12, in the cold envelope and the hot core, respectively. While, more than a hundred of sulphur lines could identified in the hot core region of CygX-N30. We modeled the detected sulphur lines and derived the corresponding column density and excitation temperature of the S-species, in the different environments and compared the sources to each other. We imaged the emission of the sulphur bearing species, analysed and compared their spatial extents. We complemented our observational results with *in-situ* laboratory experiments, reproducing the ISM conditions, with a focus on the H_2S molecule. We studied the H_2S reactivity with hydrogen atoms and CO, in a cold environment (T~10 K). This study allowed us to draw a pattern among the different part of the envelope and corresponding chemistries, i.e., the cold and warm chemistry, while connecting the laboratory findings to the observational results. We could also point out chemical differences among protostars, and identify the behaviour of the sulphur species towards a so-called typical protostar.

2. The second article focuses on the well-known shock region, BHR71. The studied region is the so-called SiO-knot, defined by Gusdorf *et al.* (2011) as a rich chemical region, free from any potential envelope contamination. We used ALMA high-resolution data of $1''$ to analyse a region of $20''$ size over this SiO-knot position. Over the observed seven sulphur species, we had a clear detection ($>3\sigma$) of two sulphur bearing species (CS and SO) as well as CH_3OH and H_2CO in band 7. Their molecular emissions were analyzed and several regions of $1''$ radius were delimited and used in the analysis. Based on their emission at the different studied region, their corresponding column density and excitation temperature were found. This observational study was coupled with a modeling approach. We used the Paris-Durham code to determine the physical parameters. of the shock (i.e., type of shock, shock velocity, etc.). The selection of the best-fit model was based on comparison of the simulated H_2 0–0S(0) to S(5) emission with the H_2S emission observed by *Spitzer*. Each region of $1''$ diameter were considered in the analysis, which led to the selection of a best-fit model. The simulated atomic emissions of the selected model were then compared to atomic oxygen emission, at 63.2 μm

and 145.5 μm, from *Herschel* and the atomic sulphur emission at 25.2 μm from *Spitzer*. The selected shock model was then compared to the high-resolution ALMA observations. For the first time, this region was studied at such high resolution. Moreover, this study pointed the complexity of the chemistry in a region constantly replenished by an outflow.

3. The third article provides a closer look at the H_2S emission towards the most luminous protostars of the Cygnus-X complex (CygX-N30). In this study, we focus on the H_2S lines at 216.71 GHz, 228.56 GHz and 300.505 GHz. Out of the three lines, emission from only two lines could be detected. Their integrated intensity maps were examined and the spectra of each transition at each of the central continuum cores of the CygX-N30 (MM1a and MM1b) have been analyzed and modeled. From the analysis, the column density of H_2S at each of the two regions was determined and compared with previously derived S-bearing species in this region (cf., Article 1.). This study allowed us to discuss the possible origin of H_2S, the expected reservoir of atomic sulphur in the protostar, as well as the H_2S correlation with the icy dust grains, characteristic of the surface chemistry in the protostars.

4.2 PUBLICATIONS

This thesis lead to several scientific publications, which are summarized in the following:

- M. el Akel, L. E. Kristensen, R. leGal, S. J. van der Walt, R.L. Pitts, F. Dulieu, 2021, in press. "Unlocking the sulphur chemistry in intermediate-mass protostars of Cygnus X".

- M. el Akel, A. Gusdorf, G. Pineau-des-Forêts, L. E. Kristensen, R. Le Gal, T. Bourke, D. Riquelme, J. Pety. "High-angular resolution observations of the chemically active BHR71 outflow with ALMA: physical and chemical conditions". [**submitted**]

- M. el Akel, R. Le Gal, R. L. Pitts, L.E. Kristensen. "H_2S, a key driver of the sulphur chemistry in Cygnus-X N30?" [**in preparation**]

- S. J. van der Walt, L. E. Kristensen, J. K. Jørgensen, H. M. Calcutt, S. Manigand, M. el Akel, R. Garrod, K. Qiu, 2021, A&A, 655, A86."Protostellar Interferometric Line Survey of the Cygnus X region (PILS-Cygnus) – First results: observations of CygX-N30".

4.2.1 *Contribution overview*

I. *Unlocking the sulphur chemistry in intermediate-mass protostars of Cygnus X*

The laboratory experiments and analysis have been carried out by myself. The observations and data reduction of observations from IRAM-30m have been performed by myself. The calibration steps of the SMA data have been performed by Charl van der Walt. While the data analysis of both dataset (IRAM-30m and SMA) have been performed by myself. Lars E. Kristensen and Romane leGal provided input and suggestions on the analysis and interpretation of the data, as well as in the writing process. Charl J. van der Walt, Rebecca L. Pitts and Francois Dulieu provided extra comments for improving the paper.

II. *High-angular resolution observations of the chemically active BHR71 outflow with ALMA: physical and chemical conditions*

The ALMA data analysis have been performed by myself, as well as the data interpretation from ALMA, APEX, *Spitzer* and *Herschel*, and the writing of the paper. Antoine Gusdorf and Lars E. Kristensen provided continuous support in the data reduction, analysis and interpretation of the data. Guillaume Pineau des Forêts gave substantial input in the data analysis and writing process of the article. Romane leGal, Riquelme Denise, Bourke Tyler and Jérome Pety provided extra comments for

improving the paper.

III. *H_2S, a key driver of the sulphur chemistry in Cygnus X-N30?*

The calibration, imaging, data analysis and writing process of the article have been carried out by myself. Romane le Gal provided valuable insights on the data interpretation and helped with the writing process. Rebecca L. Pitts and Lars E. Kristensen provided extra comments for improving the paper.

Bibliography

1. E. Artur de la Villarmois *et al.*, *A&A* **614**, A26, (https://doi.org/10.1051/0004-6361/201731603) (2018).

2. M. Asplund *et al.*, *ARA&A* **47**, 481–522, eprint: https://doi.org/10.1146/annurev.astro.46.060407.145222, (https://doi.org/10.1146/annurev.astro.46.060407.145222) (2009).

3. A. A. Boogert, P. A. Gerakines, D. C. Whittet, *ARA&A* **53**, 541–581, arXiv: 1501.05317 [astro-ph.GA] (Aug. 2015).

4. P. J. Dagdigian, *MNRAS* **494**, 5239–5243 (June 2020).

5. M. N. Drozdovskaya *et al.*, *MNRAS* **476**, 4949–4964, arXiv: 1802.02977 [astro-ph.SR] (June 2018).

6. J. Goicoechea *et al.*, *A&A* **456**, 565–580, arXiv: astro-ph/0605716 [astro-ph] (Sept. 2006).

7. A. Gusdorf *et al.*, *Astronomy Astrophysics* **532**, A53, ISSN: 1432-0746, (http://dx.doi.org/10.1051/0004-6361/201116758) (July 2011).

8. E. Herbst, E. F. van Dishoeck, *ARA&A* **47**, 427–480 (Sept. 2009).

9. E. B. Jenkins, *ApJ* **700**, 1299–1348, (https://doi.org/10.1088%2F0004-637x%2F700%2F2%2F1299) (July 2009).

10. A. Jiménez-Escobar, G. M. Muñoz Caro, *A&A* **536**, A91, (https://doi.org/10.1051/0004-6361/201014821) (2011).

11. G. Mitchell, *ApJ* **287**, 665–670 (Dec. 1984).

12. D. Neufeld *et al.*, *A&A* **577**, A49, arXiv: 1502.05710 [astro-ph.GA] (May 2015).

13. Y. Oya *et al.*, *ApJ* **824**, 88, arXiv: 1605.00340 [astro-ph.SR] (June 2016).

14. G. Pineau des Forêts *et al.*, *MNRAS* **262**, 915–928 (June 1993).

15. R. G. Smith, *MNRAS* **249**, 172–176, ISSN: 0035-8711, eprint: https://academic.oup.com/mnras/article-pdf/249/1/172/18523351/mnras249-0172.pdf, (https://doi.org/10.1093/mnras/249.1.172) (Mar. 1991).

16. B. Tabone *et al.*, *A&A* **607**, L6, arXiv: 1710.01401 [astro-ph.SR] (Nov. 2017).

17. F. F. S. van der Tak *et al.*, *A&A* **412**, 133–145, ISSN: 1432-0746, (http://dx.doi.org/10.1051/0004-6361:20031409) (Nov. 2003).

18. S. J. van der Walt *et al.*, *Astronomy Astrophysics* **655**, A86, ISSN: 1432-0746, (http://dx.doi.org/10.1051/0004-6361/202039950) (Nov. 2021).

19. V. Wakelam *et al.*, *A&A* **437**, 149–158, arXiv: astro-ph/0503462 [astro-ph] (July 2005).

5

Unlocking the sulphur chemistry in intermediate-mass protostars of Cygnus X Connecting the cold and warm chemistry

M. el Akel[2,1], L.E. Kristensen[2], R. Le Gal[3,4], S.J. van der Walt [2], R.L. Pitts[2], F. Dulieu[1]

1   CY Cergy Paris Université, Observatoire de Paris, PSL University, Sorbonne Université, CNRS, LERMA, F-95000, Cergy, France.
2   Niels Bohr Institute & Centre for Star and Planet Formation, University of Copenhagen, Øster Voldgade 5–7, 1350 Copenhagen K., Denmark
3   Center for Astrophysics |Harvard & Smithsonian, 60 Garden St., Cambridge, MA 02138, USA
4   IRAP, Université de Toulouse, CNRS, CNES, UT3, F-31000 Toulouse, France

Abstract

Context. The chemistry of sulphur-bearing species in the interstellar medium remains poorly understood but might play a key role in the chemical evolution of star-forming regions.

Aims. By coupling laboratory experiments to observations of sulphur-bearing species in different parts of star-forming regions, we aim to understand the chemical behavior of the sulphur species in cold and warm regions of protostars, and we ultimately hope to connect them.

Methods. We performed laboratory experiments in which we tested the reactivity of hydrogen sulfide (H_2S) on a cold substrate with hydrogen and/or carbon monoxide (CO) under different physical conditions that allowed us to determine the products from sulphur reactions using a quadrupole mass spectrometer. The laboratory experiments were complemented by observations. We observed two luminous binary sources in the Cygnus-X star-forming complex, CygnusX-N30 and N12, covering a frequency range of 329–361 GHz at a spatial resolution of 1.''5 with the SubMillimeter Array (SMA). This study was complemented by a 3 mm line survey of CygnusX-N12 covering specific frequency windows in the frequency ranges 72.0–79.8 GHz at a spatial resolution of 34.''0–30.''0 and 84.2–115.5 GHz at a spatial resolution of 29.''0–21.''0, with the IRAM-30m single-dish telescope. Column densities and excitation temperatures were derived under the local thermodynamic equilibrium approximation.

Results. We find that OCS is a direct product from H_2S reacting with CO and H under cold temperatures (T <100 K) from laboratory experiments. OCS is

therefore found to be an important solid-state S-reservoir. We identify several S-species in the cold envelope of CygX-N12, principally organo-sulphurs (H_2CS, CS, OCS, CCS, C_3S, CH_3SH, and HSCN). For the hot cores of CygX-N12 and N30, only OCS, CS and H_2CS were detected. We found a difference in the S-diversity between the hot core and the cold envelope of N12, which is likely due to the sensitivity of the observations toward the hot core of N12. Moreover, based on the hot core analysis of N30, the difference in S-diversity is likely driven by chemical processes rather than the low sensitivity of the observations. Furthermore, we found that the column density ratio of N_{CS}/N_{SO} is also an indicator of the warm ($N_{CS}/N_{SO}>1$), cold ($N_{CS}/N_{SO}<1$) chemistries within the same source. The line survey and molecular abundances inferred for the sulphur species are similar for protostars N30 and N12 and depends on the protostellar component targeted (i.e., envelope or hot core) rather than on the source itself. However, the spatial distribution of emission toward CygX-N30 shows differences compared to N12: toward N12, all molecular emission peaks on the two continuum sources, whereas emission is spatially distributed and shows variations within molecular families (N, O, and C families) toward N30. Moreover, this spatial distribution of all the identified S-species is offset from the N30 continuum peaks. The sulphur-bearing molecules are therefore good tracers to connect the hot and cold chemistry and to provide insight into the type of object that is observed.

key words. Astrochemistry, Stars: formation, Methods: laboratory, Individual sources: CygnusX-N12, CygnusX-N30

5.1   INTRODUCTION

Sulphur chemistry in star-forming regions has for decades been the center of an unresolved challenge between observations and models. It is therefore impossible at this stage to constrain its chemistry or to determine the main S-reservoirs (e.g., Ruffle *et al.*, 1999; Kama *et al.*, 2019; Navarro-Almaida *et al.*, 2020; Le Gal *et al.*, 2021).

Sulphur is one of the most abundant elements (S/H ~ 1.3×10^{-5}, Asplund *et al.*, 2009) in the interstellar medium (ISM) (Goicoechea *et al.*, 2006; Howk *et al.*, 2006; Neufeld *et al.*, 2015), but is considerably depleted from its cosmic value in the gas phase toward a wide variety of molecular environments, for instance, by more than 99.9 % in cold and dense molecular environments (Tieftrunk *et al.*, 1994; Wakelam *et al.*, 2004; Wakelam and Herbst, 2008; Jenkins, 2009; Vastel *et al.*, 2018). This drop in abundance is suspected to play a major role in the chemistry of star-forming regions (Jenkins, 2009; Rivière-Marichalar *et al.*, 2019). Furthermore, the reduced gas-phase abundances of sulphur species suggest that they primarily form on the icy dust grain surfaces and later sublimate to the gas phase (Jiménez-Escobar and Muñoz Caro, 2011), while some species remain locked on the icy dust grains (Millar and Herbst, 1990; Ruffle *et al.*, 1999).

Astrochemical models predict that H_2S might be the dominant reservoir of the atomic sulphur in these regions, although H_2S is poorly observed in these regions because the emission lines are weak (Smith, 1991; van der Tak *et al.*, 2003; Boogert *et al.*, 2015; Jiménez-Escobar and Muñoz Caro, 2011). Moreover, a large quantity of sulphur is also predicted to be in the form of organo-sulphurs[1] trapped on icy grains (Laas and Caselli, 2019). However, the dominant reservoir of sulphur is still unknown. Furthermore, the warm chemistry model of Charnley (1997) suggests that the abundance ratios of X_{SO}/X_{H_2S} and X_{SO}/X_{SO_2} are well suited as molecular clocks for determining the hot-core evolution, as SO_2 is efficiently formed from H_2S within 10^5 yr ($T<230$ K) and then SO is produced from SO_2 (van der Tak *et al.*, 2003; Buckle and Fuller, 2003). In this case, the dominant S-reservoir may change significantly over time. The X_{SO_2}/X_{SO}, X_{SO_2}/X_{H_2S}, and X_{OCS}/X_{H_2S} abundance ratios are commonly used as chemical clocks for the hot-core regions (Wakelam *et al.*, 2011), where SO, OCS and SO_2 are also often used to trace shocked regions (Mitchell, 1984; Leen and Graff, 1988; Pineau des Forêts *et al.*, 1993; Viti *et al.*,

[1]A molecular species consisting of at least one atom of sulphur and one atom of carbon is considered an organo-sulphur.

2001; Podio *et al.*, 2015; Artur de la Villarmois *et al.*, 2018), and OCS can efficiently trace the infalling-rotating envelope (Oya *et al.*, 2016).

The complete sulphur chemistry is currently not fully understood, but improvements to the models are made constantly. This includes, for example, Woods *et al.* (2015), who constrained the amount of sulphur locked up in the form of refractory residue and included in their models (1) laboratory findings from Garozzo *et al.* (2010), where cosmic-ray (CR) impacts were simulated on ice H_2S, leading to the production of CS_2. (2) OCS production from CS_2 and O_2 from Garozzo *et al.* (2010) and Ward *et al.* (2012). From these studies, Woods *et al.* (2015) concluded that the modeled amount of sulphur, which is locked, that is, left on the grain after ice desorption, would be $\sim 10^{-8}$. This has been followed up by T. H. G. Vidal *et al.* (2017), T. Vidal and Wakelam (2018), and T. Vidal *et al.* (2019), who constructed a model for low-mass protostars for which they followed the S-chemistry through various evolutionary stages of the protostar. From their models, NS and OCS are expected to be possible tracers of the initial temperature of the parent cloud, while H_2CS is a possible tracer of the initial density and free-fall time (T. Vidal *et al.*, 2019). Sulphur chemistry is therefore a powerful tool for determining some physical conditions within the protostars.

Several spectral surveys targeting different star-forming regions, such as the prestellar core L1544, the surroundings of the solar-like protostar IRAS16293-2422, or in the envelopes of high-mass protostars, have shown a large diversity of sulphur-bearing species (Vastel *et al.*, 2018; Drozdovskaya *et al.*, 2018; van der Tak *et al.*, 2003). For the case of high-mass protostars, van der Tak *et al.* (2003) concluded for the nine studied sources (van der Tak *et al.*, 2003, cf. Table 1 there) that OCS is the main sulphur reservoir in grain mantles, not H_2S, and that the abundance of SO_2 increases from the outer envelope ($T<100$ K) to the inner envelope, or the hot core ($T>100$ K). Furthermore, sulphur-bearing molecules are often considered as good tracers of the hot-core evolution, as their abundance is highly dependent on the physical and chemical variations.

Over the years, the sulphur chemistry in the ISM has been studied from different angles, from observations to models and laboratory experiments. The latter are key to understanding sulphur chemistry and the formation of S-bearing species. The enthalpy of sulphur species is generally not high, making it easy to break their bonds (e.g., the S–H bond is 363 kJ mol^{-1}), and form a large variety of sulphur compounds (Jiménez-Escobar *et al.*, 2014). H_2S photolysis is efficiently performed to form H_2S_2, HS, HS_2 , and S_2. In the presence of H_2O, the photodissocation process would lead to products such as SO_2, SO_4^-, HSO_3^-, HSO_4^-, H_2SO_2, H_2SO_4, and H_2S_2 (Jiménez-Escobar and Muñoz Caro, 2011). However, as of today, no laboratory experiments have been performed to trace the origin of organo-sulphurs from H_2S.

The current disagreement of some aspects of the models (i.e., S-molecular diversity and abundances), observations, and laboratory experiments have led to a limited understanding of the entire sulphur chemistry in star-forming regions. The different pieces of the puzzle have not yet been assembled. Here we focus on understanding warm ($T>100$ K) and cold ($T<100$ K) S-chemistry toward intermediate-mass protostars in the Cygnus-X complex located at 1.3–3 kpc, CygX-N12 and CygX-N30, through the means of a line survey (Odenwald and Schwartz, 1993; Rygl *et al.*, 2012). These two sources have been selected because of their mass and luminosity (Motte *et al.*, 2007). Moreover, their relative isolation compared to the other protostars of the Cygnus-X complex allows us to reduce the probability that the S-chemistry is influenced by other nearby protostars. To assess the sulphur chemistry, line surveys are invaluable tools, as they provide an unbiased view of the chemistry. If these line surveys are executed at different wavelengths, ?oir? example, at 3 mm and at submillimeter wavelengths, they provide access to the different components of a protostellar system, such as the large-scale cold envelope and the inner hot core. These complementary observations enable the comparison between the chemistries in these different regions and for different physical conditions.

The observational results are complemented by dedicated laboratory experiments based on the reactivity of H_2S with the most abundant species in the ISM, H_2 and CO. The laboratory data aim at reproducing the cold surface chemistry occurring with H_2S on the dust grains to understand the observed abundance of the S-species. The laboratory experiments centered on the reactivity of the S-molecule, H_2S, because of its molecular configuration, that is, the stable molecular combination of one atom of

sulphur with the most abundant element in the ISM, hydrogen. The combination of laboratory experiments and observational studies allows us to retrace the chemical reactions occurring in star-forming regions by combining the observed species with the laboratory results found in a controlled environment.

The structure of the paper is as follows. Section 5.2 presents the laboratory experimental setup as well as a description of how the experiments have been carried out. In Section 5.3 we explain the observational setup and the data reduction. The results from laboratory and observational studies are presented in Section 5.4, followed by the discussion in Section 5.5. Section 5.6 provides a summary of our main findings.

5.2 LABORATORY EXPERIMENTS

5.2.1 *Apparatus*

The experiments were performed in the Laboratoire d'Etude du Rayonnement et de la Matière en Astrophysique et Atmosphères (LERMA), which is part of the Observatory of Paris, on the apparatus called VErs de NoUvelles Syntheses (VENUS) (Congiu *et al.*, 2020). This apparatus consists of an ultra high vacuum (UHV) main stainless steel chamber in which the pressure reaches $\sim 10^{-11}$–10^{-10} mbar. This main chamber currently has four injection entries, allowing us to experiment with different molecules simultaneously and/or in sequence. Within the main chamber, a circular gold-coated sample is placed (playing the role of the dust grain), attached to the cold head part of a helium cryostat. The cryostat lets us vary the sample temperature from 7 K to 350 K by means of a regulated resistive heater attached to the back of the sample holder.

All the experiments made with this apparatus consist of two main steps: (1) injection of the molecules on the sample, which can be done simultaneously or in sequence (hydrogenation included). The injection process is performed under specific conditions such as a controlled temperature and low pressure (10^{-11}– 10^{-10} mbar) during a specific time interval. The chemical processes can be monitored by a Fourier Transform Reflection Absorption Infrared Spectrometer (FT-RAIRS), which shows the abundance of each molecule over time via its infrared spectrum (if the molecule is infrared active). The FT-RAIRS records the spectral region between 900 cm^{-1} (~ 11.1 μm) and 4000 cm^{-1} (~ 2.5 μm) with a resolution of 4 cm^{-1}. (2) During the heating of the sample in the main chamber, a thermally programmed desorption (TPD) is performed, where the temperature of the substrate is increased linearly with time. During this process, the flux intensity and composition of the desorbed molecules are measured with a quadrupole mass spectrometer (QMS). A full schematic map of the apparatus is shown in Fig. 5.1.

The quantity of molecules we used is expressed in monolayers (1 ML = 10^{15} molecules cm^{-2}); one monolayer corresponds to full coverage of the substrate by one layer of molecules. For the case of a solid substrate, for example, amorphous H$_2$O substrate, it corresponds to the number of adsorption sites. However, when the substrate is porous, for example, porous H$_2$O, the number of sites is not constant and several ML are required to entirely cover the substrate.

A key component of these experiments is hydrogenation, where atomic hydrogen is deposited on the surface. Atomic H is generated from the dissociation of H$_2$ in a quartz tube by a microwave source at a power of 60 W at 2.45 GHz. H atoms (and the remaining H$_2$ molecules) are thermalized upon surface impact with the walls of the quartz tube and are injected at a temperature slightly above room temperature; however, they are thermalized on pico-second timescales on the surface.

5.2.2 *Experiments*

Two different sets of experiments were performed: (1) hydrogenation of H$_2$S, and (2) reactivity of H$_2$S, CO, and H, in the presence or absence of O$_2$. To quantitatively compare the results from the different experiments, some experimental conditions (i.e., injection of molecular fluxes, quantity of injected molecules, heating process) were kept constant for both sets, while some were varied one at a time (i.e., injection temperature and hydrogenation time). These are detailed below.
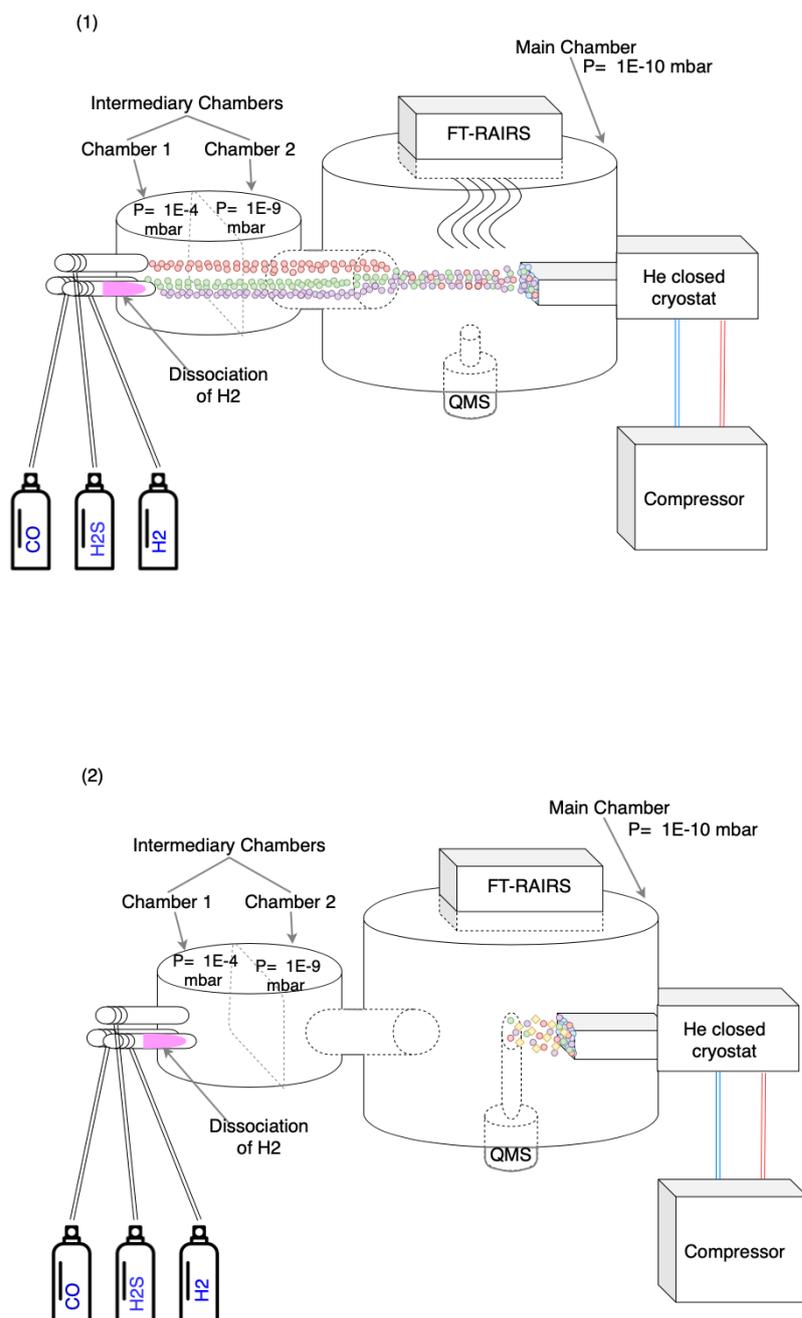
FIGURE 5.1: Schematic of the VENUS apparatus: (1) Molecules (H_2S and CO) and H atoms (dissociated hydrogen) are injected into the first chamber through the different injection pipes under a pressure of 10^{-4} mbar. After passing through the second chamber, with a pressure closer to that of the main chamber, the molecules enter the main chamber and are focused onto the gold-coated substrate. While injecting the molecules, the FT-RAIRS records the infrared spectrum of the molecules arriving at the surface of the substrate. This graphical representation of the molecules displays a codeposition of CO, H_2S, and H. (2) The FT-RAIRS is stopped and the main chamber is heated while the QMS placed in front of the substrate is on. In this way, all the molecules that sublimate can be recorded by the QMS.

The hydrogenation process consists of injecting dissociated H_2 at a constant flux of $\phi(\mathrm{H}) = 5 \pm 1 \times 10^{12}$ molecules $\mathrm{cm}^{-2}\,\mathrm{s}^{-1}$. Furthermore, a constant ramp rate of 12 K min^{-1} was used to perform the TPD from the deposition temperature to 240 K, recording m/z from 18 to 66. The amount of desorbed material was calculated by integrating the area for each m/z curve with the OriginPro 8.0 software[2] and comparing the molecular mass spectra from the NIST Webbook Database[3].

[2] https://www.originlab.com

[3] https://webbook.nist.gov/chemistry/form-ser/

One of the key species in these experiments is CO. In order to exclude the presence of atmospheric N_2 in the chamber (both having a $m/z = 28$), we used ^{13}CO ($m/z = 29$) in our experiments, referenced as CO, instead of ^{12}CO.

For both experimental sets, constant fluxes of $\phi(H_2S) = 2.0 \pm 0.5 \times 10^{12}$ molecules cm^{-2} s^{-1} and $\phi(CO) = 1.7 \pm 0.5 \times 10^{12}$ molecules cm^{-2} s^{-1} were used. These fluxes correspond to a time exposure of about 8 min and 10 min for achieving 1 ML on the gold substrate of H_2S and CO, respectively.

For the hydrogenation of H_2S, that is, {H_2S}+{H}, 1 ML of H_2S was first deposited on the surface, then H-atoms were sent for 1, 2, 3, 5, 10, and 15 min. These experiments were performed at 10 K, 30 K, and 50 K, that is, H_2S and H were both injected into the testing chamber at the same temperature. Then the TPD was performed starting from the deposition temperature.

For the reactivity of H_2S + CO +H, all the reactants were sent simultaneously on the substrate (hydrogenation included) for 15 min, corresponding to 1.5 ML of H_2S and 1.76 ML of CO. Two injection temperatures were tested: 10 K and 22 K. These two were chosen as 10 K is the minimum temperature reached by VENUS, and because CO starts desorbing at ~20 K. Testing these two temperatures allowed us to investigate the sensitivity of the H_2S reactivity with respect to the low-temperature regime. The laboratory data presented in this paper are from the QMS, therefore the data are only recorded once all products are on the surface. Detecting the desorption of a species during the hydrogenation is thus not possible from our experimental data set.

5.3   OBSERVATIONS

The focus of this paper is the study of sulphur chemistry in the cold envelope and the hot core of intermediate-mass protostars of the Cygnus-X complex. For this study, two sets of observations were therefore required to target the cold and hot chemistry with interferometric and single-dish data, respectively. All the observational parameters are summarized in Table 5.1.

TABLE 5.1: Observational details of the SMA and IRAM observations.

Parameters		SMA Maunakea		IRAM-30m
		CygX-N12	CygX-N30	CygX-N12
Phase center α^a		20^{h}36^{m}57^{s}6	20^{h}38^{m}36^{s}6	20^{h}36^{m}57^{s}6
δ^a		42°11′30″0	42°37′32″0	42°11′30″0
Date of Observations		21/06–10/11/2017	20/06–19/10/2017	14–18/08/2019
Spatial resolution		1″5	1″5	27″0 ± 6
Line sensitivity^b		0.15 Jy km s^{-1} beam^{-1}	0.15 Jy km s^{-1} beam^{-1}	3 mK for 3 mm band

^{a} Coordinates are in the J2000 format.

^{b} The line sensitivity is in ~0.48 km s^{-1} channels for SMA data and in 0.8 km s^{-1} channels for IRAM data.

5.3.1   *Observations with the IRAM-30m telescope*

The observations were performed in August 2019 for CygX-N12 with a 3 mm line survey from 72.0–79.8 GHz and 84.2–115.5 GHz, using the 30m telescope of the IRAM facility in Pico Veleta. The broadband EMIR receiver in configuration E090 and the FTS spectrometer in its 200 kHz resolution mode were used for the observations. The weather at the time of the observations was excellent (τ=0.07 in average), with typical system temperatures of 119 K.

The flux calibration was performed on Uranus and nearby sources K3-50A and NGC7027, depending on the observing night. The GILDAS [4] software (Grenoble Image and Line Data Analysis Software, Gildas Team, 2013) was used for the data reduction and analysis.

Data reduction consisted first of identifying line-free channels by eye. These were then used to subtract a linear baseline from the remaining parts of the spectrum. This was done separately for each spectral range we targeted. The data were brought

[4]https://www.iram.fr/IRAMFR/GILDAS/

from the antenna temperature scale to the main-beam temperature scale using a main-beam efficiency, η_{MB} of 0.81. The noise level was measured from the line-free channels, and was found to be ~ 3 mK in 0.8 km s^{-1} channels.

5.3.2   *Observations with the SMA*

The submillimeter observations were taken from the PILS-Cygnus survey targeting the ten brightest sources in Cygnus-X complex, observed in June–November 2017. The data were taken with the SMA facility on Maunakea, in a combination of compact and extended configurations for a final resolution of 1″5. The chosen setup covers the entire frequency range of 329–361 GHz. From this survey, two binary sources were studied, the most massive and luminous one CygX-N30 ($\alpha = 20^{\mathrm{h}}38^{\mathrm{m}}36^{\mathrm{s}}6$, $\delta = 42°37'32″0$ [J2000]), and CygX-N12 ($\alpha = 20^{\mathrm{h}}36^{\mathrm{m}}57^{\mathrm{s}}6$, $\delta = 42°11'30″0$ [J2000]), an intermediate-mass protostar that is relatively isolated. Along with frequency coverage, we obtained continuum emission at 0.8 mm wavelengths for both sources. For full details of the observing strategy, data reduction, and cleaning, see van der Walt *et al.* (2021). The data were reduced and imaged with CASA[5] (Common Astronomy Software Applications, McMullin *et al.*, 2007), while line analysis was done with the CASSIS[6] software (Centre d'Analyse Scientifique de Spectres Instrumentaux et Synthétiques, Vastel *et al.*, 2015).

[5]https://casa.nrao.edu

[6]http://cassis.irap.omp.eu

5.4   RESULTS

In this paper, we investigate three approaches to understand the impact of the cold and hot S-chemistry toward protostars: (1) laboratory experiments reproducing ISM conditions and simulating grain S-chemistry in cold conditions, (2) IRAM-30m observations of the cold envelope of CygX-N12, and (3) SMA observations of the hot core of CygX-N12 and CygX-N30. These observations of protostars allow us to target the S-chemistry in the hot core of intermediate-mass protostars. It was pointed out by van der Walt *et al.* (2021) that the observed hot core toward CygX-N30 is not a traditional hot core, that is, a core in which the gas near the protostar is heated by the accretion luminosity, leading to a jump in the abundance of molecules when the icy mantles sublimate. However, we use the term hot core in this paper to mean the warm gas toward both sources, regardless of their actual physical origin.

5.4.1   *Cold S-chemistry from the laboratory experiments*

The laboratory experiments were performed in several steps in order to fully understand the behavior of H_2S in the presence of CO and H. To determine whether the deposition temperature affects the reactions involving H_2S, hydrogenation experiments (i.e., H_2S+H) were performed at different deposition temperatures and for different hydrogenation times. The different species were identified based on their mass fragmentation in the QMS. A voltage of 30 eV was used to ionize the desorbing species, a voltage chosen so as to lower cracking (dissociation) of the molecules in the QMS. In turn, this leads to more of the desorbing mass being present in the parent mass, as demonstrated by our group (Nguyen *et al.*, 2019). The recorded final quantity of H_2S was found by integrating the primary molecular mass of the component in the TPD spectrum (A_{TPD}), in this case $m/z = 34$, and converting it into a fraction with respect to the initial deposition of H_2S (equivalent to 1 ML of H_2S). The results are displayed in Fig. 5.2. We observed a strong decrease in the amount of H_2S remaining on the surface at 10 K, while at 30 K, the decrease is small (10% decrease) and larger at 50 K, where it decreases to a plateau at $\sim$25% under the maximum.

No products other than H_2S and HS were found in the mass spectrum (in particular, no S_2, m/z=64, or H_2S_2, m/z=66, as shown in Appendix 5.A). The sensitivity limit of the QMS is $\sim$20 cps (counts per second). Therefore, we do not strictly exclude that S_2 and H_2S_2 are formed (both having a desorption temperature below 240 K, i.e., $\sim$140 K for H_2S_2 and $\sim$230 K for S_2; Jiménez-Escobar and Muñoz Caro, 2011). If they are present, their signal intensity is $\lesssim$10% of the H_2S signal, which is not considered as major products of the H_2S hydrogenation. We conclude that the loss at 10 K is due to chemical desorption processes (Dulieu *et al.*, 2013). In
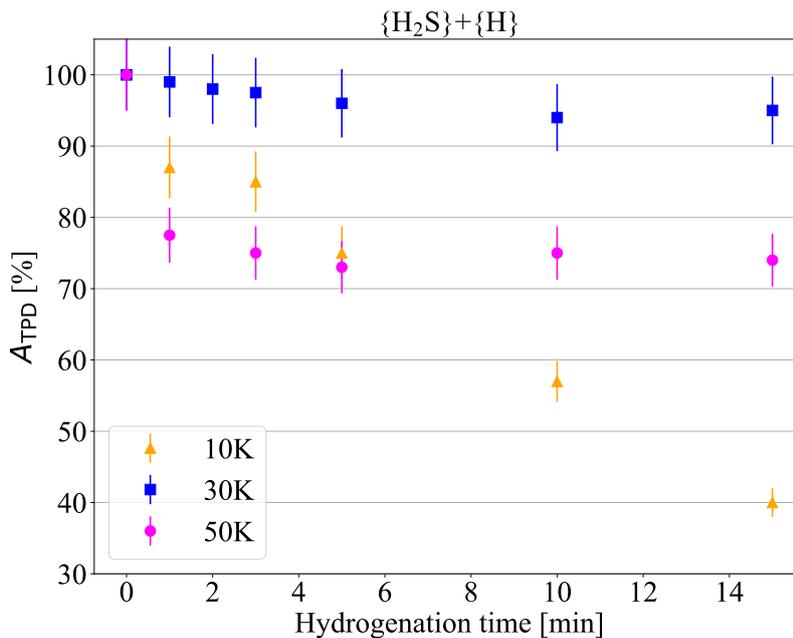
FIGURE 5.2: Integrated area of the $m/z = 34$ (H_2S) curve as a percentage of the initial amount of H_2S injected in the experiment at each temperature. The area is calculated from the QMS while performing a TPD, resulting from hydrogenation of 1 ML of H_2S during varying time, and at varying deposition temperature of H_2S (10 K, 30 K, and 50 K).

these processes, the molecules are returned to the gas phase upon the energy released by chemical desorption, as also demonstrated by Oba *et al.* (2018) in that system. The hydrogenation of H_2S leads to a circular solid-state chemistry (H_2 abstraction followed by H addition) as outlined here:

$$H_2S + H \rightarrow HS + H_2 \qquad (5.1a)$$

$$HS + H \rightarrow H_2S. \qquad (5.1b)$$

The second reaction, involving two radicals, is very exoergic and is expected to have a very high chemical desorption efficiency (Minissale *et al.*, 2016), whereas the first reaction is less exoergic and therefore is not subject to high chemical desorption efficiency. Reaction (5.1b) probably has an entrance barrier, in which case the reaction competes with H+H → H_2 and H desorption.

At 10 K, the reaction can proceed through diffusive reactivity (the Langmuir-Hinshelwood mechanism), eventually helped by tunnelling effects. At 30 K, the residence time of H on the surface is very low, and even the H+H reaction cannot proceed efficiently on compact amorphous ice (Amiaud *et al.*, 2007). The Eley-Rideal mechanism (direct reaction with an H atom with kinetic energy ~ 300 K) is still at play. It appears, however, that it is not efficient, especially when taking into consideration that the chemical desorption is efficient for the second reaction, but that this second reaction can also return the initial H_2S, and so a looping mechanism is necessary to observe a strong reduction. In contrast, at 50 K we observed a larger disappearance of surface H_2S. This is probably due to the desorption of HS. The plateau, made of H_2S unreactive molecules, would correspond to the molecules whose orientation of adsorption is not favorable to the Eley-Rideal mechanism. If this interpretation is correct, we can infer an adsorption energy of ~ 1500 K for the HS molecule, which is more compatible with the value calculated in Oba *et al.* (2018) (1200 K) than with the value proposed in Wakelam *et al.* (2017) (2700 K), although admittedly, our method is not very accurate.

In Figure 5.3 the quantity of H_2S and CO left from the reaction $^{13}CO + H_2S + H$ is shown at two deposition temperatures, 10 K and 22 K, during a 15 min codeposition.
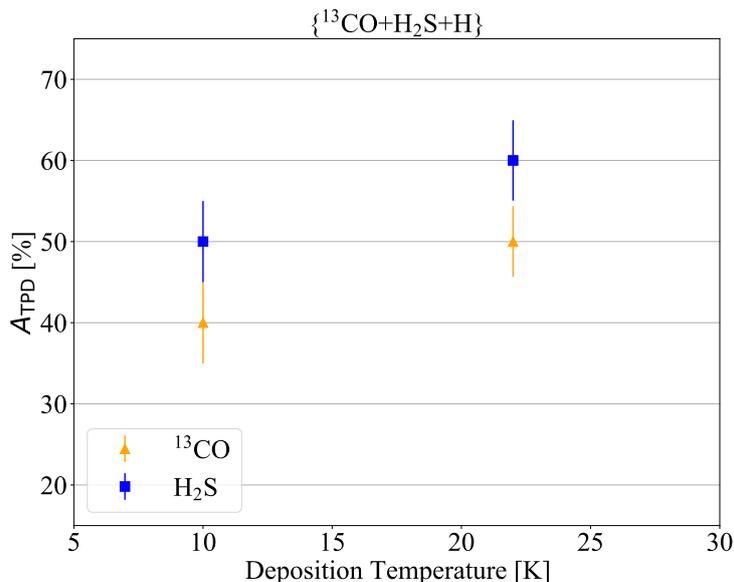
FIGURE 5.3: Area of $m/z =34$ (H_2S, blue squares in the fig.) and $m/z = 29$ (^{13}CO, orange triangles) as a percentage of the initial amount of H_2S (1.5 ML) or ^{13}CO (1.76 ML) injected in the experiment during the reaction {H_2S + ^{13}CO +H }. The area is calculated from the QMS while performing a TPD. The temperature has been varied (10 K and 22 K), while the deposition quantity was kept the same (i.e., corresponding to 15 min of injection).

This figure shows that H_2S has a highly reactive behavior when associated with CO, in addition to hydrogenation.

CO hydrogenation (like H_2S) has an entrance barrier, and its reactivity, leading to H_2CO and CH_3OH, is very reduced at 22 K (see, e.g., Watanabe and Kouchi, 2002; Fuchs *et al.*, 2009). At 10 K, we first note that if H_2S is slightly less consumed in the presence of CO, the CO reduction is stronger than in case of hydrogenation of CO alone. At 22 K the reduction is stronger for both H_2S and CO. This demonstrates cross-linkages between the two hydrogenations, so that HS or HCO are now active reactants in the chain of reactions.

Moreover, this codeposition reaction of H_2S, CO, and H shows a larger diversity of products than the sole hydrogenation of H_2S. From the recorded mass spectrum of this reaction, several molecules could be traced back according to their individual mass spectrum from the NIST-Webbook database. Several species could be clearly determined, such as H_2CO, HCO, OCS, H_2S, CO_2 , and CO. Of these, H_2CO and OCS were detected in approximately equal amounts.

H_2CO is likely the result of direct hydrogenation:

$$CO + H \rightarrow HCO \qquad (5.2a)$$

$$HCO + H \rightarrow H_2CO. \qquad (5.2b)$$

Per analogy to the formation of CO_2, through the {CO+OH} reaction (Noble *et al.*, 2012; Oba *et al.*, 2018; Ioppolo *et al.*, 2011) via the HOCO intermediate, OCS is possibly formed following this chain of reactions:

$$H_2S + H \rightarrow HS \qquad (5.3a)$$

$$HS + CO \rightarrow HSCO \qquad (5.3b)$$

$$HSCO + H \rightarrow OCS + H_2 . \qquad (5.3c)$$
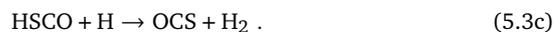
To test the strength of the chemical link of CO and HS to form OCS, we conducted one last experiment, introducing some O_2 in addition to CO and H_2S. O_2 reacts with H atoms without barrier, and readily forms OH groups on the surface, which

also makes CO_2 a final product, and, of course, produces water. The aim of this experiment is twofold: first, we explore conditions more directly related with the interstellar conditions because water formation is probably the main driver of the molecular mantle formation on interstellar dust grains; second, we test the robustness of the previous reaction scheme including a restricted budget of H atoms, as could be the case in dark cloud conditions (Tielens and Hagen, 1982). In other words, we study the possibility of OCS formation in a more oxidizing environment.

Under these conditions, we observed a strong production of water, but CO_2 and OCS were also produced in almost equal quantity, even though they remained minor products dominated by unreacted CO and H_2S, due to a large consumption of H to form water. Nevertheless, we conclude that H_2S and CO interactions on solid cold environments produce OCS as a first outcome even in presence of competing reaction pathways whose end-products are H_2O, CO_2 or CH_3OH. Finally, we note here that traces (less than a percent) of many other organo-sulphur compounds may have been found, but their exact composition is hard to determine with mass spectroscopy alone. For example, CS has the same mass as CO_2, and isotopologs of C and S complicate the analysis. Nonenergetic pathways or H-driven chemistry in the present case do not show the same chemical complexity as obtained in energetic experiments (Jiménez-Escobar and Muñoz Caro, 2011).

5.4.2 *Cold S-chemistry from observations*

The line survey of the CygX-N12 protostar revealed a rich sulphur environment in its cold envelope. Over the 43 GHz of bandwidth, 55 sulphur-molecular transitions were detected, as shown in Table 5.2 and listed in Table 5.B.1. Figures 5.C.1-5.C.3 show parts of the spectrum in which S-lines were identified. The line profiles are narrow (~ 1–3 km s^{-1}) and Gaussian in nature, as is expected when the profiles trace a single cold, quiescent component; in this case, the cold outer envelope of the protostar.

The sulphur lines detected in this survey (cf. Table 5.B.1) were identified by eye in combination with the CDMS database[7] through an iterative process. First, the species already abundantly observed toward protostars were investigated along with their isotopologs. Then, the remaining unknown lines were investigated separately by comparing all possible options with respect to the frequency at which the line was observed by sorting the candidates by their upper level energy (E_{up}) and Einstein A coefficient (A_{ij}): E_{up} lower than 150 K and A_{ij} higher than 10^{-10} s^{-1} were used as threshold values. When we had several possible candidates, they were investigated over a larger window of the spectrum to determine whether more transitions were expected according to the CDMS catalog, but were not seen. Conversely, if most of the lines were seen in the spectrum, the candidate was considered as the right molecule. This analysis was first carried out with the WEEDS package from GILDAS (Maret *et al.*, 2011) and confirmed with CASSIS to ensure that each detection was correctly assigned. Using this line identification scheme, a total of 317 lines were identified from 88 different molecules (including isotopologs). Eighteen percent of the total amount of lines we detected still remain unassigned. The species that were not S-bearing will be presented in a forthcoming study.

The optically thin emission from the detected S-molecules were then modeled with the CASSIS software, v.5.1.1. We assumed a local thermodynamic equilibrium (LTE) approximation.

The modeling was done by varying the column density, line width, and excitation temperature (from 7 K to 50) of the species. The best fit was found by a χ^2 optimization model, which is an iterative process based on these parameters. The error margin was determined by running the model four times for the same molecules by changing the intervals over which the parameters were varied and/or number of combinations of the variables (i.e., excitation temperature, line width, column density, and the velocity at local standard of rest).

In this way, the best fit for all detected species was determined. The modeling parameters found for each S-molecule, shown in Table 5.3, were validated with CASSIS. For some S-species, particularly SO and SO_2, a specific modeling could not be realized on all the transitions we saw (i.e., saturation of the column densities for several T_{ex}) because the lines are optically thick. Therefore, the column density of SO was derived from the observed optically thin emission of its isotopolog ^{34}SO,

TABLE 5.2: Detected S-species in the cold envelope of CygX-N12.

Molecules	# lines[a]	E_{up}[b] [K]
OCS	4	12.3-26.3
$OC^{33}S$	1	20.7
$C^{34}S$	1	7
$C^{33}S$	1	6.9
CS	1	7.1
^{13}CS	1	6.7
$^{13}C^{34}S$	1	6.5
H_2CS	5	9.9-62.6
$H_2C^{34}S$	4	9.7-62.4
CCS	8	19.2-33.6
C_3S	4	25.2-47.4
$CC^{13}CS$	3	25.2-37.7
CH_3SH	4	7.3-13.6
$H^{34}SCN$	3	15.1-69.6
HSCN	3	19.8-79.3
HCS^+	1	6.1
SO	4	9.2-38.6
SO_2	3	7.7-54.7
^{34}SO	1	9.1
NS	1	8.8
NS^+	1	7.2

[a] Number of lines detected in the spectrum.

[b] E_{up} range of the detected molecules.

using the isotopic ratio, $^{32}S/^{34}S = 22.5$ (Lodders, 2003). Only the main isotopolog of SO_2 was observed toward the cold envelope: consequently, we were only able to derive lower limits for its abundance, using LTE consideration for a realistic range of excitation temperatures (i.e., 10 K–40 K). When only one transition was observed (e.g., NS^+, NS, HCS^+), the excitation temperature was assumed to be 15 ± 5 K. This is the expected temperature range in the cold envelope, and the ranges on the inferred column densities correspond to this range in excitation temperature. The excitation temperature does not necessarily correspond to the gas temperature, but as we additionally assumed that the level populations are in LTE, this is the best that can be done. Furthermore, for the species with multiple observed transitions, for example, OCS and C_3S, we find that this excitation temperature is reasonable.

Based on the column density of each species found with LTE modeling and isotopic ratios, we determined their abundances from the ratio of the corresponding column density over the H_2 averaged column density, N_{H_2} in the observed region. The latter can be estimated as follows (Hildebrand, 1983):

$$N_{H_2} = \frac{M}{\mu_{H_2}\, m_H\, \pi\, FWHM^2} \,, \tag{5.4}$$

where M is the cloud mass, $\mu_{H_2}=2.8$ the mean molecular weight per hydrogen (Kauffmann et al., 2008) molecule, m_H the mass of atomic hydrogen, and $FWHM$ is the deconvolved full width at half maximum size.

A mass of 86 $M_\odot$ was determined from single-dish observations assuming no correction for any ?free-free? contamination on the integrated flux, optically thin dust emission, a dust opacity of 0.01 cm^{-2} g^{-1} (Ossenkopf and Henning, 1994), and

TABLE 5.3: Overview of the sulphur line LTE modeling for the optically thin emission of CygnusX-N12 targeting the cold chemistry.

Molecules	N_{sp}[b] [cm^{-2}]	T_{ex}[b] [K]	$FWHM$[b] [km s^{-1}]
OCS	$1.5^{+1.7}_{-0.6} \times 10^{14}$	13±5	3.0
OC^{33}S	$1.5^{+1.2}_{-0.5} \times 10^{13}$	15±5	3.5
C^{34}S	$4.5^{+0.6}_{-3.5} \times 10^{13}$	15±5	3.5
C^{33}S	$4.5^{+0.5}_{-2.3} \times 10^{12}$	15±5	2.5
CS	$9.0^{+1.7}_{-3.0} \times 10^{14}$	22±5	3.0
^{13}CS	$1.6^{+0.1}_{-0.8} \times 10^{13}$	15±5	3.0
^{13}C^{34}S	$6.0^{+1.7}_{-5.0} \times 10^{11}$	15±5	2.5
H$_2$CS	$1.3^{+1.4}_{-0.4} \times 10^{14}$	30±5	3.0
H$_2$C^{34}S	$5.0^{+2.0}_{-4.0} \times 10^{12}$	23±5	3.0
CCS	$1.6^{+2.4}_{-0.6} \times 10^{13}$	8^{+5}[c]	1.5
C$_3$S	$2.5^{+1.2}_{-1.6} \times 10^{12}$	16±5	2.0
CC^{13}CS	$2.0^{+0.2}_{-1.1} \times 10^{12}$	14±5	2.0
CH$_3$SH	$1.0^{+2.0}_{-0.2} \times 10^{13}$	8±5	3.5
H^{34}SCN	$1.5^{+1.0}_{-0.5} \times 10^{11}$	15±5	5.5
HSCN	$1.0^{+0.7}_{-0.3} \times 10^{12}$	13±5	2.5
HCS$^+$	$1.1^{+0.6}_{-0.2} \times 10^{13}$	10^{+5}[c]	3.5
SO[a]	$2.7^{+1.8}_{-1.7} \times 10^{14}$	8–15	3.0
SO$_2$[a]	1.2–3×10^{14}	10–40	3.0
^{34}SO	$1.2^{+1.0}_{-0.3} \times 10^{13}$	15±5	3.0
NS	$2.7^{+2.0}_{-1.7} \times 10^{13}$	15±5	3.0
NS$^+$	$8.5^{+0.5}_{-2.5} \times 10^{11}$	15±5	2.2

[a] The column density of the optically thick emission from SO and SO$_2$ was determined using the isotopic ratios ^{32}S/^{34}S = 22.5.

[b] A source size of 18″.0 was used.

[c] If only the upper or lower limit is given, the best model for the molecule was achieved at the given main value (i.e., T_{ex}) and no lower or upper limit from this value was found.

Motte *et al.*, "The earliest phases of high-mass star formation: a 3 square degree millimeter continuum mapping of Cygnus X"

a dust temperature of 20 K (Motte *et al.*, 2007). Combining the cloud mass and the FWHM size of 0.1 pc from the single-dish observation of [Motte *et al.*, 2007], we find a column density, N_{H_2}, of 1.2× 10^{23} cm^{-2}.

Figure 5.4 displays the abundances of all the detected sulphur species. No specific trend is found among all the abundances, as they vary by up to two orders of magnitude. The highest column densities are seen for the main isotopologs, that is, CS, H$_2$CS, OCS, SO, and SO$_2$, with the latter four showing a similar range of column densities: $N_{H_2CS}/N_{CS} \approx 1.4 \times 10^{-1}$, $N_{OCS}/N_{CS} \approx 1.6 \times 10^{-1}$, $N_{SO}/N_{CS} \approx 3 \times 10^{-1}$, and $N_{SO_2}/N_{CS} \approx 1.3$-$3.3 \times 10^{-1}$.
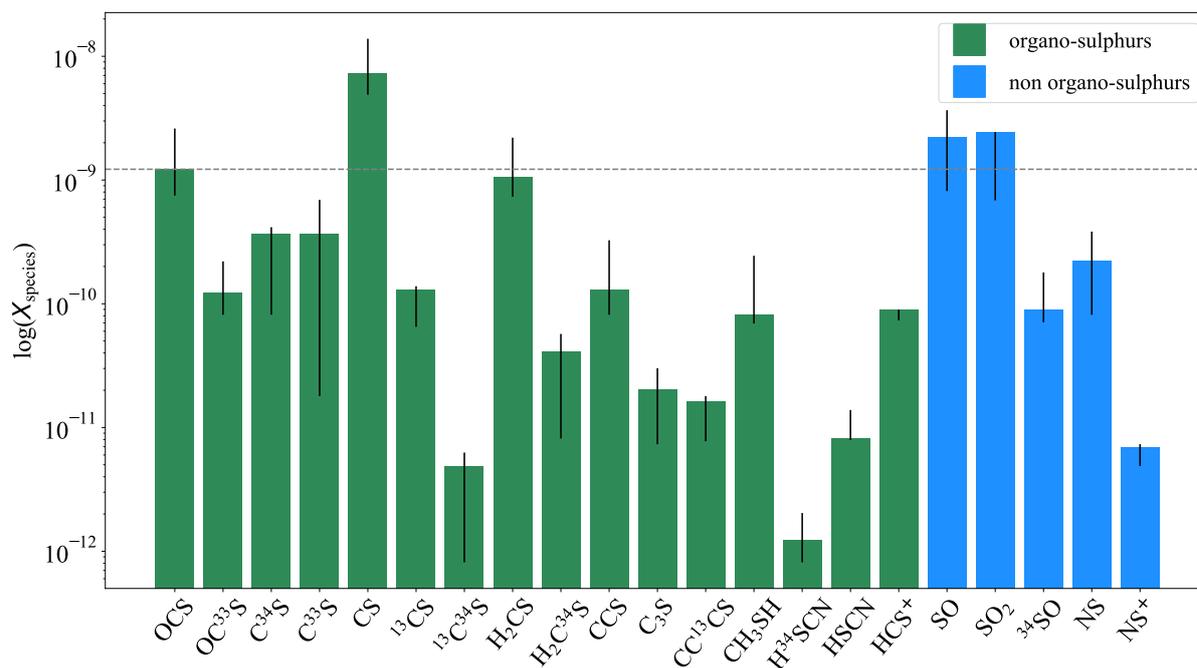
FIGURE 5.4: Abundance of S-species detected toward CygX-N12 using the derived S-abundances from Table 5.3 and N_{H_2} of $1.2\times$ 10^{23} cm^{-2} (see text). The dotted line represents the abundance above which 20 % of the sulphur sample lies.
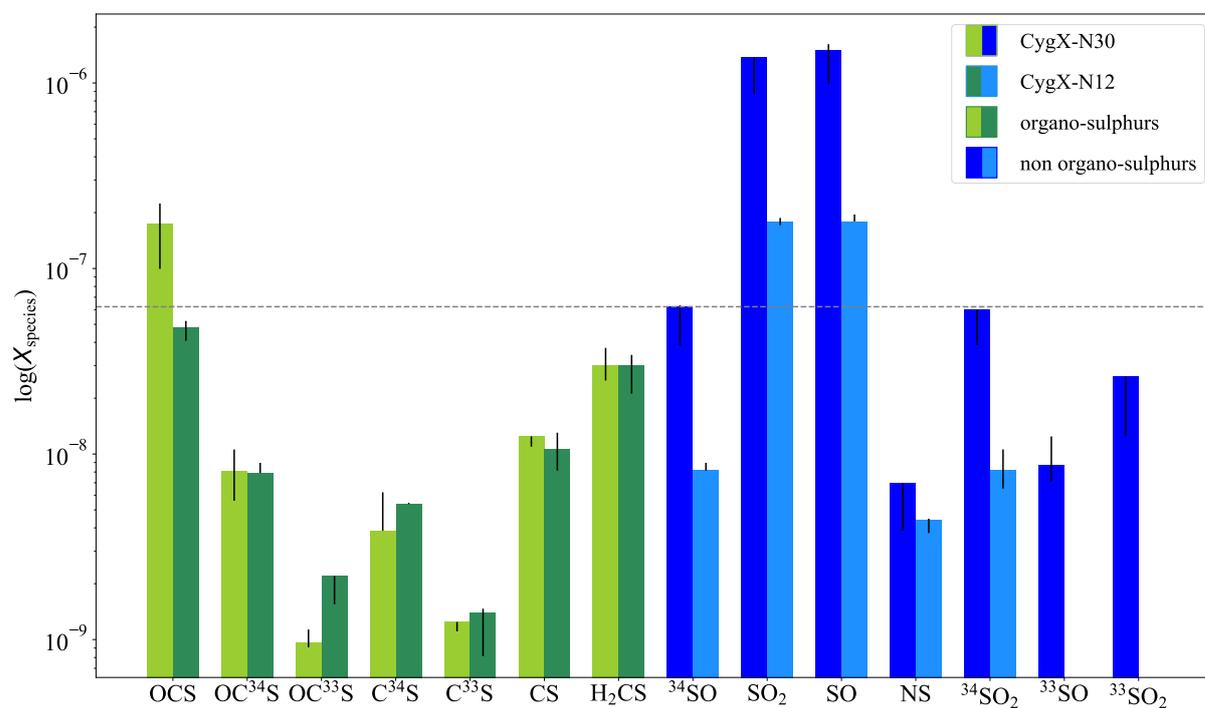

FIGURE 5.5: Abundance of S-species detected toward the hot-core CygX-N30 and CygX-N12 using the derived S-abundances from Table 5.5 and N_{H_2} of 8×10^{23} cm^{-2} and 1.2×10^{23} cm^{-2} for CygX-N30 and CygX-N12, respectively (see text). The dotted line represents the abundance above which ~20 % of the sulphur sample lies.

The lowest column densities are observed for NS^+, HSCN, and C_3S, with ratios with respect to CS of $N_{NS^+}/N_{CS} \approx 9.4 \times 10^{-4}$, $N_{HSCN}/N_{CS} \approx 1.1 \times 10^{-3}$, and $N_{C_3S}/N_{CS} \approx 2.7 \times 10^{-3}$. There is no apparent correlation between the column densities and whether the species is an organo-sulphur or not.

5.4.3 *Warm S-chemistry*

The warm chemistry was investigated toward two sources, CygX-N12 and CygX-N30. These two sources both show multiple continuum peaks (Bontemps *et al.*, 2010; Minh, 2016) within the inner few arcseconds. Specifically, the chemistry was investigated toward the peak continuum positions of these two sources alone, whereas the remaining results will be presented in a forthcoming paper (van der Walt et al. in prep.).

The same initial steps as for the cold chemistry survey were performed. First, all the sulphur species were identified from the spectrum ranging from 329 GHz to 361 GHz, with the combination of visual identification and verification with the CDMS database over the entire spectrum. However, when analyzing the possible candidates for a certain emission line for the hot-core data, unlike with the cold chemistry, no constraint was given for the upper level energy, while the Einstein coefficient was constrained to A_{ij} higher than 10^{-10} s^{-1} as for the cold chemistry. The relevant parts of the spectrum for the S-species are shown in Figures 5.C.5 through 5.C.7 for CygX-N30 and in Figures 5.C.8 through 5.C.9 for CygX-N12.

An overview of the detected S-species toward both sources is listed in Table 5.4, summarizing the observed molecules, number of lines, and upper-level energy. Complete lists of the detected transitions toward CygX-N12 and N30 are provided in Appendix 5.B, Tables 5.B.2 and 5.B.3, respectively. The observed sample consists of 14 different molecular species, 8 of which are isotopologs for CygX-N30. Strong lines of several organo-sulphur species could be identified from the 105 lines of sulphur-bearing species, such as H_2CS, CS, and OCS. However, they represent only ~18 % of the total S-sample we found, which are mostly dominated by SO, SO_2, and corresponding isotopologs. The spectrum of CygX-N12 shows a slightly lower diversity of S-molecules, with 12 different species, including 6 isotopologs for a total of 53 sulphur lines we detected. In contrast to CygX-N30, the SO and SO_2 lines in N12 were weaker and more difficult to detect than the organo-sulphurs (cf. line spectra in Appendix 5.C).

We performed LTE modeling on the optically thin emission of S-species derived from the spectrum at two different locations, MM1a and MM2 for CygX-N30 and -N12, respectively (cf. Figure 5.6). The modeling parameters and the corresponding error margins were determined in a similar way as for the observations of the cold chemistry, but considering an excitation temperature up to 350 K (cf. Sect. 5.4.2).

The best-fit parameters found from the LTE modeling analysis we used for the modeling are listed in Table 5.5. As for the cold-envelope, optically thick emission was seen for the SO and SO_2 lines. However, their corresponding isotopologs ^{34}SO and $^{34}SO_2$ are optically thin, and assuming $^{32}S/^{34}S = 22.5$ (Lodders, 2003), the expected abundance of SO and SO_2 with respect to the averaged H_2 column density can be derived. Moreover, the LTE modeling on the observed sulphur-lines toward N30 was found to have similar modeling parameters as those inferred by van der Walt *et al.* (2021) for the same source.

N_{H_2} was calculated using Equation (5.4). As for the H_2 column density estimation of the cold envelope of CygX-N12, assumptions of optically thin dust emission and no free-free contamination on the integrated flux were considered. Using a mass of 563 $M_\odot$ derived from 1.2 mm integrated flux, for CygX-N30, a FWHM size of 0.1 pc, dust opacity of 0.01 cm^2 g^{-1} and a mean wieght of 2.8, a H_2 density of 8×10^{23} cm^{-2} was estimated for CygX-N30 (Motte *et al.*, 2007). The same H_2 density for CygX-N12 as derived in Sect. 5.4.2 was used for the hot core. The derived H_2 column densities for the inner hot core of CygX-N30 and N12 were determined from their corresponding large-scale envelope. However, these values are not accurate for the targeted region, the hot core, and we realize that other more accurate values for N30 can be found in the literature (Rygl *et al.*, 2012). We emphasize that the main goal is to determine the trends among the different species, and therefore quoting the exact abundances is not the focus of this paper.

TABLE 5.4: Detected S-species in the hot core of CygX-N30 and CygX-N12.

Molecules	CygX-N30[a]		CygX-N12[a]	
	# lines[b]	E_{up}[c] [K]	# lines[b]	E_{up}[c] [K]
OCS	2	236.9–253.8	2	236.9–253.9
$OC^{33}S$	3	233.97–267.96	3	233.97–267.96
$OC^{34}S$	3	231.16–264.75	3	231.16–264.75
CS	1	65.8	1	65.8
$C^{34}S$	1	64.7	1	64.7
$C^{33}S$	1	65.2	1	65.2
H_2CS	8	90.59–301.07	7	90.59–209.10
SO	6	15.81–142.8	3	78.78–87.48
^{34}SO	4	25.31–86.07	3	77.34–86.07
SO_2	35	31.29–349.82	14	31.29–219.53
$^{34}SO_2$	28	35.1–319.52	13	35.1–274.74
NS	2	69.69–69.84	2	69.69–69.84
^{33}SO	3	78.03–86.75	-	-
$^{33}SO_2$	8	89.09–184.93	-	-

[a] Spectrum from the position MM1a and MM2 for CygX-N30 and -N12 (see Figures 5.6 and 5.7), respectively, corresponding to a continuum peak of each of the binary sources.
[b] Number of lines detected in the spectrum.
[c] E_{up} of the detected S-species.

Figure 5.5 summarizes the abundances of all the sulphur species detected toward both CygX-N30 and N12. For both sources, as expected, the highest abundances are seen for SO and SO_2, followed by OCS and H_2CS, while the lowest abundances are seen for CS and NS. The high abundance of the main organo-sulphur isotopologs, despite their low diversity and poor observed transitions sample, underlines the expected major role of three specific molecules, namely CS, OCS and H_2CS. However, we can point out some differences between the two sources: (1) S-column densities observed toward CygX-N12 are one to two orders of magnitude lower than for CygX-N30. (2) The excitation temperatures of several species tend to be higher for CygX-N12, (3) more isotopologs of SO and SO_2 are observed toward N30, and (4) the FWHM of the N12 S-O and N-S species are less than half of the widths from N-30 ($FWHM_{SO}=6$ km s^{-1} and $FWHM_{SO}=1.5$ km s^{-1}, for N30 and N12, respectively).

Figure 5.6 for CygX-N30 displays the integrated intensity maps (moment-zero maps) for each S-species. As shown by the large number of observed transitions of SO and SO_2, the highest integrated intensity (S_ν) peaks are observed for these two sulphur-bearing molecules, both peaking at 100–120 Jy beam^{-1} km s^{-1}. This range is thus considered as the S_ν maxima for S-chemistry. A 20–40 % lower S_ν ($\sim$ 60–80 Jy beam^{-1} km s^{-1}) relative to the SO and SO_2 maxima is observed as maxima of CS and H_2CS, and a 40–60 % decrease in the S_ν peaks (40–60 Jy beam^{-1} km s^{-1}) is found for OCS and NS.

The spatial distribution of the sulphur species shows some differences depending on the associated molecular family. This was only observed toward CygX-N30. The detected S-species are categorized into three families: C-S, N-S, and O-S families. The C-S family contains OCS[8], CS, H_2CS , and the corresponding isotopologs; the O-S family includes SO, SO_2 , and the corresponding isotopologs, while NS is the only member of the N-S family. Differences are seen in their peak locations and the overall intensity distribution around their peak.

In CygX-N30, the organo-sulphur species in general have a wide central peak and an extended emission distribution, covering the continuum contours nearly uniformly from $2\sigma - 8\sigma$. Their peak regions are elliptical over contours from 2σ to 4σ. NS shows a different pattern, with emission toward MM1a and MM1b, two small circular peaks, and a limited spatial extent from 2σ to 6σ. The S-O family has a similar pattern, with a spatial extent from 2σ to 6σ. Moreover, all the emission is seen to peak toward the N-W from MM1a, while no emission is seen in the N and

[8] OCS is considered as part of the C-S family instead of the O-S family because it contains C=S bonds and not O=S bonds.

TABLE 5.5: Overview of the LTE modeling for the optically thin sulphur lines of CygnusX-N30 and N12 targeting the warm chemistry.

Molecules	CygX-N30[a]			CygX-N12[a]		
	N_{sp}[c] [cm^{-2}]	T_{ex}[c] [K]	*FWHM*[c] [km s^{-1}]	N_{sp}[c] [cm^{-2}]	T_{ex}[c] [K]	*FWHM*[c] [km s^{-1}]
OCS	$1.4^{+0.4}_{-0.6} \times 10^{17}$	150^{+50}_{-20}	5.0	$5.9^{+0.5}_{-0.9} \times 10^{15}$	280^{+10}_{-20}	6.0
OC^{34}S	$6.5 \pm 2.0 \times 10^{15}$	170^{+50}	5.0	$9.7^{+0.4} \times 10^{14d}$	280	3.0
OC^{33}S	$7.7^{+1.4}_{-0.4} \times 10^{14}$	130^{+20}_{-10}	1.5	$2.7_{-0.8} \times 10^{14d}$	270_{-90}[d]	2.5
C^{34}S	$3.1^{+1.9} \times 10^{15d}$	170^{+30d}	4.5	$6.6^{+0.1} \times 10^{14d}$	280	5.5
C^{33}S	$1.0_{-0.5} \times 10^{15d}$	170^{+30}	4.5	$1.7^{+0.1}_{-0.7} \times 10^{14}$	260^{+20}_{-10}	4.0
CS	$1.0_{-0.2} \times 10^{16d}$	190^{+50}_{-20}	4.5	$1.3 \pm 0.3 \times 10^{15}$	160^{+50}_{-10}	4.5
H$_2$CS	$2.4^{+0.6}_{-0.4} \times 10^{16}$	140 ± 50	5.5	$3.7^{+0.5}_{-1.1} \times 10^{15}$	140^{+40}_{-20}	3.5
^{34}SO	$5.0^{+0.1}_{-1.9} \times 10^{16}$	290^{+10}_{-60}	6.0	$1.0^{+0.1} \times 10^{15d}$	230^{+60d}	1.5
SO$_2$[b]	$1.1_{-0.4} \times 10^{18d}$	130^{+30}_{-10}	6.5	$2.2^{+0.2} \times 10^{16d}$	200^{+30d}	2.0
SO[b]	$1.2^{+0.1}_{-0.4} \times 10^{18}$	290^{+10}_{-60}	6.0	$2.2^{+0.2} \times 10^{16d}$	230^{+60d}	1.5
NS	$5.6_{-2.5} \times 10^{15d}$	170^{+30d}	6.0	$5.4^{+0.1}_{-0.8} \times 10^{14}$	210^{+20}_{-40}	3.0
^{34}SO$_2$	$4.8_{-1.7} \times 10^{16d}$	130^{+30}_{-10}	6.5	$1.0^{+2.0} \times 10^{15d}$	200^{+30d}	2.0
^{33}SO	$7.0^{+3.0}_{-1.3} \times 10^{15}$	130^{+60}_{-30}	6.5	-	-	-
^{33}SO$_2$	$2.1_{-1.1} \times 10^{16d}$	200_{-50}[d]	6.5	-	-	-
CCS[e]	$< 10^{15}$	190^{+50}_{-20}	4.5	$< 10^{15}$	160^{+50}_{-10}	4.0
C$_3$S[e]	$< 10^{15}$	190^{+50}_{-20}	4.5	$< 10^{15}$	160^{+50}_{-10}	4.5
CH$_3$SH[e]	$< 10^{16}$	190^{+50}_{-20}	4.5	$< 10^{15}$	160^{+50}_{-10}	4.5
HSCN[e]	$< 10^{15}$	190^{+50}_{-20}	4.5	$< 10^{15}$	160^{+50}_{-10}	4.5

[a] This includes the positions MM1a and MM2 for CygX-N30 and N12 (see Figure 5.6), respectively, corresponding to a continuum peak of each of the binary sources.

[b] The column density of the optically thick emission from SO and SO$_2$ was determined using the isotopic ratios ^{32}S/^{34}S = 22.5 (Lodders, 2003). Moreover, the same T_{ex} and *FWHM* as of their corresponding ^{34}S isotopolog were used.

[c] The source size used to model the emission toward both sources is 1″5.

[d] If only the upper or lower limit is given, the best-fit model for the molecule is achieved at the given main value (i.e., T_{ex}, N_{sp}) and no lower or upper limit of this value is found.

[e] These molecules have not been detected. An upper limit of their column density has been determined based on T_{ex} and *FWHM* from the other species within the same family.

N-E parts. Their peaks are circular and condensed, extending up to 4σ.

Figure 5.7 displays the moment-zero maps toward CygX-N12. In contrast to CygX-N30, the peak intensity maxima of all the species do not exceed ~30 Jy beam^{-1} km s^{-1}, and no clear differentiation in the range of intensity values is detected among the S-species. The spatial extent of all S-species is similar; the species peak at exactly the continuum peaks, MM1 and MM2. All the species have a circular emission of ~2σ radius around the peak center.
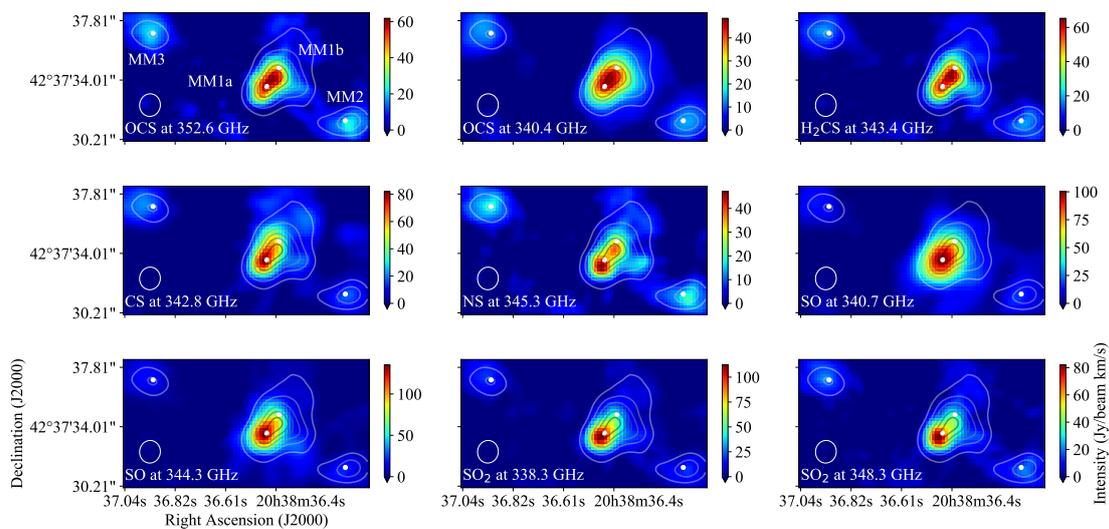
FIGURE 5.6: Integrated intensity maps of OCS at 352.6 GHz and 340 GHz, CS at 342.8 GHz and H_2CS at 343.4 GHz, NS at 345.8 GHz, SO at 340.7 GHz and at 344.3 GHz, and SO_2 at 338.3 GHz and at 348.3 GHz toward CygX-N30. The primary binary cores of the CygX-N30 are denoted by MM1a and MM1b, while MM2 and MM3 are secondary cores. The right arrow provides the scaling for the intensity of the observed molecule. The red area depicts intensity peaks, and the blue area represents no emission. The contours represent the continuum starting from 2σ to 12σ with a spacing of 2σ. The white circle in the bottom left corner represents the beam size.
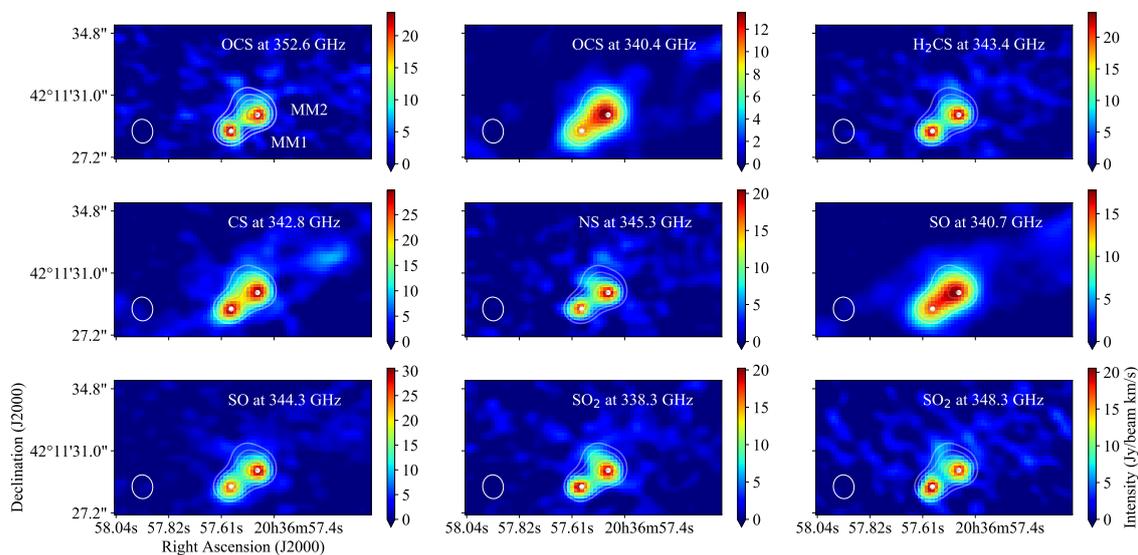
FIGURE 5.7: Integrated intensity maps of OCS at 352.6 GHz and 340 GHz, CS at 342.8 GHz and H_2CS at 343.4 GHz, NS at 345.8 GHz, SO at 340.7 GHz and at 344.3 GHz, and SO_2 at 338.3 GHz and at 348.3 GHz toward CygX-N12. The primary binary cores of the CygX-N12 are denoted by MM1 and MM2 (Bontemps *et al.*, 2010). The right arrow provides the scaling for the intensity of the observed molecule. The red area depicts intensity peaks, and the blue area represents no emission. The contours represent the continuum starting from 2σ to 10σ with a spacing of 2σ. The white circle in the bottom left corner represents the beam size.

5.5   DISCUSSION

In the following, the results of each subpart, the laboratory results, and the observations of the cold and warm S-chemistries are discussed first. Finally, these discussions are synthesized into a summarizing discussion of what has been learned from the combination of laboratory experiments and observations of S-bearing molecules in different parts of the molecular envelopes surrounding intermediate-mass protostars.

5.5.1   *Laboratory experiments of cold S-chemistry*

H_2S is highly reactive not only to hydrogenation, but also to CO, resulting in the formation of OCS. These surface reactions were seen at low temperatures (T<100 K), which suggests that this chemistry occurs already in the cold envelope of the protostars. These are the only regions in which CO will be frozen out on the dust grains.

Variation in the reaction temperature of H_2S (15 K and 22 K) when mixed with CO and H did not demonstrate a strong effect on the reactivity rate of either H_2S or CO. By contrast, with the hydrogenation of H_2S alone, a significant variation of H_2S left in the sample could be seen from one temperature to another (∼ 35% variation between 10 K and 50 K and ∼ 55% variation between 10 K and 30 K). The weak temperature correlation implies that the sulphur chemistry leading to organo-sulphur species is produced at a high reaction rate both in the precollapse stage ($T \sim 10$ K) and in the collapsing envelope ($T \gtrsim 30$ K) of the protostar, while the hydrogenation of H_2S is efficient only in the precollapse region.

For both reactions, {H_2S + CO+ H} and {H_2S + CO+ H + O_2}, H_2S was found as a remaining product. Two possibilities might explain the remaining quantity of H_2S in the sample:

1. The initial [H_2S/CO] quantity ratio was too high, and a saturation limit was reached. The initial reactants would not be fully consumed if too few free H atoms remained, explaining the remaining high quantities of CO and H_2S in the experimental sample.

2. The introduced amount of O_2 has negatively influenced the reactivity of H_2S with CO and H, as these last two species might have more likely reacted with O_2 than with H_2S. Therefore, it joins the conclusion from point (1), namely too few free H atoms remaining in the sample for the reactivity with H_2S to entirely occur.

Our laboratory results allowed us to compare the grain-surface chemistry developed by Laas and Caselli (2019) and Deeyamulla and Husain (2006) to draw a plausible schematic chemical network of the cold chemistry reproduced in the laboratory experiments. To do this, we considered three main species as the starting points of the chemistry (H_2S, CO, and O_2) reacting principally with H. In this scenario, OCS is the only organo-sulphur produced from the hydrogen abstraction of H_2S and combination with CO. The production of OCS among other sulphur species (CS_2, H_2CS, etc.), in ices containing H_2S and abundant C-compounds, that is, CH_3OH and CO, was already reported by Jiménez-Escobar *et al.* (2014) when these ice mixtures were irradiated. The absence of other detected organo-sulphurs is due to the strength of the C=O bond, which requires too much energy ($\Delta H = 1076.38$ kJ mol^{-1}) and cannot be broken by basic surface chemistry. Therefore, it was not included in this experimental setup.

Although it is possible that the amount of O_2 in the experiments has negatively affected the quantity of OCS and H_2S in the sample by impacting their reactivity, our experiments also suggest that the production of OCS is strongly efficient from H_2S on grain surfaces, and the hydrogenation of H_2S and CO highly influences its abundance. Our laboratory experiments confirm the efficient hydrogen abstraction mechanism of H_2S that was already experimentally observed by Oba *et al.* (2018) and was modeled by Garrod *et al.* (2007) and Lamberts and Kästner (2017). This strong hydrogen abstraction mechanism occurring with H_2S was initially, and naively, compared to the H_2O chemistry as -O is chemically similar as -S to first order, and the same hydrogen abstraction phenomenon occurs. Moreover, for H_2O, this H-addition leads to the formation of H_2O_2 , as experimentally tested by Oba *et al.* (2014) and Miyauchi

et al. (2008), but the corresponding S-molecule, H_2S_2, was not seen for H_2S in a basic surface chemistry without external energy, which suggests that the sulphur chemistry behaves chemically differently from H_2O. The formation of H_2S_2 would thus be formed by UV photochemistry of H_2S in a H_2O ice-matrix (Jiménez-Escobar and Muñoz Caro, 2011; Jiménez-Escobar *et al.*, 2014).

Our study reports the H_2S reactivity with CO in a controlled environment. The presence of H_2S in the ISM has always been an unresolved challenge (van der Tak *et al.*, 2003; Jiménez-Escobar *et al.*, 2014; Doty *et al.*, 2002; Laas and Caselli, 2019). From the modeling side, a high quantity of H_2S is predicted on grain surfaces. However, it has not been observed in large quantities so far. Some expect H_2S and HS to be S-reservoirs in the ISM (T. H. G. Vidal *et al.*, 2017). Our study demonstrated that when considering H_2S already formed and trapped in solid state, H_2S will likely rapidly react, leading to the efficient production of organo-sulphur compounds. The reduced sample of organo-sulphurs found in the laboratory is explained by the high enthalpy of C=O bonds. Thus, it is unlikely that H_2S remains an S-reservoir on the grains surface. To complete this laboratory study and the derived chemical network, comparison with observational data of the cold envelope of protostars are key.

5.5.2 *Observations of cold S-chemistry*

From the number of species we detected, which encompass sulphur species and complex organics, 22 % were found to be sulphur molecules, 77 % of which can be classified as organo-sulphur species. In the 78 % of non-sulphur molecules we found, a large number of zeroth- and first-generation organic molecules as defined by Herbst and van Dishoeck (2009) were detected. These reflect that several orders of reactions have occurred, which was confirmed by the presence of zeroth-generation molecules, such as CH_3OH. We therefore expect that the observed S-species are also zeroth- and first-generation species, but that their actual abundances depend on both the evolutionary stage of the protostar and the location within the protostellar envelope. They also underline the high reactivity in the targeted environment due to the freeze-out of the molecules on the dust grains.

This study focuses only on the chemical pattern formed from surface chemistry on dust grains, considering only the environmental conditions (i.e., temperatures) to vary and high freeze-out rate (i.e., the hydrogen number density $> 10^5$ cm^3; Schmalzl *et al.*, 2014). Therefore, it is assumed that grain properties such as the composition, sizes, and distribution of grains and the nonporous grain surface are constant and do not influence the S-reactivity.

Moreover, the large diversity of organo-sulphurs and the total column density ratios of the detected organo-sulphurs (OS) and non-organo-sulphurs (NOS) (i.e., $\sum N(\text{NOS})/\sum N(\text{OS}) = 0.29$) suggest that this trend indicates that a large fraction of S is locked up in organo-sulphurs. It emphasizes an efficient chemistry with organic compounds in the gas-phase and on dust grains in the cold environment (10–30 K), as is found in the collapsing envelope (Laas and Caselli, 2019).

The highest inferred abundances are seen for CS, OCS, H_2CS, SO, and SO_2. From a chemical point of view, both the S-O and C-S families are thus considered good tracers of the cold envelope. We might rely on the diversity observed in S-molecules and on targeting the cited main isotopic S-molecules, specifically CS, as tracers for the cold envelope assuming a homogeneous chemistry throughout the envelope, as suggested observationally by van der Tak *et al.* (2000) and Jørgensen *et al.* (2004) and based on models by Doty *et al.* (2002).

The high abundance of SO and SO_2 was unexpected as these molecules are known to trace warm gas, such as toward the hot core and outflow or jet regions (Singh and Chakrabarti, 2012; Minh, 2016; Artur de la Villarmois *et al.*, 2019). The high abundance and low diversity of S-O molecules suggest that these molecules are produced already in the cold envelope from oxidation of atomic S on the dust grains. Here they remain intact and do not proceed to form more complex products. The desorption of these species at low temperatures might result from nonthermal processes such as photodesorption, sputtering, and reactive desorption. Photodesorption occurs when there is local heating of the grain surface induced by external irradiation (e.g., UV, X-ray; Westley *et al.*, 1995; Öberg *et al.*, 2009). The sputtering is also an efficient nonthermal process. In this case, particles collide with the grain surface, inducing strong enough kinetic energy to desorb the species present on the

grain, while the reactive desorption refers to the energy released by the chemical reactions, leading to the desorption of the species (Vasyunin and Herbst, 2013). However, at this stage, it is unknown which process dominates the desorption of SO and SO_2 in this cold environment. These three mechanisms provide a means for releasing S-O molecules into the gas phase even in the cold parts of the envelope, however.

5.5.3 *Observations of warm S-chemistry*

The interferometric observations of the hot core enable not only investigating the molecular diversity, but also the spatial distribution of their emission. This analysis, performed for the peak continuum positions toward CygX-N12 and N30, shows that similarities and discrepancies of the S-chemistry in the warm gas could be distinguished between the two sources.

From the spectral analysis, similarities between the spectral line surveys toward the two sources CygX-N12 and N30 could be deduced from the observations. In particular, the diversity of organo-sulphurs is low, as only OCS, H_2CS, and CS are detected, in contrast to the S-species observed in the cold envelope of CygX-N12. This reduced diversity toward CygX-N12 and N30 is also observed toward the well-studied low-mass protostar, IRAS 16293–2422B by Drozdovskaya *et al.* (2018), and was used in hot-core models of T. Vidal and Wakelam (2018). Therefore, the concordance among the detected organo-sulphurs toward CygX-N12 and N30, IRAS 16293–2422B and models makes it unlikely that N12 and N30 are possible outliers in terms of hot-core S-chemistry. This also suggests that the diversity of organo-sulphurs in the warm gas is not dependent on the mass of the protostar. However, more sources must clearly be observed to verify this conclusion.

The only organo-sulphurs detected in the warm gas, OCS, H_2CS, and CS, also show the highest column densities of the organo-sulphurs in the cold envelope of N12 ($N_{H_2CS} = 1.3^{+1.4}_{-0.3} \times 10^{14}$ cm^{-2}, $N_{OCS} = 1.5^{+1.7}_{-0.6} \times 10^{14}$ cm^{-2}, $N_{CS} = 9.0^{+1.7}_{-3.0} \times 10^{14}$ cm^{-2}). Moreover, their column densities in the warm gas are one order of magnitude higher than in the cold gas. Therefore, the detected organo-sulphurs in the warm gas might partially originate from the cold envelope, collapsing toward the hot core, as they have likely been efficiently produced in the cold environment from successive hydrogenations and oxidations of atomic sulphur. The remaining organo-sulphurs we detected might then be produced in the warm gas.

Consequently, for sources N12 and N30, we investigated the nondetection of the organo-sulphurs that were detected in the cold envelope of CygX-N12, but not in the two hot cores (i.e., CCS, C_3S, CH_3SH, and HSCN). We used the CASSIS software to build synthetic spectra and to determine the upper limits. In order to determine an upper limit, the excitation temperature was first fixed such that it matched the averaged temperature found from the main species in the same molecular family, in this case, the C-S family. For N30, this temperature is 190^{+50}_{-20} K, and for N12, it is 160^{+50}_{-10} K. Next, we varied the column density of these species, and the resulting spectrum was investigated across the spectral range. When a simulated emission line appeared at the 3σ level, that is, above the noise level, the corresponding column density was taken as the 3σ upper limit. This was done for CCS, C_3S, CH_3SH, and HSCN, and their values are given in Table 5.5. Typically, they are 10^{15}–10^{16} cm^{-2}. The formation routes of these species were also later investigated and shown in Fig. 5.9, and a further discussion of the upper limits is provided in Section 5.5.5.

Of all S-molecules we detected, those observed toward CygX-N30 have higher column densities than those toward N12 (N_{sp-N30}/N_{sp-N12}=10-10^2). These are explained by N30 being 33.8 times brighter than N12 ($L_{bol} = 740^{+80}_{-90}$ L$_\odot$, L_{FIR}=33.8 × 10^3 L$_\odot$ for N12; Pitts et al. 2021b (in prep.)) and more massive (($M = 563$ $M_\odot$ for N30 and $M = 86$ $M_\odot$ for N12) Motte *et al.*, 2007). Therefore, for a given sensitivity, the column densities of the S-species are sensitive to the mass of the observed protostar.

The highest abundances of S-species toward CygX-N12 and N30 are seen for SO and SO_2, confirming that these are good sulphur tracers of the warm chemistry of protostars, as previously suggested by van der Tak *et al.* (2003) and Artur de la Villarmois *et al.* (2019), for example. Moreover, these two molecules show the largest differences in column densities between the cold envelope (c) and hot core (h) of N12, with $N^h_{SO}/N^c_{SO} \approx 81$ and $N^h_{SO_2}/N^c_{SO_2} \approx 180$, while for the organo-sulphurs,

we found lower variations between the cold and warm chemistry: $N^{\text{h}}_{\text{OCS}}/N^{\text{c}}_{\text{OCS}} \approx 39$, $N^{\text{h}}_{\text{H}_2\text{CS}}/N^{\text{c}}_{\text{H}_2\text{CS}} \approx 28$ and $N^{\text{h}}_{\text{CS}}/N^{\text{c}}_{\text{CS}} \approx 1.4$. These large differences might underline that the observed SO and SO_2 in the hot core do not only come from the collapsed envelope, but are also produced in the warm gas.

An interesting difference appears in the $FWHM$ of the organo-sulphurs when compared to the non-organo-sulphur species toward the two sources. For both sources, the $FWHM$ of the organo-sulphurs is similar, $\sim$ 4–5 km s^{-1}. However, for N30, the non-organo-sulphurs show an increase in the $FWHM$ to $\sim$6.0–6.5 km s^{-1}, whereas this decreases toward N12 to 1.5–2.0 km s^{-1} for most species. This difference in line widths between the sources might indicate a slower motion in the hot core of CygX-N12 than N30. The non-organo-sulphurs appear to be more sensitive to the motion of the protostars, although a survey of more sources at higher angular resolution is required to clearly demonstrate this effect. N30 is more massive than N12, and gravitational collapse should therefore occur faster (Klassen *et al.*, 2016).

High column densities were observed for OCS and H_2CS in both protostars (i.e., $N_{\text{OCS}} = 1.4^{+0.4}_{-0.6} \times 10^{17}$ cm^{-2}, $N_{\text{H}_2\text{CS}} = 2.4^{+0.6}_{-0.4} \times 10^{16}$ cm^{-2} for N30 and $N_{\text{OCS}} = 5.9^{+0.5}_{-0.9} \times 10^{15}$ cm^{-2}, $N_{\text{H}_2\text{CS}} = 3.7^{+0.5}_{-1.1} \times 10^{15}$ cm^{-2} for N12), thus making them good tracers of the warm chemistry as well. As pointed out previously, it is plausible that the high abundances of OCS and H_2CS observed in the hot regions are related to the cold chemistry through the collapsing envelope (Wakelam *et al.*, 2011; Jørgensen *et al.*, 2004, and references therein), as these have relatively high column densities in the outer envelope (cf. $N_{\text{OCS}_\text{h}}/N_{\text{OCS}_\text{c}} \approx 39$, $N_{\text{H}_2\text{CS}_\text{h}}/N_{\text{H}_2\text{CS}_\text{c}} \approx 28$ for N12).

For the case of H_2CS, the extensive models of the sulphur chemistry in hot cores from T. Vidal and Wakelam (2018) and T. Vidal *et al.* (2019) suggested that at $T \sim 100$ K, H_2CS has not entirely desorbed from the surface and its abundance depends on the surface and gas-phase chemistries. In their model, H_2CS is likely to be produced by the following reactions:

$$S + CH_3 \rightarrow H_2CS + H \tag{5.5a}$$

$$H_3CS^+ + e^- \rightarrow H_2CS + H \tag{5.5b}$$

$$HCS_{(s)} + H_{(s)} \rightarrow H_2CS_{(s)}, \tag{5.5c}$$
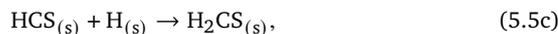
while the destruction of H_2CS occurs on the dust grain and in the gas phase, as shown by the following reactions:

$$H_2CS + HCNH^+ \rightarrow H_3CS^+ + HCN \tag{5.6a}$$

$$H_2CS + C \rightarrow CH_2 + CS \tag{5.6b}$$

$$H_2CS_{(s)} + H_{(s)} \rightarrow CH_2SH_{(s)} \tag{5.6c}$$

$$H_2CS_{(s)} + H_{(s)} \rightarrow CH_3S_{(s)}, \tag{5.6d}$$
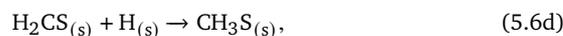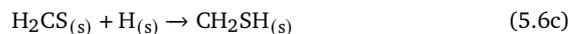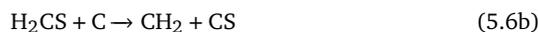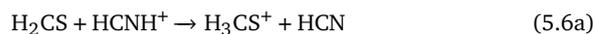
in which the subscript (s) denotes the solid state of the species, that is, reactions on the dust grain. Furthermore, H_3CS^+ formed in Eq. (5.6a) re-forms to H_2CS from the dissociative recombination of H_3CS^+ with e$^-$. At higher temperatures ($T \sim 300$ K), H_2CS is entirely in the gas phase, and its only destruction paths are described by Eq.s (5.6a) and (5.6b). Therefore, H_2CS in the hot core is not necessarily destroyed as it re-forms through H_3CS^+ and the low abundance of atomic carbon does not lead to a highly efficient destruction path of Eq. (5.6b). This might explain the high H_2CS abundance in the warm gas.

In the case of OCS, the models from T. Vidal and Wakelam (2018), T. Vidal *et al.* (2019) and Druard and Wakelam (2012) predict a high abundance of OCS due to its production on grain surfaces and in the gas phase through the following set of reactions:

$$SO + CH \rightarrow H + OCS \tag{5.7a}$$

$$O + HCS \rightarrow H + OCS \tag{5.7b}$$

$$S + HCO \rightarrow H + OCS \tag{5.7c}$$

$$CS + OH \rightarrow H + OCS \tag{5.7d}$$

$$O_{(s)} + CS_{(s)} \rightarrow OCS_{(s)} \tag{5.7e}$$

$$S_{(s)} + CO_{(s)} \rightarrow OCS_{(s)}, \tag{5.7f}$$
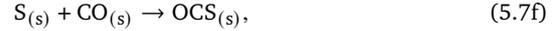
while its destruction is expected to occur through several paths, as outlined here:

$$OCS + CH \rightarrow CO + CS + H \tag{5.8a}$$

$$OCS + HCO^+ \rightarrow HOCS^+ + CO \tag{5.8b}$$

$$OCS + H_3^+ \rightarrow HOCS^+ + H_2 \tag{5.8c}$$

$$OCS + C \rightarrow CS + CO. \tag{5.8d}$$
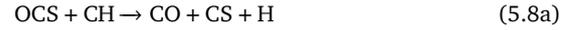
However, Eq.s (5.8b) and (5.8c) produce HOCS$^+$, which will dissociatively recombine to form either CS or OCS, and Eq.(5.8d) is expected to be efficient for only the first 10 years of the simulation, due to the low abundance of atomic C. Furthermore, at high temperatures ($T \approx 300$ K), the drop in CH abundance leads to an inefficient OCS destruction from Eq. (5.8a). Therefore, the low destruction rates of OCS compared to its production rates might explain its high abundance in the warm gas.

Furthermore, the same high column densities for OCS, SO CS, SO$_2$, and H$_2$CS were observed for IRAS 16293-2422, for which the derived density ratio $N_{CS}/N_{OCS} \approx 10^{-1}$ describes a lower density of CS than OCS (Le Gal *et al.*, 2019; Drozdovskaya *et al.*, 2018). The same trend is observed for the warm gas of N30 and N12, which has ratios of $N_{CS}/N_{OCS} \approx 0.07$ and $N_{CS}/N_{OCS} \approx 0.22$ for N30 and N12, respectively. If CS is optically thin, these density ratios found toward IRAS 16293-2422, CygX-N12, and N30 suggest that OCS production is more effective in the warm gas than the CS production, in contrast to what is seen for the cold envelope of N12 ($N_{CS}/N_{OCS} \approx 6$).

From the moment-zero maps from the sulphur emissions toward CygX-N30, a similar trend could be observed for the S-species within a specific S-family. As illustrated in Fig. 5.8, the distinction among families is based on the S-peak location and on the spatial extent of the S-emission.

In all the S-species we detected, their peak emission is shifted from the continuum sources, MM1a and MM1b. In the S-O and N-S families as well as for CS, their intensity peaks have a shift of ~0.″75, ~0.″2, southwest of MM1a, while other species of the C-S family have a shift of ~0^{s}2, ~0.″2, northeast of MM1a. This peak shift from MM1a is observed for all the COMs of CygX-N30, as discussed by van der Walt *et al.* (2021), and is likely explained by N30 not being a traditional hot core, in contrast to N12.

Despite the emission peak shifts for N30, a specific and different spatial distribution of all S-species was seen in the families. The organo-sulphurs show an extended pattern around the two binary components (MM1a and MM1b), their spatial distribution is more extended and not concentrated on a specific source, in contrast to the O-S family, which is concentrated around MM1a, as also pointed out by van der Walt *et al.* (2021). It might be suggested that C-S is associated with both sources (i.e., MM1a and MM1b), while the O-S family is primarily associated with MM1a. Only one molecule could be identified in the N-S family (NS). It is not possible to draw clear conclusions regarding an entire S-family based on only one species. However, as the two other families show the same characteristics for all their species, it is likely that the molecules within the N-S family follow the same trend, as also observed for N-species, CH$_3$CN, HC^{15}N, HC$_3$N, and HNCO in N30 by van der Walt *et al.* (2021).
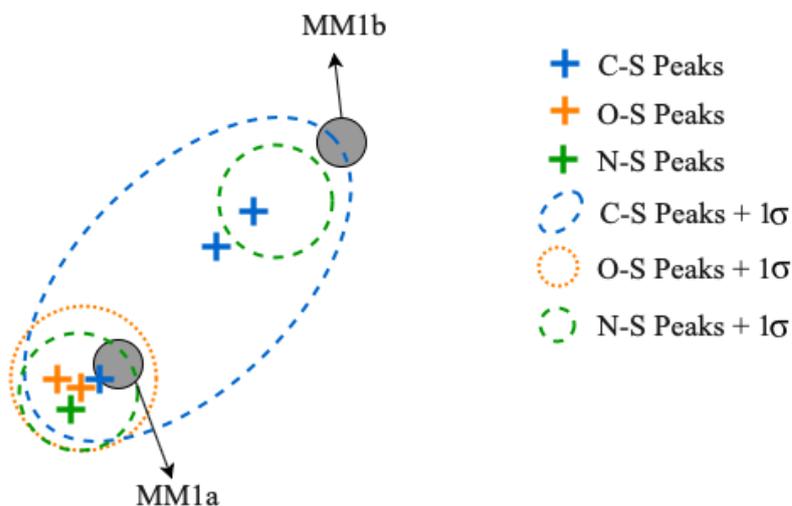
FIGURE 5.8: Cartoon of the locations of sulphur species characterized w.r.t. chemical families (i.e., N-S, O-S and C-S) of CygX-N30 around the MM1 source. Concentrations of the sulphurs peaks located in specific regions depending on the corresponding sulphur family. Results from the SMA-PILS Cygnus survey. CygX-N30 was observed at 0.8 mm.

This differentiation in molecular spatial distribution has already been discussed by Garrod and Widicus Weaver (2013), who suggested that it is correlated with changes in local physical conditions. Differentiation in spatial extent is also seen for N- and O-bearing molecules in Orion KL, which are likely to trace separate physical environments (Favre *et al.*, 2011; Widicus Weaver and Friedel, 2012; Zapata *et al.*, 2011; Friedel and Snyder, 2008; Crockett *et al.*, 2015; Pagani *et al.*, 2017). Furthermore, Neill *et al.* (2011) discussed this difference in spatial extent as a possible consequence of gas-phase reactions that might alter the initial spatial distributions. This initial spatial distribution is created by similar physical mechanisms (e.g., molecular desorption from the dust grains, shocks); however, in the subsequent gas-phase reprocessing, the limiting reactants set any further chemical processing, and these reactants are typically the less-abundant species. Both explanations might be applicable for CygX-N30, namely that the chemical gradient traces a physical gradient in temperature, density, or other physical parameters, but it is likely not the cause of this gradient in physical properties, but rather a consequence of it. Moreover, a wider spatial extent was seen for the C-S family in which the organo-sulphurs have a lower abundance than O-S species, probably explaining the stronger effect on their spatial extent (Neill *et al.*, 2011).

Although the line analysis and derived abundances show similarities between CygX-N12 and N30, their moment-zero maps show different patterns. It is clear that for both sources, CygX-N30 and N12, the diversity of S-species is similar for the warm gas. Furthermore, a similar trend between the sources is also seen for the abundance ratios. However, for CygX-N12, Figure 5.7 shows that the spatial distribution for the same angular resolution does not differ among the species, in contrast to N30. This suggests that the spatial extent of the sulphur molecules depends on the type of object that is targeted (e.g., traditional hot core or not) and not on the region (cold envelope versus hot core). In the case of a traditional intermediate-mass source as N12, the molecular emission is expected to only overlap with the continuum emission, while for atypical sources (e.g., N30, Orion KL), the spatial distribution provides information on the type of sulphur species and physical environment of the warm gas (Favre *et al.*, 2011; Widicus Weaver and Friedel, 2012; Neill *et al.*, 2011).

5.5.4   *Combining the cold S-chemistry from the observations and the laboratory*

The results from the laboratory do not entirely match the observational results of the cold envelope of CygX-N12, as the only sulphur species detected in the laboratory was OCS, while the cold envelope displays a large diversity of organo-sulphurs. The high amount of H_2S left in the sample ($\sim$ 8 %) suggests that the chemical reactions

are not completed and longer exposure to H would lead to a larger quantity of OCS. Moreover, the absence of a strong energy source such as a UV field would be one factor limiting the reactivity of our experiments, but not the only principal cause affecting the diversity of organo-sulphurs we found. However, in a cold environment such as the cold envelope, the UV field is not strong, and therefore this absence of UV is more characteristic of such a cold environment. We emphasize here that the laboratory experiments display the products from the grain surfaces chemistry, while the observations of the cold envelope display the products resulting from the gas-phase chemistry and from the desorption of species produced on the dust grains. Both occur in the cold envelope simultaneously and are thus complementary. However, they cannot be directly compared without knowing the (nonthermal) desorption yields, and these are at present unknown for the S-bearing species.

Combining the observational results with our laboratory knowledge, a schematic chemical network for the grain chemistry in cold environment is inferred. We based the reactions on those that were demonstrated by T. Vidal *et al.* (2019), T. H. G. Vidal *et al.* (2017), T. Vidal and Wakelam (2018), Laas and Caselli (2019), Vastel *et al.* (2018) and Deeyamulla and Husain (2006) and references therein. The chemical network is shown in Figure 5.9 and represents a possible path for the production of S-species in star-forming regions. It is important to underline that this chemical network does not target a specific chemistry (i.e., warm or cold chemistry), but provides an overview of the reactions leading to the S-species.

This version of the chemical network from the laboratory points out the experimental limitations, but highlights the link between OCS and the other organo-sulphurs, as well as the central role of H_2S in the sulphur chemistry. The reason for this is that one of the main dissociation products of H_2S is HS, which has a high reactivity, both on the grain and in the gas. As shown in Figure 5.9, external energy (e.g., UV radiation) would be required for the production of some of its daughter molecules such as CS, C_2S, C_3S, and H_2CS, which would be expected to be formed from the photodissociation of C=O bonds from OCS or its reaction with C or CH. Furthermore, the production of OCS from HS and CO found from the laboratory experiments contradicts the results from Laas and Caselli (2019), which describes this reaction as not allowed, and T. Vidal *et al.* (2019), in which the main production route for OCS on the grain surface is from Eq. (5.7f). This new production route of OCS on the grain surface requires further theoretical investigation.

Due to the high reactivity and abundance of CO and H in the ISM, the abundance of the initial reactants of this network (e.g., H_2S) is expected to be low and thus be revealed through reservoirs of their products (OCS, HCS, etc.). Thus, the initial abundance of H_2S may be inferred from its products (OCS and CS) as detected in the envelope, and this molecule is a zeroth-generation molecule (Herbst and van Dishoeck, 2009). H_2S is a primary reactant of the S-chemistry, it is not considered as a good tracer of the cold chemistry, as most of the H_2S is expected to react with H and dissociated C=O, thus lowering its abundance. One should focus instead on the subsequent S-reservoirs (primarily OCS, then CS, H_2CS, etc.) to derive its initial abundance in the early stage of the protostellar evolution. However, H_2S is considered as a primary component of S-chemistry in this region due to the large amount and type of organo-sulphurs we detected, which is expected to result from H_2S and CO hydrogenation as found from the laboratory experiments.

In the observational data, the highest column density of the detected species is seen for CS in the cold envelope, underlining that CS is efficiently produced, as also suggested by Palumbo *et al.* (1997), by different production routes. The main routes of CS are from the reactions of S with C_2 and CH (Vastel *et al.*, 2018) as well as the electronic dissociative recombination of HCS^+ with e^-. However, as described by Eq.s (5.8d), the chemical reaction in the gas state producing CS from OCS is possible, but not exclusive (T. Vidal and Wakelam, 2018; Deeyamulla and Husain, 2006).

FIGURE 5.9: Sulphur solid- and gas-state chemical network derived from laboratory experiments, observational study of CygX-N12 and N30 (i.e., S-species observed in the cold- and warm-gas chemistries), and previous theoretical studies from T. Vidal *et al.* (2019), T. H. G. Vidal *et al.* (2017), T. Vidal and Wakelam (2018), Laas and Caselli (2019), Vastel *et al.* (2018) and Deeyamulla and Husain (2006). The products found in the laboratory are highlighted in the blue boxes, and the species from the observation of cold gas of CygX-N12 are shown inside the dotted green boxes. The species detected toward CygX-N12 and N30 in the warm gas are shown inside the orange boxes. The straight lines represent the reactions with an additional reactant, shown by the plus. The dotted line represents the reaction found from the laboratory experiments. The gas-phase reactions are shown by black arrows, and the red arrows indicate the solid-state chemistry.

5.5.5 *Combining warm and cold S-chemistries*

The observations presented in this paper connect the sulphur chemistry through the warm and cold environment among intermediate-mass protostars of the Cygnus-X star-forming complex. The largest diversity of S-molecules is observed toward the cold envelope. This suggests that the outer part of the protostar contains all the possible S-species that play a role in its chemistry. Moreover, the limited diversity in S-species in the warm gas (i.e., hot-core regions) found toward N12 and N30 has also been observed for other sources such as IRAS 16293–2422B and was used in hot-core models (Drozdovskaya *et al.*, 2018; T. Vidal and Wakelam, 2018). As specified previously (see Sect. 5.2), the cold envelope is the coolest part of the protostellar system, the combination of the dust and low temperature allows a rich surface chemistry to occur, and most of the molecules are thought to principally form on dust grains at low temperatures (Jørgensen *et al.*, 2020).

The larger diversity of S-molecules in the cold envelope compared to the hot core does not automatically imply that the four nondetected S-species, CCS, C_3S, CH_3SH, and HSCN, in the hot core are not there. To determine whether they may be present in the hot core, the upper limits of their column densities were investigated. A comparison of the column densities in the cold envelope (c) and hot core (h), of these nonobserved S-species with respect to CS was made for N12. The same ratio $N_{sp}^h/N_{CS}^h = \approx 1$ for all these species was found in the hot core as the same upper limit for them was derived, while different ratios were found for the cold envelope: $N_{C_3S}^c/N_{CS}^c = N_{HSCN}^c/N_{CS}^c \approx 10^{-2}$ and $N_{CCS}^c/N_{CS}^c = N_{CH_3SH}^c/N_{CS}^c \approx 10^{-1}$.

TABLE 5.6: Comparison between cold envelope and hot core of species with respect to OCS toward N12 and N30.

| Molecules[b] | CygX-N12[a] | | CygX-N30[a] |
	cold envelope	hot core	hot core
N_{CS}/N_{OCS}	6.4	0.22	0.07
N_{SO}/N_{OCS}	1.8	3.73	8.57
N_{SO_2}/N_{OCS}	2.0	3.73	7.8
N_{NS}/N_{OCS}	0.18	0.09	0.04
N_{CCS}/N_{OCS}	0.11	≤0.17	≤7.1×10^{-3}
N_{C_3S}/N_{OCS}	1.7×10^{-2}	≤0.17	≤7.1×10^{-3}
N_{CH_3SH}/N_{OCS}	6.7×10^{-2}	≤0.17	≤7.1×10^{-3}
N_{HSCN}/N_{OCS}	6.7×10^{-3}	≤0.17	≤7.1×10^{-3}

[a] Spectrum from the position MM1a and MM2 for CygX-N30 and -N12 (see Figures 5.6 and 5.7), respectively, corresponding to a continuum peak of each of the binary sources.

[b] Only the main isotopologs detected in the cold envelope and the hot cores are listed in this table.

When comparing the ratios from the cold envelope and the hot core, we used OCS as a reference frame. In Table 5.6 we show the column-density ratios for the detected and non-detected species for the cold envelope and the hot cores of N12 and N30, respectively. The detected species all show similar column density ratios within a factor of a few, which suggests that the chemistry in the cold envelope and the hot cores of these different species does not vary significantly. This suggests that the sulphur chemistry in the hot core is to a high degree inherited from the cold envelope. At the upper limits, the sensitivity of the observations is clearly too low for N12 for us to conclude anything: the non-detections are consistent with a scenario in which the species are inherited from the cold envelope with the same column-density ratio. For N30, on the other hand, we find that CCS, C_3S, and CH_3SH should have been detected if their column-density ratios follow the other ratios. This suggests that their abundance may be chemically lowered either on the way to the hot core

or in the hot core itself. As this difference is not driven by sensitivity issues, the conclusion is that the sulphur chemistry is best studied in the cold envelope, where the observed diversity of species is highest.

Based on the derived column densities, our results match previous observational conclusions (Artur de la Villarmois *et al.*, 2018; Artur de la Villarmois *et al.*, 2019; van der Tak *et al.*, 2003; Wakelam *et al.*, 2011), that is, CS is considered as the main tracer for the cold chemistry, with the highest column density of $N_{CS} = 9.0^{+1.7}_{-3.0} \times 10^{14}$ cm^{-2}, and SO and SO$_2$ as primary tracers for the warm chemistry, $N_{SO} = 1.3^{+4.3}_{-0.7} \times 10^{18}$ cm^{-2}, $N_{SO_2} = 1.3^{+2.7}_{-0.8} \times 10^{18}$ cm^{-2}. However, for the cold envelope, the SO and SO$_2$ abundances were among the five highest abundances of the 11 detected S-species, and thus were also considered as tracers of the cold envelope. The ratio of N_{CS}/N_{SO} or N_{CS}/N_{SO_2} might therefore be considered to precisely determine the environmental conditions rather than focusing on the column density of a specific species. If the ratios are higher than one, then this is likely to be the outer part of the protostar, and inversely, ratios lower than one target the inner part of the protostars. Furthermore, this ratio has also been suggested by Bergin *et al.* (1997) to probe the C/O ratio in the targeted region, as the main production route for SO is from atomic sulphur and oxygen. This is in accordance with our use of this ratio, as in the cold envelope, the atomic oxygen is efficiently converted into H$_2$O on grains and thus its abundance in the gas is depleted, while at higher temperatures, that is, in the hot core, the released oxygen from the ice desorbs and forms more S-O species, which explains the higher densities of S-O species in the warmer chemistry.

The comparison of column densities also indicates an opposite trend in the cold and warm chemistries for CS and OCS. These species are directly related, as shown in Fig. 5.9. Their abundances in the cold envelope and hot core of N12 and N30 suggest that in a cold environment, the production of CS is enhanced by OCS through reactivity with carbon. By contrast, in the warm gas, the opposite route seems to occur, namely CS combines with OH to form OCS in the gas phase (T. Vidal and Wakelam, 2018). Moreover, in the warm gas, the high abundance observed for OCS is likely caused by a combination of gas chemistry and the thermal desorption of OCS from the icy dust grains, formed in the cold envelope, as suggested by the laboratory experiments.

5.6 CONCLUSIONS

To improve our knowledge of the sulphur chemistry in star-forming regions, we studied the cold and hot chemistries in a rich molecular complex of our Galaxy, Cygnus X. Two protostars from this complex were targeted based on their high luminosity, mass, and relative isolation from other sources. The observations were supported by laboratory experiments focusing on the H$_2$S chemistry. The main findings of this paper are summarized as follows:

1. H$_2$S shows a high reactivity when exposed to CO and H in a cold environment without any additional source of energy, leading mainly to the production of one organo-sulphur: OCS. Moreover, its reaction efficiency is not highly sensitive to variations in temperature over a range of 10–50 K.

2. H$_2$S appears to be a possible starting point of the reaction chain of sulphur chemistry and therefore is considered as the primary component for the S-chemistry. Being at the start of chemical reaction chain, its initial abundance can only be derived from its products. Thus, it cannot be considered a good tracer for the cold chemistry of a star-forming region: the focus should instead lie on its product, for instance, OCS.

3. The cold envelope hosts a large diversity of S-species, mostly organo-sulphurs. Only OCS of the observed organo-sulphurs is also expected to be formed on the icy dust grains, as suggested by the laboratory experiments, from H$_2$S reacting with CO and H. The remaining organo-sulphurs correspond to products from expected later stages of reactions of the CS chain. The diversity of organo-sulphurs we detected is a clear indicator that the sulphur chemistry has had time to evolve.

4. The highest S-species abundance in the cold envelope is observed for CS, which is expected to be efficiently produced by different routes in the gas phase, but also on grain surfaces (cf. Figure 5.9). The S-chemistry in the cold envelope is primarily led by reaction chains from CS, and this species is considered the main molecular tracer of the cold envelope regarding the S-chemistry.

5. An unexpectedly high abundance of SO and SO_2 was observed in the cold envelope, although these are typically used for tracing warm chemistry, that is, the hot core and outflows. Their high abundance and the low diversity of S-O molecules reveal that these molecules are produced in the cold envelope, but do not react with the surrounding environment and are seen in hotter regions due to the collapsing envelope.

6. Although SO and SO_2 could clearly be detected in the observations, the diversity of the sulphur sample in the hot core is poor. Only three organo-sulphurs, OCS, H_2CS, and CS, are detected toward both sources. Although the abundance of the other organo-sulphurs (CCS, C_3S, and CH_3SH) is too low to be detected toward N12, these species should have been detected toward N30 if the chemistry is similar toward both N12 and N30. This in turn suggests that the abundance of these species decreases toward the hot core of N30.

7. We observed high abundances of the organo-sulphurs OCS and H_2CS, which might also be considered good tracers of the warm chemistry. It is likely that the high abundance of OCS in the hot core is due to its nonthermal and thermal desorption from the icy dust grains. Their high observed abundance compared to CS arises because they are produced on the surface but also in the gas phase of the hot core and are not easily destroyed (cf. Eq.s (5.6a), (5.7), and (5.8b)).

8. The spatial distribution of S-species within the hot-core region depends on the targeted object. For the typical hot core of a protostar, no differentiation is expected among the S-species, while for more massive objects with a nontraditional hot core (i.e., CygnusX-N30), the spatial distribution provides information on the type of S-species and on the physics and chemistry within the hot core.

In conclusion, this study allowed us to confirm for the first time from a laboratory perspective that OCS is more likely to be a solid-state S-reservoir than H_2S, the latter being expected to be a key solid-state reactant of the sulphur chemistry in protostellar envelopes. The observational spectral surveys covering a large bandwidth provided us with a complete outlook on the S-species in different regions of intermediate-mass protostars. This allowed us to point out similarities and discrepancies among the warm and cold S-chemistry of these astrophysical objects. Moreover, we determined that the chemical S-inventory and the derived abundances are dependent on and characteristics of the environmental temperatures, while its spatial extent depends on the type of object that is targeted. Extending this analysis to a larger set of protostars is required to confirm that the trends observed in CygnusX-N12 and N30 are characteristic of protostars. Such an extension would naturally also benefit from an increase in sensitivity, that is, detecting more species in the hot cores, and in angular resolution to follow the sulphuric gas flows near the protostars.

Bibliography

1. L. Amiaud *et al.*, *The Journal of chemical physics* **127**, 144709 (Nov. 2007).

2. E. Artur de la Villarmois *et al.*, *A&A* **614**, A26, (https://doi.org/10.1051/0004-6361/201731603) (2018).

3. E. Artur de la Villarmois *et al.*, *A&A* **626**, A71, arXiv: 1904.13161 [astro-ph.SR] (June 2019).

4. M. Asplund *et al.*, *ARA&A* **47**, 481–522, eprint: https://doi.org/10.1146/annurev.astro.46.060407.145222, (https://doi.org/10.1146/annurev.astro.46.060407.145222) (2009).

5. E. A. Bergin *et al.*, *ApJ* **482**, 285–297 (June 1997).

6. S. Bontemps *et al.*, *A&A* **524**, A18, (https://doi.org/10.1051/0004-6361/200913286) (2010).

7. A. A. Boogert, P. A. Gerakines, D. C. Whittet, *ARA&A* **53**, 541–581, arXiv: 1501.05317 [astro-ph.GA] (Aug. 2015).

8. J. V. Buckle, G. A. Fuller, *A&A* **399**, 567–581, (https://doi.org/10.1051/0004-6361:20021816) (2003).

9. S. Charnley, *ApJ* **481**, 396–405 (May 1997).

10. E. Congiu *et al.*, *arXiv e-prints*, arXiv:2004.10668, arXiv: 2004.10668 [astro-ph.IM] (Apr. 2020).

11. N. Crockett *et al.*, *ApJ* **806**, 239, arXiv: 1506.03875 [astro-ph.GA] (June 2015).

12. M. Deeyamulla, D. Husain, *J. Photochem. Photobiol. A Chem.* **184**, 347 (2006).

13. S. D. Doty *et al.*, *A&A* **389**, 446–463, (https://doi.org/10.1051/0004-6361:20020597) (2002).

14. M. N. Drozdovskaya *et al.*, *MNRAS* **476**, 4949–4964, arXiv: 1802.02977 [astro-ph.SR] (June 2018).

15. C. Druard, V. Wakelam, *Monthly Notices of the Royal Astronomical Society* **426**, 354–359, ISSN: 0035-8711, eprint: https://academic.oup.com/mnras/article-pdf/426/1/354/3267553/426-1-354.pdf, (https://doi.org/10.1111/j.1365-2966.2012.21712.x) (Oct. 2012).

16. F. Dulieu *et al.*, *Scientific Reports* **3**, 1338 (Feb. 2013).

17. C. Favre *et al.*, *A&A* **532**, A32, (https://doi.org/10.1051/0004-6361/201015345) (2011).

18. D. Friedel, L. Snyder, *ApJ* **672**, 962–973, arXiv: 0709.3232 [astro-ph] (Jan. 2008).

19. G. W. Fuchs *et al.*, *Hydrogenation reactions in interstellar CO ice analogues*, 2009, arXiv: 0906.2292 [astro-ph.SR].

20. M. Garozzo *et al.*, *A&A* **509**, A67, (https://doi.org/10.1051/0004-6361/200913040) (2010).

21. R. Garrod, S. Widicus Weaver, *Chemical reviews* **113** (Sept. 2013).

22. R. Garrod, S. Widicus Weaver, E. Herbst, presented at the Molecules in Space and Laboratory, 99, p. 99.

23. Gildas Team, *GILDAS: Grenoble Image and Line Data Analysis Software*, May 2013, ascl: 1305.010.

24. J. Goicoechea *et al.*, *A&A* **456**, 565–580, arXiv: astro-ph/0605716 [astro-ph] (Sept. 2006).

25. E. Herbst, E. F. van Dishoeck, *ARA&A* **47**, 427–480 (Sept. 2009).

26. R. Hildebrand, *QJRAS* **24**, 267–282 (Sept. 1983).

27. J. C. Howk, K. R. Sembach, B. D. Savage, *ApJ* **637**, 333–341, arXiv: `astro-ph/0508470 [astro-ph]` (Jan. 2006).

28. S. Ioppolo *et al.*, *Monthly Notices of the Royal Astronomical Society* **413**, 2281–2287, ISSN: 0035-8711, eprint: `https://academic.oup.com/mnras/article-pdf/413/3/2281/2910431/mnras0413-2281.pdf`, (`https://doi.org/10.1111/j.1365-2966.2011.18306.x`) (May 2011).

29. E. B. Jenkins, *ApJ* **700**, 1299–1348, (`https://doi.org/10.1088%2F0004-637x%2F700%2F2%2F1299`) (July 2009).

30. A. Jiménez-Escobar, G. M. Muñoz Caro, *A&A* **536**, A91, (`https://doi.org/10.1051/0004-6361/201014821`) (2011).

31. A. Jiménez-Escobar, G. M. Muñoz Caro, Y. J. Chen, *MNRAS* **443**, 343–354, ISSN: 0035-8711, eprint: `https://academic.oup.com/mnras/article-pdf/443/1/343/4287264/stu1100.pdf`, (`https://doi.org/10.1093/mnras/stu1100`) (July 2014).

32. J. Jørgensen, A. Belloche, R. Garrod, *ARA&A* **58**, 727–778, arXiv: `2006.07071 [astro-ph.SR]` (Aug. 2020).

33. J. Jørgensen, F. Schöier, E. van Dishoeck, *A&A* **416**, 603–622, arXiv: `astro-ph/0312231 [astro-ph]` (Mar. 2004).

34. M. Kama *et al.*, *ApJ* **885**, 114, arXiv: `1908.05169 [astro-ph.EP]` (Nov. 2019).

35. J. Kauffmann *et al.*, *A&A* **487**, 993–1017, arXiv: `0805.4205 [astro-ph]` (Sept. 2008).

36. M. Klassen *et al.*, *ApJl* **823** (Mar. 2016).

37. J. C. Laas, P. Caselli, *A&A* **624**, A108, (`https://doi.org/10.1051/0004-6361/201834446`) (2019).

38. T. Lamberts, J. Kästner, *Journal of Physical Chemistry A* **121**, 9736–9741, arXiv: `1712.02088 [astro-ph.GA]` (Dec. 2017).

39. R. Le Gal *et al.*, *ApJ* **876**, 72, (`%5Curl%7Bhttps://doi.org/10.3847%2F1538-4357%2Fab1416%7D`) (May 2019).

40. R. Le Gal *et al.*, *arXiv e-prints*, arXiv:2109.06286, arXiv: `2109.06286 [astro-ph.GA]` (Sept. 2021).

41. T. Leen, M. Graff, *ApJ* **325**, 411 (Feb. 1988).

42. K. Lodders, *ApJ* **591**, 1220–1247 (July 2003).

43. S. Maret *et al.*, *A&A* **526**, A47, arXiv: `1012.1747 [astro-ph.IM]` (Feb. 2011).

44. J. McMullin *et al.*, presented at the Astronomical Data Analysis Software and Systems XVI, ed. by R. Shaw, F. Hill, D. Bell, vol. 376, p. 127.

45. T. Millar, E. Herbst, *A&A* **231**, 466–472 (May 1990).

46. Y. C. Minh, *Journal of Physics: Conference Series* **728**, 052007, (`https://doi.org/10.1088%2F1742-6596%2F728%2F5%2F052007`) (July 2016).

47. M. Minissale, E. Congiu, F. Dulieu, *A&A* **585**, A146, arXiv: `1603.02897 [astro-ph.SR]` (Jan. 2016).

48. G. Mitchell, *ApJ* **287**, 665–670 (Dec. 1984).

49. N. Miyauchi *et al.*, *Chemical Physics Letters* **456**, 27–30, arXiv: `0805.0055 [astro-ph]` (Apr. 2008).

50. F. Motte *et al.*, *A&A* **476**, 1243–1260, (`https://doi.org/10.1051/0004-6361:20077843`) (2007).

51. D. Navarro-Almaida *et al.*, *A&A* **637**, A39, arXiv: `2004.03475 [astro-ph.GA]` (May 2020).

52. J. L. Neill *et al.*, *The Journal of Physical Chemistry A* **115**, PMID: 21591798, 6472–6480, eprint: `https://doi.org/10.1021/jp200539b`, (`https://doi.org/10.1021/jp200539b`) (2011).

53. D. Neufeld *et al.*, *A&A* **577**, A49, arXiv: `1502.05710 [astro-ph.GA]` (May 2015).

54. T. Nguyen *et al.*, *A&A* **628**, A15 (Aug. 2019).

55. J. Noble *et al.*, *A&A* **543**, A5 (July 2012).

56. Y. Oba *et al.*, *Nature Astronomy* **2**, 228–232, arXiv: 1810.04669 [astro-ph.GA] (Mar. 2018).

57. Y. Oba *et al.*, *Faraday Discuss.* **168**, 185–204, (http://dx.doi.org/10.1039/C3FD00112A) (0 2014).

58. K. Öberg *et al.*, *A&A* **504**, 891–913, arXiv: 0908.1169 [astro-ph.GA] (Sept. 2009).

59. S. F. Odenwald, P. R. Schwartz, *ApJ* **405**, 706 (Mar. 1993).

60. V. Ossenkopf, T. Henning, *A&A* **291**, 943–959 (Nov. 1994).

61. Y. Oya *et al.*, *ApJ* **824**, 88, arXiv: 1605.00340 [astro-ph.SR] (June 2016).

62. L. Pagani *et al.*, *A&A* **604**, A32 (July 2017).

63. M. E. Palumbo, T. R. Geballe, A. G. G. M. Tielens, *ApJ* **479**, 839–844, (https://doi.org/10.1086%2F303905) (Apr. 1997).

64. G. Pineau des Forêts *et al.*, *MNRAS* **262**, 915–928 (June 1993).

65. L. Podio *et al.*, *A&A* **581**, A85, (https://doi.org/10.1051/0004-6361/201525778) (2015).

66. P. Rivière-Marichalar *et al.*, *A&A* **628**, A16, arXiv: 1906.09932 [astro-ph.GA] (Aug. 2019).

67. D. P. Ruffle *et al.*, *MNRAS* **306**, 691–695, ISSN: 0035-8711, eprint: https://academic.oup.com/mnras/article-pdf/306/3/691/11932145/306-3-691.pdf, (https://doi.org/10.1046/j.1365-8711.1999.02562.x) (July 1999).

68. K. L. J. Rygl *et al.*, *A&A* **539**, A79, (https://doi.org/10.1051/0004-6361/201118211) (2012).

69. M. Schmalzl *et al.*, *A&A* **572**, A81, (https://doi.org/10.1051/0004-6361/201424236) (2014).

70. C. B. Singh, S. K. Chakrabarti, *MNRAS* **421**, 1666–1670, eprint: https://onlinelibrary.wiley.com/doi/pdf/10.1111/j.1365-2966.2012.20426.x, (https://onlinelibrary.wiley.com/doi/abs/10.1111/j.1365-2966.2012.20426.x) (2012).

71. R. G. Smith, *MNRAS* **249**, 172–176, ISSN: 0035-8711, eprint: https://academic.oup.com/mnras/article-pdf/249/1/172/18523351/mnras249-0172.pdf, (https://doi.org/10.1093/mnras/249.1.172) (Mar. 1991).

72. A. Tieftrunk *et al.*, *A&A* **289**, 579–596 (Sept. 1994).

73. A. Tielens, W. Hagen, *A&A* **114**, 245–260 (Oct. 1982).

74. F. F. van der Tak *et al.*, *ApJ* **537**, 283–303, arXiv: astro-ph/0001527 [astro-ph] (July 2000).

75. F. F. S. van der Tak *et al.*, *A&A* **412**, 133–145, ISSN: 1432-0746, (http://dx.doi.org/10.1051/0004-6361:20031409) (Nov. 2003).

76. S. J. van der Walt *et al.*, *Astronomy Astrophysics* **655**, A86, ISSN: 1432-0746, (http://dx.doi.org/10.1051/0004-6361/202039950) (Nov. 2021).

77. C. Vastel *et al.*, presented at the SF2A-2015: Proceedings of the Annual meeting of the French Society of Astronomy and Astrophysics, pp. 313–316.

78. C. Vastel *et al.*, *MNRAS* **478**, 5514–5532, arXiv: 1806.01102 [astro-ph.GA] (Aug. 2018).

79. A. Vasyunin, E. Herbst, *ApJ* **769**, 34, arXiv: 1303.7266 [astro-ph.GA] (May 2013).

80. T. H. G. Vidal *et al.*, *MNRAS* **469**, 435–447, ISSN: 1365-2966, (http://dx.doi.org/10.1093/mnras/stx828) (Apr. 2017).

81. T. Vidal, V. Wakelam, *MNRAS* **474**, 5575–5587, arXiv: 1711.11406 [astro-ph.SR] (Mar. 2018).

82. T. Vidal *et al.*, *MNRAS* **486**, 5197–5215, arXiv: 1905.05592 [astro-ph.GA] (July 2019).

83. S. Viti *et al.*, *A&A* **370**, 1017–1025, (https://doi.org/10.1051/0004-6361:20010300) (2001).

84. V. Wakelam, F. Hersant, F. Herpin, *A&A* **529**, A112, arXiv: 1103.2860 [astro-ph.GA] (May 2011).

85. V. Wakelam *et al.*, *A&A* **422**, 159–169, (https://doi.org/10.1051/0004-6361:20047186) (2004).

86. V. Wakelam *et al.*, *Molecular Astrophysics* **9**, 1–36, ISSN: 2405-6758, (https://www.sciencedirect.com/science/article/pii/S2405675817300271) (2017).

87. V. Wakelam, E. Herbst, *ApJ* **680**, 371–383, arXiv: 0802.3757 [astro-ph] (June 2008).

88. M. D. Ward, I. A. Hogg, S. D. Price, *MNRAS* **425**, 1264–1269, ISSN: 0035-8711, eprint: https://academic.oup.com/mnras/article-pdf/425/2/1264/4022966/425-2-1264.pdf, (https://doi.org/10.1111/j.1365-2966.2012.21520.x) (Sept. 2012).

89. N. Watanabe, A. Kouchi, *ApJ* **571**, L173–L176 (June 2002).

90. M. S. Westley *et al.*, *Nature* **373**, 405–407 (July 1995).

91. S. Widicus Weaver, D. Friedel, *The Astrophysical Journal Supplement Series* **201**, 16, (https://doi.org/10.1088%2F0067-0049%2F201%2F2%2F16) (June 2012).

92. P. M. Woods *et al.*, *MNRAS* **450**, 1256–1267, arXiv: 1503.07227 [astro-ph.SR] (June 2015).

93. L. Zapata, J. Schmid-Burgk, K. Menten, *A&A* **529**, A24, arXiv: 1009.1426 [astro-ph.GA] (May 2011).

Appendix

LABORATORY TEMPERATURE DESORPTION PROFILE

This appendix shows one of the temperature-programmed desorption profiles we used for this study. It provides an overview of the mass decomposition observed by the QMS. In Figure 5.A.1 we show the hydrogenation of the H_2S at 10 K during 15 min. The data were rebinned by a factor of 4 for clarity, such that the temporal resolution is 4 sec as opposed to 1 sec (in temperature units, this difference 0.8 K vs. 0.2 K). Results are shown for values of m/z of 32 (S), 34 (H_2S), 36 ($H_2^{34}S$), 64 (S_2), and 66 (H_2S_2 or $S^{34}S$). The secondary peak for $m/z = 34$ (H_2S) at ~ 140 K is likely caused by a small amount of H_2S that is trapped in H_2O, which desorbs at this temperature. For $m/z = 64$ and 66, the spectra were multiplied by a factor of 3 to illustrate the nondetections at high temperature. Both molecules have desorption temperatures below 240 K (Jiménez-Escobar *et al.*, 2014).
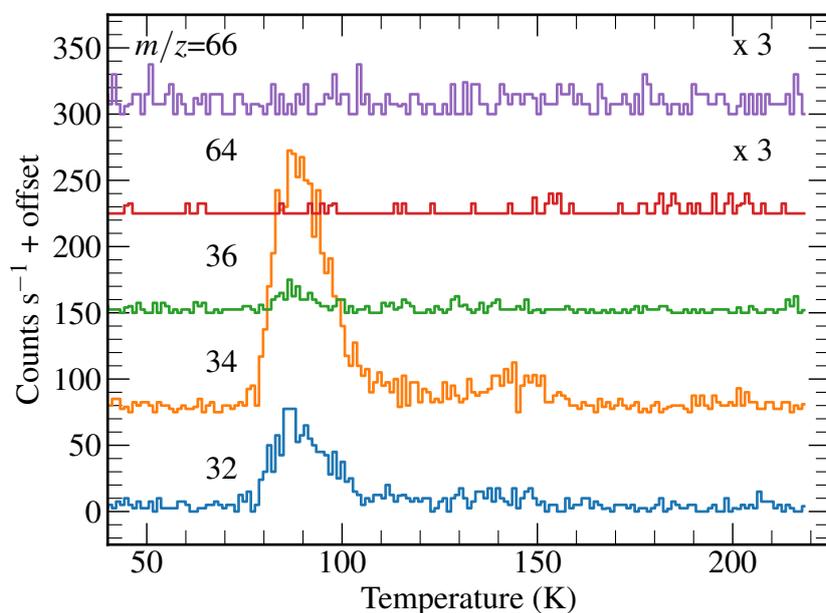
FIGURE 5.A.1: Temperature-programmed desorption profiles obtained after hydrogenation of H_2S at 10 K for 15 min. The TPD is performed from 40 K to $\sim$220 K, and the values of m/z are shown for each spectrum (see the main text for the species to which they correspond). The spectra have been rebinned by a factor of 4 for clarity, and are offset from one another by 80 counts s^{-1}.

LINE IDENTIFICATION

Tables 5.B.1–5.B.5 list all the molecules we detected toward CygX-N12 and N30 in the cold and warm chemistries, as well as their transition and upper-level energy.

TABLE 5.B.1: Detected S-species toward CygX-N12 - cold chemistry

Molecule	Transition	Frequency [MHz]	E_{up} [K]	A_{ij} [s^{-1}]
		C-S Family		
OCS	6 – 5	72976.779	12.3	1.07×10^{-6}
OCS	7 – 6	85139.103	16.3	1.7146×10^{-6}
OCS	8 – 7	97301.208	21.0	2.5813×10^{-6}
OCS	9 – 8	109463.063	26.3	3.6988×10^{-6}
OC^{33}S	8 – 7	96076.055	20.7	2.4854×10^{-6}
CS	2 0 – 1 0	97980.953	7.1	1.6792×10^{-5}
^{13}C^{34}S	2 – 1	90926.026	6.5	1.3419×10^{-5}
^{13}CS	2 0 – 1 0	92494.308	6.7	1.4125×10^{-5}
C^{34}S	2 0 – 1 0	96412.950	6.9	1.5997×10^{-5}
C^{33}S	2 0 – 1 0	97172.064	7.0	1.6378×10^{-5}
H$_2$CS	3 2 2 – 2 2 1	103039.902	62.6	8.2453×10^{-6}
H$_2$CS	3 0 3 – 2 0 2	103040.447	9.9	1.4841×10^{-5}
H$_2$CS	3 2 1 – 2 2 0	103051.842	62.6	8.2482×10^{-6}
H$_2$CS	3 1 3 – 2 1 2	101477.805	22.9	1.2601×10^{-5}
H$_2$CS	3 1 2 – 2 1 1	104617.027	23.2	1.3806×10^{-5}
H$_2$C^{34}S	3 1 3 – 2 1 2	99774.0749	22.76	1.1977×10^{-5}
H$_2$C^{34}S	3 2 2 – 2 2 1	101283.379	62.4	7.8306×10^{-6}
H$_2$C^{34}S	3 0 3 – 2 0 2	101284.314	9.7	1.4095×10^{-5}
H$_2$C^{34}S	3 1 2 – 2 1 1	102807.3384	23.05	1.3103×10^{-5}
CCS	6 5 – 5 4	72323.789	19.2	1.5963×10^{-5}
CCS	6 6 – 5 5	77731.711	21.8	2.0346×10^{-5}
CCS	7 6 – 6 5	86181.391	23.3	2.7778×10^{-5}
CCS	7 7 – 6 6	90686.381	26.1	3.2918×10^{-5}
CCS	7 8 – 6 7	93870.107	19.9	3.744×10^{-5}
CCS	8 8 – 7 7	103640.759	31.1	4.9786×10^{-5}
CCS	8 9 – 7 8	106347.726	25.0	5.4839×10^{-5}
CCS	9 8 – 8 7	113410.186	33.6	6.5343×10^{-5}
C$_3$S	13_12	75147	25.25	3.2633×10^{-5}
C$_3$S	15 – 14	86708.379	33.3	5.0378×10^{-5}
C$_3$S	18 – 17	104048.455	47.4	8.751×10^{-5}
CC^{13}CS	15 – 14	86708.522	33.3	5.0378×10^{-5}
CC^{13}CS	16 – 15	92488.645	37.7	6.1255×10^{-5}
CH$_3$SH	3 0 3 0 – 2 0 2 0	75862.859	7.3	3.6145×10^{-6}
CH$_3$SH	3 0 3 1 – 2 0 2 1	75864.405	8.7	3.6176×10^{-6}
CH$_3$SH	4 0 4 0 – 3 0 3 0	101139.111	12.1	8.8825×10^{-6}
CH$_3$SH	4 0 4 1 – 3 0 3 1	101139.632	13.6	8.89×10^{-6}
HSCN	8 2 6 – 7 2 5	91746.785	74.3	4.4001×10^{-5}
HSCN	8 0 8 – 7 0 7	91750.636	19.8	4.6944×10^{-5}
HSCN	9 2 8 – 8 2 7	103210.4015	79.27	6.3938×10^{-5}
HCS$^+$	2 – 1	85347.890	6.1	1.1096×10^{-5}
		O-S Family		
SO	2 2 – 1 1	86093.950	19.3	5.25×10^{-6}
SO	2 3 – 1 2	99299.870	9.2	1.1252×10^{-5}
SO	5 4 – 4 4	100029.640	38.6	1.0825×10^{-6}
SO	3 2 – 2 1	109252.220	21.1	1.0803×10^{-5}
^{34}SO	2 3 – 1 2	97715.317	9.1	1.0728×10^{-5}
SO$_2$	6 0 6 – 5 1 5	72758.243	19.2	2.7685×10^{-6}
SO$_2$	3 1 3 – 2 0 2	104029.418	7.7	1.0059×10^{-5}
SO$_2$	10 1 9 – 10 0 10	104239.295	54.7	1.1217×10^{-5}

TABLE 5.B.2: Detected S-species toward CygX-N12 - warm chemistry

Molecule	Transition	Frequency [MHz]	E_{up} [K]	A_{ij} [s^{-1}]
		N-S Family		
NS	3 1 3 4 – 2-1 2 3	115153.935	8.8	2.3295×10^{-5}
NS	3 1 3 3 – 2-1 2 2	115156.812	8.8	1.9567×10^{-5}
NS	3 1 3 2 – 2-1 2 1	115162.982	8.8	1.7472×10^{-5}
NS	3 1 3 2 – 2-1 2 2	115185.336	8.8	5.5914×10^{-6}
NS$^+$	2 – 1	100198.474	7.2	2.2056×10^{-5}
		C-S Family		
OCS	28–27	340449.2733	236.95	1.15×10^{-4}
OCS	29–28	352599.5703	253.88	1.28×10^{-4}
OC^{33}S	28–27	336163.734	233.97	1.1×10^{-4}
OC^{33}S	29–28	348161.174	250.68	1.24×10^{-4}
OC^{33}S	30–29	360157.731	267.96	1.37×10^{-4}
OC^{34}S	28–27	332129.6702	231.16	1.07×10^{-4}
OC^{34}S	29–28	343983.2336	247.67	1.19×10^{-4}
OC^{34}S	30–29	355835.9326	264.75	1.32×10^{-4}
CS	7 0 – 6 0	342882.8503	65.83	8.4×10^{-4}
C^{34}S	7 0 – 6 0	337396.459	64.77	8.0×10^{-4}
C^{33}S	7 0 – 6 0	340052.5755	65.28	8.19×10^{-4}
H$_2$CS	10 1 10 – 9 1 9	338083.1953	102.43	5.77×10^{-4}
H$_2$CS	10 0 10 – 9 0 9	342946.4239	90.59	6.08×10^{-4}
H$_2$CS	10 2 9 – 9 2 8	343322.0819	143.31	5.86×10^{-4}
H$_2$CS	10 3 8 – 9 3 7	343409.9625	209.10	5.56×10^{-4}
H$_2$CS	10 3 7 – 9 3 6	343414.1463	209.10	5.56×10^{-4}
H$_2$CS	10 2 8 – 9 2 7	343813.1683	143.38	5.88×10^{-4}
H$_2$CS	10 1 9 – 9 1 8	348534.3647	105.19	6.32×10^{-4}
		O-S Family		
SO	8 7 – 7 6	340714.155	81.25	4.99×10^{-4}
SO	8 8 – 7 7	344310.612	87.48	5.19×10^{-4}
SO	8 9 – 7 8	346528.481	78.78	5.38×10^{-4}
^{34}SO	8 7 – 7 6	333900.9827	79.86	4.69×10^{-4}
^{34}SO	8 8 – 7 7	337580.1467	86.07	4.89×10^{-4}
^{34}SO	8 9 – 7 8	339857.2694	77.34	5.08×10^{-4}
SO$_2$	21 2 20 – 21 1 21	332091.4311	219.53	1.51×10^{-4}
SO$_2$	4 3 1 – 3 2 2	332505.2415	31.29	3.29×10^{-4}
SO$_2$	18 4 14 – 18 3 15	338305.9931	196.80	3.27×10^{-4}
SO$_2$	20 1 19 – 19 2 18	338611.8103	198.88	2.87×10^{-4}
SO$_2$	13 2 12 – 12 1 11	345338.5377	92.98	2.38×10^{-4}
SO$_2$	16 4 12 – 16 3 13	346523.8784	164.46	3.39×10^{-4}
SO$_2$	19 1 19 – 18 0 18	346652.1691	168.14	5.22×10^{-4}
SO$_2$	14 4 10 – 14 3 11	351873.8732	135.87	3.43×10^{-4}
SO$_2$	12 4 8 – 12 3 9	355045.5169	111.00	3.40×10^{-4}
SO$_2$	11 4 8 – 11 3 9	357387.5795	99.95	3.38×10^{-4}
SO$_2$	8 4 4 – 8 3 5	357581.4486	72.36	3.06×10^{-4}
SO$_2$	6 4 2 – 6 3 3	357925.8478	58.58	2.6×10^{-4}
SO$_2$	20 0 20 – 19 1 19	358215.6327	185.33	5.83×10^{-4}
SO$_2$	19 4 16 – 19 3 17	359770.6846	214.26	3.85×10^{-4}
^{34}SO$_2$	21 2 20 – 21 1 21	330667.565	218.58	1.45×10^{-4}
^{34}SO$_2$	23 3 21 – 23 2 22	332173.573	274.74	2.54×10^{-4}
^{34}SO$_2$	16 4 12 – 16 3 13	332836.225	162.90	3.02×10^{-4}
^{34}SO$_2$	14 4 10 – 14 3 11	338785.6873	134.34	3.08×10^{-4}

TABLE 5.B.3: Detected S-species toward CygX-N30 – warm chemistry

Molecule	Transition	Frequency [MHz]	E_{up} [K]	A_{ij} [s^{-1}]
$^{34}SO_2$	5 3 3 – 4 2 2	342208.8572	35.10	3.1×10^{-4}
$^{34}SO_2$	20 1 19 – 19 2 18	342231.6332	198.24	3.06×10^{-4}
$^{34}SO_2$	12 4 8 – 12 3 9	342332.0131	109.51	3.06×10^{-4}
$^{34}SO_2$	10 4 6 – 10 3 7	344245.3459	88.38	2.96×10^{-4}
$^{34}SO_2$	13 4 10 – 13 3 11	344807.9147	121.46	3.17×10^{-4}
$^{34}SO_2$	15 4 12 – 15 3 13	344987.5847	148.13	3.27×10^{-4}
$^{34}SO_2$	11 4 8 – 11 3 9	344998.1602	98.48	3.05×10^{-4}
$^{34}SO_2$	21 4 18 – 21 3 19	352082.921	250.42	3.65×10^{-4}
$^{34}SO_2$	15 2 14 – 14 1 13	358987.9711	118.72	2.92×10^{-4}
		N-S Family		
NS	8 -1 7.5 6.5 – 7 1 6.5 5.5	345824.13	69.69	7.21×10^{-4}
NS	8 1 7.5 8.5 – 7 -1 6.5 7.5	346220.137	69.84	7.39×10^{-4}
		C-S Family		
OCS	28-27	340449.2733	236.95	1.15×10^{-4}
OCS	29-28	352599.5703	253.88	1.28×10^{-4}
$OC^{33}S$	28-27	336163.734	233.97	1.1×10^{-4}
$OC^{33}S$	29-28	348161.174	250.68	1.24×10^{-4}
$OC^{33}S$	30-29	360157.731	267.96	1.37×10^{-4}
$OC^{34}S$	28-27	332129.6702	231.16	1.07×10^{-4}
$OC^{34}S$	29-28	343983.2336	247.67	1.19×10^{-4}
$OC^{34}S$	30-29	355835.9326	264.75	1.32×10^{-4}
CS	7 0 – 6 0	342882.8503	65.83	8.4×10^{-4}
$C^{34}S$	7 0 – 6 0	337396.459	64.77	8.0×10^{-4}
$C^{33}S$	7 0 – 6 0	340052.5755	65.28	8.19×10^{-4}
H_2CS	10 1 10 – 9 1 9	338083.1953	102.43	5.77×10^{-4}
H_2CS	10 0 10 – 9 0 9	342946.4239	90.59	6.08×10^{-4}
H_2CS	10 4 6 – 9 4 5	343309.8296	301.07	5.12×10^{-4}
H_2CS	10 2 9 – 9 2 8	343322.0819	143.31	5.86×10^{-4}
H_2CS	10 3 8 – 9 3 7	343409.9625	209.10	5.56×10^{-4}
H_2CS	10 3 7 – 9 3 6	343414.1463	209.10	5.56×10^{-4}
H_2CS	10 2 8 – 9 2 7	343813.1683	143.38	5.88×10^{-4}
H_2CS	10 1 9 – 9 1 8	348534.3647	105.19	6.32×10^{-4}
		O-S Family		
SO	2 1 – 1 0	329385.477	15.81	1.42×10^{-5}
SO	11 10 – 10 10	336553.8112	142.88	6.12×10^{-6}
SO	3 3 – 2 3	339341.459	25.51	1.45×10^{-5}
SO	8 7 – 7 6	340714.155	81.25	4.99×10^{-4}
SO	8 8 – 7 7	344310.612	87.48	5.19×10^{-4}
SO	8 9 – 7 8	346528.481	78.78	5.38×10^{-4}
^{34}SO	8 7 – 7 6	333900.9827	79.86	4.69×10^{-4}
^{34}SO	8 8 – 7 7	337580.1467	86.07	4.89×10^{-4}
^{34}SO	3 3 – 2 3	337892.2466	25.31	1.40×10^{-5}
^{34}SO	8 9 – 7 8	339857.2694	77.34	5.08×10^{-4}
^{33}SO	8 7 5.5 – 7 6 4.5	337199.3711	80.54	4.65×10^{-4}
^{33}SO	8 8 9.5 – 7 7 8.5	340839.6391	86.75	5.03×10^{-4}
^{33}SO	8 9 8.5 – 7 8 7.5	343087.2979	78.03	5.09×10^{-4}
SO_2	11 6 6 – 12 5 7	331580.244	148.957	4.35×10^{-5}
SO_2	21 2 20 – 21 1 21	332091.4311	219.53	1.51×10^{-4}
SO_2	4 3 1 – 3 2 2	332505.2415	31.29	3.29×10^{-4}
SO_2	8 2 6 – 7 1 7	334673.3526	43.15	1.27×10^{-4}

TABLE 5.B.4: Table 5.B.3 continued

Molecule	Transition	Frequency [MHz]	E_{up} [K]	A_{ij} [s^{-1}]
		O-S Family		
SO$_2$	23 3 21 – 23 2 22	336089.2284	276.02	2.67×10^{-4}
SO$_2$	16 7 9 – 17 6 12	336669.581	245.12	5.84×10^{-5}
SO$_2$	18 4 14 – 18 3 15	338305.9931	196.80	3.27×10^{-4}
SO$_2$	20 1 19 – 19 2 18	338611.8103	198.88	2.87×10^{-4}
SO$_2$	28 2 26 – 28 1 27	340316.4059	391.80	2.58×10^{-4}
SO$_2$	21 8 14 – 22 7 15	341275.5244	369.14	6.86×10^{-5}
SO$_2$	5 5 1 – 6 4 2	345148.9708	75.14	9.81×10^{-6}
SO$_2$	13 2 12 – 12 1 11	345338.5377	92.98	2.38×10^{-4}
SO$_2$	16 4 12 – 16 3 13	346523.8784	164.46	3.39×10^{-4}
SO$_2$	19 1 19 – 18 0 18	346652.1691	168.14	5.22×10^{-4}
SO$_2$	24 2 22 – 23 3 21	348387.80	292.74	1.91×10^{-4}
SO$_2$	10 6 4 – 11 5 7	350862.756	138.85	4.40×10^{-5}
SO$_2$	5 3 3 – 4 2 2	351257.2233	35.89	3.36×10^{-4}
SO$_2$	14 4 10 – 14 3 11	351873.8732	135.87	3.43×10^{-4}
SO$_2$	12 4 8 – 12 3 9	355045.5169	111.00	3.40×10^{-4}
SO$_2$	15 7 9 – 16 6 10	356040.6442	230.40	6.40×10^{-5}
SO$_2$	10 4 6 – 10 3 7	356755.1899	89.83	3.28×10^{-4}
SO$_2$	13 4 10 – 13 3 11	357165.3904	122.97	3.51×10^{-4}
SO$_2$	15 4 12 – 15 3 13	357241.1932	149.68	3.62×10^{-4}
SO$_2$	11 4 8 – 11 3 9	357387.5795	99.95	3.38×10^{-4}
SO$_2$	8 4 4 – 8 3 5	357581.4486	72.36	3.06×10^{-4}
SO$_2$	9 4 6 – 9 3 7	357671.8206	80.64	3.20×10^{-4}
SO$_2$	7 4 4 – 7 3 5	357892.4422	65.01	2.87×10^{-4}
SO$_2$	6 4 2 – 6 3 3	357925.8478	58.58	2.6×10^{-4}
SO$_2$	17 4 14 – 17 3 15	357962.9049	180.11	3.73×10^{-4}
SO$_2$	5 4 2 – 5 3 3	358013.1536	53.07	2.18×10^{-4}
SO$_2$	4 4 0 – 4 3 1	358037.8869	48.48	1.45×10^{-4}
SO$_2$	20 0 20 – 19 1 19	358215.6327	185.33	5.83×10^{-4}
SO$_2$	25 3 23 – 25 2 24	359151.1581	320.93	3.10×10^{-4}
SO$_2$	19 4 16 – 19 3 17	359770.6846	214.26	3.85×10^{-4}
SO$_2$	20 8 12 – 21 7 15	360721.8287	349.82	7.72×10^{-5}
^{34}SO$_2$	8 2 6 – 7 1 7	330191.103	42.77	1.19×10^{-4}
^{34}SO$_2$	21 2 20 – 21 1 21	330667.565	218.58	1.45×10^{-4}
^{34}SO$_2$	23 3 21 – 23 2 22	332173.573	274.74	2.54×10^{-4}
^{34}SO$_2$	16 4 12 – 16 3 13	332836.225	162.90	3.02×10^{-4}
^{34}SO$_2$	13 2 12 – 12 1 11	338320.3564	92.45	2.27×10^{-4}
^{34}SO$_2$	14 4 10 – 14 3 11	338785.6873	134.34	3.08×10^{-4}
^{34}SO$_2$	5 3 3 – 4 2 2	342208.8572	35.10	3.1×10^{-4}
^{34}SO$_2$	20 1 19 – 19 2 18	342231.6332	198.24	3.06×10^{-4}
^{34}SO$_2$	12 4 8 – 12 3 9	342332.0131	109.51	3.06×10^{-4}
^{34}SO$_2$	10 4 6 – 10 3 7	344245.3459	88.38	2.96×10^{-4}
^{34}SO$_2$	19 1 19 – 18 0 18	344581.0445	167.41	5.16×10^{-4}
^{34}SO$_2$	13 4 10 – 13 3 11	344807.9147	121.46	3.17×10^{-4}
^{34}SO$_2$	15 4 12 – 15 3 13	344987.5847	148.13	3.27×10^{-4}
^{34}SO$_2$	11 4 8 – 11 3 9	344998.1602	98.48	3.05×10^{-4}
^{34}SO$_2$	8 4 4 – 8 3 5	345168.6641	70.94	2.75×10^{-4}
^{34}SO$_2$	9 4 6 – 9 3 7	345285.6199	79.20	2.88×10^{-4}
^{34}SO$_2$	7 4 4 – 7 3 5	345519.6563	63.61	2.59×10^{-4}
^{34}SO$_2$	6 4 2 – 6 3 3	345553.0927	57.19	2.35×10^{-4}

TABLE 5.B.5: Table 5.B.3 continued

Molecule	Transition	Frequency [MHz]	E_{up} [K]	A_{ij} [s^{-1}]
$^{34}SO_2$	5 4 2 – 5 3 3	345651.2934	51.69	1.96×10^{-4}
$^{34}SO_2$	4 4 0 – 4 3 1	345678.7871	47.10	1.31×10^{-4}
$^{34}SO_2$	17 4 14 – 17 3 15	345929.349	178.51	3.37×10^{-4}
$^{34}SO_2$	19 4 16 – 19 3 17	348117.4691	212.61	3.50×10^{-4}
$^{34}SO_2$	21 4 18 – 21 3 19	352082.921	250.42	3.65×10^{-4}
$^{34}SO_2$	25 3 23 – 25 2 24	356222.25	319.52	2.97×10^{-4}
$^{34}SO_2$	20 0 20 – 19 1 19	357102.1824	184.55	5.81×10^{-4}
$^{34}SO_2$	23 4 20 – 23 3 21	358347.3159	291.93	3.86×10^{-4}
$^{34}SO_2$	15 2 14 – 14 1 13	358987.9711	118.72	2.92×10^{-4}
$^{34}SO_2$	24 2 22 – 23 3 21	359651.7298	292.00	2.20×10^{-4}
$^{33}SO_2$	16 4 12 – 16 3 13	339480.7723	163.66	1.71×10^{-6}
$^{33}SO_2$	3 2 12 – 12 1 11	341723.1266	92.71	1.99×10^{-6}
$^{33}SO_2$	14 4 10 – 14 3 11	345133.1204	135.08	3.23×10^{-4}
$^{33}SO_2$	19 1 19 – 18 0 18	345584.7147	167.77	5.19×10^{-4}
$^{33}SO_2$	12 4 8 – 12 3 9	348491.9464	110.23	3.19×10^{-4}
$^{33}SO_2$	10 4 6 – 10 3 7	350303.689	89.09	3.01×10^{-4}
$^{33}SO_2$	13 4 10 – 13 3 11	350788.1698	122.19	3.27×10^{-4}
$^{33}SO_2$	20 0 20 – 19 1 19	357658.8622	184.93	5.80×10^{-4}
N-S Family				
NS	8 -1 7.5 6.5 – 7 1 6.5 5.5	345824.13	69.69	7.21×10^{-4}
NS	8 1 7.5 8.5 – 7 -1 6.5 7.5	346220.137	69.84	7.39×10^{-4}

5.c LINE SPECTRA

The spectra of the cold envelope and hot core of CygX-N12 are shown in Figures 5.C.1-5.C.4 and 5.C.8-5.C.9, respectively. The spectra of the hot core of N30 are displayed in Figures 5.C.5-5.C.7. The detected S-species are shown in all the spectra.
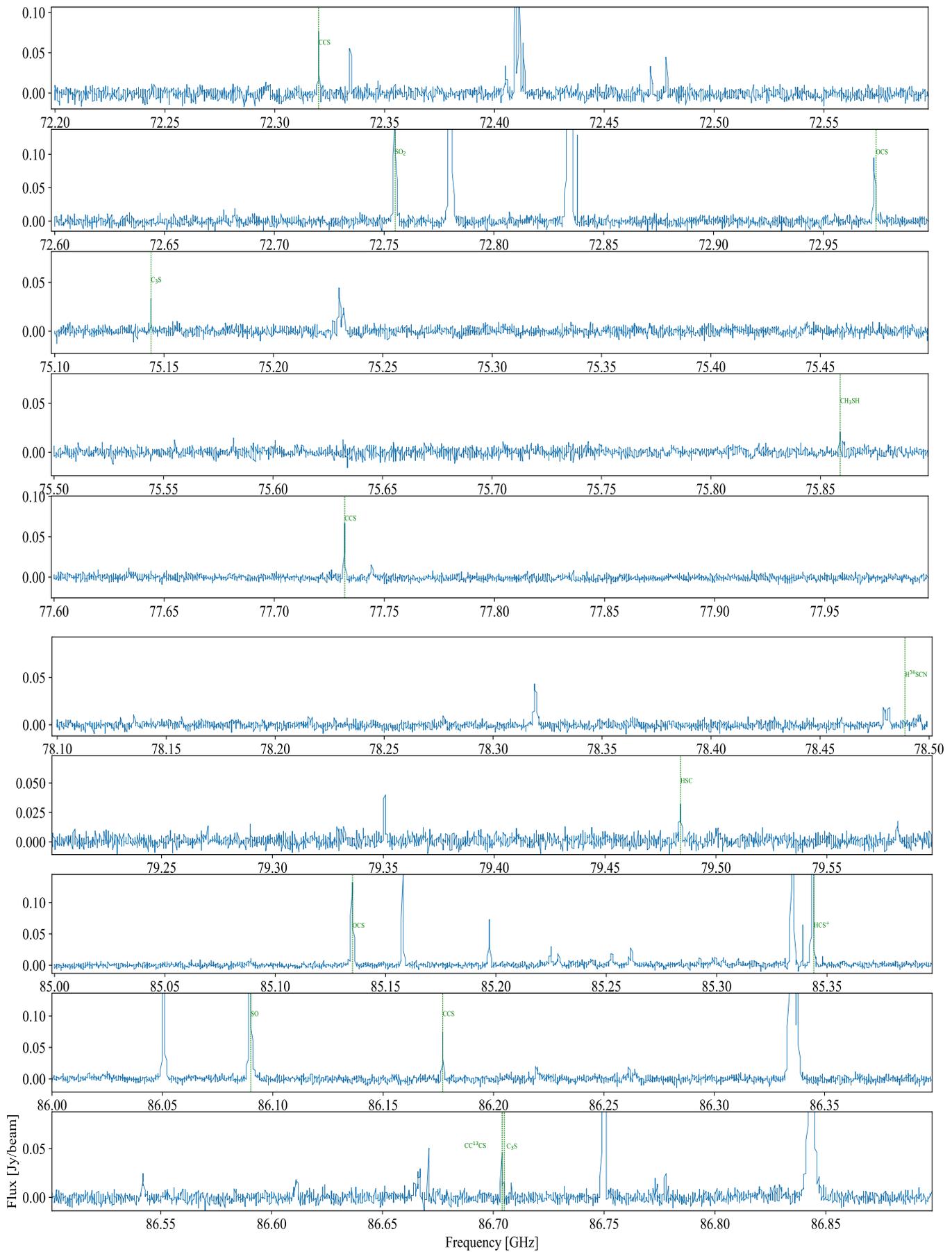
FIGURE 5.C.1: Spectrum in the range 72.2–86.9 GHz toward the source CygX-N12. Transitions of the sulphur species are identified.

FIGURE 5.C.2: Spectrum in the range 90.62–99.8 GHz toward the source CygX-N12. Transitions of the sulphur species are identified.
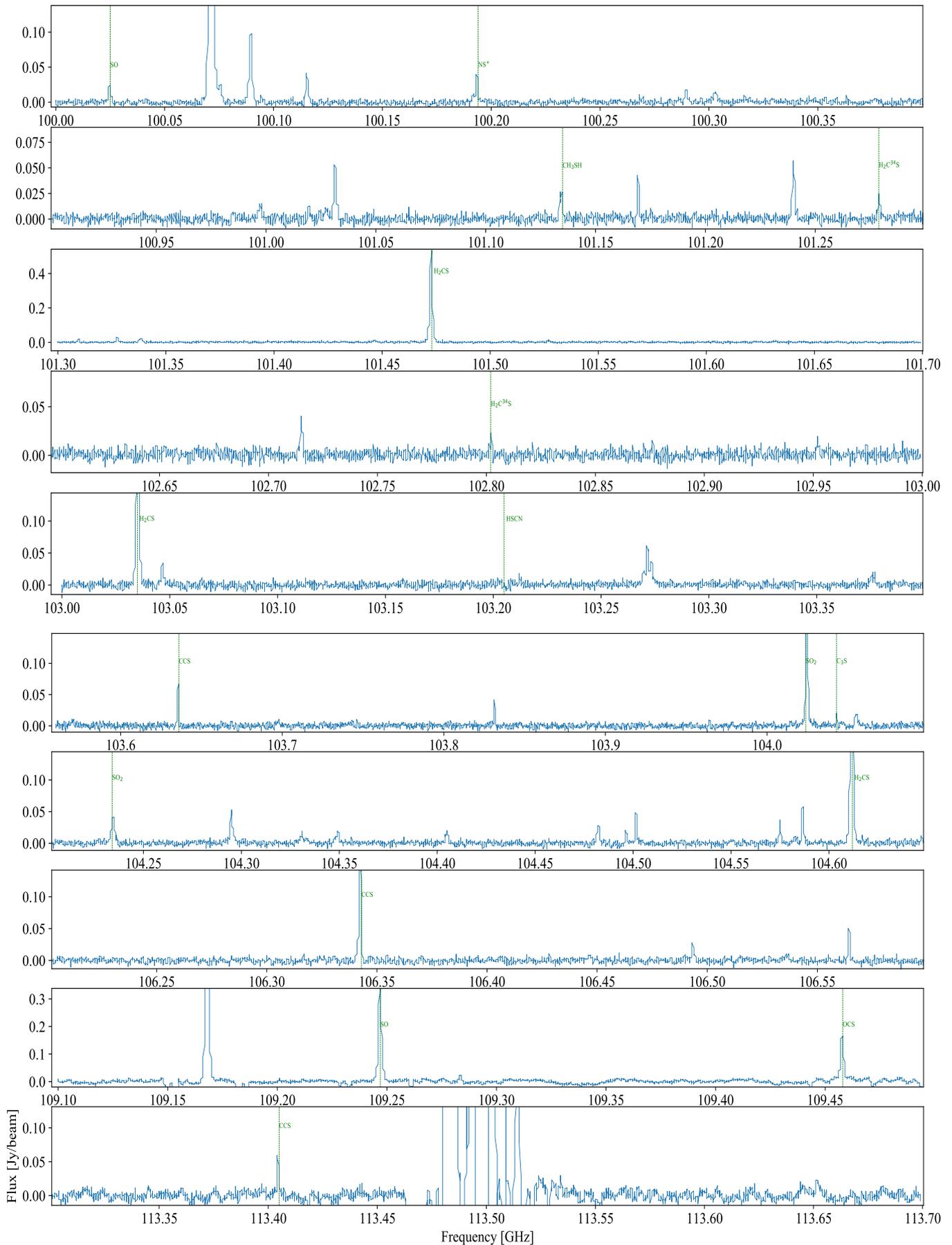
FIGURE 5.C.3: Spectrum in the range 100–113.7 GHz toward the source CygX-N12. Transitions of the sulphur species are identified.

FIGURE 5.C.4: Spectrum in the range 115–115.4 GHz toward the source CygX-N12. Transitions of the sulphur species are identified.

FIGURE 5.C.5: Spectrum in the range 329.2-340 GHz toward the source CygX-N30. Transitions of the sulphur species are identified.

FIGURE 5.C.6: Spectrum in the range 340-352 GHz toward the source CygX-N30. Transitions of the sulphur species are identified.

FIGURE 5.C.7: Spectrum in the range 352-361 GHz toward the source CygX-N30. Transitions of the sulphur species are identified.
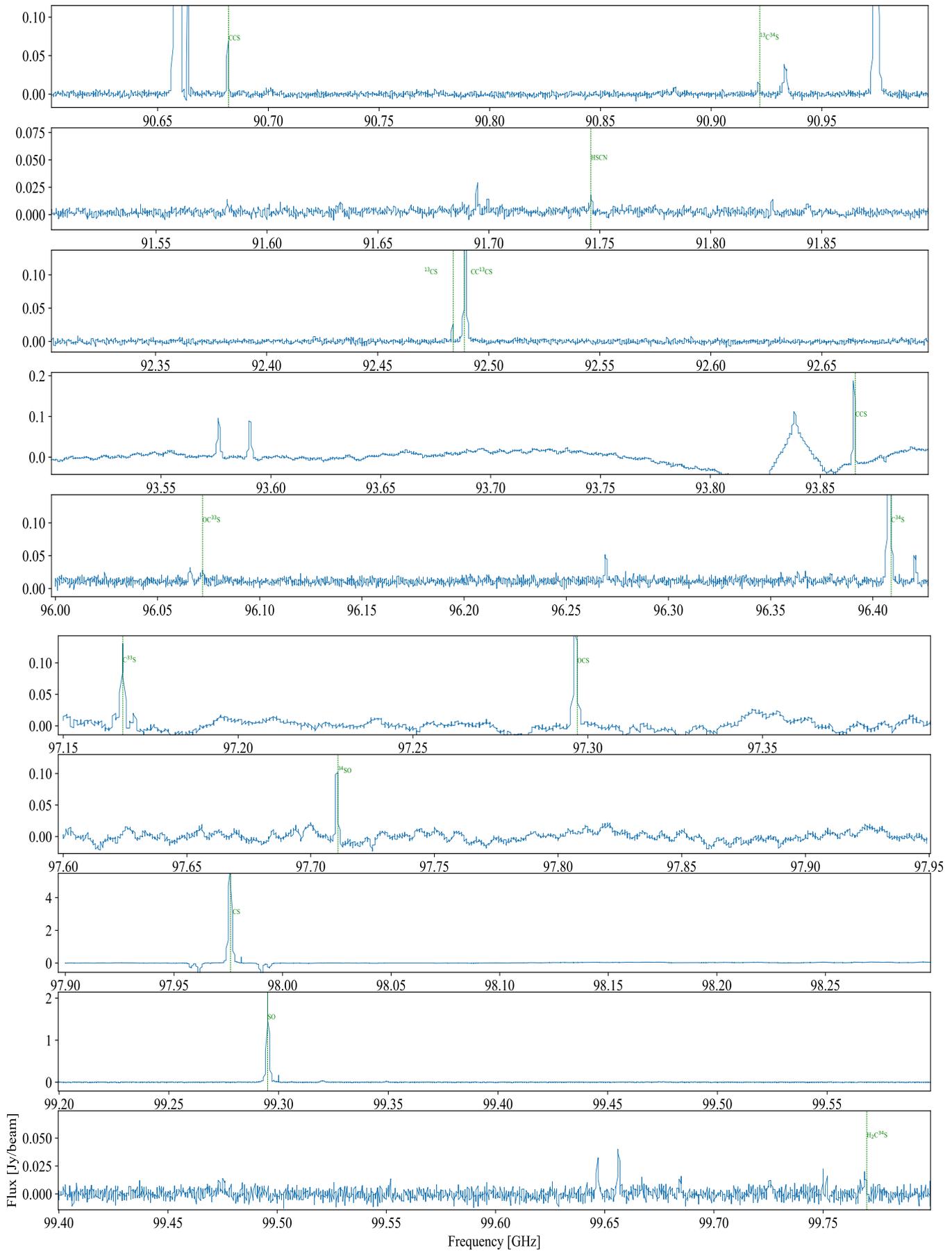
FIGURE 5.C.8: Spectrum in the range 330-344 GHz toward the source CygX-N12. Transitions of the sulphur species are identified.

FIGURE 5.C.9: Spectrum in the range 344-360.5 GHz toward the source CygX-N12. Transitions of the sulphur species are identified.
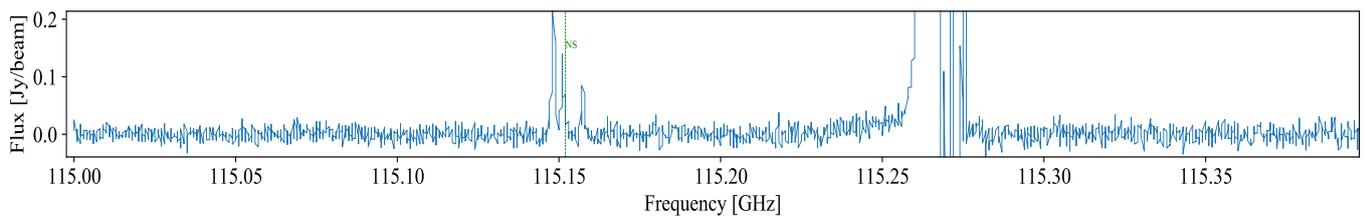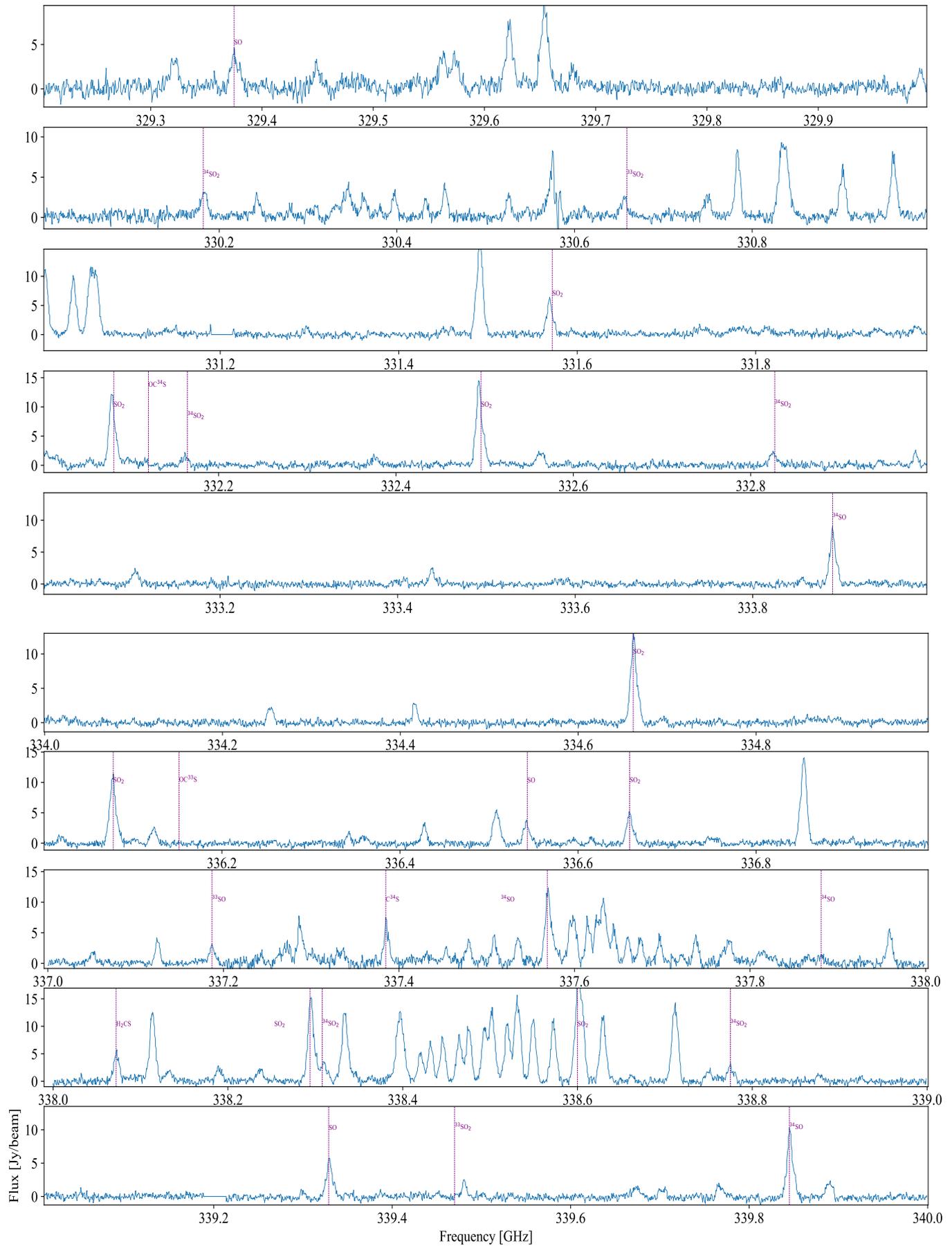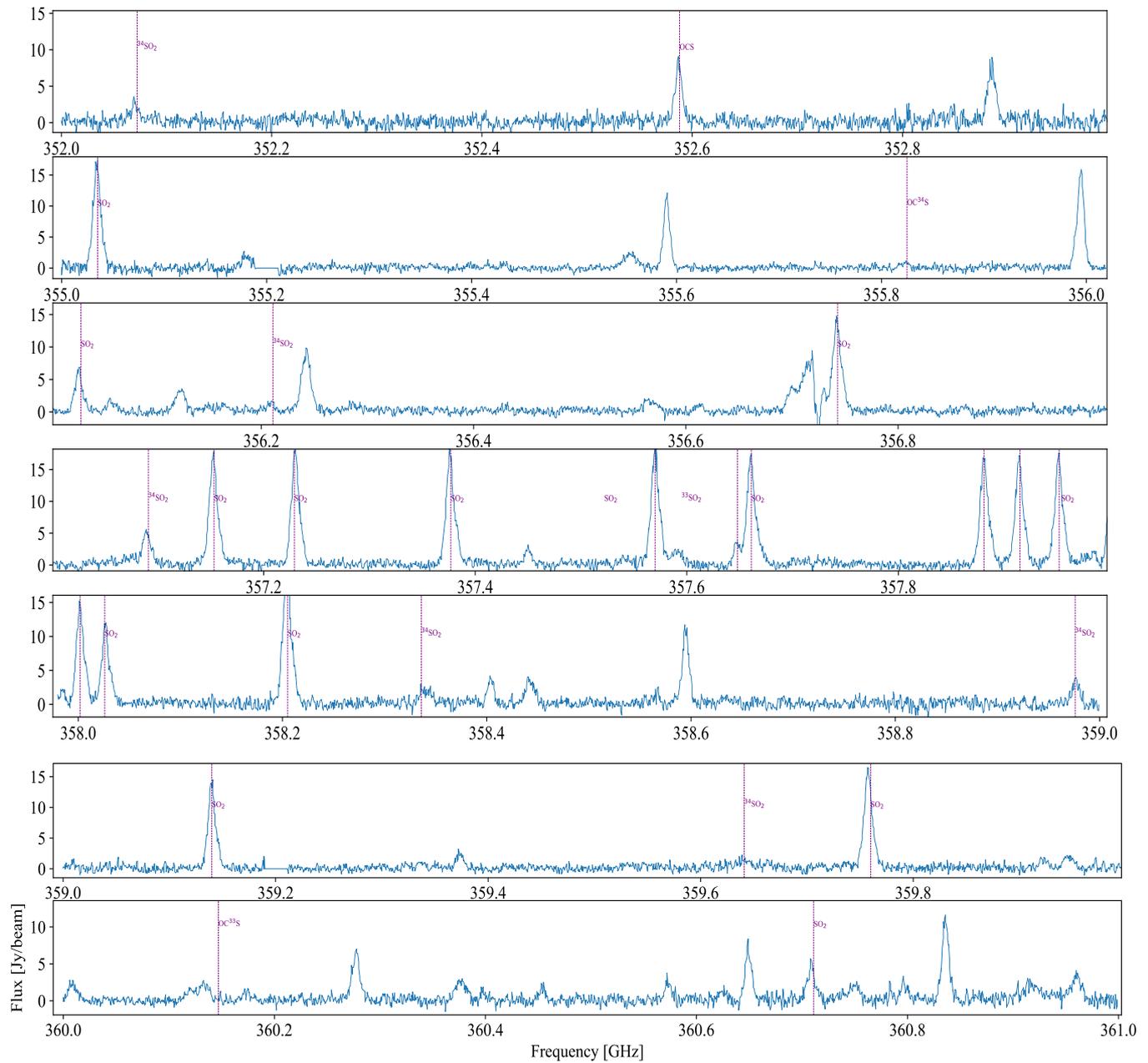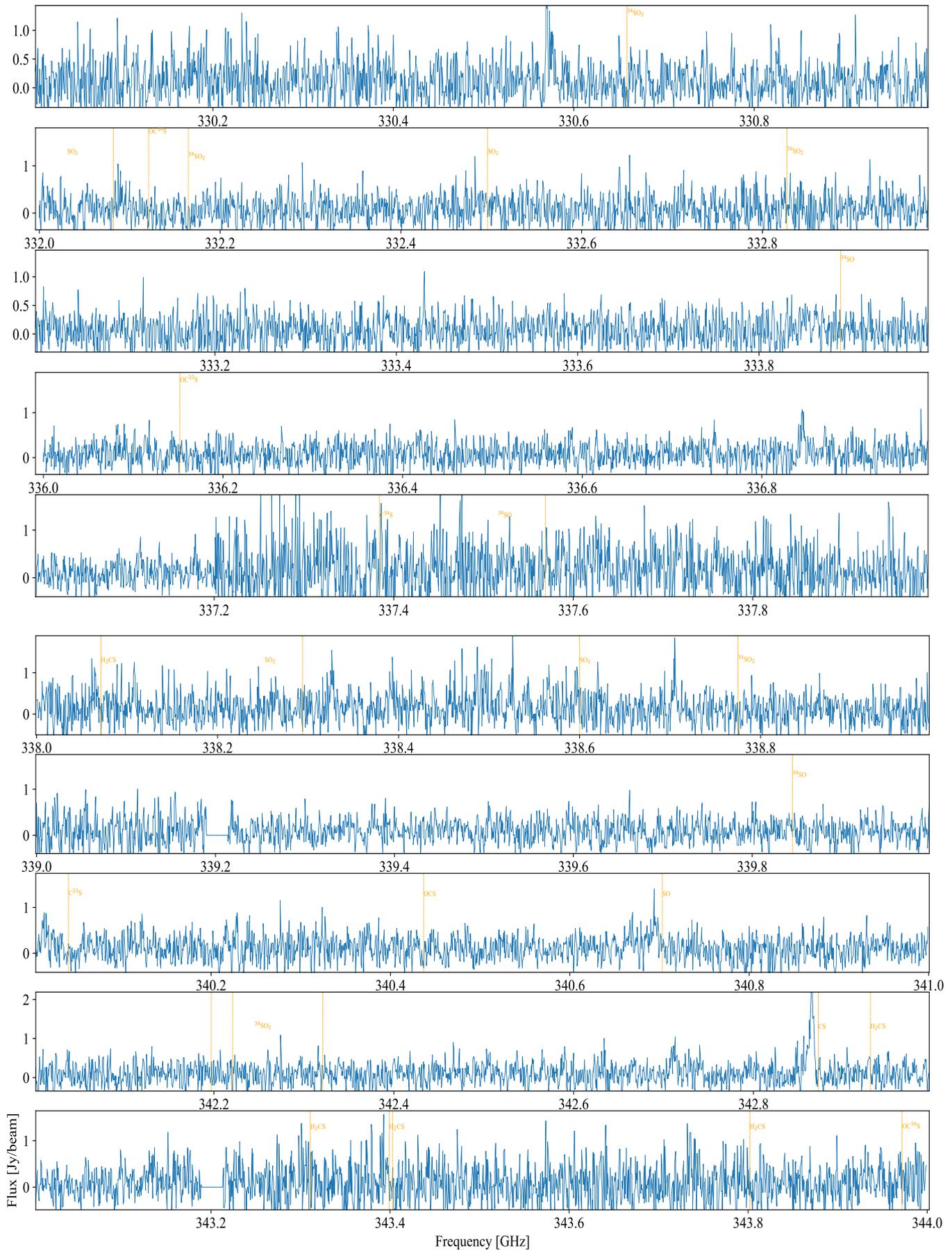
6

High-angular resolution observations of the chemically active BHR71 outflow with ALMA physical and chemical conditions

M. el Akel[1,2], A. Gusdorf[3,4], G. Pineau des Forêts[4,5], L. E. Kristensen[1], R. LeGal [6,7], T. L. Bourke[8], D. Riquelme[9], J. Pety[6]

[1] Niels Bohr Institute, University of Copenhagen, Øster Voldgade 5–7, 1350 Copenhagen, Denmark
[2] CY University, Observatoire de Paris, CNRS, LERMA, F-95000 Cergy, France
[3] Observatoire de Paris, PSL, Sorbonne Université, CNRS, LERMA, 75014 Paris, France
[4] Laboratoire de Physique de l'École normale supérieure, ENS, Université PSL, CNRS, Sorbonne Université, Université de Paris, Paris, France
[5] Université Paris-Saclay, CNRS, Institut d'Astrophysique Spatiale, 91405 Orsay, France
[6] IRAM, 300 rue de la Piscine, 38406 Saint-Martin-d'Hères, France
[7] Univ. Grenoble Alpes, CNRS, IPAG, F-38000 Grenoble, France
[8] SKA Organisation,Jodrell Bank Observatory, Lower Withington, Macclesfield, Cheshire SK11 9DL,UK
[9] Max-Planck-Institut für Radioastronomie, Auf dem Hügel 69, 53121 Bonn, Germany

Abstract

Context. Shocks and outflows are unique chemical laboratories: the gas is heated and compressed, which strongly affects the abundances of both gas-phase and grain species. Understanding the physics of a shock thus requires understanding the dominant chemical reactions, and vice versa.

Aims. We aim at understanding the dominant chemical processes in the BHR71 outflow by comparing high-angular-resolution ALMA observations of several molecular species with a grid of shock models.

Methods. We present high resolutions ALMA observations of key species, CS, SO, CH_3OH and H_2CO of the chemically active outflow, BHR71. We combined this dataset with prior observations of CO (3–2) emission by ALMA/ACA and APEX, H_2 0–0 S(0) to S(7) and [S I] $^3P_1 - ^3P_2$ emission by *Spitzer*-IRS, and [O I] emission by *Herschel*/PACS. We compared these observations with stationary shock models calculated using the the Paris-Durham code. We analysed eleven regions of 1″ radius in a 20″×20″ region centered on the

shock position around the so-called SiO-knot. The best-fitting shock models were identified by comparing a grid of models with H_2 excitation diagrams and atomic oxygen fluxes at 63.2 μm and 145.5 μm, extracted over these eleven regions. Finally, a comparison is made between the column densities of the observed species (CS, SO, CH_3OH and o-H_2CO) and the models.

Results. We detected four rotational transitions with ALMA: SO (8_7–7_6), CS (7–6), CH_3OH (7_1–6_1 A^-) and o-H_2CO ($5_{1,5}$–$4_{1,4}$) toward the SiO knot in the BHR71 outflow. Their integrated intensity maps display a similar overall shape. Moreover, with the unprecedented spatial and spectral resolution of ALMA, we identify a northern region dominated by larger radial velocities and a southern region dominated by lower radial velocities. When comparing the H_2 emission to shock models, this emission at each of the eleven regions are reproduced by a J-type shock. The best-fit model parameters are a pre-shock density of 10^5 cm^{-3}, a shock velocity of 20 km s^{-1}, and a transverse magnetic field scaling parameter b of 0.1. These shock conditions also match the [O I] emission at 63.2μm and 145.5μm. The models allowed us to constrain the column density of atomic S in the gas phase. We found that the column densities of CS, SO, H_2CO and CH_3OH generated in shock models are up to 4 orders of magnitude below the observed values. This indicates that the abundance of these species probably comes from previous shocks in this region.

key words. Astrochemistry, star: formation, ISM: jets and outflows, ISM: individual objects: BHR71, Submillimeter: ISM

6.1 INTRODUCTION

The process of outflow is sometimes associated with ejection in the form of bipolar jets. These jets carve cavities in the surrounding interstellar medium (ISM) (e.g., Bally and Lada, 1983; B. T. Draine and McKee, 1993; Frank *et al.*, 2014; Bally, 2016), and the jets may extend to parsec-scales from the accreting central protostar (Dougados *et al.*, 2000; Bally *et al.*, 2007; Arce *et al.*, 2007). When the ejected material interacts with the surrounding medium, it generates shock waves. In these waves, the ambient gas is compressed, accelerated and heated, giving rise to unique physical and chemical conditions in the ISM. However, understanding these conditions is far from trivial and thus observations at high angular resolution as well as of diverse molecular species and transitions are required to understand the driving physical and chemical mechanisms at play.

Bipolar outflows have been the subject of extensive chemical studies over the years (Bachiller, 2006). In such environments, the composition of the ambient medium is modified by (a) processing of grains (e.g., sputtering, Suutarinen *et al.*, 2014); (b) high temperatures enhancing the gas-phase chemistry as the energy barriers of several reactions can be overcome (Bachiller *et al.*, 2001). These two types of chemical processes naturally depend on the shock characteristics and the conditions of the medium in which it propagates. In particular, the sulphur chemistry appears to be affected by the chemical processes occurring in shocks: the abundances of species such as SO, SO_2, and OCS appear enhanced in shocked regions (e.g., Oya *et al.*, 2016; Tabone *et al.*, 2017; Artur de la Villarmois *et al.*, 2019). The reason for this enhancement is unclear, but likely involves a combination of sputtering of ices and gas-phase processes, i.e., (a) and (b) above.

The physical shock structure (e.g., the density and temperature profiles) is intimately linked to the chemistry. For example, various species contribute to the gas cooling and the ionization state of the gas affects how the gas couples to the magnetic field (Flower and Pineau des Forêts, 1995) and one can not be fully understood without the other (Flower and Pineau des Forêts, 2013; Burkhardt *et al.*, 2019). Over the years, sophisticated tools have been developed to understand the physics and chemistry in outflows, such as the Paris-Durham shock model (Godard *et al.*, 2019), which provides detailed insights into the shock physical (e.g., temperature, velocities, energetics) and chemical (species abundances, dominant reactions) conditions. In this study, we selected a well-known shock region in the protostellar outflow system,

BHR71, to examine at high angular resolution the interplay between physics and chemistry.

The BHR71 outflow system, also known as DC 297.22-2.8 or Sa 136, is located at a distance of 200 pc (Henning and Launhardt, 1998) and is moving at a velocity of -4.5 km s^{-1} (Bourke *et al.*, 1997). Previous continuum observations of this isolated star forming region by Bourke *et al.* (1997) identified two protostellar sources: IRS1 (L=13.5 $L_\odot$) and IRS2 (L=0.5 $L_\odot$), separated by 3400 AU. This binary system was later confirmed by Tobin *et al.* (2019). A global view of the region can be shown in Figure 6.3.1. In particular the so-called 'SiO knot' position (Gusdorf *et al.*, 2011) and the field of view of our observations are shown.

Bourke *et al.* (1997) first discovered and mapped the BHR71 outflow in ^{12}CO (1–0) and ^{13}CO (1–0) emission. The outflow was subsequently mapped in H$_2$ emission, both from the ground (e.g., Giannini *et al.*, 2004) and space with the *Spitzer* Space Telescope (Neufeld *et al.*, 2006; Giannini *et al.*, 2011). These observations were compared to shock models, suggesting that the emission originated in Jump (J) type shocks with shock velocities of $\sim$ 30–50 km s^{-1} and a pre-shock density of 10^4 cm^{-3}. Gusdorf *et al.* (2011) identified a chemically rich region of the outflow from observations of SiO(5–4), (6–5) and (8–7), now referred to as the "SiO" knot. In Gusdorf *et al.* (2015), SiO, CO and H$_2$ observations over a large beam of 24$''$ were compared to shock models. The best-fit model was found to be a non-stationary continuous and jump (CJ)[1] shock with a pre-shock density of 10^4 cm^{-3}, a shock velocity of 22 km s^{-1} and a shock age of 3800 years. Benedettini *et al.* (2017) confirmed the findings from Gusdorf *et al.* (2015). They also suggested the presence of more than one shock structure, i.e., atomic shock structure, within the large beam due to discrepancies found between the [O I] emission and the model which successfully reproduced the H$_2$, CO and SiO emission.

In spite of all of these observations and modeling efforts, the "pure" shock position of the SiO knot has not been studied at arcsecond resolution in molecular line tracers other than H$_2$. Observations of a seemingly similar outflow position on the Northern hemisphere, L1157-B1, revealed that such resolution is required for properly disentangling the different physical (and chemical) components of an outflow shock (e.g., Codella *et al.*, 2020, and references therein). Thus, with this paper, we present high-angular-resolution observations ($\sim 1''$, or 200 AU at the distance of BHR71) of a number of molecular lines. These observations, together with archival H$_2$, [O I] and [S I], will be compared to model results from the Paris-Durham code with the goal of determining the physical conditions and chemical composition of the shock.

This article is structured as follows. Section 6.2 describes all the observational datasets used. In Section 6.3, the observational results are presented, both of the new ALMA observations and the archival data. Section 6.3.6 contains the data analysis. Section 6.4 is dedicated to the Paris-Durham shock model, in which the code is described and its outputs are compared to the observations. From the comparison between data and model predictions, the physical and chemical conditions within BHR71 are discussed, in Section 6.5. Furthermore, these results are compared to similar sources in this section. Finally, the key conclusions of this article are summarized in Section 6.6.

[1] This type of shock is characterised by a continuous deceleration of the charged fluid and a velocity jump of the neutral fluid.

6.2 OBSERVATIONS

This study combines several sets of observations of this region. ALMA 12m observations targeting sulphur-species and ALMA-ACA and APEX observations of CO 3–2 are combined with archival observations of *Spitzer* observations of H$_2$ and [S I] and *Herschel* observations of [O I].

6.2.1 *Sulphur bearing species observations: ALMA*

Observations were performed on the 4th and 7th of December 2019 with the ALMA as part of the project 2019.1.01282.S, targeting six sulphur species in Band 7 (i.e., at select frequencies in the range of 340–356 GHz). On both nights, the quasar J1107-4449 was used for bandpass and flux calibration, while the quasar J1147-6753 was used for complex gain calibration. The system temperature, T_{sys}, varied

TABLE 6.2.1: Line characteristics of the targeted and bonus species at the SiO-knot, above and below the dashed line respectively.

Species	Transition	E_{up} (K)	A_{ij} ($\times 10^{-4}$ s^{-1})	Freq. (GHz)	Detected[a]	n_c (100 K)[b] (cm^{-3})
SO	8_7-7_6	81	5.0	340.7142	Y	1.5×10^6
CS	7–6	66	8.4	342.8829	Y	2.6×10^6
HCS$^+$	8–7	74	8.4	341.3502	N	n.a.[c]
p-H$_2$CS	$10_{0,10}-9_{0,9}$	91	6.1	342.9464	N	n.a.[c]
SO$_2$	$14_{4,10}-14_{3,11}$	136	3.4	351.8739	N	n.a.[c]
OCS	29–28	254	1.3	352.5996	N	n.a.[c]
SO$_2$	$12_{4,8}-12_{3,9}$	111	3.4	355.0455	N	n.a.[c]
CH$_3$OH	7_1-6_1 A$^-$	80	1.7	341.4156	Y	1.7×10^6
o-H$_2$CO	$5_{1,5}-4_{1,4}$	63	12	351.7686	Y	2.0×10^6

[a] Detections are marked as Y and non-detections as N

[b] The critical density (n_c) is the density at which the collisional de-excitation has the same probability to occur as the radiative de-excitation and is defined as A_{ul} / C_{ul}. The spectroscopic data are taken from the Leiden Atomic and Molecular Database[2] (LAMDA, Schöier et al., 2005).

[c] n.a. stands for non applicable. Only the critical density of the detected species are listed here.

TABLE 6.2.2: Observational characteristics of the spectral windows.

SPW	δv (km s^{-1})	rms (mJy beam^{-1})	Lines
1	0.5	4.2	HCS$^+$ 8–7, CH$_3$OH 7_1-6_1 A$^-$
2	0.5	2.8	SO 8_7-7_6
3	0.5	3.7	H$_2$CS $10_{5,5}-9_{5,4}$, CS 7–6
4	0.5	7.7	SO$_2$ $14_{4,10}-14_{3,11}$, H$_2$CO $5_{1,5}-4_{1,4}$
5	0.5	4.7	OCS 29–28
6	0.5	6.9	SO$_2$ $12_{4,8}-12_{3,9}$

between 136 and 257 K. The observations were centered on the SiO-knot position (α: 12^{h}01^{m}33^{s}8, δ: −65°07′34′′ [J2000]) and a 7-point mosaic was performed covering a field-of-view of 20′′ (green rectangle in Figure 6.3.1) for an on-source integration time of 89 min. Such mosaic pointing was necessary to reach a uniform coverage and sensitivity over the entire extent of the SiO knot. The targeted species characteristics are shown in Table 6.2.1.

tabular

The data were reduced in the ALMA pipeline using the CASA[3] (Common Astronomy Software Applications, McMullin et al., 2007) software package, version 6.2. Spectral baseline correction was performed with the Gildas software[4] (Gildas Team, 2013, Grenoble Image and Line data Analysis Software). The spectra were resampled to 0.5 km s^{-1}, and a linear spectral baseline was subtracted from the dataset. The resulting beam size is 1′′×0.8′′, and the largest angular scale recovered is 15.82′′. The rms noise levels in 0.5 km s^{-1} channels are provided in Table 6.2.2.

6.2.2 *CO observations: ALMA and APEX*

We present observations carried out in Cycle 4 (project ID: 2016.1.00291.S) with the ALMA 7 m array using 11 of the 7 m antennas with maximum baselines of 45.0 m, on four different days (26th of November, 3rd, 4th and 6th of December, 2016 with respective on-source integration times of 16.9, 13.0, 16.9 and 16.9 minutes). These observations target CO (3–2), SiO (8–7), HCO$^+$ (4–3) and CH$_3$OH ($4_{1,4}$–$3_{0,3}$). We used a high-resolution wide-band setup in Band 7, with a 2 GHz effective bandwidth (from 344.79 to 346.79 GHz) with a spectral resolution of 0.48 MHz, that is 0.42 km s^{-1}. The primary beam at this frequency is 29′′7. The observed field (see Figure 6.3.1) was made from a mosaic of 33 pointings. This field-of-view is shown by the yellow rectangle in Figure 6.3.1. The system temperature, T_{sys}, varied between

113 and 198 K. The data were calibrated using standard procedures in CASA 4.7.2. A full bandwidth continuum was created using all scheduling blocks and all channels. Cleaning was done using the CLEAN algorithm. There was no noticeable continuum. Imaging was done for 200 channels with a spacing of 2 km s^{-1}. The synthesized beam varies between (4.''3–4.''7)×(3.''9–4.''0), with a position angle between –16 and –61.7°. The peak and rms on image were between 19.8–28.9 mJy beam^{-1} and 5.8–8.0 mJy beam^{-1} respectively. The expected sensitivity was between 0.5 and 0.9 mJy beam^{-1}. Descriptions of CO (3–2) observations conducted with APEX/FLASH instruments are detailed in Gusdorf *et al.* (2015).

Both datasets cover entirely the field-of-view of 20$^{''}$×20$^{''}$ observed with the 12-m array for the various S-species, as can be seen in panels b and c of Figure 6.3.1.

The GILDAS/MAPPING software was used to create the short-spacing visibilities (Pety and Rodríguez-Fernández, 2010) not sampled by the ALMA 7m array from the 12m single-dish APEX/FLASH instrument. These pseudo-visibilities were merged with the interferometric (alone) observations in the UV plane. Each mosaic field was then imaged and a dirty mosaic was built. The dirty image was deconvolved using the Högbom CLEAN algorithm.

6.2.3   *H_2 and [S I] observations: Spitzer/IRS*

To complement our ALMA data, we used the already published Cycle 4 *Spitzer*/IRS observations of the H_2 pure rotational transitions, 0–0 S(0) to 0–0 S(7), as well as [S I] $^3P_1$–$^3P_2$ at 25.2 μm toward BHR71 (Neufeld *et al.*, 2009). The observations are centered at α: 12^{h}01^{m}36^{s}3, δ: -65°08'53.''02 (J2000) and partially covers a region of ≈100$^{''}$×200$^{''}$. The map does not include the N-E structure of the shock (Δ(RA) ≈–10$^{''}$, Δ(dec) ≈+90$^{''}$ from the center of the observations), which is observed through the previous ALMA observations. This can been seen in panels b) and c) of Figure 6.3.1, where the white contours displaying the $H_2$0–0S(5) emission do not cover the entire field-of-view of the ALMA observations (top-right corner of the green rectangle). The data reduction is described in detail in Neufeld *et al.* (2009). The angular resolution varies between 3$^{''}$ and 10$^{''}$, depending on the wavelength of the transition.

6.2.4   *[O I] observations: Herschel/PACS*

For this study, the already published *Herschel*/PACS observations of the [O I] $^3P_1$–$^3P_2$ line at 63.2 μm, and the $^3P_0$–$^3P_1$ line at 145.5 μm, with a spatial resolution of 9$^{''}$ and 11$^{''}$, respectively, are used. The observations are centered at α: 12^{h}01^{m}35^{s}44 δ: -65°08'55.''97 (J2000), and cover a region of 33$^{''}$×33$^{''}$, centered on-source. Maps of a sample of outflows in these transitions were presented and studied by Nisini *et al.* (2015). The data were reduced with HIPE[5] v10.0. More details on the data calibration can be found in Nisini *et al.* (2015) and Benedettini *et al.* (2017).

6.3   RESULTS

Eight sulphur lines were targeted from six species (CS, SO, HCS$^+$, H_2CS, SO$_2$, and OCS; Table 6.2.1). Of these lines, two were detected, SO 8$_7$–7$_6$ and CS 7–6, while only upper limits were obtained for the others. In order to cover both the H_2CS and CS 7–6 lines on the same spectral band, the CS line was unfortunately placed so close to the edge that the full profile is not covered. Two additional lines were detected as a bonus, H_2CO 5$_{1,5}$–4$_{1,4}$ at 351.769 GHz and CH$_3$OH 7$_1$–6$_1$ A$^-$ at 341.416 GHz. The H_2CO transition was located at the edge of the spectral window, and so the line profile was not completely covered.

In the following, the morphology of the emission is examined through the use of integrated intensity maps. These are then combined with velocity-information from the spectral line profiles.
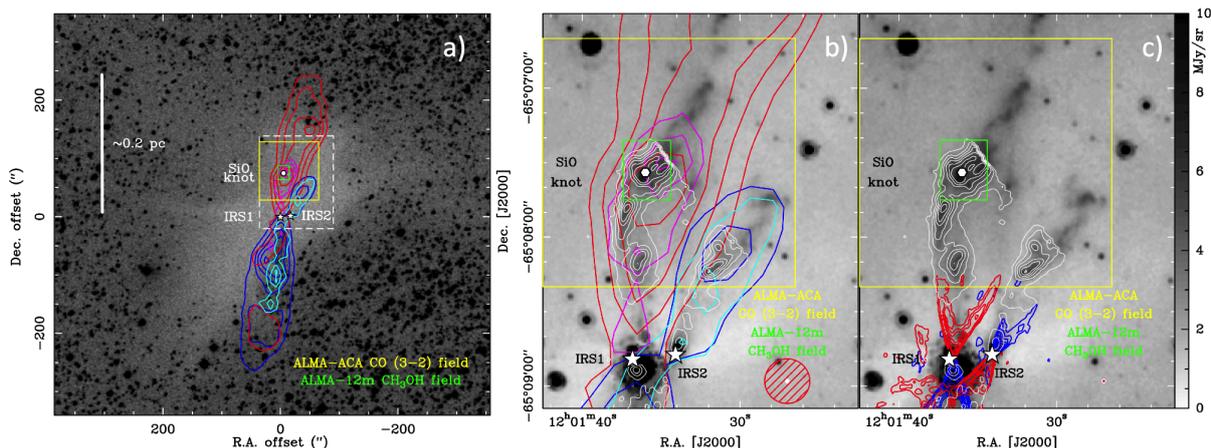
FIGURE 6.3.1: *a)* A view of the double outflow breaking out from its parental Bok globule in BHR71. The greyscale image is from the DSS2-red acquired with the UK Schmidt Telescope (©1993–1995 by the Anglo-Australian Telescope Board). The pink, red, blue and cyan contours show the CO (3–2) emission from the APEX-FLASH dataset presented in Gusdorf *et al.* (2015) integrated respectively in the velocity ranges [26;86]; [−4.5;26]; [−35;−4.5]; and [−95;−35] km s^{-1}, and shown from 20% to 100% of the maximum in steps of 20% (red and blue), and from 30% to 100% of the maximum in steps of 30% (pink and cyan). *b)* The same contours, overlaid on the *Spitzer*-IRAC map of the 8 μm emission (black and white) and the *Spitzer*-IRS white contours of the H$_2$ 0–0S(5) line emission (from 50% to 100% of the maximum in steps of 10%) described in Neufeld *et al.* (2009). The spatial resolution (∼18″) of APEX at the CO (3–2) frequency is shown with the hatched red circle in the lower right corner, while the pixel size of *Spitzer*-IRS is given by the white circle. *c)* The same *Spitzer* data as in *b)* overlaid with the red and blue contours of the CO (2–1) emission seen by ALMA at about 1″ resolution (indicative red circle shown in the lower right corner) and presented in Tobin *et al.* (2019), integrated over the [−4.5;20] and [−29;−4.5] km s^{-1} ranges, from 10% to 100% of the maximum in steps of 10%. On all panels: the position of the SiO knot highlighted by Gusdorf *et al.* (2011) is shown with a white hexagon; the positions of the IRS1 and IRS2 protostars driving the outflows are indicated with black and white stars, and the field of the data presented here are shown with a yellow and green rectangle.
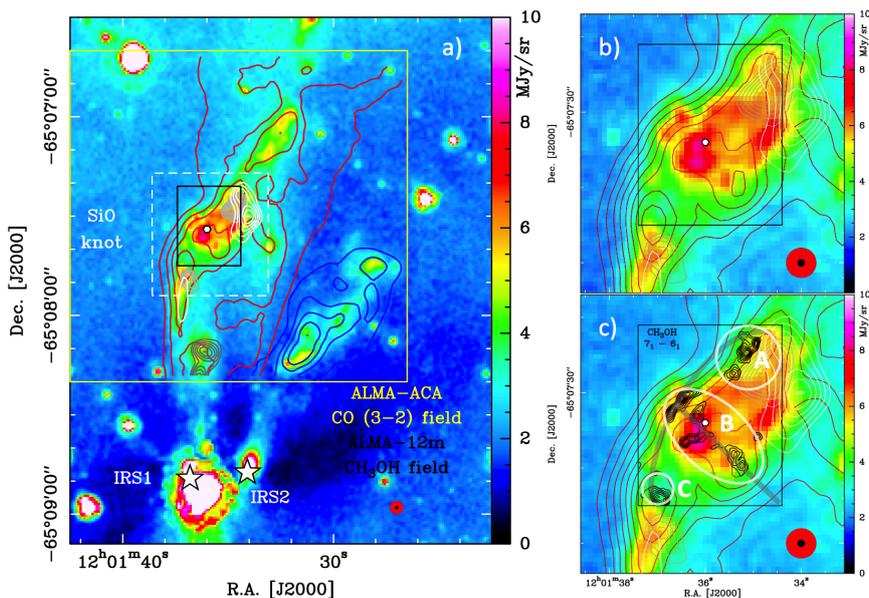

FIGURE 6.3.2: Zoom-in on the field indicated by the dashed white rectangle in Figure 6.3.1a and in the b and c panels of Figure 6.3.1. The background image is the *Spitzer*-IRAC map of the 8 μm emission, shown in colours. On all panels, the SiO knot position is indicated with a black and white hexagon, and a black rectangle indicates the field of the 12m-only ALMA observations of CH$_3$OH (but also H$_2$CO, CS and SO); the observing lobes of the ALMA-ACA CO(3–2) observations (∼ 4″) and that of the ALMA-12m only observations (∼ 1″) are shown in the lower right corner. *a)* The emission contours from our CO (3–2) ALMA-ACA dataset merged with our APEX dataset, integrated: in blue between −95 and −4.5 km s^{-1} and in red between −4.5 and +86 km s^{-1}, both shown from 20 to 100% of the maximum in steps of 20%; in dark grey, between +60 and +86 km s^{-1}, in light grey between +45 and +60 km s^{-1} and in white between +20 and +45 km s^{-1}, all shown from 50 to 100% of the maximum in steps of 10%. *b)* and *c)* Zoom-ins on the dashed white rectangle of panel *a)*, showing the same dataset, with the red contours in steps of 10% this time. In panel *c)*, the CH$_3$OH 7_1–6_1 line emission observed with the ALMA-12m only array is shown in black contours, integrated between −8 km s^{-1} to 10 km s^{-1}. We highlighted the bow/arrow structures in grey, and indicated the three regions we identified in the emission of the various species observed here: A, B, and C.

6.3.1 *Velocity structure of shocks around the SiO knot*

Our ALMA–ACA and APEX CO (3–2) observations allow us to study the structure of shocks in targeted region. Figure 1a shows the large-scale emission as observed by APEX. The spectral resolution offered by FLASH allows to disentangle not only the red and blueshifted lobes from the outflows powered by IRS1 and IRS2, but also the molecular jets that appear at higher velocities (26 to 86 km s^{-1} for redshifted lobes, −95 to −25 km s^{-1} for blueshifted ones). The curved shape of all of these jet lobes is a strong indication that precession might be taking place in both cases (e.g., Terquem *et al.*, 1999; Masciadri and Raga, 2002), as in the case of, e.g., the very similar L1157 outflow (Podio *et al.*, 2016).

Figures 6.3.2 and 6.3.3 show the ALMA–ACA data merged with our APEX observations, while Figure 6.F.7 shows the standalone ALMA–ACA observations. In these figures, the CO (3–2) emission is shown:

- over the whole extent of the velocity range where redshifted gas is significantly detected, from −4.5 to 86 km s^{-1} in red contours. This range is dominated by the outflow cavities and the internal shock structures;
- at the highest velocities from 60 to 86 km s^{-1} in dark grey contours, which reveals one bullet at the vertical of the IRS1 protostar in figures 6.3.2(a) and 6.F.7(a). This rather faint high-velocity bullet could be a trace of a molecular jet associated to the outflow driven by IRS1;
- at high (from 45 to 60 km s^{-1}) and moderate (from 20 to 45 km s^{-1}) velocities, in light grey and with contours, respectively. This component traces the cavity walls and the APEX of the SiO knot shock region.

Altogether these components suggest that a molecular, high-velocity jet is precessing within the cavity carved by the earlier bursts of ejection activity, and might interact with this cavity a the present epoch. The SiO knot seems to correspond to an episode of interaction between the jet and the cavity, given the presence of a distribution of almost all possible CO velocities in the targeted region (as can be seen in Figures 6.3.2 and 6.F.7). Overall, the SiO knot region seems to have been processed or even created by more than one shock structure.

6.3.2 *Comparison between the CO and CH$_3$OH emission*

Previous observations of the flow by, e.g., Gusdorf *et al.* (2015) illustrate the large-scale flow morphology toward BHR71 (400″×400″) at an angular resolution of 24″. This larger flow originates from the IRS1 source (Figure 6.3.1). Panels b) and c) from Figure 6.3.1 display a zoom-in of the studied region, with existing datasets of this region. In panel b) the *Spitzer*–IRAC map of the 8 μm emission, the H$_2$ 0–0S(5) emission from *Spitzer*–IRS and the APEX CO(3–2) emission are shown. While panel c) displays the same *Spitzer* data and the CO(2–1) emission from ALMA. Figure 6.3.2 provides an overview of the overall morphology of the outflow with CO (3–2) data at the highest available resolution for this region (blue and red contours, corresponding to different integration velocity windows). Panel b) displays a zoom of the region of interest (black rectangle), and the corresponding CO (3–2) emission as contours. Panel c) complements panel b) with the spatial extent of methanol emission integrated over the full line profile from −8 km s^{-1} to 10 km s^{-1} (see Sect. 6.3.4 below).

The CO 3–2 emission peaks around the location of the SiO knot (marked with a white hexagon), demonstrating that emission on 3–4″ (∼ 6–800 AU) scales show significant substructure. We compared then the CO emission with the emission of CH$_3$OH because methanol is an excellent shock tracer: methanol is sputtered of the grains in outflows and enters the gas phase (e.g., Suutarinen *et al.*, 2014). The methanol emission displays a crossbow shape from S-W to the N-E and from the center to the S-E (cf., Figure 6.3.2, panel c). One part peaks on the CO 3–2 peak, whereas the other methanol emission peaks surround the CO emission.

The methanol emission morphology is further explored by means of channel maps, shown in Appendix 6.A. These maps cover the entire velocity range from −8 km s^{-1} to 10 km s^{-1} in steps of 2 km s^{-1}. These channel maps allow us to differentiate the low- and high-velocity gas. In this case, we here define:

- The low (LV) velocity range from -8 km s^{-1} to -2 km s^{-1}
- The high (HV) velocity range from -2 km s^{-1} to 10 km s^{-1}

The bulk of emission is just redshifted of the source velocity of -4.5 km s^{-1}, from -4 to $+2$ km s^{-1}, i.e., in the LV gas. One clump of emission appears at higher velocities (~ 2 to 10 km s^{-1}, at position A0). Based on the global morphology of the integrated methanol emission, three regions are identified with respect to the SiO-knot: region (A) located to the north at $-7''$,$+10''$ from the SiO knot position. Region (B) encompasses the SiO-knot and has a radius of $\approx 5''$. Finally, region (C) is located in the south-west at $+5''$, $-10''$ from the SiO knot.

6.3.3 *Morphology of other emission*

We investigate the spatial distribution of the detected species with ALMA 12m (e.g., CS, SO CH$_3$OH and H$_2$CO) through integrated intensity maps over the full observed line profiles, from -8 km s^{-1} to 10 km s^{-1} for SO and CH$_3$OH. The H$_2$CO is at the edge of the spectral window, and thus only emission up to 4 km s^{-1} is recorded. Similarly for CS, where emission up to 10 km s^{-1} is recorded. Naturally this means that the integrated emission is a lower limit, but it is difficult to asses by how much. The integrated intensity maps are shown in Fig. 6.3.3, where emission is compared to both CO 3–2 and *Spitzer*-IRAC at 8 μm emission, as they both trace the shock propagation.

We observed a close match between both CO and H$_2$ signatures of the shock and our ALMA-12m observations, which have comparable angular resolution. Moreover, the CO maps allow us a better spectral coverage as they cover a wider range of velocities (up to 86 km s^{-1}) than the ALMA-12m dataset. From Figure 6.3.2, it can be seen that the ALMA-12m observations coincide only with the medium velocity range of the CO emission (cf. grey and white contours of Fig. 6.3.2, corresponding to 20–60 km s^{-1}.)

Eventually another missing point is that the detected line emission from the four transitions with ALMA-12m does not coincide with the highest velocity CO emission (in grey and white in contours in Figure 2 and 3 upper panels), but with the medium velocity CO emission. Interestingly, on the other hand, the molecules detected by ALMA all show up in the same regions, as can be seen in Figure 3 upper panels.

The four species are detected in the same region over the SiO knot (Figs. 6.3.2 and 6.3.3) and they locally peak in the three regions, A, B and C. However, their extent and peak locations (i.e., within 20% of their maximum) differ among the lines:

- CH$_3$OH and H$_2$CO have peaks toward all three regions.
- H$_2$CO displays the most extended spatial distribution of the four detected species.
- CS has peaks at regions (A) and (B) and tends to have a compact spatial extent, contrary to SO which has peaks at regions (B) and (C).

From these maps, we selected eleven regions for further analysis. These correspond to the peak locations of all the observed molecules, and are displayed in Fig. 6.3.3. These positions are categorized into three groups corresponding to the three regions discussed earlier: A, B and C, separated from each other by an offset of $\sim 10''$ in Dec. Each of the eleven regions has a radius of $1''$, i.e., approximately twice the resolution of $\sim 1''$ (FWHM). The locations of these regions are provided in Table 6.3.1, which also provides the integrated intensity of each species. The integrated intensity of each species for each region has been determined from the averaged integrated intensities of each pixel over a circle of $1''$radius. The number of pixels varies from 126 to 132, depending on the region.

TABLE 6.3.1: Characteristics of the regions of interest.

Region	α	δ	CH$_3$OH		o-H$_2$CO		CS		SO	
			$\int T_{MB}\,dv$[a]	rms[a,b,c]	$\int T_{MB}\,dv$[a]	rms[a,b,c]	$\int T_{MB}\,dv$[a]	rms[a,b,c]	$\int T_{MB}\,dv$[a]	rms[a,b,c]
A0	12^{h}01^{m}35^{s}142	−65°07′22.61″	1.1	0.7	4.1	1.9	13.5	7.6	1.7	1.2
A1	12^{h}01^{m}35^{s}132	−65°07′24.78″	2.6	1.2	19.9	6.5	4.5	2.8	4.0	2.0
A2	12^{h}01^{m}34^{s}934	−65°07′23.53″	1.9	1.2	10.5	5.5	2.9	1.9	2.7	1.4
B0	12^{h}01^{m}36^{s}288	−65°07′30.11″	1.4	0.8	11.1	3.4	8.6	5.6	7.4	3.3
B1	12^{h}01^{m}36^{s}476	−65°07′30.96″	2.8	1.3	24.2	8.3	9.0	4.8	4.6	2.2
B2	12^{h}01^{m}36^{s}737	−65°07′32.80″	2.0	1.1	14.4	4.3	8.9	4.5	7.3	3.0
B3	12^{h}01^{m}36^{s}174	−65°07′33.33″	1.9	0.6	21.4	3.6	6.1	2.0	8.3	2.5
B4	12^{h}01^{m}35^{s}892	−65°07′35.63″	1.8	0.8	12.8	4.1	9.2	3.8	2.4	1.3
B5	12^{h}01^{m}35^{s}236	−65°07′39.84″	1.6	0.5	18.2	4.9	6.3	2.4	1.4	0.4
B6	12^{h}01^{m}34^{s}642	−65°07′33.13″	0.1	0.2	3.7	2.0	3.7	1.5	5.6	1.8
C0	12^{h}01^{m}36^{s}997	−65°07′44.18″	2.8	0.9	24.8	4.4	9.0	2.5	10.0	2.6

[a] in units of K km s^{-1}.

[b] it corresponds to 3σ detection.

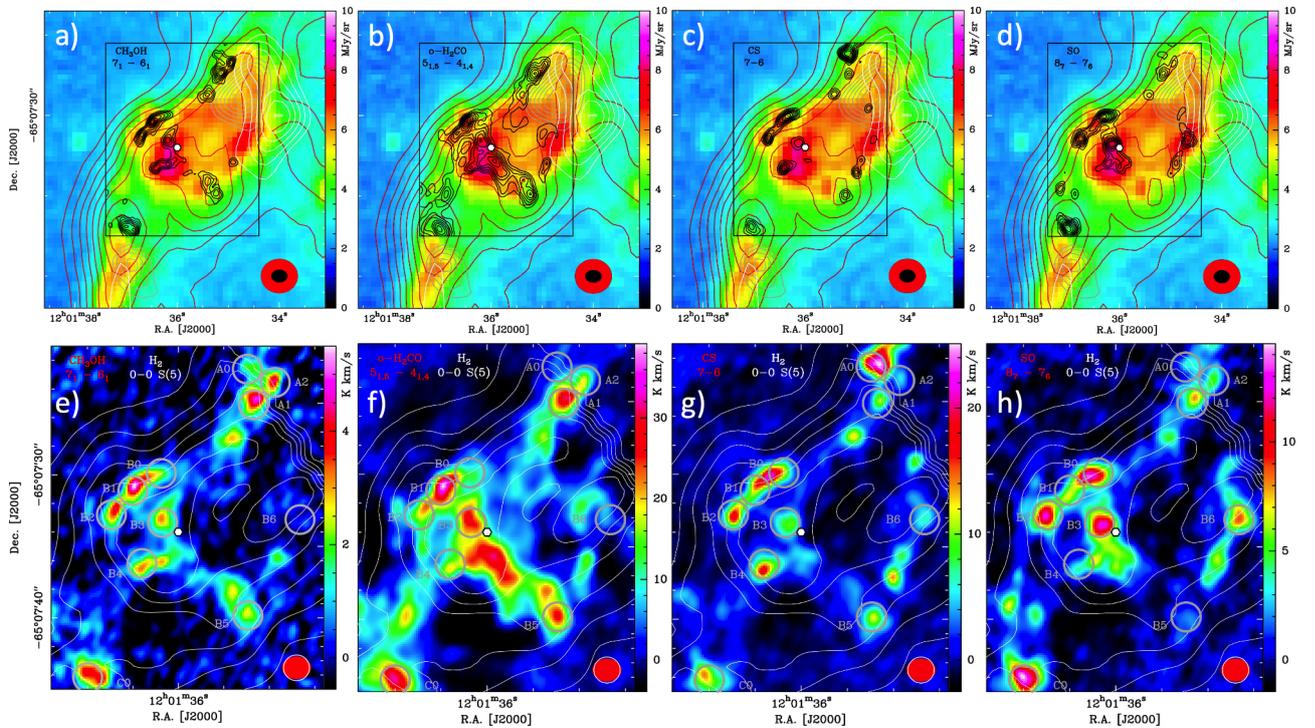[c] the rms was determined from the *mean* function in *GREG* Software of GILDAS.

FIGURE 6.3.3: *Upper panels:* zoom-ins on the same field with the same background (*Spitzer*-IRAC at 8 μm in colours, merged ALMA-ACA and APEX-FLASH CO (3–2) in contours), respectively showing the CH$_3$OH, o-H$_2$CO, CS and SO emission integrated between [−8,10] km s^{-1} for CH$_3$OH, [−10,4] km s^{-1} for H$_2$CO, [−8,10] km s^{-1} for CS and [−10,10] km s^{-1} for SO, in black contours between 20% and 100% of the maximum in steps of 10% (panels *a)*, *b)*, *c)*, and *d)*). The more precise beam of ALMA-ACA and ALMA-12m only is shown in the lower right corner (red and black ellipses). The black rectangle is the field of the ALMA-12m only observations. *Lower panels:* the color scale shows the zoom-ins on the ALMA-12m only observations displayed from −10% to the maximum of emission and integrated between [−8,10] km s^{-1} for CH$_3$OH, [−10,4] km s^{-1} for H$_2$CO, [−8,10] km s^{-1} for CS and [−10,10] km s^{-1} for SO (panels *e)*, *f)*, *g)*, *h)*). The data is overlaid on the same white contours of the H$_2$ 0–0 S(5) line emission seen by *Spitzer*-IRS shown in Figure 1b and 1c. The positions analysed here are reported on all these panels. In the lower right corner, a red ellipse shows the lobe of the ALMA-12m only observations, and a white circle shows the pixel size of *Spitzer*-IRS at this line's wavelength. On all panels, the SiO knot position is shown with a black and white hexagon.

6.3.4 *Molecular line spectra*

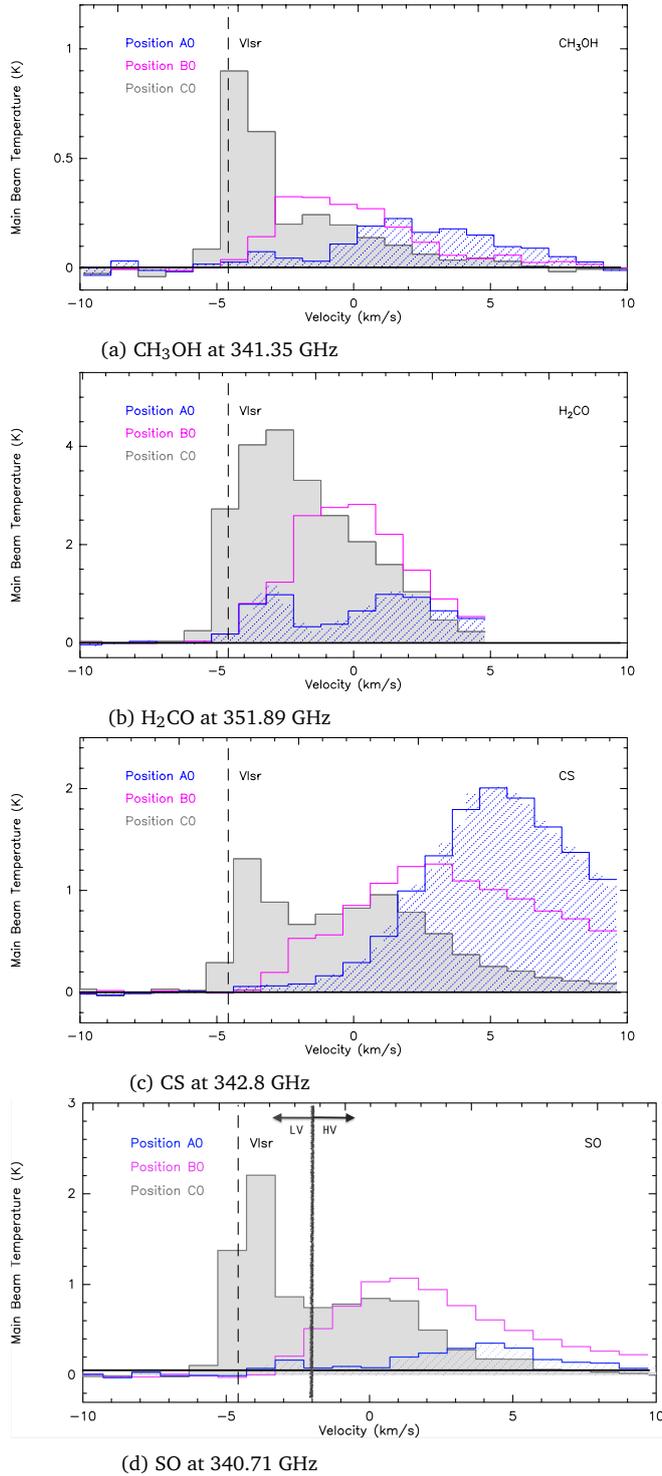For each region, we extracted spectra of the four observed species.

(a) CH_3OH at 341.35 GHz

(b) H_2CO at 351.89 GHz

(c) CS at 342.8 GHz

(d) SO at 340.71 GHz

FIGURE 6.3.4: Main beam temperature spectra in K of the molecules a-CH_3OH, o-H_2CO, CS and SO at the position A0 (blue dashed), B0 (magenta not filled) and C0 (grey filled), over the velocity range of -10 km s^{-1} to 10 km s^{-1}. For all the spectra a spectral resolution of 1 km s^{-1} was chosen for clarity. The BHR71 source velocity of 4.5 km s^{-1} is shown by the dashed vertical line. The H_2CO spectrum is truncated at 5 km s^{-1}, as this is the edge of the spectral window; the same for CS at 10 km s^{-1}. In panel (d), the LV and HV components are indicated with arrows.

Figure 6.3.4 shows these spectra at three positions: A0, B0 and C0; the spectra for the remaining positions are shown in Appendix 6.C.

Line emission is detected in all the three positions. All the spectra extracted at the A0 position show a higher velocity component with a peak at +3 km s^{-1} for CH$_3$OH and H$_2$CO and at 5 km s^{-1} for CS and SO. H$_2$CO is the outlier here as it shows double-peaked emission with a peak at both −3 km s^{-1} and +2 km s^{-1}. For the spectra at the B0 position, the profiles tend to peak at 0 km s^{-1} for CH$_3$OH, H$_2$CO and SO and at 3 km s^{-1} for CS. The spectra toward C0 show a double peak with one component peaking near the source velocity of −4.5 km s^{-1} and another peaking close to 0 km s^{-1} after. The emission is stronger toward the peak at the source velocity. It is clear that the three targeted regions have emission peaking at different velocities.

Both CH$_3$OH and H$_2$CO appear to have a similar full-half width maximum (FHWM) regardless of their position, varying from 4 km s^{-1} to 6 km s^{-1}, while the FHWM of CS is > 8 km s^{-1}. However, we note that this is a limit, as the full extent of the CS profile is not covered. SO, on the other hand, extends to velocities of +16 km s^{-1} at the most extreme, toward the B3 position (Appendix 6.C). Still, the bulk of the emission (∼ 90%) is at low velocities, < 10 km s^{-1}.

6.3.5 *Molecular column densities*

Based on the intensity maps of the ALMA observations, the upper level column densities, N_u, of each species can be estimated from the total integrated emission $\int T_{MB} dv$. In the case of non-detected species, the inferred column densities are the upper limits of these, based on the noise intensity (σ). Under the assumptions of a filling factor of 1 and the emission being optically thin, i.e., each emitted photon is assumed to escape the cloud, the upper level column densities are determined as follows:

$$\frac{N_u}{g_u} = \frac{8\pi k \nu^2}{hc^3} \frac{\int T_{MB} dv}{A_{ul} g_u} \tag{6.1}$$

where c the speed of light, and k is Boltzmann's constant. A_{ul} and g_u are the Einstein A coefficient and level degeneracy, respectively, and ν is the frequency. For further determining the column density, the assumption is that the level populations are primarily set by collisions, i.e., they are in local thermodynamic equilibrium (LTE). From the upper level column density, the total column density can be determined:

$$N_{tot} = \frac{N_u}{g_u} \frac{Q(T_{ex})}{e^{-E_u/(kT_{ex})}} \tag{6.2}$$

where E_u is the energy of the upper level, T_{ex} is the excitation temperature and Q is the partition function.

The spectroscopic parameters are taken from CDMS (Endres *et al.*, 2016). We verify each of the assumptions used in the following:

- A filling factor of 1 is assumed due to the homogeneity of the emission on 2″ scales.
- In the case of LTE, the density of the principal collider, n_{H_2}, is above the critical density of the observed species. We verify this assumption *a posteori* in Section 6.4.1.
- The RADEX tool, which is a non-LTE radiative transfer code (van der Tak *et al.*, 2007), was used to validate the optically thin assumption. Therefore, we determined the column density for each species under which the assumption is valid, namely for column densities lower than ∼8×10^{14} cm^{-2} for CS, ∼5×10^{15} cm^{-2} for SO, ∼1×10^{16} cm^{-2} for CH$_3$OH and ∼3×10^{14} cm^{-2} for H$_2$CO, for an H$_2$ density of 10^6 cm^{-3}, and FWHM of 8 km s^{-1} for CS and of 6 km s^{-1} for SO, H$_2$CO and CH$_3$OH.

As only one line per species was observed, the exact excitation temperature is undetermined. Therefore, the variation of derived total column densities was investigated over a temperature range of 50 K–250 K (Fig. 6.3.5). This was performed for intensities obtained from the three regions, A, B and C (Fig. 6.3.2). The total column densities are derived from the integrated emission, $\int T_{MB} dv$, shown in Table 6.3.1. In Figure 6.3.5, the maximum integrated value per region (i.e., A, B and

C) is shown, while in Figure 6.F.9 of Appendix F, all the subregional variations are displayed. It is clear from Figure 6.3.5 that the total column density varies little over the three regions, by a factor between 2 and 6[6]. In the subsequent analysis, three rotational temperatures of 75 K, 150 K and 225 K are used for inferring the column densities from the ALMA observations, as they are typical for a shock region. The range of temperatures leads to a N_{tot} variation in the order of 20% for SO and CH_3OH, and of 50% for CS and H_2CO. We determined a column density of ~2–6×10^{13} cm^{-2} for CS, ~1–6×10^{14} cm^{-2} for SO, ~0.6–2×10^{14} cm^{-2} for CH_3OH and ~0.3–2×10^{14} cm^{-2} for H_2CO.

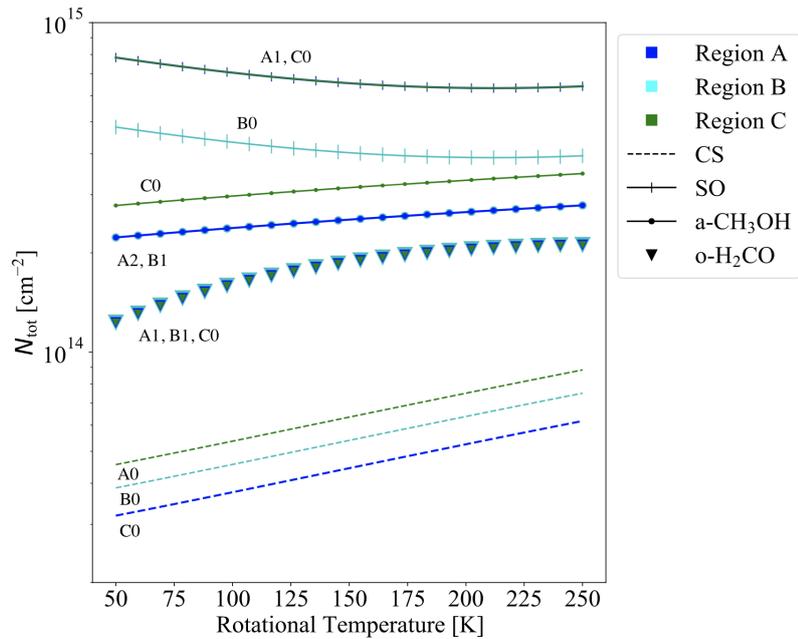[6]based on the fully detected lines only.

FIGURE 6.3.5: Column density of all the detected lines over temperature range of 50–250 K. The total column densities are derived from Equations (6.1) and (6.2) over a temperature range of 50 K-250 K and using the maximum intensity peak per region corresponding to A1, B1, C0 regions for H_2CO, A2, B1, C0 regions for CH_3OH, A1, B0, C0 regions for SO and A0, B0, C0 regions for CS. The o-H_2CO emission has the same maximum in the three regions of interest. Consequently, the three regions share the same plot. The same trend occurs for SO at regions A and B.

The column densities inferred for CS and H_2CO are lower limits: their lines are placed at the edge of the spectral window, and the full line profile was not covered. The peak of emission appears to be covered for all positions, however, and we thus estimate that at most we are missing 50–70% of the emission for CS, and likely much less for H_2CO. Furthermore, spatial filtering by the interferometer is not included in the calculation of the column densities. The largest angular scale recovered is 15.82″. Given the clumpy nature of the outflow, we do not expect that significant amounts of emission are filtered out, but without single-dish observations it is not possible to demonstrate this quantitatively.

Four additional transitions of sulphur-bearing species were targeted: HCS^+, H_2CS, SO_2, and OCS. However, none of them were detected. We infer upper limits on their column densities in the same manner as for the actual detections; i.e., we use excitation temperatures of 75, 150 and 225 K. Similarly, we assume optically thin emission with level populations in LTE. The upper limits of the emission for each species is 5.3×10^{-3} K, 8.6×10^{-3} K, 8.3×10^{-3} K and 6.8×10^{-3} K, for HCS+, H_2CS, OCS and SO_2, respectively. From these noise levels, a column density of ~2–3×10^{10} cm^{-2} for HCS^+, ~3–9×10^{12} cm^{-2} for OCS, ~1–2×10^{13} cm^{-2} for SO_2 and ~6–7×10^{11} cm^{-2} for p-H_2CS were found, for temperatures of 75, 150 and 225 K, considering 3σ detection. The entire set of inferred column densities are later discussed and shown in Section 4.4.

6.3.6   *Complementary data results and analysis*

Through this study, we aim at comparing our ALMA observations, specifically the observed molecular column densities, to shock models. Such comparison potentially provides insights on the chemical conditions in this outflow region. It was previously shown by Benedettini *et al.* (2017) and Gusdorf *et al.* (2011) that both atomic and molecular species are strong tools for constraining the shock processes with the Paris-Durham shock code. Therefore, the selection of the models appropriately describing the shock is made based on additional sets of observations of H_2, [O I] and [S I].

H_2 is the most abundant molecule in dense clouds and thus in the gas into which the jet propagates. It is a key species allowing us to constrain the shock conditions. Complementary observations of [O I] provide insights on the structure of the shock, as the oxygen-bearing molecules are efficiently dissociated by strong shocks. Finally, comparison with [S I] emission is made for constraining the initial abundance of the atomic sulphur and its proportionality in the gas phase and on the grains.

For the later comparison of the observations with the models, we used the column densities of H_2 through rotational diagrams and the integrated intensities of [O I] and [S I].

H_2 observations

The *Spitzer*/IRS observations of the H_2 pure rotational transitions, already analysed by Neufeld *et al.* (2009) and Gusdorf *et al.* (2015), are used. The integrated intensities of all the H_2 transitions were extracted at the eleven regions, A0 to C0 (Fig. 6.3.3). Regions A0 and A2 are located on the edge of the *Spitzer* map, and certain transitions of H_2 are thus not covered. Moreover, all the H_2 transitions do not have the same resolution, varying between 3″ and 10″ (Neufeld *et al.*, 2006). Therefore, to exclude that small variations in the size of the studied regions greatly affect the extracted intensity, we extracted the H_2 integrated intensity at the eleven studied regions, and varied the size of the observed regions using a radius of 1″, 2″ and 4″. The H_2 integrated intensities from the different aperture sizes were then compared. We found an H_2 integrated intensity variation of at most ~30% and 40% for region A, and ~5% and 10% for regions B and C, when comparing 1″ to 2″ radius and 1″ to 4″ radius, respectively.

Similarly to the case for the molecular emission observed with ALMA and under the same assumptions, for each studied region, the upper-level column density of each H_2 transition was determined using Eq. (6.1). A relative uncertainty of ±15% was applied to the integrated intensity, which is the standard calibration uncertainty for near/mid infrared instruments. A visual extinction, A_v, of 2, characteristic of the BHR71 region (Giannini *et al.*, 2004), was applied to the observed integrated intensity as follows:

$$I_0 = I_\lambda \times 10^{A_\lambda/2.5} \tag{6.3}$$

where, I_0 and I_λ are the corrected and observed integrated intensities, respectively. A_λ corresponds to the extinction at the wavelength λ, which is derived from a linear extrapolation of the A_λ/A_v ratio provided by Rieke and Lebofsky (1985) and B. Draine and Lee (1984). The analysis assumes optically thin emission, which typically is the case for H_2 emission (e.g., Maret *et al.*, 2009). The results are displayed in Fig. 6.4.1 in the form of rotational diagrams, where $\ln(N_u/g_u)$ versus E_u/k_B is shown.

All the locations show similar distribution of $\ln(N/g)$ vs E_{up} (top panel). For the sake of clarity, the regions are shown in batches of two to four, displayed in the middle and bottom panels. These rotational diagrams show a positive curvature, suggesting that the gas traces more than one temperature. For this reason, we do not attempt to infer a global excitation temperature or column density. Moreover, the goal is to use these data for comparison with shock models. The para-level populations are offset downward from their ortho-counterparts, which is indicative of an ortho/para-ratio deviating from the high-temperature ($\gtrsim$ 300 K) equilibrium value of 3. We do not explore the implications further here, but list the inferred ortho/para-ratio values in Appendix 6.E.

TABLE 6.3.2: Fluxes in units of erg cm^{-2} s^{-1} sr^{-1}, of H$_2$, [O I] and [S I] lines.[a]

Region	H$_2$									[O I]		[S I]
	S(0)	S(1)	S(2)	S(2)	S(3)	S(4)	S(5)	S(6)	S(7)	63.2μm	145.5μm	25μm
	$\times10^{-6}$	$\times10^{-5}$	$\times10^{-5}$	$\times10^{-5}$	$\times10^{-4}$	$\times10^{-4}$	$\times10^{-4}$	$\times10^{-4}$	$\times10^{-4}$	$\times10^{-4}$	$\times10^{-6}$	$\times10^{-5}$
A0	n.a.[b]	3.1 ($\pm$0.5)	5.3($\pm$0.8)	2.6($\pm$0.4)	0.9($\pm$0.1)	0.7($\pm$0.1)	1.2($\pm$0.2)	0.3($\pm$0.1)	0.8($\pm$0.1)	1.2($\pm$0.2)	7.5($\pm$1.1)	1.0($\pm$0.2)
A1	2.6($\pm$0.4)	3.3($\pm$0.5)	5.4($\pm$0.8)	4.8($\pm$0.7)	2.1($\pm$0.3)	1.5($\pm$0.2)	3.2($\pm$0.5)	0.8($\pm$0.1)	1.7($\pm$0.3)	1.4($\pm$0.2)	8.7($\pm$1.3)	1.2($\pm$0.2)
A2	n.a.[b]	3.7($\pm$0.6)	6.1($\pm$0.9)	n.a.[b]	n.a.[b]	n.a.[b]	n.a.[b]	n.a.[b]	n.a.[b]	1.2($\pm$0.2)	7.8($\pm$1.2)	1.0($\pm$0.2)
B0	5.3($\pm$0.8)	3.0($\pm$0.4)	6.8($\pm$1.0)	7.2($\pm$1.1)	2.4($\pm$0.4)	1.9($\pm$0.3)	3.7($\pm$0.6)	1.1($\pm$0.2)	2.5($\pm$0.4)	1.7($\pm$0.3)	9.1($\pm$1.4)	1.6($\pm$0.2)
B1	5.1($\pm$0.8)	3.4($\pm$0.5)	7.3($\pm$1.1)	7.6($\pm$1.1)	2.3($\pm$0.3)	2.0($\pm$0.3)	3.8($\pm$0.6)	1.1($\pm$0.2)	2.6($\pm$0.4)	1.7($\pm$0.3)	8.6($\pm$1.3)	1.5($\pm$0.2)
B2	4.7($\pm$0.7)	3.5($\pm$0.5)	7.3($\pm$1.1)	7.0($\pm$1.0)	2.2($\pm$0.3)	1.8($\pm$0.3)	3.8($\pm$0.6)	1.1($\pm$0.2)	2.5($\pm$0.4)	1.6($\pm$0.2)	7.9($\pm$1.2)	1.5($\pm$0.2)
B3	5.4($\pm$0.8)	4.8($\pm$0.7)	9.6($\pm$1.4)	8.5($\pm$1.3)	3.3($\pm$0.5)	2.7($\pm$0.4)	5.6($\pm$0.8)	1.6($\pm$0.2)	3.9($\pm$0.6)	1.8($\pm$0.3)	9.3($\pm$1.4)	1.7($\pm$0.3)
B4	4.5($\pm$0.7)	5.0($\pm$0.8)	7.8($\pm$1.2)	7.9($\pm$1.2)	3.5($\pm$0.5)	2.3($\pm$0.3)	5.0($\pm$0.8)	1.6($\pm$0.2)	4.2($\pm$0.6)	1.7($\pm$0.3)	8.5($\pm$1.3)	1.6($\pm$0.2)
B5	2.8($\pm$0.4)	3.3($\pm$0.5)	5.0($\pm$0.8)	3.1($\pm$0.5)	1.6($\pm$0.2)	1.0($\pm$0.2)	2.4($\pm$0.4)	0.5($\pm$0.1)	1.5($\pm$0.2)	1.4($\pm$0.2)	7.7($\pm$1.2)	1.3($\pm$0.2)
B6	3.9($\pm$0.6)	4.2($\pm$0.6)	6.7($\pm$1.0)	5.2($\pm$0.8)	2.8($\pm$0.4)	1.8($\pm$0.3)	3.9($\pm$0.6)	1.2($\pm$0.2)	2.7($\pm$0.4)	1.5($\pm$0.2)	8.6($\pm$1.3)	1.4($\pm$0.2)
C0	1.8($\pm$0.3)	3.1($\pm$0.5)	4.9($\pm$0.7)	4.1($\pm$0.6)	1.4($\pm$0.2)	1.4($\pm$0.2)	2.5($\pm$0.4)	0.8($\pm$0.1)	1.7($\pm$0.3)	1.1($\pm$0.2)	5.2($\pm$0.8)	0.8($\pm$0.1)

[a] Fluxes extracted at the eleven studied regions, of a size of 1″ radius (cf. Table 6.3.1 for the coordinates of the region).

[b] n.a. stands for non applicable. The fluxes can be non available for a specific region if they lay outside the observational window.

[O I] and [S I] observations

We use the atomic oxygen observations from *Herschel* of the [O I] $^3P_1$–$^3P_2$ line at 63.2 μm, and the [O I] $^3P_0$–$^3P_1$ line at 145.5 μm. These observations have spatial resolutions of 9″ and 11″, respectively. The integrated intensities of both transitions have been extracted at eleven positions of interest (i.e., A0 to C0). The values do not show variations among all the different regions, i.e., within the same order of magnitude, for both transitions.

We also used the *Spitzer* observations of the [S I] $^3P_1$–$^3P_2$ line at 25.2 μm, and performed the same methodology for extracting [S I] fluxes as done for [O I]. As observed for [O I] fluxes, small [S I] flux variations are detected among the different regions studied, i.e., fluxes within 0.8–1.7×10^{-5} erg cm^{-2} s^{-1} sr^{-1}. The fluxes are reported in Table 6.3.2.

6.4 COMPARISON TO SHOCK MODELS

In the following, observations are compared to shock models from the Paris-Durham shock code[7] (Flower and Pineau des Forêts, 2013; Godard *et al.*, 2019). This numerical tool simulates a 1D plane-parallel shock wave, and solves for the physical conditions in the shock region (e.g., temperature, density) in parallel with the chemical conditions (e.g., molecular abundances, H$_2$ level population). For this work, the grid of shock models presented in Flower and Pineau des Forêts (2013) is used. The grid consists of C-type and J-type shocks with pre-shock densities of 10^4, 10^5, and 10^6 cm^{-3}. Shock velocities are in the range of 10–40 km s^{-1}, and finally the value of the scaling factor of the transverse magnetic field strength is $b = 0.1$ or $b = 1.0$ for J- and C-type shocks, respectively. We note here that this factor is such that $B(\mu G) = b\sqrt{n_H \text{ cm}^{-3}}$. For this work, only stationary shock waves are considered.

6.4.1 *Model comparison to H$_2$ excitation diagrams*

H$_2$ emission is perhaps the most widely used tracer for physical conditions in shocks (e.g., Wilgenbus *et al.*, 2000; Kristensen *et al.*, 2007; Nisini, 2008; Maret *et al.*, 2009; Neufeld *et al.*, 2009). The levels are readily excited in the warm/hot gas ($T > 500$ K), and the lines are typically bright. The H$_2$ excitation conditions depend on a combination of shock parameters, of which the pre-shock density, the shock velocity, and the strength of the transverse magnetic field are the most important.

We here seek to reproduce the observed rotational diagrams. This is done by looking for trends, rather than trying to obtain *the* best-fit model. We computed a small grid of models and performed a χ^2 analysis for comparing the observations to the models (i.e., the rotation diagrams, Fig. 6.4.1).

TABLE 6.4.1: Best-fit analysis: corresponding model and value from χ^2 analysis.

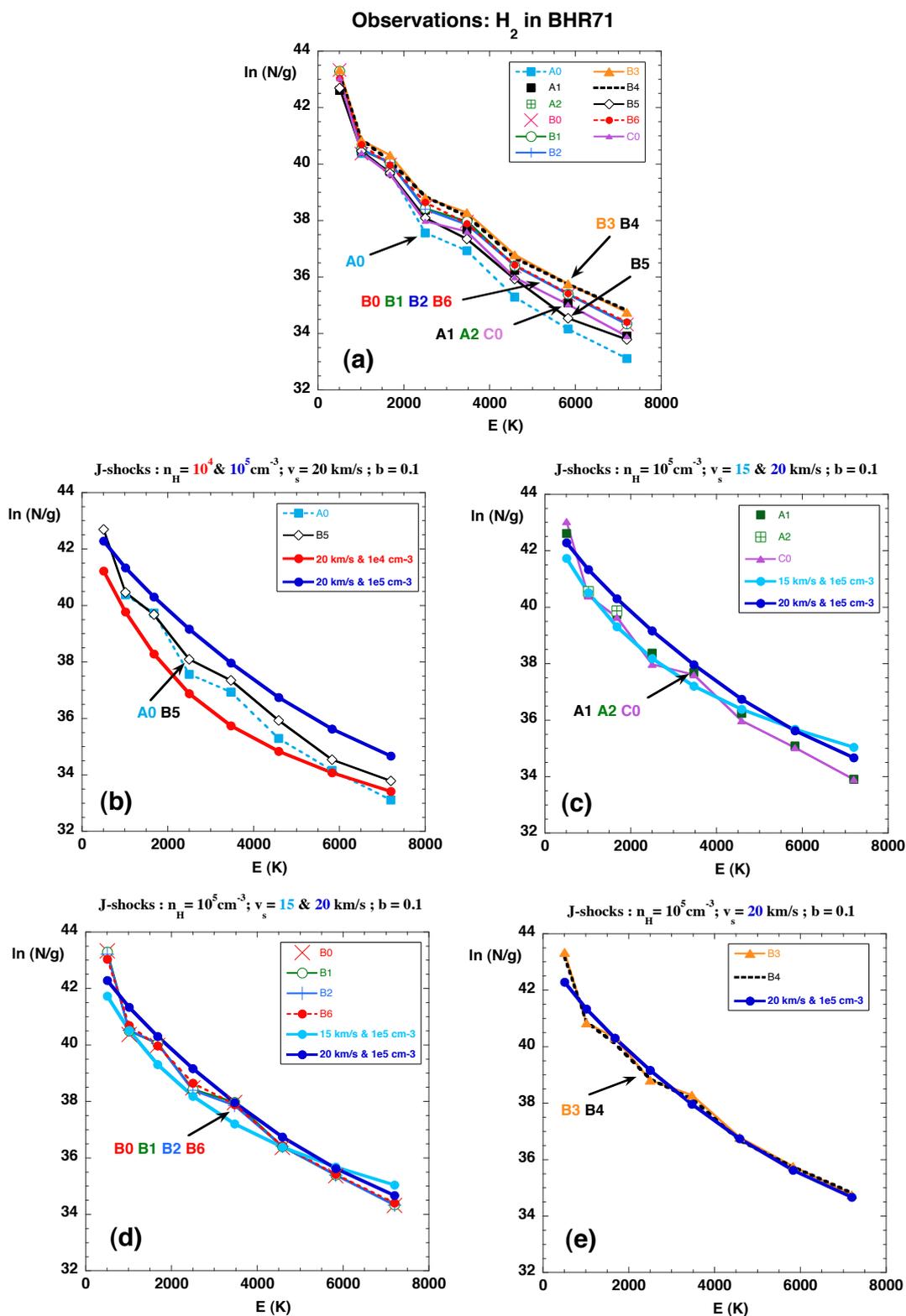| Region	Model		χ^2
	n_H(cm^{-3})	v_{shock} (km s^{-1})	
A0	10^5	20	0.22
A1	10^5	20	0.19
A2	10^4	15	0.68
B0	10^5	20	0.15
B1	10^5	20	0.15
B2	10^5	20	0.15
B3	10^5	20	0.11
B4	10^5	20	0.11
B5	10^5	20	0.23
B6	10^5	20	0.15
C0	10^5	20	0.20

FIGURE 6.4.1: H$_2$ excitation diagrams of (a) Observations: the ten of the eleven targeted regions (Fig. 6.3.3) derived from the *Spitzer*/IRS observations for transitions 0–0 S(0) to 0–0 S(7). These plots include error bars of ∼ 15% on the integrated intensity, but these error bars are smaller than the symbol size. (b), (c), (d) and (e) Best-fit model results as done by eye.

The χ^2 analysis consisted of determining the statistical difference between the ln(N/g) models and observations. A summary of the minimum χ^2 per region and the corresponding model can be found in Table 6.4.1.

In Figure 6.4.1, the best fits for eleven regions are shown; these are also tabulated in Table 6.4.1. Several results appear:

1. The rotational diagrams are best described by J-type shocks, which have a weak transverse magnetic field ($b = 0.1$);

2. Only models with a pre-shock density of 10^4 and 10^5 cm^{-3} reproduce the observations, with n_H of 10^5 cm^{-3} dominating toward the eleven regions;

3. The best-fit models have velocities between 15 and 20 km s^{-1}.

6.4.2 *Atomic oxygen*

The extracted integrated emission from the [O I] ^{3}P$_1$–^{3}P$_2$ (at 145.5 μm) and ^{3}P$_0$–^{3}P$_1$ (at 63.2 μm) fine-structure transitions at the eleven regions of interest were compared to the models found from the H$_2$ comparison. We note here that the shock models from Flower and Pineau des Forêts (2013) include the latest collisional rate coefficients between O and H (Abrahamsson *et al.*, 2007).

The comparison between the observations and the different models is shown in Fig. 6.4.2. This comparison corroborates the results obtained for H$_2$: the observations are best reproduced by pre-shock density of 10^5 cm^{-3} and a velocity of 20 km s^{-1} (and also by a shock with a pre-shock density of 10^4 cm^{-3} and a velocity of 25 km s^{-1}).
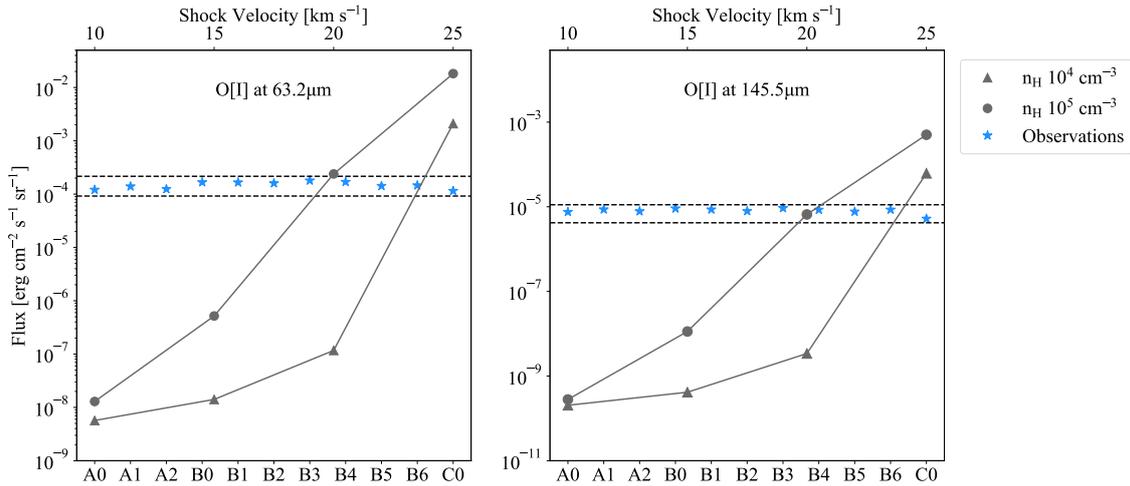

FIGURE 6.4.2: Observed and modelled integrated intensities from [O I] lines on the left at 63.2 μm and on the right at 145.5 μm. The fluxes are from shock models with pre-shock density (n_H) of 10^4 cm^{-3} (triangles) and 10^5 cm^{-3} (circles). The top x-axis describes the different shock velocities. The *Herschel* fluxes are extracted over a 1″radius, at the eleven targeted regions (Fig.6.3.3). The bottom x-axis represents all the extracted positions. The horizontal dashed lines show the observational range with a margin of 20% above the maximum value and below the minimum value.

6.4.3 *Atomic sulphur*

As can be seen from Figure 6.4.3, the best-fit models from the comparison to H$_2$ emission typically overpredict the emission. The exception is for a low velocity of 15 km s^{-1} and a low density (10^4 cm^{-3}): all other models predict emission that is higher than the observed one by a factor of ~ 5 or more. Particularly, the model that best reproduces the [O I] emission (20 km s^{-1} and 10^5 cm^{-3}) overestimates the observed [S I] emission by more than two orders of magnitude. Moreover, the observed [S I] emission is optically thin, in which case the observed intensity scales

with the column density of atomic sulphur. The modeled column densities and intensities are provided in Table 6.4.2.

TABLE 6.4.2: Atomic sulphur intensity and column density w.r.t to the best-fit models.

Model		[S I]	
n_H	v_{lsr}	Intensity	N_S
$[cm^{-3}]$	$[km\ s^{-1}]$	$[erg\ cm^{-2}\ s^{-1}\ sr^{-1}]$	$[cm^{-2}]$
10^4	15	3×10^{-5}	2×10^{15}
10^4	20	1×10^{-4}	2×10^{15}
10^5	15	8×10^{-4}	4×10^{15}
10^5	20	7×10^{-3}	7×10^{15}

In the shock models presented here, the initial abundance of atomic bearing species is assumed to be split between 80% in the gas phase, and 20% on grain mantles out of a total elemental abundance of 1.86×10^{-5} (Flower and Pineau des Forêts, 2003, Table 1). Moreover, in the absence of an external UV field, atomic sulfur is by far the most abundant sulfur species (Hily-Blant *et al.*, 2021). For matching the observations, i.e., [S I] intensity of 10^{-5} erg cm^{-2} s^{-1} sr^{-1}, the initial amount of sulphur in the gas phase taken in the models should be strongly depleted. In the case of a J-type shock velocity of 20 km s^{-1} and pre-shock density of 10^{-5} cm^3, we should have only 0.1% of the sulfur in the gas phase (8% for the model $n_H=10^{-4}$ cm^{-3}, $v_s=20$ km s^{-1}). This strong depletion of atomic sulphur in the gas phase might also be due to the presence of ionizing radiation (Anderson *et al.*, 2013).
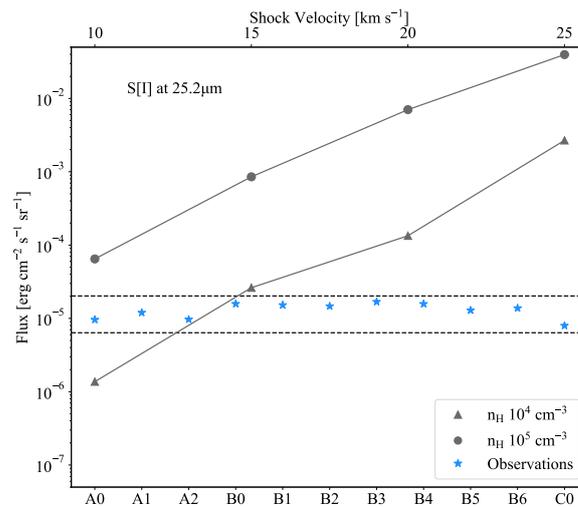

FIGURE 6.4.3: Sulphur flux from shock models with pre-shock density (n_H) of 10^4 cm^{-3} (triangles) and 10^5 cm^{-3} (octagons). The top x-axis describes the different shock velocities. The observational data are from *Spitzer*/IRS, and extracted over a 1″radius at the eleven regions (Fig. 6.3.3). The bottom x-axis represents all the extracted positions. The horizontal dashed lines show the observational range with a margin of 20% above the maximum value and below the minimum value.

6.4.4 *Molecular column densities*

The final step is to compare the predictions of the shock models to the molecular (CS, SO, CH$_3$OH, and H$_2$CO) column densities. The column densities are integrated from the local densities, calculated at each point of the shock layer, until the gas temperature reaches 15 K in the post-shock gas. This is done to ensure that only the column density relevant for the shock is compared to the observed column densities. Otherwise molecules will remain in the gas phase until they freeze out on the grains. The model column densities are reported in Table 6.5.1.

In Figure 6.5.1, the observed column densities of the detected (CS, SO, CH$_3$OH and H$_2$CO) species are displayed for three excitation temperatures (75, 150 and 225 K). These are compared to the column densities calculated in the best-fit shock models. We also included the column densities from the best-fit shock model from Gusdorf *et al.* (2015). Our inferred column densities of CS and CH$_3$OH are in agreement with the ones from Garay *et al.* (1998): N(CS)$\sim$10^{13} cm^{-2}, N(CH$_3$OH)$\sim$10^{14} cm^{-2}, although their observing positions with an offset of (0,2) and (-1,2) in arcminutes from α: 12^{h}01^{m}37^s, δ: $-$65°08′53″5 [J2000], are not perfectly matching our field of observations, but are spatially close.

For the comparison between observed and modeled column densities, we are, as for the case of H$_2$, not tuning the models to provide an exact match to observations; instead we examine general trends. The comparison between the observed column densities and the model densities reveal that only the CS column density is successfully reproduced by the models. The SO column density is underestimated by 2–3 orders of magnitude, which is also the case for CH$_3$OH. H$_2$CO is underestimated by 4–5 orders of magnitude. Thus, although we are looking at general trends, there clearly is not a good match between observations and models. From Figure 6.5.1, the following could be pointed out:

- The main reservoir of H$_2$CO and CH$_3$OH in J-type shocks is in the ice. There is no significant sputtering of the ices in such shocks (e.g., Suutarinen *et al.*, 2014), and the species therefore remain in the ice. The absence of sputtering is further discussed in Section 6.5.2. To examine the total column density in the shocks of these two species, the total column density is shown in Fig. 6.5.1; these are also tabulated in Table 6.5.1. As for the CJ-type shock models from Gusdorf *et al.* (2015), the CH$_3$OH and H$_2$CO column densities are now overproduced.

- The only reservoirs of CS and SO are in the gas phase, i.e., these are formed in the gas phase (Pineau des Forêts *et al.*, 1993). Therefore these species are not directly affected by the grains physical processes (e.g., sputtering, etc.).

6.5 DISCUSSION

6.5.1 *Physical conditions*

The models that best reproduce the observed H$_2$ line emission are stationary *J*-type shocks. The shock parameters are in the range of 10^4–10^5 cm^{-3} for the density, and a velocity range of 15–20 km s^{-1} with a low transverse magnetic field strength scaling parameter: b=0.1, corresponding to 10–30 μG, which are typical values for globules[8] (Myers *et al.*, 2020).

The fact that all the surveyed locations are best reproduced by the same set of shock parameters is unexpected, as the locations show different velocity structures in the ALMA spectra and in the maps shown (cf. Figures 6.3.2 and 6.3.3). For example, the spectra obtained toward the A regions show more HV gas, region B is a mixture of HV and LV gas, whereas region C is dominated by LV gas (Fig. 6.3.2, particularly panel c). However, we are viewing the projection of a three-dimensional shock structure, likely with differing radial velocities across the field. When projected onto the sky, some variation in the observed radial velocities are expected, even if they are tracing the same set of shock parameters.

It should be noted, that we are not exploring a full grid of models in order to obtain the best possible solution, but rather focus on which ranges of input parameters reproduce observations within the lobe. The observational constraints do not change much from one position to the other, which clearly explains the narrow range of model solutions. Any differences that we see between different regions should therefore be taken as trends.

[8]the studied outflow is spectrally differentiable from its parental Bok globule (cf. Figure 6.3.1) as pointed out by Corporon and Reipurth (1997)

TABLE 6.5.1: Total column density inferred from observations, extracted at the peak positions of regions A0, B0 and C0, and models.

| Region | $T_{\rm rot}$ (K) | $N_{\rm tot}$ [cm^{-2}] | | | | | | | |
		CS[a]	SO	CH$_3$OH	H$_2$CO[a,c]	HCS^{+}[b]	OCS[b]	SO$_2$[b]	p-H$_2$CS[b]
A	75	3×10^{13}	1×10^{14}	6×10^{13}	3×10^{13}	$< 2\times10^{11}$	$< 9\times10^{12}$	$< 2\times10^{13}$	$< 7\times10^{11}$
	150	4×10^{13}	1×10^{14}	6×10^{13}	3×10^{13}	$< 2\times10^{11}$	$< 3\times10^{12}$	$< 1\times10^{13}$	$< 6\times10^{11}$
	225	6×10^{13}	1×10^{14}	7×10^{13}	4×10^{13}	$< 3\times10^{11}$	$< 3\times10^{12}$	$< 1\times10^{13}$	$< 6\times10^{11}$
B	75	2×10^{13}	4×10^{14}	6×10^{13}	7×10^{13}	$< 2\times10^{11}$	$< 9\times10^{12}$	$< 2\times10^{13}$	$< 7\times10^{11}$
	150	3×10^{13}	4×10^{14}	6×10^{13}	1×10^{14}	$< 2\times10^{11}$	$< 3\times10^{12}$	$< 1\times10^{13}$	$< 6\times10^{11}$
	225	4×10^{13}	3×10^{14}	7×10^{13}	1×10^{14}	$< 3\times10^{11}$	$< 3\times10^{12}$	$< 1\times10^{13}$	$< 6\times10^{11}$
C	75	2×10^{13}	6×10^{14}	2×10^{14}	2×10^{14}	$< 2\times10^{11}$	$< 9\times10^{12}$	$< 2\times10^{13}$	$< 7\times10^{11}$
	150	3×10^{13}	5×10^{14}	2×10^{14}	2×10^{14}	$< 2\times10^{11}$	$< 3\times10^{12}$	$< 1\times10^{13}$	$< 6\times10^{11}$
	225	4×10^{13}	5×10^{14}	2×10^{14}	2×10^{14}	$< 3\times10^{11}$	$< 3\times10^{12}$	$< 1\times10^{13}$	$< 6\times10^{11}$
	Models[e]								
$n_{\rm H}$ (cm^{-3})	$v_{\rm shock}$ (km s^{-1})								
10^4	15	2×10^{13}	4×10^{12}	1×10^{11}	7×10^{9}	2×10^{10}	4×10^{8}	2×10^{11}	-
10^4	20	2×10^{13}	4×10^{11}	5×10^{11}	6×10^{9}	8×10^{10}	3×10^{8}	3×10^{9}	-
10^5	15	2×10^{13}	1×10^{12}	6×10^{11}	5×10^{9}	1×10^{10}	4×10^{8}	3×10^{9}	-
10^5	20	5×10^{13}	4×10^{12}	3×10^{13}	4×10^{10}	6×10^{10}	1×10^{9}	8×10^{11}	-
	CJ Model	3×10^{14}	4×10^{14}	3×10^{16}	9×10^{15}	7×10^{11}	2×10^{14}	5×10^{14}	-

[a] Line profile located at the edge of the band; the column density is a lower limit.

[b] $<3\sigma$ detection.

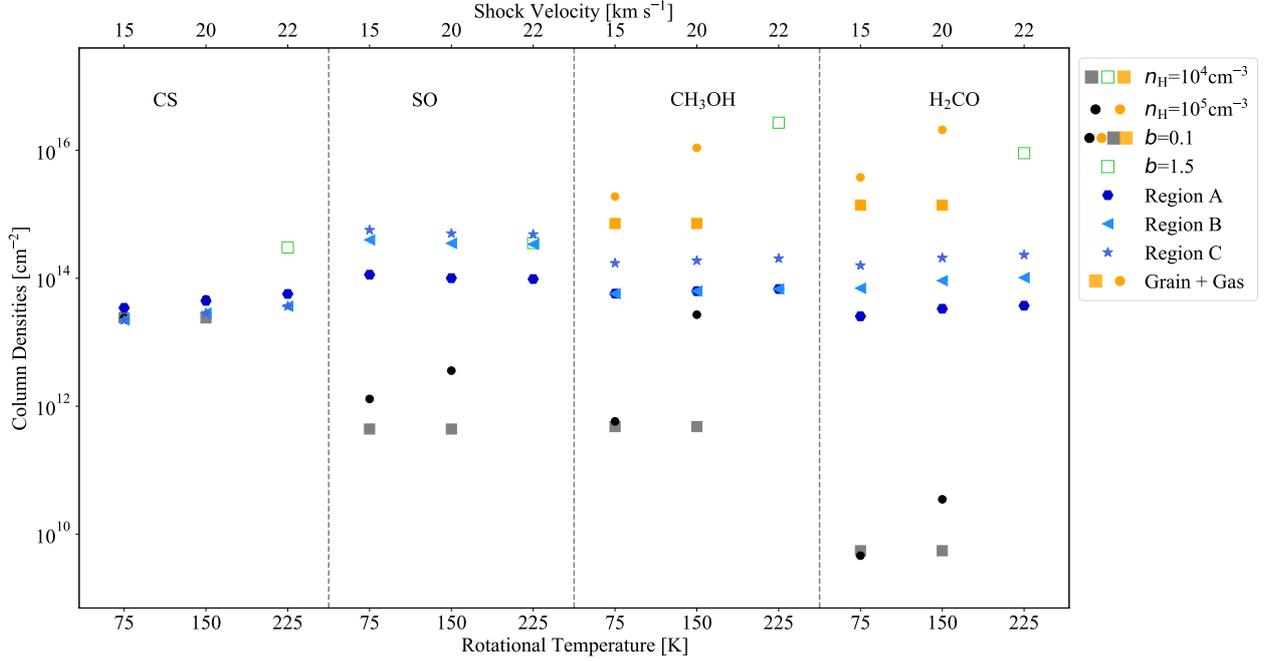[c] An ortho-to-para ratio of 3 was considered.

FIGURE 6.5.1: Inferred column densities from the observations of CS, SO, CH$_3$OH, and H$_2$CO, in blue tones. These species are categorized into Regions A, B and C which correspond to sub-regions A0, B0 and C0. Each column density is derived for three rotational temperature, 75 K, 150 K and 225 K. The column densities from the best-fit shock models are overlaid in grey and green tones. The top axis represent the shock velocities of 15, 20 and 22 km s^{-1}. The other characteristics of the shock model such as the pre-shock density and parameter b, are shown with the rectangle/circle shapes and empty/filled shapes, respectively. The sum of the column densities of a species in the gas phase and on ice is shown in orange.

The inferred shock conditions are fairly typical for this type of region, when limiting the scope to stationary shocks (e.g., Maret *et al.*, 2009), as also discussed in detail in Gusdorf *et al.* (2015). Gusdorf *et al.* (2015) used non-stationary shock models to model the H_2 emission but over a much larger spatial scale encompassing all the shocked regions observed here (24″ versus the 1″ resolution here). For these larger scales they found that the emission was best reproduced with a CJ-type non-stationary shock model, where the shock velocity was 22 km s^{-1}, the pre-shock density was 10^4 cm^{-3}, the magnetic scaling factor was $b = 1.5$, and the inferred age was 3800 years. The main difference with respect to the results presented here, is the presence of a partly magnetized part of the shock, existing for a specific amount of time (3800 years). Gusdorf *et al.* (2015) focused solely on the fitting of the molecular emission (H_2 pure rotational lines, CO, and SiO) and thus the primary difference is with respect to the observations.

6.5.2 *Chemical conditions*

In a first step, the observed molecular column densities (Sect. 6.4.4) are compared to the column densities extracted from the models. The model column densities are extracted over the full width of the shock, i.e., where the temperature exceeds 15 K. The observed and model column densities are reported in Table 6.5.1; this Table includes the column densities obtained in the same shock models which Gusdorf *et al.* (2015) concluded was the best fit. They are illustrated in Fig. 6.5.1. Of the detected species, the observed column densities all exceed the model densities; for the most extreme cases (SO and CH$_3$OH) by up to five orders of magnitude. The non-stationary shock model from Gusdorf *et al.* (2015), on the other hand, matches the observed column densities of CS and SO but overestimates the ones of H_2CO and CH$_3$OH. Clearly the models fail to successfully reproduce simultaneously the observed column densities, suggesting that something is missing or incomplete in the assumptions going into the modeling efforts.

H_2CO and CH$_3$OH

One of the key lines detected at the different shock positions is methanol, CH$_3$OH. This molecule forms predominantly on the surfaces of icy grains, and it is liberated into the gas phase through sputtering (e.g., Suutarinen *et al.*, 2014). Sputtering mainly occurs in C-type shocks, where the velocity differential between the charged grains and the neutral gas is the cause of sputtering (Flower and Pineau des Forêts, 1995). The weak magnetic field inferred from the models (10–30 μG) is not strong enough to decouple the charged and neutral fluids. The question naturally arises: where does the methanol then come from?

As remarked by Gusdorf *et al.* (2015), the region has likely been exposed to previous shock events, as is also evident from Fig. 6.3.1. If any of these are caused by C-type shocks with sufficient velocity, then they may have sputtered CH$_3$OH into the gas phase. As these shocks were in the past, they will no longer be present in the observed beam, and therefore not be observed with H_2 and atomic oxygen, with the current analysis. However, some sputtered molecules might still be in the gas phase, and not freeze back out onto the grains. The freeze-out time can be estimated from the following expression (e.g., Schmalzl *et al.*, 2014):

$$t_{\mathrm{fr}} = 10^6 \text{ yr} \left(\frac{m_{\mathrm{mol}}}{32 m_{\mathrm{H}}} \right)^{0.5} \left(\frac{T_{\mathrm{gas}}}{100 \text{ K}} \right)^{-0.5} \left(\frac{n_{\mathrm{H}}}{10^4 \text{ cm}^{-3}} \right)^{-1}, \qquad (6.4)$$

where t_{fr} is the freeze-out time, m_{mol} is the mass of the molecule, T_{gas} is the gas temperature, and n_{H} the density. Even for the highest density inferred from the shock conditions, 10^5 cm^{-3}, the freeze-out time-scale is orders of magnitude higher than the dynamical time of the shock, i.e., $\sim 10^3$–10^4 years. Thus, if molecules have been sputtered into the gas phase, they remain in the gas phase.

These two effects, that the region may have been exposed to shocks previously and has not had time to fully chemically reset, provide strong clues as to what is occurring chemically in this region. In the J-type shock models, as mentioned above, there is no sputtering: everything that is on the grains before the shock stays on the

grains. If we now take the full column densities, i.e., add together the gas and ice components, we artificially account for what would have been sputtered in a previous shock event. These column densities are illustrated in Fig. 6.5.1. The qualitative agreement between observations and models is now significantly improved, with models overpredicting the observed column densities. This suggests that it is not necessary to sputter all the ices off the grains. We emphasize again, the purpose in not to match the observations one to one, but rather look at broad trends.

We verified that the observed molecular trend shown in Figure 6.5.1 is observed for all the eleven studied regions. The detected molecular column densities toward the different positions, i.e., upper limits not included, vary by up to an order of magnitude (cf. Appendix 6.F). This is unlike the shock conditions, as traced by H_2 emission, which appear similar toward all positions. H_2 traces the warm or hot gas ($T >$ a few 100 K), and the cooling time of this gas is of the order of years to a few tens of years (Flower and Pineau des Forêts, 2013). Thus, the H_2 emission traces the currently shocked gas. The chemistry, on the other hand, reflects past shock events in this scenario, and the chemical variations in the post-shock gas from any previous event must therefore be present on the scales observed here, i.e., scales of a few arcsec or up to ~ 500 AU. In other words, the H_2 emission traces current activity, whereas the molecular species contain a record of past shock events.

Another possibility is that the shocks are preceded by weak magnetic precursors. These precursors would have to be weak enough not to cause a significant change in the H_2 intensities, but strong enough that they lead to effective sputtering. This combination is unlikely to exist: for shock velocities $\gtrsim 10$ km s^{-1}, which is what is needed for grain mantle sputtering (Suutarinen *et al.*, 2014), the H_2 become significant (Kristensen *et al.*, 2007). Thus, this scenario is unlikely to occur, and it is most likely that the region has been exposed to a previous shock which has (partially) sputtered the ices off the grains.

S-bearing species

The S-bearing species of our observations consist of the detected CS and SO, as well as upper limits of HCS$^+$, OCS, SO$_2$ and H$_2$CS. Depending on the studied molecule, several conclusions were drawn:

- The shock models tend to reproduce the CS column density. CS is expected to predominantly form in the gas phase and remains there during the passage of the shock wave, so its column density should not be significantly affected by the current shock nor the previous ones (Garay *et al.*, 1998).
- The column densities on the upper limits are also still matched.
- One species still stands out, however: SO. Clearly the poor match (2–3 orders of magnitude below the observed) implies that something is unaccounted for in the models. Unlike the case of H$_2$CO and CH$_3$OH, SO ice is not included in the models, and thus the same explanation for the mismatch between observations and models cannot be used here.

Above (Sect. 6.4.3), we matched the observed intensity of atomic S to the models. In the models, atomic S is assumed to be either in the gas phase or on the grains, and on the grains it is effectively turned into H$_2$S ice. Chemical models suggest that other S-bearing species also form on the grains in a cold environment (i.e., protostellar envelope), including SO but excluding CS, which means that ice-H$_2$S should be treated as a reservoir of S-bearing ices (Vidal *et al.*, 2017). These frozen-out molecules will then be liberated through the same processes which liberate CH$_3$OH into the gas phase.

Furthermore, we demonstrated in Sect. 6.4.3 that for the best-fit models (densities of 10^4 and 10^5 cm^{-3}, velocities of 15 and 20 km s^{-1}, but the higher densities and velocities favored by the [O I] emission), the [S I] emission was overestimated. In that Section, we referred to the remaining atomic S as ice-S, but this reservoir will naturally either freeze out and be converted to other species (H$_2$S), or react with other species in the warm shocked gas. Either way, if it cannot be in atomic form, it must be in molecular form.

The shock models predict that ice-H$_2$S has a column density of $\sim 10^{15}$ cm^{-2} for pre-shock densities of 10^4 cm^{-3}, and column densities of 8–60 $\times 10^{15}$ cm^{-2} for pre-shock densities of 10^5 cm^{-3}, both for velocities of 15 and 20 km s^{-1}. For

comparison, the maximum SO column density is $\sim 7 \times 10^{14}$ cm^{-2}. Thus, if a fraction of the icy H$_2$S is converted into SO on the grain, this would account for the observed SO column density.

The conversion from H$_2$S to SO in the gas phase, used in the Paris-Durham shock models, is currently made through the radical SH (Millar and Williams, 1993) but also, from the OCS species, as follows:

$$H_2S \xrightarrow{H} SH \xrightarrow{H} S \xrightarrow{O_2} SO \qquad (6.5a)$$

$$H_2S \xrightarrow{H} SH \xrightarrow{O} SO \qquad (6.5b)$$

$$H_2S \xrightarrow{H, CO} OCS \xrightarrow{O} SO \qquad (6.5c)$$

The products, SH and OCS, from the reactivity of H$_2$S with other compounds, e.g., H, CO, were already found to be present on the icy dust grains (el Akel et al. 2021, in press,). Therefore, if the intermediary products from the reactivity from H$_2$S, namely OCS and SH, are desorbed from the dust grains, their further reactivity in the gas phase would likely form SO. This would suggest, as for CH$_3$OH and H$_2$CO, the presence of previous shock waves which have sputtered these molecules in the gas phase. In other words, if additional SO formation paths, considering the grain surface reactions, were added to the models, this would likely account for the observed SO column density in the gas phase.

6.5.3 *Comparison with other sources*

In order to put BHR71 into a broader context, we compared the observed column-density ratios to observations of shock regions in the lobe of other class 0 outflows:

- L1448, IRAS04166 are observations from Tafalla *et al.* (2010), with the 30m telescope at the S-wing position;
- HH114-MMS is observed with the 30m telescope by Tafalla and Hacar (2013);
- L1157-B1 combines observations 30m telescope from Holdship *et al.* (2019) and Plateau de Bure Interferometer, PdBI, observations from Fontani *et al.* (2014);
- NCG1333-IRAS2A combines observations from the Onsala Space Observatory 20 m telescope and the Caltech Submillimeter Observatory, carried by Jørgensen *et al.* (2004).

In Fig. 6.5.2, we compared the column densities of the detected four species (CS, SO, CH$_3$OH and H$_2$CO) toward these five sources with the ones toward the BHR71/SiO-knot position. The inferred column densities have been made from more than one observed line.

From this Figure, it is clear that:

- I04166 and L1448 display lower column densities of S-species and an underproduction of H$_2$CO. The observed low column density of CS compared to the other sources, suggests a poor sulphur environment, as this molecule is not altered by a shock. It is however not possible to conclude on the low column density of H$_2$CO for this source, as it displays a similar column density for CH$_3$OH, as the other sources.
- A difference of 1 up to 2 orders of magnitude higher is observed for the CH$_3$OH column density towards NGC1333-IRAS2A. A possible explanation is the absence of a UV-irradiation which would have efficiently converted CH$_3$OH into other species (e.g., OH, CH$_2$OH, CH$_3$, etc., Öberg *et al.*, 2009).

The molecular variations pointed towards these sources suggest the presence of different physical processes altering the chemistry occurring in these regions. However, this sources comparison pointed out that in the BHR71, L1157-B1 and HH114-MMS regions, the same chemistry is likely to occur, and these sources might be driven by similar physical conditions.

We finally consider the $N(SO)/N(SO_2)$ ratio towards all these outflow regions. A particular attention is given to this ratio as we found discrepancies with the amount of predicted SO by the models and the inferred amount from the observations, towards BHR71. Such comparison would allow us to identify, if any, discrepancies in the S-O species towards the different outflows, which might be caused by environmental
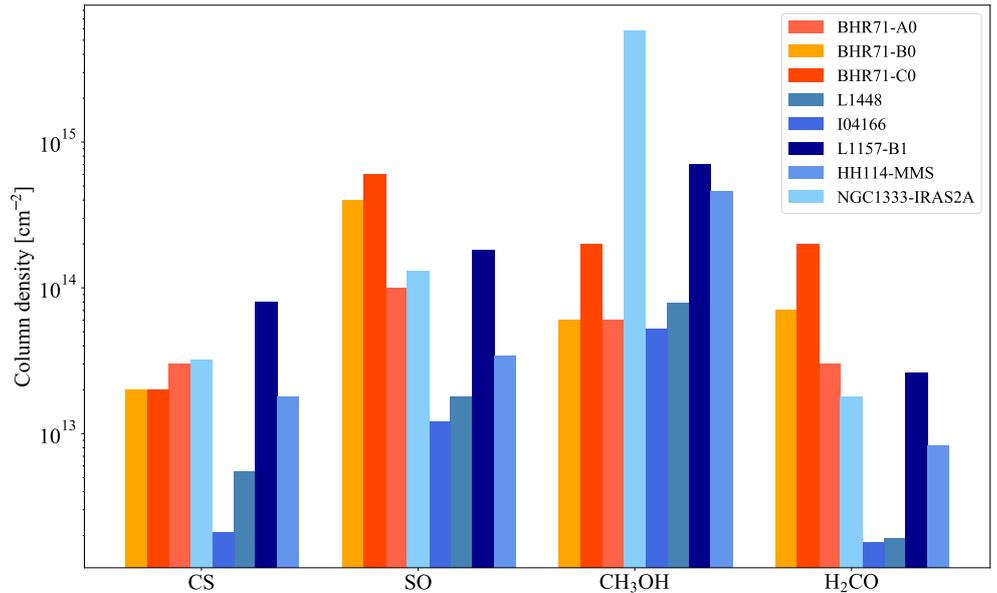
FIGURE 6.5.2: Column densities of CS, SO, CH$_3$OH and H$_2$CO inferred from observations of BHR71, L1157-B1 (Fontani *et al.*, 2014; Holdship *et al.*, 2019), L1448 and I04166 (Tafalla *et al.*, 2010), HH114-MMS (Tafalla and Hacar, 2013) and NGC1333-IRAS2A (Jørgensen *et al.*, 2004). The column densities of BHR71 are taken at position A0, B0 and C, as a point of comparison for a rotational temperature of 75 K (Table 6.5.1).

differences in these regions. Moreover, the principal formation route of SO is through atomic sulphur and oxygen but, is also via other species (cf., Section 6.5.2). While SO$_2$ is mainly formed from atomic oxygen and SO, in the gas phase. A discrepancy in the $N(\mathrm{SO})/N(\mathrm{SO_2})$ ratio might point out differences in the environmental conditions (e.g., less/higher oxidised environment, etc.) altering the S-O chemistry in the region.

We determined a $N(\mathrm{SO})/N(\mathrm{SO_2})$ ratio between 2 and 6 for the sources L1448, I04166 and L1157-B1. A SO$_2$ column density was not inferred towards HH114-MMS and NGC1333-IRAS2A but, from Taquet *et al.* (2020) observing the NGC1333 source at position IRAS4A, a $N(\mathrm{SO})/N(\mathrm{SO_2})$ of 2.5 was found. These values are in accordance with the ratio of 5 towards BHR71-A0, with a variation of a factor ~5 with respect to the other two positions (B0 and C0). However, we emphasize that the SO$_2$ column density is an upper limit towards BHR71, and consequently explains this uncertainty factor. The akin $N(\mathrm{SO})/N(\mathrm{SO_2})$ ratio indicates that the studied sources have similar oxidised environment, and the production of SO$_2$ is balanced with respect to the amount of SO in the gas phase. It, therefore, suggests that all these sources have a similar S-O chemistry in the gas phase, but differs in quantity (i.e., column density) based on the physical processes which have led to the SO production (e.g,. presence of a shock history).

6.6 CONCLUSION

In this article, we combined the observations of the chemically rich protostellar shock (the SiO knot) of BHR71 from ALMA, *Spitzer*/IRS, and *Herschel*. The shock region of BHR71 at the SiO-knot has been investigated at arcsecond resolution. We studied eleven sub-regions of 2″ diameter spread over a 20×20″ field centered at the SiO-knot position. The sub-regions selected correspond to the integrated intensity peaks of the detected species, CS, SO, CH$_3$OH and H$_2$CO of our ALMA-12m observations. The high-resolution data from these observations allowed us to analyse the molecular emission and also their spatial extent over the studied region.

We selected the best-fitting shock models from a large grid of models performed

with the Paris-Durham shock code, based on a comparison of the observed H_2 excitation diagrams, which have been extracted at the eleven studied regions. The eleven regions show similar H_2 excitation, i.e., the physical conditions at each shock position are similar. These are characterized by a J-type shock with a pre-shock density of 10^5 cm^{-3}, a shock velocity of 20 km s^{-1}, and a low magnetic field (b=0.1). These models also successfully reproduce the observed [O I] 63 and 154 μm emission observed by *Herschel*. The [S I] emission observed by *Spitzer*, on the other hand, is overestimated in the models. This suggests a lower abundance of atomic S in the gas-phase that what is currently in the models. Finally, the observed column densities, i.e., the detected species and the inferred upper limits, were compared to the models. Only by inferring a previous shock event, which sputtered molecular ices off the grains, can the observed the column densities of the non sulphur bearing species be explained. Given that this region has already experienced at least one shock event, this seems like a plausible scenario.

The observed SO column density is not well reproduced by the models. In the models, all atomic S that freezes out onto the grains are converted into H_2S, and we propose that if a small fraction of this H_2S is converted into SO, this could account for the observed SO column density. This scenario suggests that additional chemical reactions on the grains from H_2S are occurring. The production of SO is therefore from a mixture of grain and gas phase chemistry, rather that the production of SO from H_2S sole in the gas phase.

Finally, comparing the observed column densities for this source to others reveals that BHR71 displays a similar chemistry and physical conditions than in several other outflow regions, such as L1157-B1 and HH114-MMS. Moreover, a similar $N(SO)/N(S_2O)$ ratio is found towards all the studied sources. We found that they are likely to all have a similar oxidised environment and the S-O chemistry is driven by the physical processes enhancing the initial production of SO, such as the previous shock history.

ACKNOWLEDGEMENTS

Bibliography

1. E. Abrahamsson, R. Krems, A. Dalgarno, *ApJ* **654**, 1171–1174 (Jan. 2007).

2. D. E. Anderson *et al.*, *ApJ* **779**, 141 (Dec. 2013).

3. H. Arce *et al.*, presented at the Protostars and Planets V, ed. by B. Reipurth, D. Jewitt, K. Keil, p. 245, arXiv: `astro-ph/0603071 [astro-ph]`.

4. E. Artur de la Villarmois *et al.*, *A&A* **626**, A71, arXiv: `1904.13161 [astro-ph.SR]` (June 2019).

5. R. Bachiller *et al.*, *A&A* **372**, 899–912 (June 2001).

6. R. Bachiller, presented at the Complex Molecules in Space: Present Status and Prospects with ALMA, 11, p. 11.

7. J. Bally, C. Lada, *ApJ* **265**, 824–847 (Feb. 1983).

8. J. Bally, B. Reipurth, C. Davis, presented at the Protostars and Planets V, ed. by B. Reipurth, D. Jewitt, K. Keil, p. 215.

9. J. Bally, *Annual Review of Astronomy and Astrophysics* **54**, 491–528, eprint: `https://doi.org/10.1146/annurev-astro-081915-023341`, (`https://doi.org/10.1146/annurev-astro-081915-023341`) (2016).

10. M. Benedettini *et al.*, *A&A* **598**, A14, (`https://doi.org/10.1051/0004-6361/201629451`) (2017).

11. T. L. Bourke *et al.*, *ApJ* **476**, 781–800 (Feb. 1997).

12. A. M. Burkhardt *et al.*, **881**, 32, (`https://doi.org/10.3847/1538-4357/ab2be8`) (Aug. 2019).

13. C. Codella *et al.*, *A&A* **635**, A17, arXiv: `2001.00217 [astro-ph.SR]` (Mar. 2020).

14. P. Corporon, B. Reipurth, presented at the Herbig-Haro Flows and the Birth of Stars, ed. by B. Reipurth, C. Bertout, vol. 182, p. 85.

15. C. Dougados, C. Lavalley, S. Cabrit, presented at the Imaging the Universe in Three Dimensions, ed. by W. van Breugel, J. Bland-Hawthorn, vol. 195, p. 356.

16. B. Draine, H. Lee, *ApJ* **285**, 89 (Oct. 1984).

17. B. T. Draine, C. F. McKee, *ARA&A* **31**, 373–432 (Jan. 1993).

18. C. P. Endres *et al.*, *Journal of Molecular Spectroscopy* **327**, New Visions of Spectroscopic Databases, Volume II, 95–104, ISSN: 0022-2852, (`https://www.sciencedirect.com/science/article/pii/S0022285216300340`) (2016).

19. D. Flower, G. Pineau des Forêts, *MNRAS* **275**, 1049–1056 (Aug. 1995).

20. D. Flower, G. Pineau des Forêts, *Monthly Notices of the Royal Astronomical Society* **343**, 390–400, ISSN: 0035-8711, eprint: `https://academic.oup.com/mnras/article-pdf/343/2/390/18415803/343-2-390.pdf`, (`https://doi.org/10.1046/j.1365-8711.2003.06716.x`) (Aug. 2003).

21. D. Flower, G. Pineau des Forêts, *MNRAS* **436**, 2143–2150 (Dec. 2013).

22. F. Fontani *et al.*, *ApJ* **788**, L43 (June 2014).

23. A. Frank *et al.*, *Protostars and Planets VI*, (`http://dx.doi.org/10.2458/azu_uapress_9780816531240-ch020`) (2014).

24. G. Garay *et al.*, *The Astrophysical Journal* **509**, 768–784, (`https://doi.org/10.1086/306534`) (Dec. 1998).

25. T. Giannini *et al.*, *A&A* **419**, 999–1014, arXiv: `astro-ph/0402395 [astro-ph]` (June 2004).

26. T. Giannini *et al.*, *The Astrophysical Journal* **738**, 80, (`https://doi.org/10.1088/0004-637x/738/1/80`) (Aug. 2011).

27. Gildas Team, *GILDAS: Grenoble Image and Line Data Analysis Software*, May 2013, ascl: `1305.010`.

28. B. Godard *et al.*, *A&A* **622**, A100, arXiv: 1901.04273 [astro-ph.GA] (Feb. 2019).

29. A. Gusdorf *et al.*, *Astronomy Astrophysics* **532**, A53, ISSN: 1432-0746, (http://dx.doi.org/10.1051/0004-6361/201116758) (July 2011).

30. A. Gusdorf *et al.*, *A&A* **575**, A98, (https://doi.org/10.1051/0004-6361/201425142) (2015).

31. T. Henning, R. Launhardt, *A&A* **338**, 223–242 (Oct. 1998).

32. P. Hily-Blant *et al.*, *arXiv e-prints*, arXiv:2112.01076, arXiv: 2112.01076 [astro-ph.GA] (Dec. 2021).

33. J. Holdship *et al.*, *The Astrophysical Journal* **878**, 64, ISSN: 1538-4357, (http://dx.doi.org/10.3847/1538-4357/ab1cb5) (June 2019).

34. J. Jørgensen, F. Schöier, E. van Dishoeck, *A&A* **416**, 603–622, arXiv: astro-ph/0312231 [astro-ph] (Mar. 2004).

35. L. Kristensen *et al.*, *A&A* **469**, 561–574 (July 2007).

36. S. Maret *et al.*, *ApJ* **698**, 1244–1260, arXiv: 0904.0603 [astro-ph.SR] (June 2009).

37. E. Masciadri, A. Raga, *ApJ* **568**, 733–742 (Apr. 2002).

38. J. McMullin *et al.*, presented at the Astronomical Data Analysis Software and Systems XVI, ed. by R. Shaw, F. Hill, D. Bell, vol. 376, p. 127.

39. T. Millar, D. Williams, *Dust and chemistry in astronomy*.

40. P. C. Myers *et al.*, *ApJ* **896**, 163, arXiv: 2005.04307 [astro-ph.GA] (June 2020).

41. D. A. Neufeld *et al.*, *The Astrophysical Journal* **649**, 816–835, (https://doi.org/10.1086/506604) (Oct. 2006).

42. D. A. Neufeld *et al.*, *The Astrophysical Journal* **706**, 170–183, (https://doi.org/10.1088/0004-637x/706/1/170) (Oct. 2009).

43. B. Nisini, in *Jets from Young Stars II*, ed. by F. Bacciotti, L. Testi, E. Whelan, vol. 742, p. 79.

44. B. Nisini *et al.*, *ApJ* **801**, 121, arXiv: 1501.03681 [astro-ph.SR] (Mar. 2015).

45. K. Öberg *et al.*, *A&A* **504**, 891–913, arXiv: 0908.1169 [astro-ph.GA] (Sept. 2009).

46. Y. Oya *et al.*, *ApJ* **824**, 88, arXiv: 1605.00340 [astro-ph.SR] (June 2016).

47. J. Pety, N. Rodríguez-Fernández, *A&A* **517**, A12+, arXiv: 1004.4415 [astro-ph.IM] (July 2010).

48. G. Pineau des Forêts *et al.*, *MNRAS* **262**, 915–928 (June 1993).

49. L. Podio *et al.*, *Astronomy Astrophysics* **593**, L4, ISSN: 1432-0746, (http://dx.doi.org/10.1051/0004-6361/201628876) (Sept. 2016).

50. G. Rieke, M. Lebofsky, *ApJ* **288**, 618–621 (Jan. 1985).

51. M. Schmalzl *et al.*, *A&A* **572**, A81, (https://doi.org/10.1051/0004-6361/201424236) (2014).

52. F. Schöier *et al.*, *A&A* **432**, 369–379, arXiv: astro-ph/0411110 [astro-ph] (Mar. 2005).

53. A. Suutarinen *et al.*, *Monthly Notices of the Royal Astronomical Society* **440** (Feb. 2014).

54. B. Tabone *et al.*, *A&A* **607**, L6, arXiv: 1710.01401 [astro-ph.SR] (Nov. 2017).

55. M. Tafalla, A. Hacar, *A&A* **552**, L9, (https://doi.org/10.1051/0004-6361/201321303) (2013).

56. M. Tafalla *et al.*, *Proceedings of The International Astronomical Union* **280** (Jan. 2010).

57. V. Taquet *et al.*, *Astronomy Astrophysics* **637**, A63, ISSN: 1432-0746, (http://dx.doi.org/10.1051/0004-6361/201937072) (May 2020).

58. C. Terquem *et al.*, *ApJ* **512**, L131–L134, arXiv: `astro-ph/9812155 [astro-ph]` (Feb. 1999).

59. J. Tobin *et al.*, *The Astrophysical Journal* **870**, 81 (Jan. 2019).

60. F. F. S. van der Tak *et al.*, *A&A* **468**, 627–635, (`https://doi.org/10.1051/0004-6361:20066820`) (2007).

61. T. H. G. Vidal *et al.*, *MNRAS* **469**, 435–447, ISSN: 1365-2966, (`http://dx.doi.org/10.1093/mnras/stx828`) (Apr. 2017).

62. D. Wilgenbus *et al.*, *A&A* **356**, 1010–1022 (Apr. 2000).

Appendix

6.a CHANNEL MAPS OF CH$_3$OH

In Figure 6.F.1, the integrated intensity maps of methanol (CH$_3$OH (7_1–6_1)) are shown over its entire emission (from -8 km s^{-1} to 10 km s^{-1}) with an integration step of 2 km s^{-1}. The purpose of the velocity decomposition is to determine which part of the emission is targeting the low and high velocity gas component. From this Figure, it can be seen that:

- region C (i.e., C0) strongly emits in the velocity range $[-6,-2]$ km s^{-1} (panels (b) and (c)) and a weaker integrated intensity up to $[0,2]$ km s^{-1} (panel (e));
- in region A (i.e., A0, A1 and A2), the peaking velocity range of the integrated emission strongly is between $[-4,2]$ km s^{-1} (panels (c)–(e)) with a weaker emission going down to $[-6,-4]$ km s^{-1} (panel (b)) and up to $[6,8]$ km s^{-1} (h). This region is the only one showing emission at the so-called high velocity range;
- the middle region (region B) does not show emission in the lowest velocities range, but has a strong emission between $[-4,2]$ km s^{-1} and a weaker one in the velocity channel $[2,4]$ km s^{-1}. The emission in this region can therefore not be categorized in the high-velocity emission as region A nor in the low-velocity emission as region C. This region is considered a mix with high and low velocity gas components.

6.b MOLECULAR LINE EMISSION AT THE SIO-KNOT

The line emission of CS, SO, CH$_3$OH and o-H$_2$CO extracted at the SiO-knot position are shown in Figure 6.F.2. The spectra have been extracted at this position as it is known to be one the most chemically active region of the outflow (Gusdorf *et al.*, 2011). The resolution of 1 km s^{-1} is used as it is the highest spectral resolution of our dataset. Such resolution is considered in order to separate the low and high gas-velocity, if any difference can be depicted.

6.c MOLECULAR LINE EMISSION AT ALL POSITIONS

In the following appendix, the line emission of CS, SO, H$_2$CO and CH$_3$OH, extracted at all positions not displayed in Figure 6.3.4 are shown. These positions include A1, A2 and B1 up to B6.

6.d INTEGRATED INTENSITY MAPS COMPARISON CO (3–2)- ALMA/ACA

The Figure 6.F.7 display the CO(3–2), SiO (8–7), CH$_3$OH (7_{-1}–6_{-1}) emission from ALMA-12m and ALMA-ACA observations, CH$_3$OH ($4_{1,4} - 3_{0,3}$) and HCO$^+$ (4–3). From this Figure, several conclusions can be drawn: (1) the CO (3–2) integrated over the low velocity range [—95 and –4.5] km s^{-1} shown by the blue contours in panels a) and e), display the cavity borders. While the CO (3–2) integrated over the high velocity range $[-4.5$ and $85]$ km s^{-1} shown with the red contours in the same panel displays the jet. Such differentiation between the cavity and the jet allow us to trace the jet path and its interaction with the cavity. (2) The CH$_3$OH observed with ACA traces the same gas as the one observed with our ALMA observations (panel f) and Fig.6.3.2 panel c)). Therefore, the integrated emission follows an crossbow shape and we observe peaks of the integrated emission in the regions A, B and C. The close match of CH$_3$OH (7_{-1}–6_{-1}) and CH$_3$OH ($4_{1,4}$ ̄$3_{0,3}$) integrated over the same velocity range as in our ALMA observations (cf. Section 6.3.3) confirms our CH$_3$OH detection. (3) The SiO shown in panels c) and g) traces the same regions A, B and C as pointed in this study. This match with SiO observations underlines that

these studied are effectively shock regions. (4) The HCO$^+$ does not entirely overlap with the CH$_3$OH (7_{-1}–6_{-1}) emission. It is therefore likely that HCO$^+$ traces different physics and chemistry of the outflow.

6.e ORTHO-TO-PARA RATIO

Right panel of Figure 6.F.8 displays the observed ortho/para ratio, OPR, derived for each region, using the inferred H$_2$ column densities of the transitions H$_2$0–0 S(0) to 0–0 S(7), shown in Fig 6.F.8, left panel. Based on our data, no clear distinction can be made among all the locations, as they all have OPR lower than 1. This is in accordance with OPR of other outflows (Maret *et al.*, 2009), which are purely observationally derived, contrary the OPR of Neufeld *et al.* (2009) in which an OPR ~ 2.4 was derived, based on parametric shock models. The Region A2 is not included due to the lack of observed transitions as this region lays in the border of *Spitzer* observations and all the H$_2$ transitions are not observed within the same field of view, cf. Neufeld *et al.* (2009). An OPR lower than 3 is an indicator, in high temperature regions (T>300 K), of an inefficient para-to-ortho conversion. A variation of the OPR is only possible through exchange reactions which are lengthy processes (e.g., 0.1 Myr at a cosmic ray of 10^{16} s-1 and gas density of 10^4 cm^{-3}, Pagani *et al.*, 2013). .

In equilibrium, the OPR is strongly dependent on the temperatures, we inferred an H$_2$ spin temperature between 45 K and 60 K in the ten regions from the following relation:

$$OPR = \frac{\sum_{J\,odd} 3(2J+1)e^{-E_j/(k_B T)}}{\sum_{J\,even} (2J+1)e^{-E_j/(k_B T)}} \tag{6.6}$$

Where g is the statistical weight, E is the energy level, T is the spin temperature and k_B is Boltzmann's constant The inferred temperature range describes a warmer region than the ambient medium. Three possibilities might explain these low OPR:

- The region was previously heated by the passage of a shock wave. As suggested by Maret *et al.* (2009), such low OPR may be indicators of previous shock structures.

- The observed OPR are not representative of the real OPR of the region. As discussed by Wilgenbus *et al.* (2000), the observational OPR using rotational transitions above v=0, J=2 are systematically lower than the OPR considering the total ortho and para column densities. This last is also lower than the OPR found in the post-shock gas.

- The models matching the observations are J-type, therefore they reach stationary state on a shorter timescale than C-type. In the case of our selected models with a pre-shock density of 10^4 cm^{-3}, the time to reach a stationary shock is 1000 years and 100 years for a pre-shock density of 10^5 cm^{-3}. On such short timescale, the cold gas does not have time to fully thermalize.

Therefore, one should be extremely careful in interpreting the OPR from observations only. They are not reliable indicator of the thermalization state of the shock and thus cannot be used for providing insights on the timescale of the observed shock.

6.f COLUMN DENSITIES EXTRACTED AT ALL POSITIONS

In Figure 6.F.9, the column densities of the detected species CH$_3$OH (green plus signs), H$_2$CO (red crosses), SO (orange dots) and CS (blue stars) are extracted at all the eleven studied regions (i.e., A0 to C0). The non detection, i.e., upper limits, are indicated by the pointing-up arrows while the partial detection, i.e., lower limits, are shown by the pointing-down arrows. From this Figure, it can be seen that the column densities of all the species do not vary by more than 1 order of magnitude, which displays an homogeneity of the observed emission toward the eleven regions.
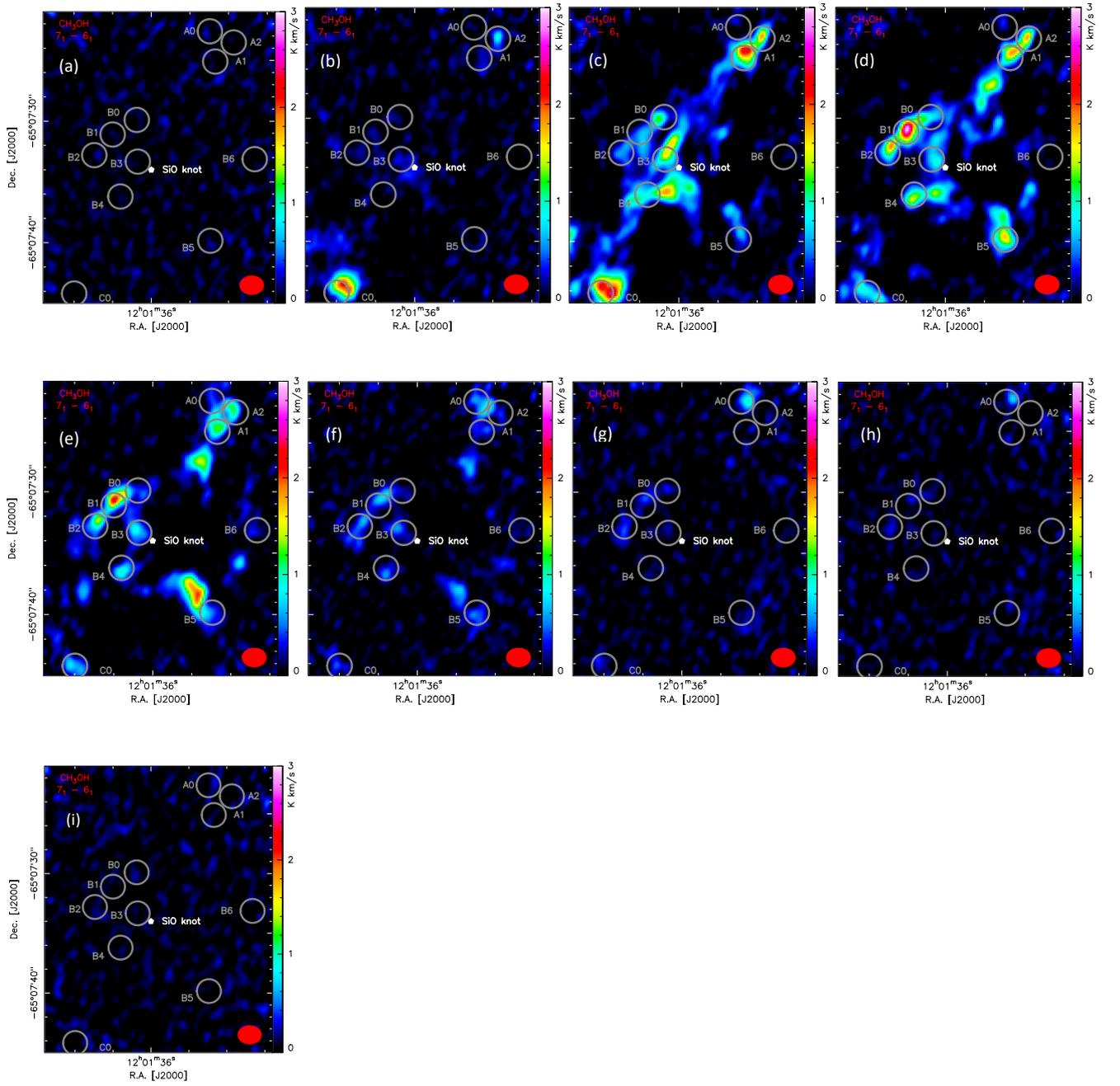
FIGURE 6.F.1: Integrated intensity maps of CH_3OH over the velocity range $[-8,10]$ km s^{-1} with an increment of 2 km s^{-1} from the panel (a) to (i) (i.e., panel (a) corresponds to the velocity range $[-8,-6]$ km s^{-1} and panel (i) corresponds to the velocity range $[8,10]$ km s^{-1}). The color scale is in units of K km s^{-1}, and is shown on the right of each panel. The beam size is shown on the bottom-right corner in red (cf. ALMA-12m, Section 6.2.1). The targeted regions of interest in this study are annotated by the grey circles (cf. Section 6.3.3).
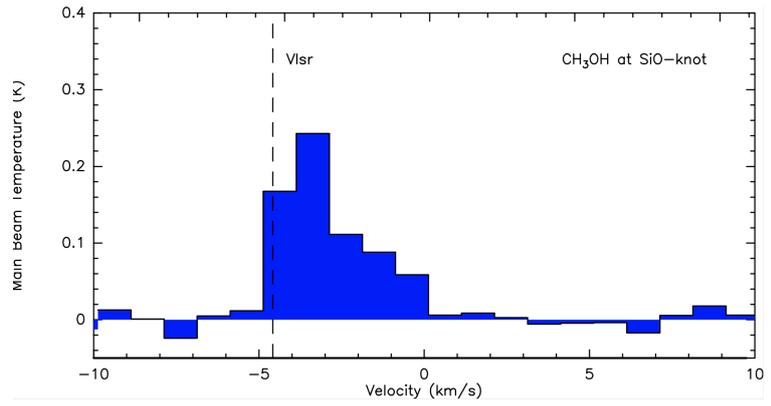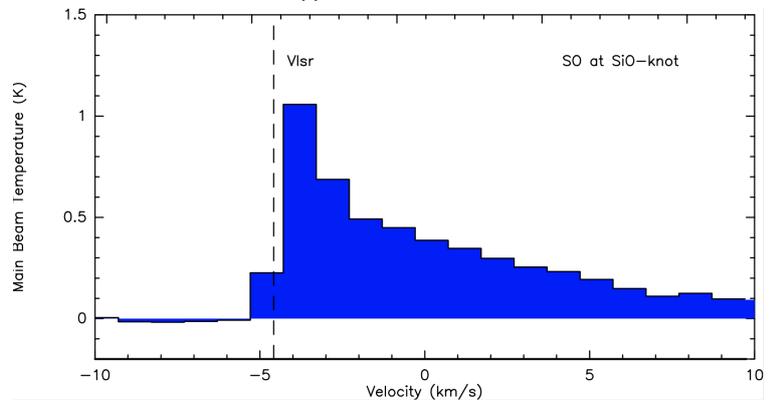
(a) CH$_3$OH at 341.35 GHz
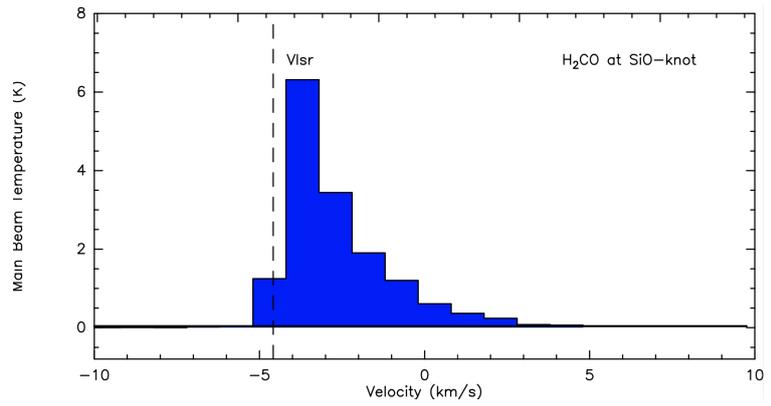
(b) H$_2$CO at 351.89 GHz
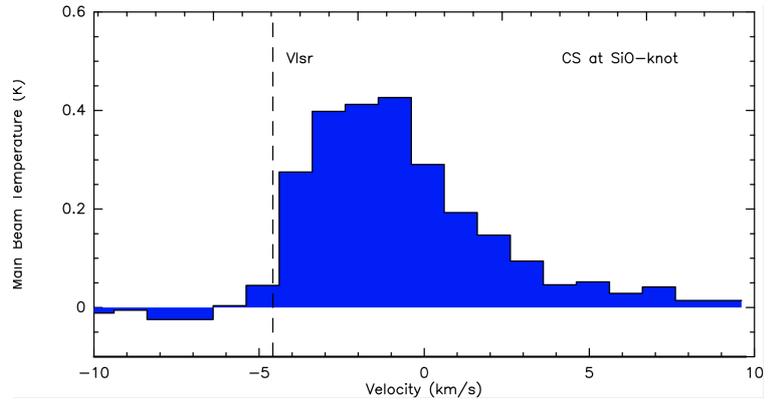
(c) CS at 342.8 GHz

(d) SO at 340.71 GHz

FIGURE 6.F.2: Spatially averaged spectra of the main beam temperature in K of the molecules a-CH$_3$OH, o-H$_2$CO, CS and SO at the SiO-knot position over the velocity range of $[-10, 10]$ km s^{-1}. For all the spectra a spectral resolution of 1 km s^{-1} was chosen to separate the low and high velocity component of emission. The BHR-71 velocity of -4.5 km s^{-1} is shown by the dashed vertical line. The H$_2$CO spectrum is truncated at 5 km s^{-1}, as this is the edge of the spectral window.

FIGURE 6.F.3: Main beam temperature spectra in K of the molecule CS at the positions A1, A2 and B1 up to B6 (A regions in blue and B regions in grey), over the velocity range of -10 km s^{-1} to 10 km s^{-1}. For all the spectra a spectral resolution of 1 km s^{-1} was chosen to distinguish the low- and high-velocity components of emission. The BHR71 source velocity of 4.5 km s^{-1} is shown by the dashed vertical line.
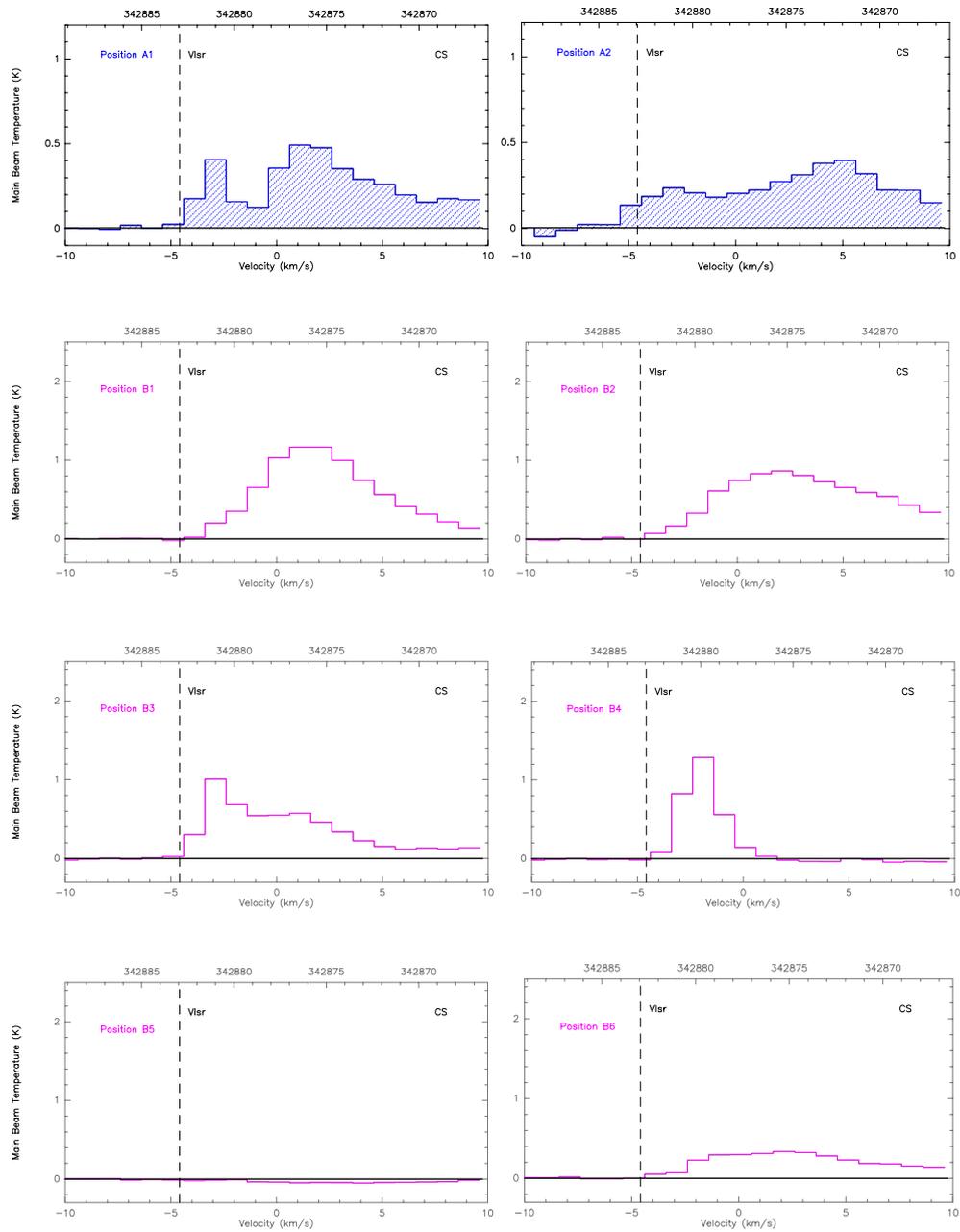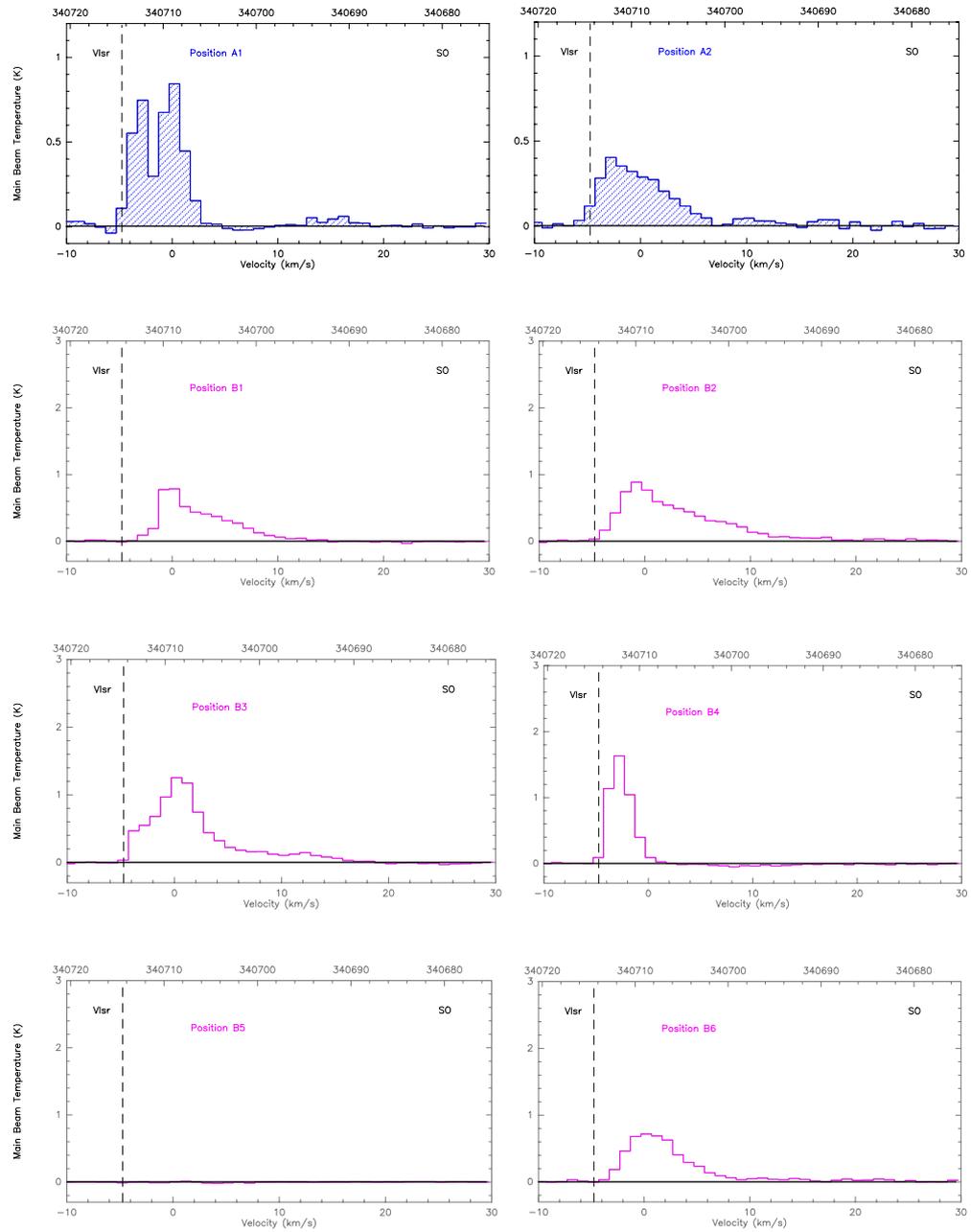
FIGURE 6.F.4: Main beam temperature spectra in K of the molecules SO at the positions A1, A2 and B1 up to B6 (A regions in blue and B regions in grey), over the velocity range of -10 km s^{-1} to 30 km s^{-1}. For all the spectra a spectral resolution of 1 km s^{-1} was chosen to distinguish the low- and high-velocity components of emission. The BHR71 source velocity of 4.5 km s^{-1} is shown by the dashed vertical line.
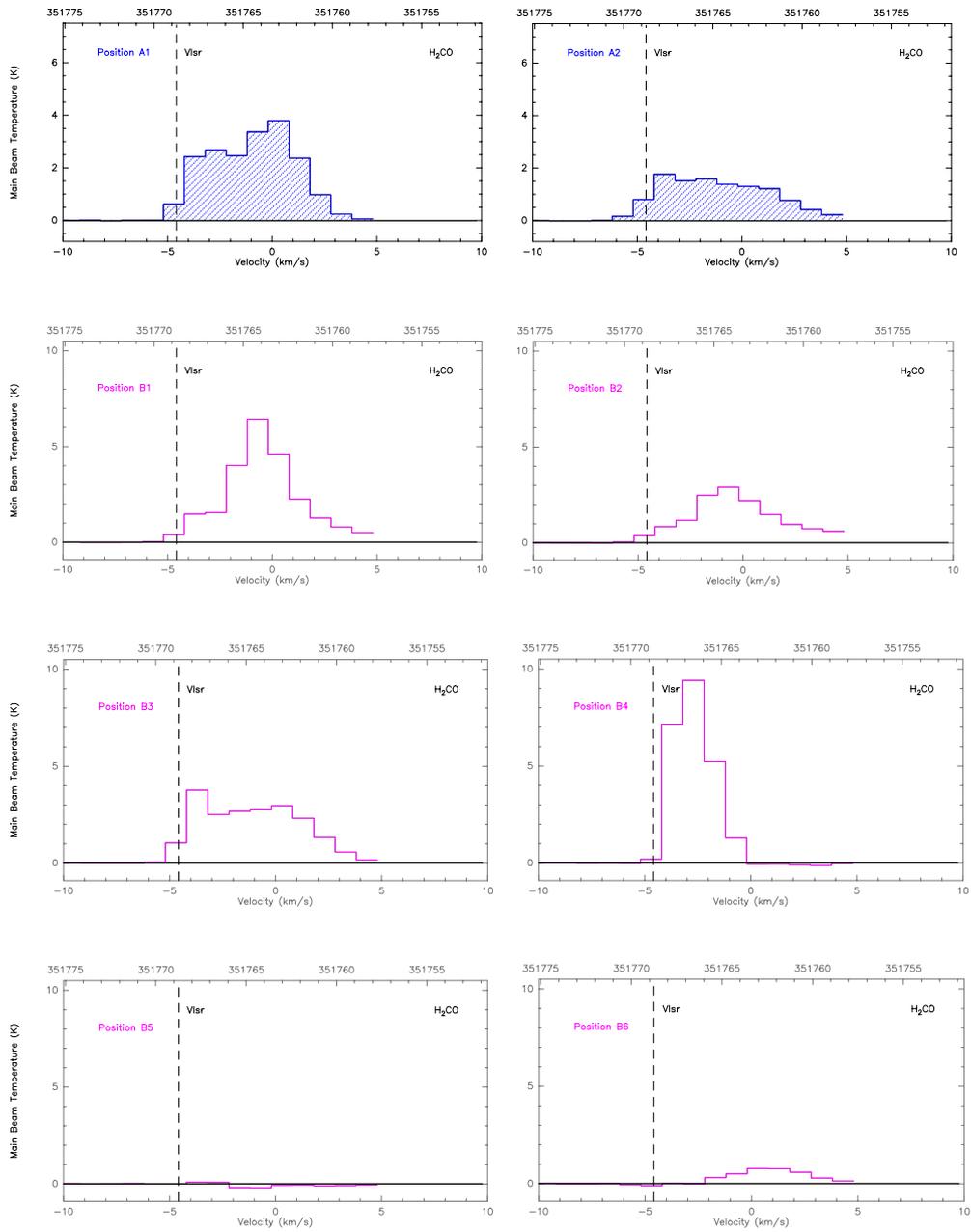
FIGURE 6.F.5: Main beam temperature spectra in K of the molecule o-H_2CO, at the positions A1, A2 and B1 up to B6 (A regions in blue and B regions in grey), over the velocity range of -10 km s^{-1} to 10 km s^{-1}. For all the spectra a spectral resolution of 1 km s^{-1} was chosen to distinguish the low- and high-velocity components of emission. The BHR71 source velocity of 4.5 km s^{-1} is shown by the dashed vertical line. The H_2CO spectrum is truncated at 5 km s^{-1}, as this is the edge of the spectral window; the same for CS at 10 km s^{-1}.
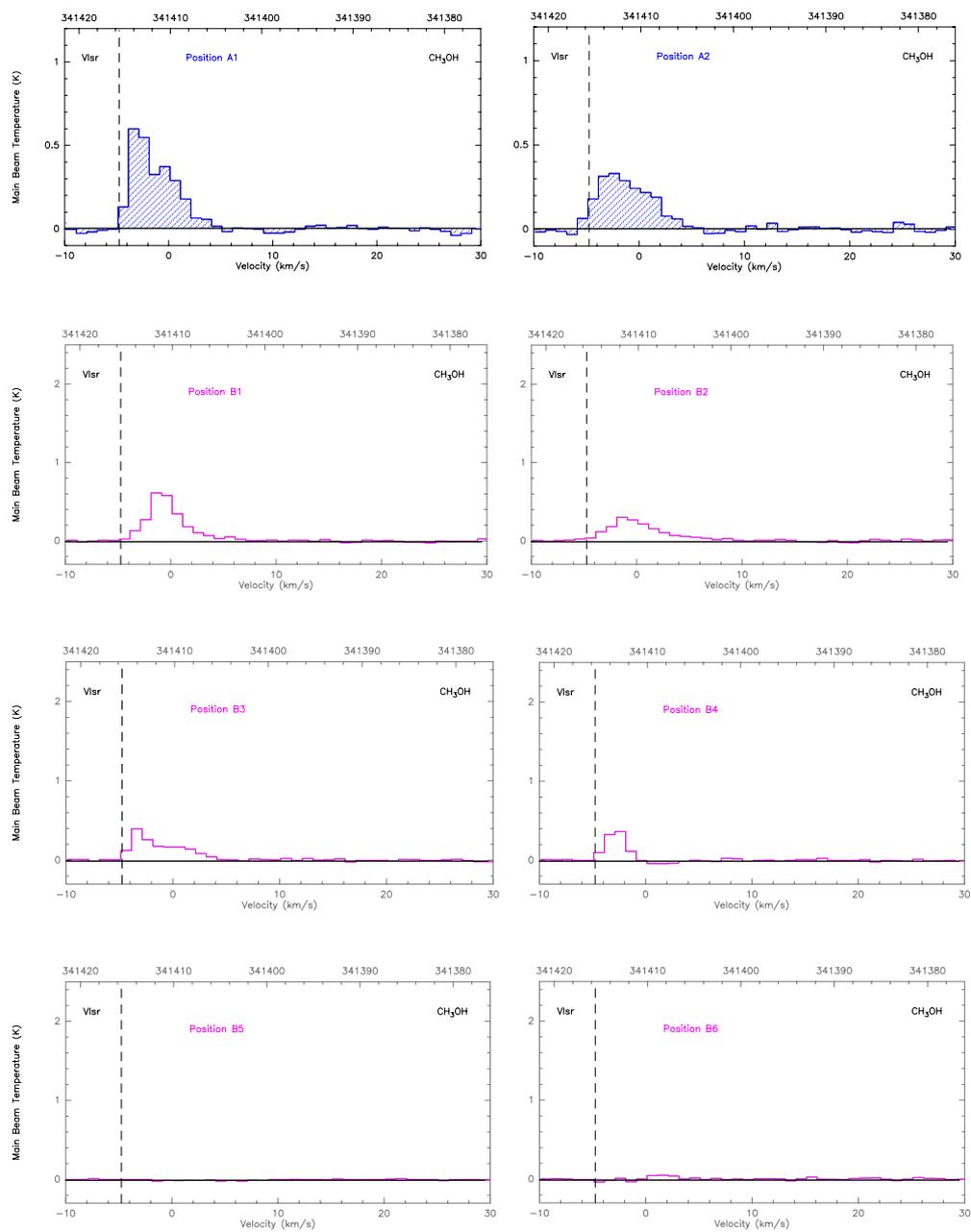
FIGURE 6.F.6: Main beam temperature spectra in K of the molecule a-CH$_3$OH at the positions A1, A2 and B1 up to B6 (A regions in blue and B regions in grey), over the velocity range of -10 km s^{-1} to 30 km s^{-1}. For all the spectra a spectral resolution of 1 km s^{-1} was chosen to distinguish the low- and high-velocity components of emission. The BHR71 source velocity of 4.5 km s^{-1} is shown by the dashed vertical line.
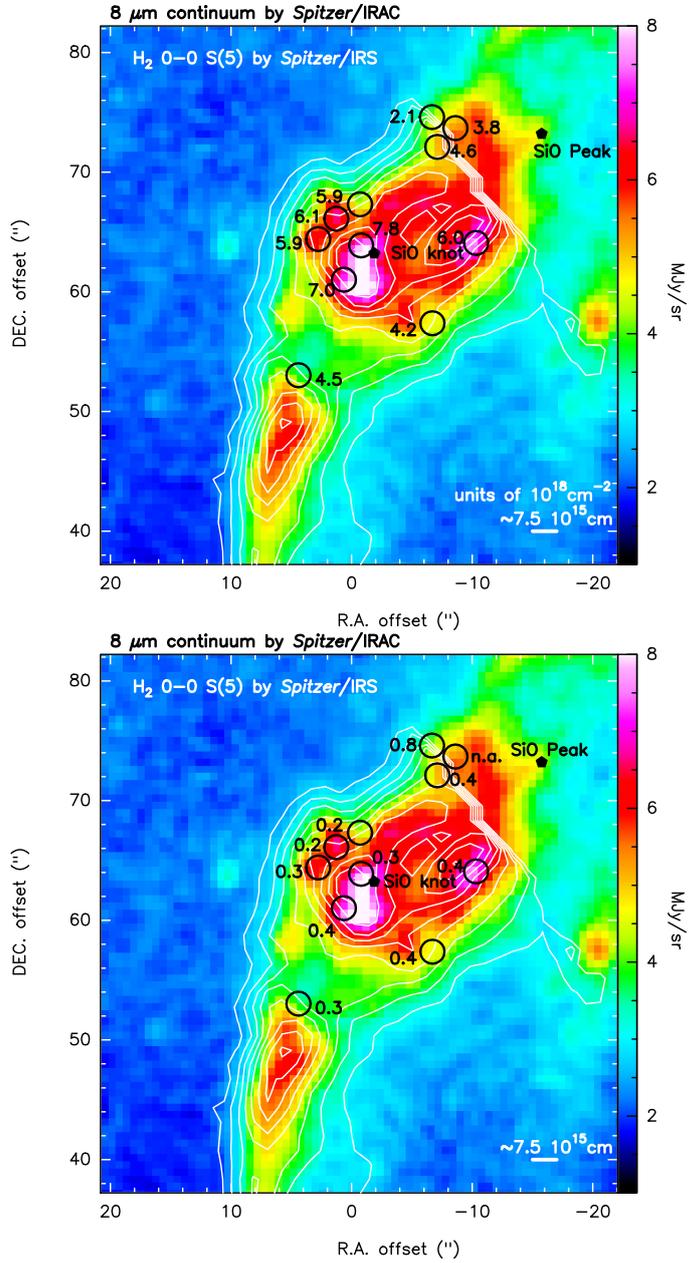
FIGURE 6.F.7: Presentation of the detections obtained in the frame of our ALMA-ACA only program, together with the CO (3–2) shown (merged with APEX data) in Figures 2 and 3. *Upper panels:* Same field as shown in Figures 1b, 1c and 2a, with the rough size of ALMA observations indicated in the lower right corner: ACA only in red, 12 m only in black. *Lower panels:* Same field as shown in Figures 2b, 2c and 3a-d, with the rough size of ALMA observations indicated in the lower right corner: ACA only in red, ALMA-12m only in black. On all panels, the background image is the *Spitzer*-IRAC map of the emission at 8 μm. In the lower panels, the CH$_3$OH emission contours from our 12m-only observations is shown in black (same as Figures 2c and 3a). a) and e): CO (3–2) contours: blue integrated between −95 and −4.5 km s^{-1} and red between −4.5 and 85 km s^{-1} shown from 20 to 100% in steps of 20%; white, light grey and dark grey from 50 to 100% in steps of 10% integrated respectively over [−4.5, 20], [45, 60], and [60, 85] km s^{-1}. b) and f): CH$_3$OH ($4_{1,4}$ ̄$3_{0,3}$) in white contours integrated between —8 and 10 km s^{-1}. c) and g): SiO (8–7) contours: red between −4.5 and 85 km s^{-1} shown from 20 to 100% in steps of 20%, blue and white from 50 to 100% in steps of 10% integrated respectively over [−95, −4.5] and [20 ,45] km s^{-1}. d) and h): HCO$^+$ (4—3) contours: red between −4.5 and 85 km s^{-1} shown from 20 to 100% in steps of 20%, blue from 50 to 100% in steps of 10% integrated over [−95, −4.5] km s^{-1}.

FIGURE 6.F.8: Integrated intensity maps of (a) background: continuum emission at 8 μm, observed by *Spitzer*/IRAC. (b) contours: H_2 0–0 S(5) emission, observed by *Spitzer*/IRS. On the left, the derived total H_2 column density, in units of 10^{18} cm^{-2}, are displayed at the different analysed locations. On the right, the ortho/para (O/P) ratio are shown for the same regions. Note: the A2 region is on the border of the observational set, the O/P ratio could not be derived.
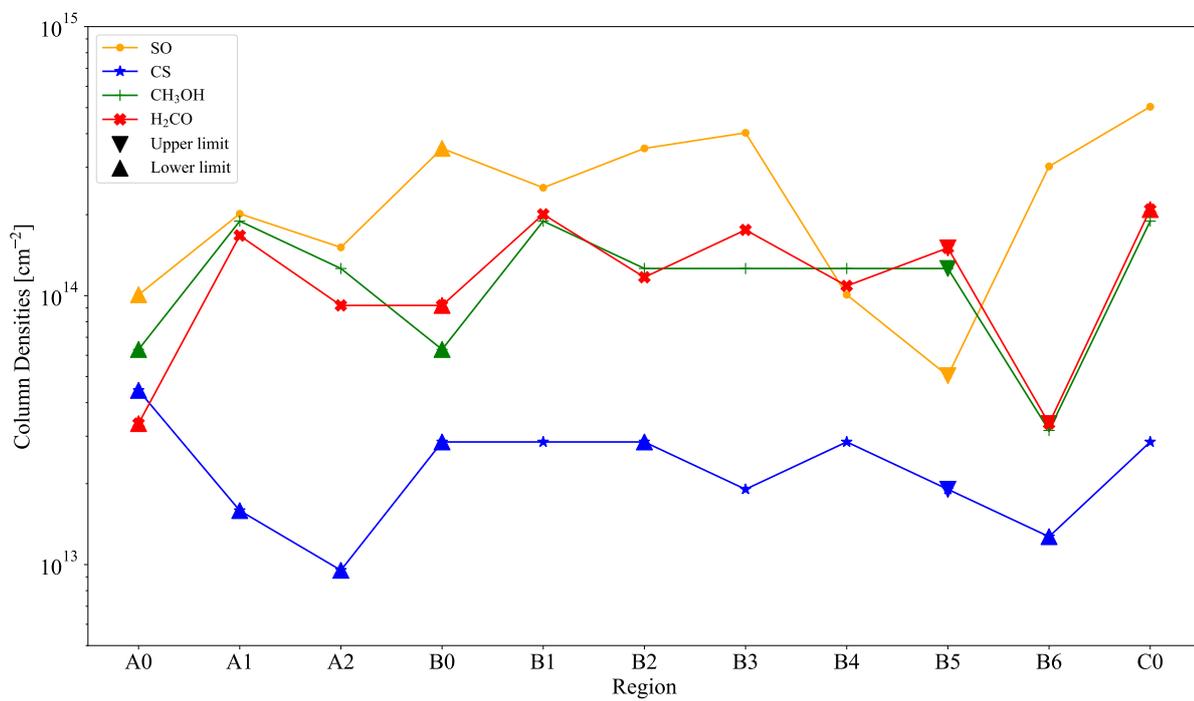
FIGURE 6.F.9: Inferred column densities from the observations of CS, SO, CH$_3$OH, and H$_2$CO, at the eleven studied regions. At each region, the emission from the ALMA-12m observations, has been extracted over 1″ radius circle. The upper and lower limits are indicated with the arrows pointing up and down, respectively.

7

H$_2$S, a key driver of the sulphur chemistry in Cygnus X-N30?

M. el Akel[1,2], R. Le Gal [3,4], R. L. Pitts[1], L. E. Kristensen[1]

[1] Niels Bohr Institute, University of Copenhagen, Øster Voldgade 5–7, 1350 Copenhagen, Denmark
[2] CY University, Observatoire de Paris, CNRS, LERMA, F-95000 Cergy, France
[3] IRAM, 300 rue de la Piscine, 38406 Saint-Martin-d'Hères, France
[4] Univ. Grenoble Alpes, CNRS, IPAG, F-38000 Grenoble, France

In the following Chapter, we present our current findings on the H$_2$S emission towards CygnusX-N30, based on our SMA observations (P.I. el Akel 2020). Our scientific aim is to investigate this H$_2$S emission and its impact on the sulphur chemistry in a warm environment (T>100 K). This study is still in a preparation stage. Observations of the same region with a higher resolution, as well as observations of more H$_2$S transitions should likely be added in this study, to confirm the current data interpretation.

Abstract

Context. The sulphur chemistry is currently poorly understood, especially its role in the evolution of star-forming regions, although sulphur is one of the most abundant species in the ISM (S/H $\sim 10^5$). In particular, the sulphur reservoir in protostars remains unknown.

Aims. With this study, we aim to understand the role of H$_2$S in a well-known protostar, Cygnus X-N30 (W75N(B)).

Methods. We used the SubMillimeter Array to observe, towards this source, the H$_2$S rotational transitions $2_{2,0}$–$2_{1,1}$, $4_{3,2}$–$5_{0,5}$, and $3_{3,0}$–$3_{2,1}$ at 216.71 GHz, 228.56 GHz, and 300.50 GHz, respectively. First, we used the intensity maps of the H$_2$S emission to infer its spatial extent. Next, the line emission was used to derive the H$_2$S column density temperature at the continuum positions. The emission morphology and column density were then compared to those of other sulphur-bearing species observed towards the same protostar. Finally, a comparison of the sulphur species detected in Cyg-N30, with special attention to H$_2$S, is made with the low-mass protostar IRAS 16293-2422.

Results. We detected line emission of H$_2$S at 216.71 GHz and at 300.50 GHz, but not at 228.56 GHz, at two fields with an offset of 1″ from the continuum cores, MM1a and MM1b. Using RADEX, an H$_2$S column density of 10^{16} cm^{-2} near MM1a and 10^{17} cm^{-2} near MM1b were inferred, for an excitation temperature of 200 K

Conclusions. The detected H_2S near the continuum cores of CygnusX-N30 is released in the gas phase via thermal desorption and mechanical processes (e.g., sputtering, etc.). We expect an important reservoir of H_2S to be part of the icy dust matrix, but also present on the top layer of the icy dust grains, where it reacts to produce other sulphur species, e.g., OCS. The high inferred column density shows that H_2S, locked up in the icy matrix, is likely to be formed in the cold envelope (T≈10 K), at the early phase of the collapse. Meanwhile, other sulphur species form from H_2S later on the grain surface during the collapse. We found that the combination of the nearby OB association, Cygnus-OB2, and the rotating disk structure of CygX-N30 are likely responsible for the increased the abundance of S-O species from H_2S.

key words. Astrochemistry, Stars: formation, Individual sources: CygnusX-N30

7.1   INTRODUCTION

Sulphur is one of the most abundant elements in the ISM (S/H $\sim 10^{-5}$, Asplund *et al.*, 2009; Yamamoto, 2017) and is a key element of biological systems (Watanabe and Hoefgen, 2019). Therefore, it is crucial to understand the evolution of the sulphur chemistry in the different phases and regions of the protostellar environment.

The observed sulphur abundance is strongly depleted in dense molecular clouds where around 0.1% of the sulphur elemental abundance is recovered (Graedel *et al.*, 1982; Tieftrunk *et al.*, 1994; Wakelam *et al.*, 2003; Vastel *et al.*, 2018). This suggests that a large amount of it is present on the icy dust grains and, possibly locked in the icy matrix (Ruffle *et al.*, 1999; Vidal *et al.*, 2017; Laas and Caselli, 2019).

Currently, the main reservoir of sulphur in the solid-state remain unclear. H_2S is considered as the primary product of atomic sulphur on icy dust grain due to the high abundance of hydrogen and its efficient mobility on the surface (Vidal *et al.*, 2017). However, several other observational studies argue that most of the atomic sulphur is in the form of organo-sulphurs trapped in the icy matrix (Millar and Herbst, 1990; Ruffle *et al.*, 1999).

Moreover, there has been no clear detection of H_2S in the ice mantles so far because its infrared band, at 2558 cm^{-1}, overlaps with the CH_3OH bands at 2530 and 2610 cm^{-1} (Navarro-Almaida *et al.*, 2020). Therefore, only upper limits of H_2S on the ice matrix could be derived (Jiménez-Escobar and Muñoz Caro, 2011). The question of missing sulphur remains thus unsolved and its reservoir(s) is yet to be identified.

Hydrogen sulphide (H_2S) was first detected towards giant molecular clouds by Thaddeus *et al.* (1972). Later studies by Minh *et al.* (1989) and Minh *et al.* (1990) have pointed out a significantly higher H_2S abundance, X_{H_2S}, by few orders of magnitude, in Orion KL ($X_{H_2S} \sim 10^{-6}$) as compared to quiescent clouds ($X_{H_2S} \sim 10^{-9}$). H_2S has since been detected towards several star-forming environments including low-mass protostars, hot cores, and shocks (Koumpia *et al.*, 2017; Holdship *et al.*, 2016; Drozdovskaya *et al.*, 2018). Comparison of abundances suggested that the presence of hydrogen sulphide is associated with the formation of stars, from which Minh *et al.* (1990) inferred a total column density of H_2S of $\sim 10^{14}$ cm^{-2}–10^{16} cm^{-2} towards several high-mass star-forming regions (e.g., Sgr B2(M),Sgr B2(N), W49N, W51(N), W51(M/S), W3(IRS 5)). These were based on the observed H_2S $1_{1,0}$–$1_{0,1}$ rotational transition, with the Five College Radio Astronomical Observatory (FCRAO) 14 m telescope (Minh *et al.*, 1990). Minh *et al.* (2010) and Minh *et al.* (2012) found later a similar range of H_2S column densities of 10^{15} cm^{-2}–10^{16} cm^{-2} towards CygX-N30, based on the observed $2_{2,0}$–$2_{1,1}$ rotational transition with the Submillimeter Array (SMA) telescope. With the *Herschel* Space Observatory, Crockett *et al.* (2014) observed 84 transitions of H_2S isotopes towards the hot core of Orion KL. Some of the levels detected by Crockett *et al.* (2014) are highly excited ($E_{up} \geq 1000$ K) and believed to be populated by radiative pumping. They concluded that the H_2S emission traces the hot core in Orion KL.

The solid-state of H_2S was also investigated in in-situ laboratory experiments. Jiménez-Escobar and Muñoz Caro (2011) and Jiménez-Escobar *et al.* (2014) irradi-

ated H_2S on ice with high energy particles, to reproduce the effect of cosmic rays. They showed that part of H_2S was decomposed into several allotropes of sulphur, reducing the abundance of H_2S in the icy matrix and increasing the abundances of OCS, SO_2 and S_8. Later, Chen *et al.* (2015) found that the UV irradiation of H_2S-CO and H_2S-CO_2 ice mixtures lead to the formation of several species, such as OCS, CS_2 and SO_2. They claimed that H_2S is formed from the hydrogenation of atomic sulphur, as suggested by Vidal *et al.* (2017), and is a key species leading to the formation of further S-bearing species. Cazaux *et al.* (2021) later confirmed the production of H_2S_x and S_x ($x > 2$) from the irradiation of H_2S ice. Moreover, el Akel et al. (2021, in press) found from laboratory experiments mimicking dense, cold astrophysical environments, that solid-state H_2S is highly reactive with atomic hydrogen and CO, without any external source of energy. This implies that H_2S is likely the gateway to solid-state sulphur-chemistry on interstellar dust grains, from which OCS and more complex sulphur-bearing species form.

Despite all the current work, from the observational, modeling, and theoretical sides, no agreement has been achieved yet on the implications of H_2S in the ice. It is unclear if all the H_2S is locked up in the icy matrix, or if a large fraction of it has reacted with the surrounding species to form other S-bearing species.

This work is an attempt to understand how H_2S is correlated with other S-bearing molecules in the hot core. For this purpose, this paper focuses on H_2S emission towards the high-mass protostellar source, CygX-N30 (W75N-B) (Motte *et al.*, 2007; van der Walt *et al.*, 2021), located in the nearby highly active star forming complex, Cygnus X ($d \sim 1400$ pc, Rygl *et al.*, 2012). CygX-N30 consists of three millimeter continuum cores, MM1, MM2, and MM3. MM1 is the brightest continuum core, itself composed of cores MM1a and MM1b. Emission from five bright sulphur-bearing molecules were detected by van der Walt *et al.* (2021) and el Akel et al. 2021 (in press), towards this source at both continuum cores: SO, SO_2, OCS, CS and H_2CS. They found a clear chemical segregation between the various S-bearing molecules: when sulphur is not associated to any carbon atoms, its intensity peak is always centered near the MM1a core. In contrast, the organic sulphur molecules, i.e. containing both C- and S-atoms, show emission around both sources (MM1-a and b).

Minh *et al.* (2010) also detected several sulphur species, i.e., SO, SO_2, H_2CS, H_2S, and CS towards this source. The inferred molecular column density of H_2S ($\sim 10^{15}$ cm^{-2}) was found to be within the range of previously inferred H_2S column densities. However, as pointed out by Minh *et al.* (2010), the H_2S emission peaks close to the main continuum cores at an offset of $0''1$. Minh *et al.* (2010) claimed that the species not peaking at the hot core are not major ice mantle components. However, that does not mean they have not been major ice components at some point in the history of the protostar.

In this paper, we conducted H_2S observations of the rotational transitions $2_{2,0}$–$2_{1,1}$, $4_{3,2}$–$5_{0,5}$ and $3_{3,0}$–$3_{2,1}$ with the SMA, centered at the MM1 continuum core of CygX-N30. Specifically, multiple H_2S transitions were targeted in order to infer excitation conditions. This paper is structured as follows. The observations are presented in Section 7.2. The results, of the line analysis and the molecular emission are provided in Section 7.3. Section 7.4 discusses the results, while the outcomes of this study are summarized in Section 7.5.

7.2   OBSERVATIONS

The observations were carried out with the SMA facility, on Mauna Kea, on the 11th of June 2020, targeting one of the brightest source of the Cygnus X complex, N30 (W75N). The observations were centered at $\alpha = 20^h38^m36.6^s$ and $\delta = 42°37'32''0$ (J2000). The observations were performed in the extended configuration, with six of the eight antennas available in the array. The maximum projected baseline was ~220 m. The 240 GHz receiver was centered at 219 GHz and covered both the 216 and 228 GHz transitions of H_2S (Table 7.3.1), while the 345 GHz receiver was centered at the 300 GHz line. The native spectral resolution of the SMA is 140 kHz, but the spectral data were rebinned by a factor of 4 to a channel size of 560 kHz. At 216 GHz this corresponds to 0.8 km s^{-1}, while it is 0.6 km s^{-1} at 300 GHz.

TABLE 7.2.1: Observational parameters

Parameters		CygX-N30
Beam size	216 GHz	1.32×0.91″
	228 GHz	1.24×0.86″
	300 GHz	0.89×0.66″
Sensitivity (1σ)	216 GHz	0.06 Jy beam^{-1}
	228 GHz	0.11 Jy beam^{-1}
	300 GHz	0.03 Jy beam^{-1}

For all the observations, MWC349A was used as the gain calibrator and the quasars 3c454.3 and 3c279 were used as bandpass calibrators. The flux calibration was performed on Neptune. The data were calibrated with the CASA[1] software, version 4.7.2 (McMullin *et al.*, 2007). The calibration consisted of first flagging edge channels as well as channels with spikes. Second, the bandpass was calibrated, before the complex gains. Finally, the absolute flux was calibrated.

The imaging was then performed with the clean algorithm of CASA, using the Briggs weighting with a robust parameter of 2 (Briggs *et al.*, 1999). A clean mask was centered on the brightest continuum core of N30 (i.e., MM1), of size 16″× 16″. The resulting beam size is 1.32″× 0.91″ at 216 GHz, and 0.89″× 0.66″ at 300 GHz. The pixel size of the cleaned image was set to 0.″2. The sensitivity varies between 0.03 and 0.11 Jy beam^{-1} in 0.8 and 0.6 km s^{-1} channels, depending on the observed rest frequency (Table 7.2.1).

[1]Common Astronomy Software Applications, https://casa.nrao.edu

7.3   RESULTS

We targeted three emission lines of H₂S, at 216.71 GHz, 228.56 GHz, and 300.50 GHz, corresponding to the H₂S transitions $2_{2,0}$–$2_{1,1}$, $4_{3,2}$–$5_{0,5}$, and $3_{3,0}$–$3_{2,1}$, respectively. The H₂S transitions at 216.71 GHz and at 300.50 GHz were targeted due to their high Einstein-A coefficient ($A_{ij} \sim 10^{-4}$–10^{-5} s^{-1}) and low upper energy level (E_u<170 K), as in a hot core region where temperatures reach T>100 K, these transitions can be easily excited. Moreover, observations performed by Jørgensen *et al.* (2011) of IRAS16293 show the H₂S line at 216.71 GHz is typically brighter than OCS 29–28, which was clearly detected by el Akel et al. 2021 (in press) for the same object using a similar spatial resolution of 1.″5. The H₂S line at 228.56 GHz displays a higher upper-level energy (E_u=250 K) and significantly lower Einstein-A coefficient (A_{ij}=7.88 × 10^{-8} s^{-1}) but, was targeted as it was already covered by the observational setup. The characteristics of the targeted lines are listed in Table 7.3.1. We performed our data analysis in three parts. First, the H₂S line spectra are analysed, then the integrated intensity maps are produced. Finally, we infer the column density of H₂S based on the line spectra analysis.

TABLE 7.3.1: Characteristics of the targeted H₂S lines

Transition	Frequency (GHz)	n_c[a] (cm^{-3})	E_{up} (K)	A_{ij} (s^{-1})
$2_{2,0}$–$2_{1,1}$	216.71	1.56×10^6	83.98	4.83× 10^{-5}
$4_{3,2}$–$5_{0,5}$	228.56	3.27×10^4	250.30	7.88× 10^{-8}
$3_{3,0}$–$3_{2,1}$	300.50	3.82×10^6	168.90	1.01× 10^{-4}

[a] Critical density, n_c, determined from A$_{ij}$/C$_{ij}$ at 100 K. The spectroscopic parameters are taken from the LAMDA database (https://home.strw.leidenuniv.nl/~moldata/H2S.html) and the collisional rates coefficients were inferred from Dubernet *et al.* (2006), Dubernet *et al.* (2009), Daniel *et al.* (2010) and Daniel *et al.* (2011).

TABLE 7.3.2: Gaussian fit parameters of the H_2S transitions.

Region	Transition	I [Jy beam^{-1}]	v_0 [km s^{-1}]	FWHM[1] [km s^{-1}]
a	$2_{2,0}$–$2_{1,1}$	0.2±0.05	4.6±2.1	5.1±0.5
	$3_{3,0}$–$3_{2,1}$	0.36±0.07	4.6±1.1	5.4±0.9
b	$2_{2,0}$–$2_{1,1}$	0.15±0.04	6.8±0.9	6.5–1.2
	$3_{3,0}$–$3_{2,1}$	0.16±0.04	5.2±1.6	3.6+1.3 −0.3

[1] Full width at half maximum (FWHM).

7.3.1 Molecular line emission

We detected emission of two out of the three targeted H_2S transitions at 216.71 GHz and 300.50 GHz. This emission was investigated at two fields of view, near the MM1a and MM1b cores, because previous studies performed by [Minh *et al.*, 2010], [van der Walt *et al.*, 2021], and el Akel et al. 2021 (in press) have shown that sulphur species peak near these continuum cores, with a typical offset of ∼1″. In this analysis, we consider the continuum cores presented in van der Walt *et al.* (2021): MM1a at $\alpha = 20^h38^m36.51^s$; $\delta = 42°37'33''48$ and MM1b at $\alpha = 20^h38^m36.42^s$; $\delta = 42°37'34''58$ (J2000).

To have the best signal to noise ratio, the line spectrum of each transition was investigated over a square of 1″ per side around each continuum core. In this way, emission from ∼ six squares of 1″×1″ were analysed around each core, and the field displaying the highest signal to noise ratio (SNR) was selected. We used such a small size because 1″ was the smallest spatial resolution in common for both transitions. These selected locations are denoted in this study as fields a and b, shown in Fig. 7.3.2.

The line spectra of each transition extracted at both fields are shown in Fig. 7.3.1. Each detected line has been fitted with a Gaussian curve, using CASSIS[2] software, version 5.1.1. The parameters of these fits are summarized in Table 7.3.2. These Figures show that both transitions at both locations display a low signal (i.e., not exceeding 0.36 Jy beam^{-1}), and that both targeted transitions display a small offset with respect to their line frequency: an offset of ∼5–7 km s^{-1}.

7.3.2 Integrated intensity maps

The moment zero maps, also called integrated intensity maps, were then investigated by integrating the line emission over a total velocity range of ∼15.5 km s^{-1}, centered at the rest frequency of each transition. The corresponding maps are shown in Figure 7.3.2. This Figure also displays the fields a and b used for extracting the line spectra in Section 3.1. As it is shown, both locations correspond to peaking regions of both transitions: region a for H_2S $3_{3,0}$–$3_{2,1}$ and region b for H_2S $2_{2,0}$–$2_{1,1}$. Moreover, the different peak locations display compact emission of ∼1″2, such that the size of these fields a and b covers ≥90% of the emission. As expected from previous studies, the highest emission of H_2S is also at a small offset of the continuum cores, as is the case for all the detected sulphur species (van der Walt *et al.*, 2021, el Akel et al. 2021 in press).

7.3.3 Column density

To quantify the column density of H_2S from the two detected lines, we used the RADEX tool[3] (van der Tak *et al.*, 2007). Considering a n_{H_2} of 10^{10} cm^{-3}, an excitation temperature of 200 K, and a defined FWHM of 5 km s^{-1}, we determined the line intensity for a specified column density of H_2S. This was performed for a column density range between 10^{14} and 10^{18} cm^{-2}.

In order to be in LTE, i.e., where level populations are driven by collision with H_2, the density of the main collision partner should be by few orders of magnitude higher than the critical density of the species of interest (cf. Table 7.3.1). We use an excitation temperature of 200 K, as in LTE, this reflects the kinetic temperature of the gas. We expect that, in such region of the protostar, this temperature is easily reached. Moreover, previous observations of S-species towards the same source, by van der Walt *et al.* (el Akel et al. 2021, in press and 2021) have shown an excitation

Minh *et al.*, "Submillimeter Array Observations Toward the Massive Star-forming Core MM1 of W75N"

van der Walt *et al.*, "Protostellar Interferometric Line Survey of the Cygnus X region (PILS-Cygnus). First results: Observations of CygX-N30"

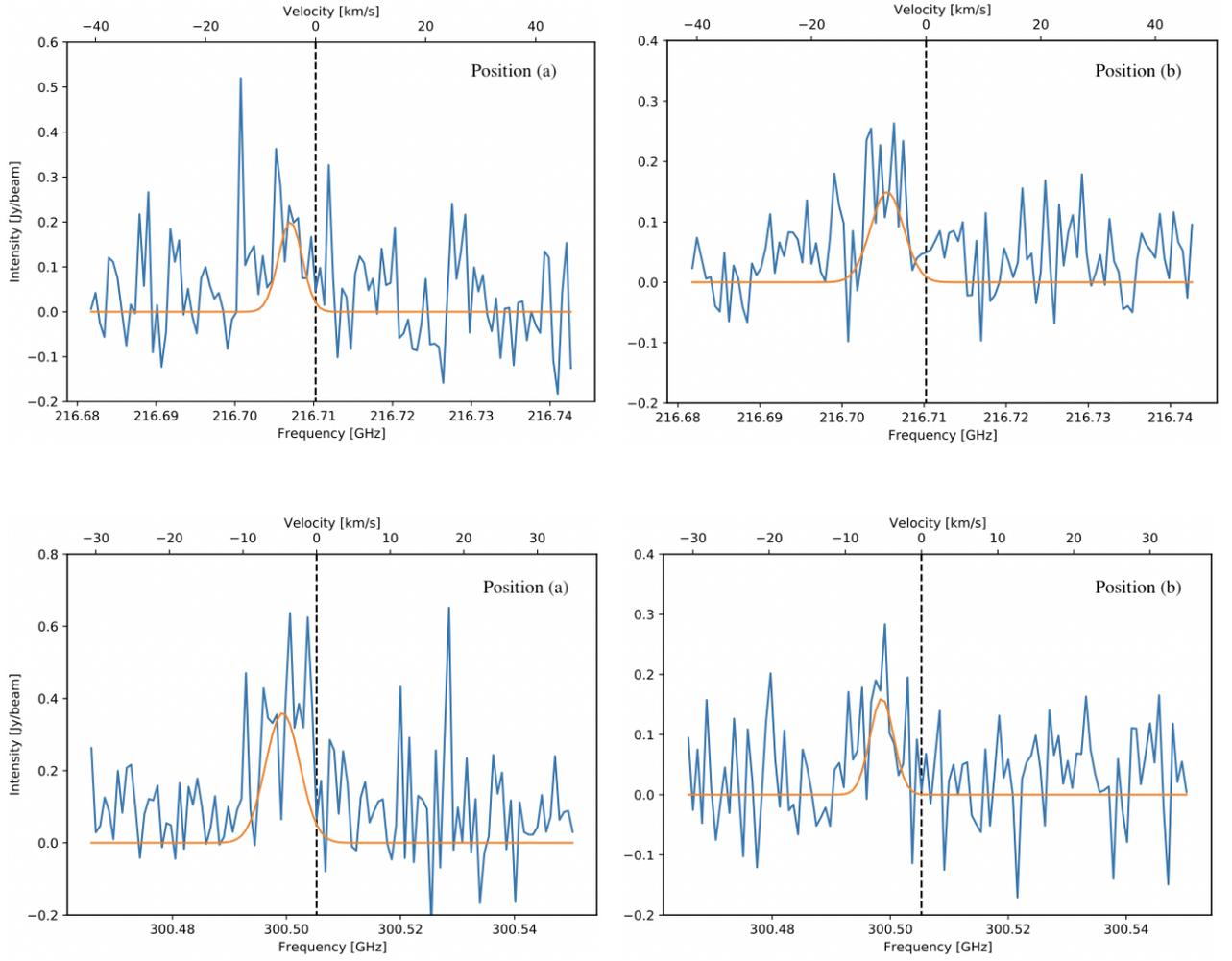[2]Centre d'Analyse Scientifique de Spectres Instrumentaux et Synthétiques, http://cassis.irap.omp.eu

[3]https://home.strw.leidenuniv.nl/~moldata/radex.html

FIGURE 7.3.1: Line spectra of H$_2$S ($2_{2,0}$–$2_{1,1}$) at 216.71 GHz (top row) and H$_2$S ($3_{3,0}$–$3_{2,1}$) at 300.50 GHz (bottom row), at field a (left column) and field b (right column), cf. Fig. 7.3.2. Each spectrum covers $\sim$ 100 km s^{-1} of velocity range. The dashed black vertical line represents the frequency of H$_2$S. A Gaussian fit has been applied to the detected H$_2$S transitions and is shown on top of the data in orange.

temperature of around 200 K, we therefore consider it as a good estimate. Finally, a FWHM of 5 km s^{-1} was used for both transitions of region a, and, for region b, FWHM of 6 km s^{-1} and 4 km s^{-1}, were used for the transitions $2_{2,0}$–$2_{1,1}$ and $3_{3,0}$–$3_{2,1}$, respectively. These values were determined from the Gaussian fit of our observations (cf. Table 7.3.2).

The RADEX tool determines the radiation temperature of the spectral line, which is equal to the main beam antenna temperature, T_B, if the beam-filling factor is 1. The integrated intensity, $\int T dv$, can then be found as follows (Quénard, 2016; van der Tak *et al.*, 2007):

$$\int T dv = \sqrt{\frac{\pi}{4 \ln 2}} \times T_B \times FWHM \tag{7.1}$$

Assuming an ortho-to-para ratio (OPR) of 3, integrated intensity ratios were determined for a range of H$_2$S column densities from 10^{14} cm^{-2} to 10^{18} cm^{-2}. These were then compared to the observed ratios of 0.5($\pm$0.1) and 1.3($-$0.5, $+$0.4) for region a and b, respectively. The observed H$_2$S ratio uses the FWHM and line intensity inferred from the Gaussian fits, displayed in Table 7.3.2. From Figure 7.3.3,
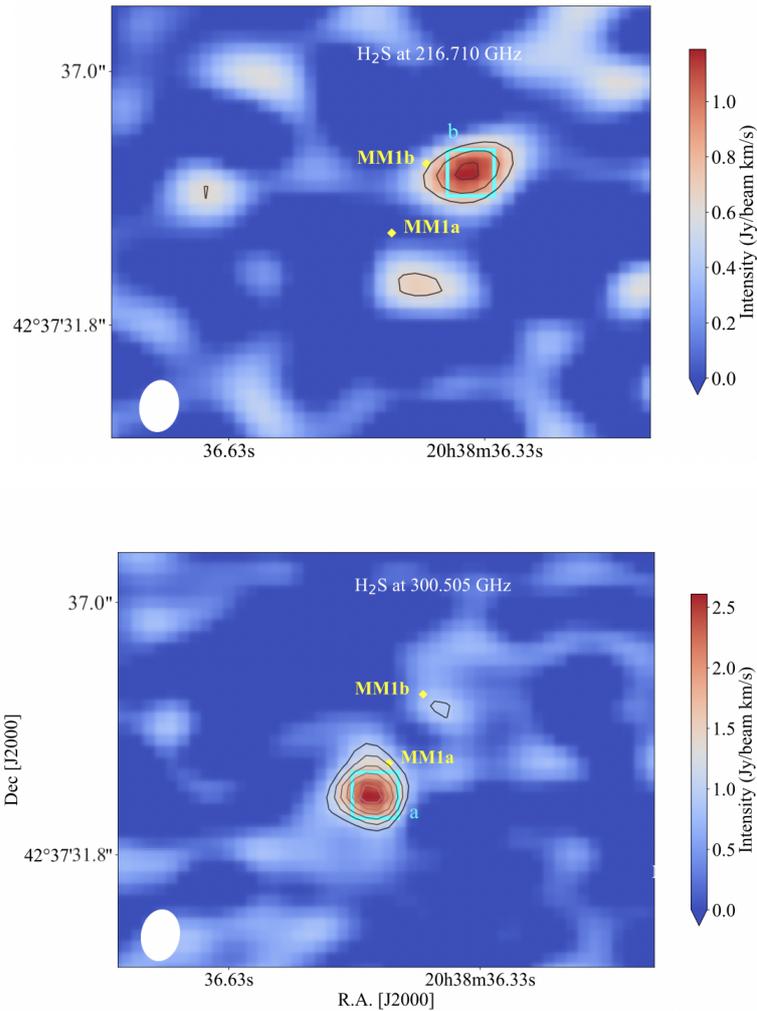
FIGURE 7.3.2: Integrated intensity maps of H_2S ($2_{2,0}$–$2_{1,1}$) at 216.71 GHz (top panel) and ($3_{3,0}$–$3_{2,1}$) at 300.50 GHz (bottom panel). The contours represent the integrated intensity emission of both H_2S transitions, starting from 3σ to 8σ and from 2.5σ to 4.5σ with a spacing of 1σ, for the emission at 300.50 GHz and 216.71 GHz, respectively. The continuum sources, MM1a and MM1b, are labeled and shown by the yellow diamonds. The continuum positions are taken from van der Walt *et al.* (2021). The beam size is displayed on the lower left corner by the white filled ellipsoid. The color bar displays the intensity in units of Jy beam^{-1} km s^{-1}. All the peak regions have been identified with a cyan rectangle and numbered as a and b.

the H_2S column density was found by comparing the observed ratio of the integrated line intensities (H_2S $2_{2,0}$–$2_{1,1}$/$3_{3,0}$–$3_{2,1}$) with the ones inferred from the RADEX analysis. An H_2S column density of $6^{+4}_{-4} \times 10^{16}$ cm^{-2} and $4^{+7}_{-2} \times 10^{17}$ cm^{-2} are found for regions a and b, respectively. The margins of error include the variations in intensity and FWHM, displayed in Table 7.3.2. The inferred column density for region a displays optically thin emission, i.e., each emitted photon is assumed to escape the cloud. In region b, meanwhile, the emission is optically thick, therefore, the inferred column density should be considered as a lower limit.
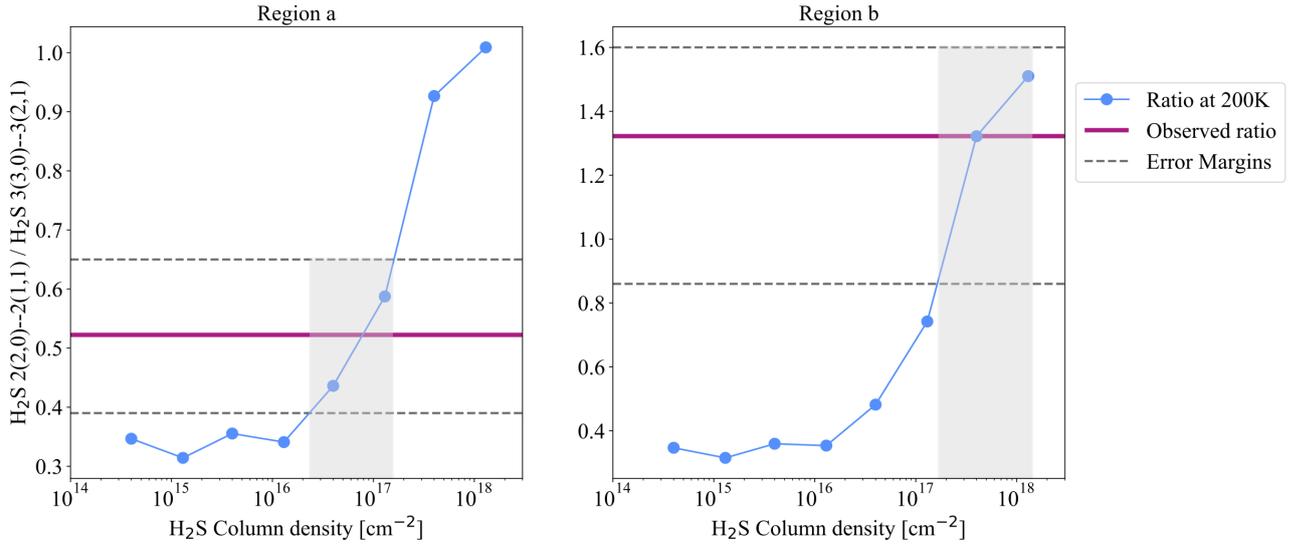
FIGURE 7.3.3: H$_2$S column density as a function of the line ratios of the integrated intensity emission of H$_2$S $2_{2,0}$–$2_{1,1}$/$3_{3,0}$–$3_{2,1}$. The line ratios are inferred from radiative transfer analysis with the RADEX tool. The integrated line intensity ratios and column densities were determined for an excitation temperature of 200 K (blue dots). The continuous line corresponds to the ratio of the observed integrated line intensities of H$_2$S $2_{2,0}$–$2_{1,1}$/$3_{3,0}$–$3_{2,1}$ for Region a (left-side figure) and for Region b (right-side figure), while the dotted grey lines represent the upper and lower limits of the line ratio. The corresponding range of column densities is highlighted by the shaded grey area.

7.4   DISCUSSION

We detected two transitions of H$_2$S towards the center of CygnusX-N30, peaking at two fields of few arcseconds from the source continuum peaks. At each location, the column density of H$_2$S has been quantified and found to be in the order of $6^{+4}_{-4} \times 10^{16}$ cm^{-2} – $>4^{+7}_{-2} \times 10^{17}$ cm^{-2}.

7.4.1   *H$_2$S column density towards CygX-N30*

Comparison with the literature

We first compared our inferred H$_2$S column density with the literature, where Minh *et al.* (2010) quantified the column density of H$_2$S towards the same source, CygX-N30, near the MM1a position. In their study, they inferred a column density of H$_2$S of $9.3 \pm 5.6 \times 10^{15}$ cm^{-2} for a rotational temperature of 200 K. Although the observational parameters from both studies (listed in Table 7.4.1) are similar, the Minh *et al.* (2010) inferred column density is slightly lower than ours, but marginally agrees within the uncertainties at around 2×10^{16} cm^{-2}. Given the few observed lines we do not consider these differences to be significant.

TABLE 7.4.1: Comparison of parameters between Minh *et al.* (2010) and this study.

Parameters	This study	Minh *et al.* (2010)
Telescope	SMA	SMA
Configuration	extended	extended
Source size	1″32×0″91	1″0×0″89
Flux H$_2$S $2_{2,0}$–$2_{1,1}$	4.3 K	4.4 K
FWHM	5.3 km s^{-1}	4.7 km s^{-1}
Rotational temperature	200 K	200 (±100) K
H$_2$S column density	$6^{+4}_{-4} \times 10^{16}$ cm^{-2}	$9.3\pm5.6\times10^{15}$ cm^{-2}

Interestingly, the fractional H_2S abundance relative to H_2[4] inferred towards CygX-N30 is around the same value of $\sim 10^{-8}$ as various hot cores of star-forming regions, such as Sgr B2(M), DR21 (OH), G29.96, etc. (Minh *et al.*, 1991; Hatchell *et al.*, 1998; Minh *et al.*, 2004; Minh *et al.*, 2012). H_2S is therefore a common, highly abundant species observed towards protostellar hot cores.

Comparison with other S-bearing species

We compared the H_2S column density with the column densities of other S-species, towards the same source. A sulphur inventory using the SMA was already performed by el Akel et al. 2021 (in press) towards CygnusX-N30, as part of the PILS-Cygnus survey (van der Walt *et al.*, 2021). They detected 105 lines of S-species, isotopes included, over the frequency range 329–361 GHz. The detected main sulphur isotopes, their line characteristics, and their inferred column densities towards MM1a, are shown in Table 7.4.2. These were determined under LTE and optically thin assumptions. In the last row of this Table, the H_2S characteristics found from our observations are also listed.

Based on the H_2S column densities inferred by el Akel et al. 2021 (in press) and van der Walt *et al.* (2021), the molecular ratios relative to H_2S were determined, as shown in Table 7.4.2. The amounts of detected CS and H_2CS were found to be 16% and 40% of the detected amount of H_2S, respectively. The largest variations in abundances were observed for the S-O species, with a variation of 1800–2000%, while the abundance of OCS was measured to be 230% of the H_2S amount. Moreover, H_2S displays similar excitation temperature and FWHM as the other S-species. This suggests that the observed H_2S is tracing gas components moving with a similar motion. However, this would need to be confirmed with detection of more H_2S transitions. The H_2S column density suggests that this molecule is an abundant S-species near the continuum cores of CygX-N30, and therefore raises the question of its origin.

TABLE 7.4.2: Properties of S-bearing species towards CygnusX-N30.

| Species	N	T_{ex}	$FWHM$	Ratio relative to H_2S
	[cm^{-2}]	[K]	[km s^{-1}]	[%]
OCS[a]	$1.4^{+0.4}_{-0.6} \times 10^{17}$	150^{+50}_{-20}	5.0	230
SO$_2$[a,c]	$1.1_{-0.2} \times 10^{18}$	130^{+30}_{-10}	6.5	1800
SO[a]	$1.2^{+0.1}_{-0.4} \times 10^{18}$	290^{+10}_{-60}	6.0	2000
CS[a]	$1.0_{-0.2} \times 10^{16}$	190^{+50}_{-20}	4.5	16
H_2CS[a]	$2.4^{+0.6}_{-0.4} \times 10^{16}$	140 ± 50	5.5	40
H_2S[b]	$6^{+4}_{-4} \times 10^{16}$	200	5	100

[a] Results taken from el Akel et al. (in press) at the MM1a position.

[b] H_2S emission extracted in field a.

[c] The emission of the species is optically thick, and the column density was inferred from the corresponding optically thin ^{34}S isotopes using an isotopic ratio of $^{32}S/^{34}S = 22.5$ (Lodders, 2003).

Where does H_2S come from?

H_2S is known to be principally produced from the surface reaction of hydrogen and the adsorbed atomic sulphur, on the icy dust grain, i.e., in a cold environment (T$\sim$10 K) (Vidal and Wakelam, 2018). Once on the surface, H_2S is formed from SH and goes through the hydrogenation abstraction process described as follows:

$$H_2S + H \leftrightarrow HS + H + H \qquad (7.2)$$
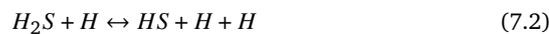
However, this reaction produces the radical HS, which reacts with its surrounding to further produce other S-bearing species, not exclusively H_2S (el Akel et al. 2021 (in press) and Vidal and Wakelam, 2018). The hydrogenation process is enhanced

[4]using a N_{H_2} of 5.3×10^{24} cm^{-2} for CygX-N30, from van der Walt *et al.* (2021).

by cold temperatures (T≤15 K) and becomes negligible with increasing temperature (Acharyya, 2014). A warmer environment would increase the mobility of radicals such as SH and thus the surface reactions, leading to production of other species than H_2S.

Moreover, Garozzo *et al.* (2010) and Chen *et al.* (2015) have shown that H_2S is efficiently converted to other sulphur compounds, e.g., OCS. Therefore, it is unlikely that all the observed H_2S comes from the top layer of the icy dust grains.

As van der Walt *et al.* (2021) previously discussed, the hot core of CygnusX-N30 is not considered a typical hot core region, where all the molecules on the dust grains desorb thermally at the same location, during the gas collapse to the protostellar center, where T>100 K. They proposed the presence of an infalling disk-structure, with the mid-plane axis going through these two continuum cores, MM1a and MM1b. This large disk structure of 3000 AU diameter was already proposed by Hutawarakorn *et al.* (2002). As CygnusX-N30 is a non-traditional hot-core with a rotating disk structure, the observed H_2S emission does not come only from thermal desorption but also from other non-thermal processes, such as, for example, sputtering and/or photodesorption.

The high abundance of H_2S in this region is therefore likely due to H_2S being initially trapped in both the bulk and on the top layer of icy dust grains. Its total release in the gas phase is due to thermal desorption, as the icy grain mantle sublimates at T>100 K, but might also result from non-thermal desorption processes, i.e., photodesorption, sputtering, and reactive desorption. Vidal and Wakelam (2018) already argued that H_2S is one of the main forms of sulphur trapped in the icy grain mantles, and might represent a shared reservoir of sulphur with HS.

In this study, two locations in CygnusX-N30 were analysed, leading to two column densities differing from each other by one order of magnitude. The studied source is a binary source, composed of two main cores, MM1a and MM1b, of which MM1b is expected to be less evolved than the other core (van der Walt *et al.*, 2021). The difference in H_2S column densities towards the two studied locations is likely related to the nearby continuum core. A higher H_2S column density was inferred near the less evolved core, MM1b, than in the region near MM1a. Minh *et al.* (2010) already observed that the methanol abundance in MM1b is an order of magnitude higher than in MM1a. A high abundance of methanol is expected in the early stage of the star formation (van der Tak *et al.*, 2003). We expect that the gas phase chemistry near MM1a had more time to develop and therefore reduce the abundance of H_2S in this region. For example, in the gas phase, H_2S is known to efficiently produce SO through SH and OCS (Millar and Williams, 1993). This might account for the difference in inferred column density towards the two regions.

7.4.2   *Comparison of the H₂S spatial distribution with other S-bearing species*

The spatial distribution of the H_2S emission was compared with those of three other S-bearing species, i.e., SO, SO_2 and OCS, detected by el Akel et al. 2021 (in press). These sulphur species were selected for comparison as SO and SO_2 are known to trace the warm chemistry (Singh and Chakrabarti, 2012; Artur de la Villarmois *et al.*, 2018), while OCS is believed to be a product of the reaction of H_2S with CO and H on icy-dust grains mantle (el Akel et al., 2021 in press. Chen *et al.*, 2015).

Moreover, contrary to these S-species, the H_2S emission displays different peak positions around MM1a and MM1b. In Figure 7.4.1, the emission of H_2S at 216.7 GHz and 300.5 GHz is shown with OCS at 340.4 GHz, SO at 344.3 GHz and SO_2 at 348.3 GHz, used as contours.

The H_2S emission at 300.5 GHz shows a close overlap with the emission of SO_2 and a partial overlap with SO emission (middle and bottom panels of Fig.7.4.1), while no overlap is observed between the two observed transitions of H_2S and OCS (top panels of Fig.7.4.1). The non overlap of the OCS and H_2S emissions (cf. top panels of Fig.7.4.1) hints that both molecules are neither formed nor desorbed simultaneously from the dust grains. As discussed in el Akel et al. 2021 (in press) and Drozdovskaya *et al.* (2018), one of the main formation pathways of OCS is through H_2S in the cold outer envelope (T~10 K). This suggests the prior formation of H_2S on grains. Moreover, OCS has a desorption temperature of ~90 K, while the desorption temperature of H_2S is ~75 K (el Akel et al., 2021 in press). This could
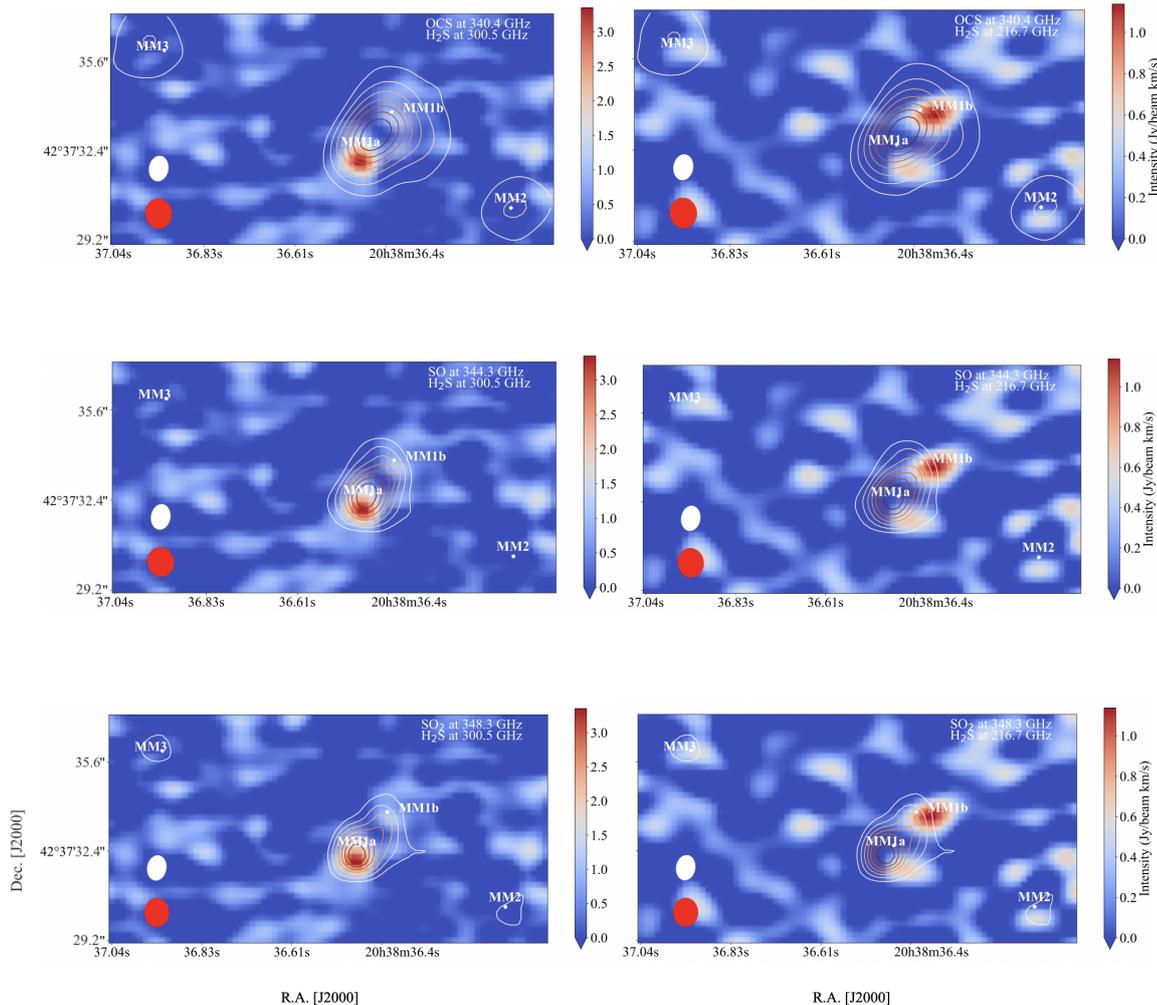
FIGURE 7.4.1: Integrated intensity maps of H_2S at 216.71 GHz (left column) and at 300.55 GHz (right column). The contours display the integrated intensity maps of OCS at 340.4 GHz (top row), SO at 344.3 GHz (middle row) and SO_2 at 348.3 GHz (Bottom row). The contours are displayed from the minimum to the maximum of the corresponding integrated intensity, with a spacing of 10%. The OCS, SO, and SO_2 data are taken from el Akel et al. (in press). The continuum cores from van der Walt *et al.* (2021) are labelled as MM1a, MM1b, MM2, and MM3. The color bar displays the integrated intensity of H_2S. The beam sizes are shown with the filled ellipsoid, in the bottom left corner, in white for the H_2S observations and in red for the contours.

explain why these molecules are not thermally desorbed at the same time during the envelope collapse towards the central region. Moreover, van der Tak *et al.* (2003) already discussed that OCS might be trapped in the icy matrix. This non overlap also suggests that these molecules might not be embedded in the same ice layer of the ice matrix. This last possibility would imply early formation of H_2S on the icy dust grains. Experiments and ice observations of these regions of interest are still needed to confirm these possibilities.

The close overlap of H_2S, SO, and SO_2 emission suggests that the H_2S molecule is likely tracing the same gas. Moreover, SO_2 is produced in the gas phase from SO, while SO has diverse formation pathways, such as the reactivity of atomic sulphur and atomic oxygen or dioxygen, but also in the gas phase, through H_2S from its production of SH, as follows (Millar and Williams, 1993; Charnley, 1997):
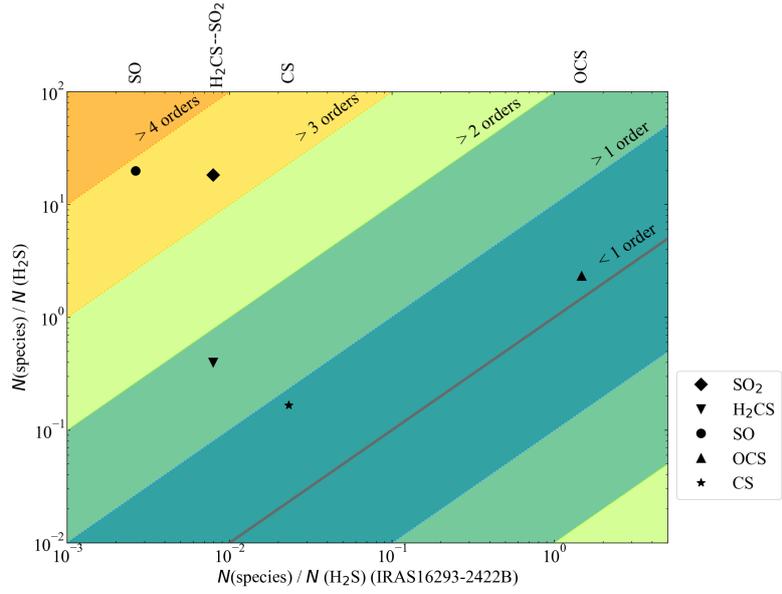
$$SH + O \rightarrow SO \qquad (7.3a)$$
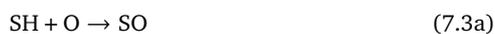
FIGURE 7.4.2: Comparison of the column density ratios of H_2CS, SO, SO_2, CS and OCS with respect to H_2S derived towards IRAS 16293-2422B (Drozdovskaya *et al.*, 2018) (x-axis) and towards the MM1a position of CygnusX-N30 (y-axis). The solid grey line represents a ratio of 1, whereas the colored area represent difference of one up to four orders of magnitude, from the 1:1 ratio.

$$SH + H \rightarrow S \xrightarrow{O_2} SO \tag{7.3b}$$

Therefore, we expect to see H_2S peaking at a similar location as these S-O species.

H_2S has a compact emission compared to the other S-species, as can be seen in Figure 7.4.1, which explains why we observed clearly distinct peak locations. These originate from the two MM1 continuum cores, from thermal and non-thermal processes, releasing the H_2S from the surface and from the ice matrix into the gas phase. This highly localised H_2S emission has already been observed towards another protostar, such as Sgr B2(M) near the continuum core, by Minh *et al.* (2004).

The early formation of H_2S on the grains was previously proposed by several studies, such as Drozdovskaya *et al.* (2018) for the protostar IRAS16293-2422(B), in which the abundances of SO, SO_2, and H_2S in the gas were claimed to be set in the early stage of the prestellar phase. Our results also show that the SO and SO_2 emission are detected at the same locations and suggests the early formation of H_2S in the ice form in clouds.

TABLE 7.4.3: Properties of S-bearing species towards CygnusX-N30 and IRAS 16293-2422.

| Species | IRAS 16293-2422[a] | | CygX-N30[b] |
| | N | N(species)/ N(H_2S) | N(species)/ N(H_2S) |
	[cm^{-2}]	[-]	[-]
OCS	2.8×10^{17}	1.5	2.3
SO_2	1.5×10^{15}	0.008	18
SO	5.0×10^{14}	0.003	20
CS	4.4×10^{15}	0.02	0.16
H_2CS	1.5×10^{15}	0.008	0.4
H_2S	1.9×10^{17}	1	1

[a] Column densities from Drozdovskaya *et al.* (2018)

[b] Column densities extracted at position MM1a, from this study and from el Akel et al., 2021, in press.

To get a broader insight into the sulphur chemistry occurring in both regions, we compared the ratios of the main sulphur isotopes detected towards both sources. These are listed in Table 7.4.3 (el Akel, 2021, in press). In Figure 7.4.2, the column densities of the detected sulphur species towards IRAS16293-2422B[5] and CygnusX-N30 (around MM1a) are displayed with respect to the column density of H_2S. The solid grey line represents equal values between the sources while the colored areas display the variations up to four orders of magnitude from the 1:1 ratio. We note from this Figure that the column density ratios $N(OCS)/N(H_2S)$ and $N(CS)/N(H_2S)$ are less than one order of magnitude greater than observed towards IRAS16293-2422B. However, $N(H_2CS)/N(H_2S)$ is almost one order of magnitude higher than towards IRAS16293-2422B. The largest differences are observed for the ratios $N(SO)/N(H_2S)$ and $N(SO_2)/N(H_2S)$, at 3 orders of magnitude greater in the CygX-N30 hot core environment than in IRAS16293-2422B's.

From this comparison, we observe an overproduction of H_2CS, SO_2, and SO towards CygX-N30 compared to IRAS 16293-2422(B). The difference in H_2CS/H_2S column density ratios between the sources is not critical ($\sim$ 1 order of magnitude). Moreover, H_2CS is not primarily formed from H_2S but, through the reactions {CH_3+S}, {CH_2OH+S} and {s-H + s-HCS}[6] (Vidal and Wakelam, 2018; Le Gal et al., 2019). We will therefore further comment only on the $N(SO)/N(H_2S)$ and $N(SO_2)/N(H_2S)$ ratios. Special attention is given to the S-O species as they are key elements of the sulphur chemistry: they might likely be dominant sulphur reservoirs in the hot core gas phase, T$\geq$100 K (Vidal et al., 2017; Gieser et al., 2019).

The main formation routes of SO_2 are in the gas phase from the reaction {SO+OH} and from the oxidation of atomic sulphur (Vidal and Wakelam, 2018). Its gas-phase abundance is also likely increased by desorption of SO_2 from the ice, at high density ($n_H > 10^8$ cm^3, assuming the isotropic standard interstellar radiation field (ISRF) (e.g., van Gelder et al., 2021; Mathis et al., 1983). A high amount of the detected SO_2 is likely to be linked to the amount of SO in the gas phase, as previously demonstrated in Charnley (1997) and Hatchell et al. (1998) and Buckle and Fuller (2003). From a purely chemical point of view, the ratio $N(SO)/N(SO_2)$ is therefore associated with the evolving stage of the hot core, with a decreasing $N(SO)/N(SO_2)$ ratio corresponding to an evolved hot core. The $N(SO)/N(SO_2)$ ratio is found to be ~0.3 in IRAS 16293-2422 (B), but also in other protostellar hot cores, e.g., AFGL2591(VLA3) and Monoceros R2 IRS 3A (Fuente et al., 2021). A $N(SO)/N(SO_2)$ ratio of ~1 is determined towards atypical hot cores, such as CygX-N30 and the Orion hot core (Gieser et al., 2019). It is possible that the mechanical processes occurring in these atypical hot cores, such as sputtering, have enhanced the amount of SO in the gas phase, contrary to a typical hot core, where only thermal desorption is expected. Therefore, this ratio is not representative of the hot core evolution when comparing conventional and unconventional sources.

SO is known to be formed from three main pathways (Vidal and Wakelam, 2018; van Gelder et al., 2021):

- The oxidation of SH. The radical SH has itself several formation paths. These are through the photodissociation of H_2S, but also its hydrogenation as mentioned earlier in Equation (7.3a). Another formation route of SH is from the photoionisation of atomic sulphur as follows:

$$S^+ + H_2CO \rightarrow SH + HCO^+ \tag{7.4}$$
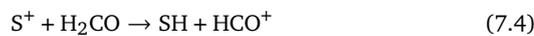
- The oxidation of S and S_2, as follows:

$$S + O_2 \rightarrow SO + O \tag{7.5a}$$

$$S_2 + O \rightarrow SO + S \tag{7.5b}$$

- The reactivity of S with OH. The radical OH results principally from the photodissociation of H_2O (Tappe et al., 2008). Meanwhile, the hydrogenation or photodissociation of SH produces atomic sulphur.

The production of SO has also other formation routes such as, {OCS+O}, {H_2O+HSO^+} and {O+HCNS} (Vidal and Wakelam, 2018; Millar and Williams, 1993).

[5]The H_2S column density was inferred assuming D/H=0.05, from Drozdovskaya et al. (2018).

[6]s- refers to the solid-state chemistry

A possibility explaining this high $N(SO)$ towards CygX-N30 is that contrary to the IRAS16293-2422B environment, CygX-30 is impacted by strong UV radiation. CygX-N30 is close to one of the most massive OB association, OB2 (separation of 23 pc at distance of 1.3 kpc, van der Walt *et al.*, 2021; Reipurth and Schneider, 2008). Therefore, CygX-N30 is subject to strong ionising radiation, compared to IRAS 16293-2422. This radiation leads to several photon processes such as photoionisation and photodissociation. These increase the abundance of ionised sulphur and of OH from photodissociation of H_2O and/or CH_3OH, which ultimately enhance the abundance of SO. This increase of OH might also enhance the production of SO_2 via its {SO+OH} formation path.

The combination of (1) the environmental conditions of CygX-N30, i.e., proximity of the OB2 association, (2) the unconventional structure, with its rotating molecular disk, and (3) the H_2S and HS species locked up in the ice matrix, lead to efficient photon processes and desorption of the locked formed of sulphur from the icy dust grains into the gas phase. All combined, they efficiently increase the abundance of SO and SO_2 in the gas.

However, considering the N_{H_2} of 5.3×10^{24} cm^{-2}, calculated by van der Walt *et al.* (2021), the total abundance of S-species, i.e., SO, SO_2, H_2S, OCS, CS and H_2CS, is in the order of ~ 10^{-7}, which only accounts for 5% of the total sulphur budget (Asplund *et al.*, 2009).

The combination of previous studies, the inferred column densities, and the integrated intensity maps of several S-bearing species allowed us to infer the different origins of H_2S observed towards the center of CygX-N30. This highlights the central role of H_2S in the sulphur chemistry, strongly affecting the production of several S-species, such as, SO, SO_2, and OCS. It is therefore likely that H_2S is produced at the early stage of the collapse and the initial amount of H_2S locked up in the ice matrix is considerably reduced with an evolving protostar, as already suggested by Charnley (1997). However, although the inferred S-abundance represents only 5% of the total sulphur budget and H_2S is a principal reactant of the S-species with the highest inferred abundances, this study does not discard that H_2S is the main reservoir of sulphur on the dust grains in the early stage of a protostar, as all the products resulting from H_2S are not considered. Further observations of refractory sulphur allotropes and H_2S_x, as well as quantification of their abundance should be made, as these species have been found to be produced from the irradiation of H_2S ice by high energy particles (Jiménez-Escobar and Muñoz Caro, 2011; Jiménez-Escobar *et al.*, 2014; Cazaux *et al.*, 2021).

Nevertheless, this paper represents an initial step towards understanding the H_2S origin in the hot cores. Observations of more H_2S transitions with on-ground telescopes and from the NIRSpec range of the James Webb Space Telescope (JWST) targeting the H_2S spectral features at 3–4μm, towards several protostars, e.g. CygX-N30, CygX-N12, IRAS 16293-2422, Sgr B2, W3(IRS 5), etc. would ultimately confirm its origin.

7.5 CONCLUSIONS

To better understand the role of H_2S in the sulphur chemistry of protostars, we observed three H_2S lines at 216.71 GHz, 228.56 GHz, and at 300.50 GHz, towards the massive protostar of the Cygnus X complex, Cygnus X-N30, with the SMA facility. The main conclusions of this paper are as follows:

(i) The H_2S lines at at 216.71 GHz (H_2S $2_{2,0}$–$2_{1,1}$) and at 300.50 GHz (H_2S $3_{3,0}$–$3_{2,1}$) were detected in regions offset by 1″ from MM1b and MM1a, respectively. H_2S column densities of $6^{+4}_{-4} \times 10^{16}$ cm^{-2} and $>4^{+7}_{-2} \times 10^{17}$ cm^{-2} are found for the H_2S transitions $2_{2,0}$–$2_{1,1}$ and $3_{3,0}$–$3_{2,1}$, respectively.

(ii) H_2S and OCS emission did not overlap in observations. This points out that these molecules are not formed simultaneously on the grains. It suggests the prior formation of H_2S, as a formation path of OCS on the grains surface is via H_2S.

(iii) The two identified peak locations of H_2S emission, both located at ~ 1″ from the continuum positions MM1a and MM1b, are due to (a) its compact emission and

(b) the presence of both continuum cores of the binary source CygX-N30. The shifts in peak locations from the continuum cores were attributed to the large rotating disk structure surrounding the protostar center.

(iv) The combination of the high inferred H_2S column density, its emission maps, and its chemical pathways in the gas and on the surface, indicate the early formation of the H_2S on grain. Therefore, most of the H_2S is expected to be locked up in the icy grain mantles, rather than on grain surfaces.

(v) The extensive comparison between CygX-N30 and IRAS 16293-2422 (B) highlighted strong differences in abundances of SO_2 and SO with respect to H_2S. The overproduction of S-O species towards CygX-N30 is attributed to its highly ionised environment (proximity to the Cygnus-OB2), but also due to the mechanical processes such as sputtering, occurring in this center region due to the rotating disk structure. The high abundance of S-O species underlines their strong direct link to the H_2S abundance.

Bibliography

1. K. Acharyya, *MNRAS* **443**, 1301–1309, ISSN: 0035-8711, eprint: https://academic.oup.com/mnras/article-pdf/443/2/1301/3661495/stu1219.pdf, (https://doi.org/10.1093/mnras/stu1219) (July 2014).

2. E. Artur de la Villarmois *et al.*, *A&A* **614**, A26, (https://doi.org/10.1051/0004-6361/201731603) (2018).

3. M. Asplund *et al.*, *ARA&A* **47**, 481–522, eprint: https://doi.org/10.1146/annurev.astro.46.060407.145222, (https://doi.org/10.1146/annurev.astro.46.060407.145222) (2009).

4. D. Briggs, F. Schwab, R. Sramek, presented at the Synthesis Imaging in Radio Astronomy II, ed. by G. Taylor, C. Carilli, R. Perley, vol. 180, p. 127.

5. J. V. Buckle, G. A. Fuller, *A&A* **399**, 567–581, (https://doi.org/10.1051/0004-6361:20021816) (2003).

6. S. Cazaux *et al.* (Oct. 2021).

7. S. Charnley, *ApJ* **481**, 396–405 (May 1997).

8. Y. Chen *et al.*, *ApJ* **798**, 80 (Jan. 2015).

9. N. Crockett *et al.*, *ApJ* **781**, 114, arXiv: 1401.2470 [astro-ph.GA] (Feb. 2014).

10. F. Daniel, M. Dubernet, A. Grosjean, *A&A* **536**, A76, (https://doi.org/10.1051/0004-6361/201118049) (2011).

11. F. Daniel *et al.*, *A&A* **517**, A13, (https://doi.org/10.1051/0004-6361/200913745) (2010).

12. M. N. Drozdovskaya *et al.*, *MNRAS* **476**, 4949–4964, arXiv: 1802.02977 [astro-ph.SR] (June 2018).

13. M. Dubernet *et al.*, *A&A* **460**, 323–329, (https://doi.org/10.1051/0004-6361:20065804) (2006).

14. M. Dubernet *et al.*, *A&A* **497**, 911–925, (https://doi.org/10.1051/0004-6361/200810680) (2009).

15. A. Fuente *et al.*, *MNRAS* **507**, 1886–1898, arXiv: 2107.14532 [astro-ph.GA] (Oct. 2021).

16. M. Garozzo *et al.*, *A&A* **509**, A67, (https://doi.org/10.1051/0004-6361/200913040) (2010).

17. C. Gieser *et al.*, *A&A* **631**, A142, (https://doi.org/10.1051/0004-6361/201935865) (2019).

18. T. E. Graedel, W. D. Langer, M. A. Frerking, *ApJS* **48**, 321 (1982).

19. J. Hatchell *et al.*, *A&A* **338**, 713–722 (Oct. 1998).

20. J. Holdship *et al.*, *Monthly Notices of the Royal Astronomical Society* **463**, 802–810, ISSN: 0035-8711, eprint: https://academic.oup.com/mnras/article-pdf/463/1/802/18471485/stw1977.pdf, (https://doi.org/10.1093/mnras/stw1977) (Aug. 2016).

21. B. Hutawarakorn, R. Cohen, G. Brebner, *Monthly Notices of the Royal Astronomical Society* **330**, 349–364, eprint: https://onlinelibrary.wiley.com/doi/pdf/10.1046/j.1365-8711.2002.05068.x, (https://onlinelibrary.wiley.com/doi/abs/10.1046/j.1365-8711.2002.05068.x) (2002).

22. A. Jiménez-Escobar, G. M. Muñoz Caro, Y. J. Chen, *MNRAS* **443**, 343–354, ISSN: 0035-8711, eprint: https://academic.oup.com/mnras/article-pdf/443/1/343/4287264/stu1100.pdf, (https://doi.org/10.1093/mnras/stu1100) (July 2014).

23. A. Jiménez-Escobar, G. Muñoz Caro, *A&A* **536**, A91, arXiv: 1112.3240 [astro-ph.EP] (Dec. 2011).

24. J. Jørgensen *et al.*, *A&A* **534**, A100, arXiv: 1109.0415 [astro-ph.SR] (Oct. 2011).

25. E. Koumpia *et al.*, *A&A* **603** (May 2017).

26. J. C. Laas, P. Caselli, *A&A* **624**, A108, (https://doi.org/10.1051/0004-6361/201834446) (2019).

27. R. Le Gal *et al.*, *ApJ* **876**, 72, (%5Curl%7Bhttps://doi.org/10.3847%2F1538-4357%2Fab1416%7D) (May 2019).

28. K. Lodders, *ApJ* **591**, 1220–1247 (July 2003).

29. J. Mathis, P. Mezger, N. Panagia, *A&A* **500**, 259–276 (Nov. 1983).

30. J. McMullin *et al.*, presented at the Astronomical Data Analysis Software and Systems XVI, ed. by R. Shaw, F. Hill, D. Bell, vol. 376, p. 127.

31. T. Millar, E. Herbst, *A&A* **231**, 466–472 (May 1990).

32. T. Millar, D. Williams, *Dust and chemistry in astronomy*.

33. Y. Minh, W. Irvine, S. J. Kim, *Journal of Korean Astronomical Society* **37**, 131–135 (Dec. 2004).

34. Y. Minh, W. Irvine, L. Ziurys, *ApJ* **345**, L63 (Oct. 1989).

35. Y. Minh *et al.*, *ApJ* **360**, 136 (Sept. 1990).

36. Y. Minh *et al.*, *ApJ* **366**, 192 (Jan. 1991).

37. Y. Minh *et al.*, *ApJ* **723**, 1231–1240 (Nov. 2010).

38. Y. Minh *et al.*, *Journal of Korean Astronomical Society* **45**, 157–166 (Dec. 2012).

39. F. Motte *et al.*, *A&A* **476**, 1243–1260, (https://doi.org/10.1051/0004-6361:20077843) (2007).

40. D. Navarro-Almaida *et al.*, *A&A* **637**, A39, arXiv: 2004.03475 [astro-ph.GA] (May 2020).

41. D. D. Quénard, Theses, Université Toulouse 3 - Paul Sabatier, Sept. 2016, (https://tel.archives-ouvertes.fr/tel-01402482).

42. B. Reipurth, N. Schneider, in *Handbook of Star Forming Regions, Volume I*, ed. by B. Reipurth, vol. 4, p. 36.

43. D. P. Ruffle *et al.*, *MNRAS* **306**, 691–695, ISSN: 0035-8711, eprint: https://academic.oup.com/mnras/article-pdf/306/3/691/11932145/306-3-691.pdf, (https://doi.org/10.1046/j.1365-8711.1999.02562.x) (July 1999).

44. K. L. J. Rygl *et al.*, *A&A* **539**, A79, (https://doi.org/10.1051/0004-6361/201118211) (2012).

45. C. B. Singh, S. K. Chakrabarti, *MNRAS* **421**, 1666–1670, eprint: https://onlinelibrary.wiley.com/doi/pdf/10.1111/j.1365-2966.2012.20426.x, (https://onlinelibrary.wiley.com/doi/abs/10.1111/j.1365-2966.2012.20426.x) (2012).

46. A. Tappe *et al.*, *ApJ* **680**, L117–L120, (https://doi.org/10.1086/589998) (May 2008).

47. P. Thaddeus *et al.*, *ApJ* **176**, L73 (Sept. 1972).

48. A. Tieftrunk *et al.*, *A&A* **289**, 579–596 (Sept. 1994).

49. F. F. S. van der Tak *et al.*, *A&A* **468**, 627–635, (https://doi.org/10.1051/0004-6361:20066820) (2007).

50. S. van der Walt *et al.*, *A&A* **655**, A86, arXiv: 2109.03640 [astro-ph.SR] (Nov. 2021).

51. F. F. S. van der Tak *et al.* (2003).

52. M. van Gelder *et al.*, *A&A* **653**, A159, arXiv: 2107.09750 [astro-ph.SR] (Sept. 2021).

53. C. Vastel *et al.*, *MNRAS* **478**, 5514–5532, arXiv: 1806.01102 [astro-ph.GA] (Aug. 2018).

54.   T. Vidal *et al.*, *MNRAS* **469**, 435–447, arXiv: 1704.01404 [astro-ph.GA] (July 2017).

55.   T. Vidal, V. Wakelam, *MNRAS* **474**, 5575–5587, arXiv: 1711.11406 [astro-ph.SR] (Mar. 2018).

56.   V. Wakelam *et al.*, *A&A* **413**, 609–622, ISSN: 1432-0746, (http://dx.doi.org/10.1051/0004-6361:20031572) (Dec. 2003).

57.   M. Watanabe, R. Hoefgen, *Journal of Experimental Botany* **70**, 4155–4170, ISSN: 0022-0957, eprint: https://academic.oup.com/jxb/article-pdf/70/16/4155/29185617/erz260.pdf, (https://doi.org/10.1093/jxb/erz260) (Aug. 2019).

58.   S. Yamamoto, *Introduction to Astrochemistry*.

8

Summary and Outlook

In this thesis, we combined laboratory, observational and modeling work to understand the implications of the sulphur chemistry on the protostellar environment.

From laboratory experiments, we started our research with hydrogen sulphide as it results from the direct hydrogenation of atomic sulphur, and is therefore considered as one of the starting elements of sulphur chemistry. We found that, on a cold surface, H_2S is highly reactive with hydrogen to produce the radical HS through the cyclic hydrogen abstraction process. Moreover, when combined with CO and H, H_2S produces the organo-sulphur, OCS.

The observational part was the core of this Ph.D, connecting the laboratory experiments and the models for the interpretation of the protostar. We observed several protostars, and the distinct environments defined by different physical conditions. The observations allowed us to determine how the sulphur chemistry is characterised in the different regions and what are typical good sulphur tracers of the cold and warm chemistry. Moreover, a larger diversity of S-bearing species is observed towards the cold envelope of protostars, rather than towards the hot core. This study pointed to the early formation of SO, SO_2 and H_2S, and suggested than part of H_2S is embedded within the ice matrix of the icy dust grains and formed at the early stage of the protostar. The study of the sulphur chemistry towards different protostars, allowed us to identify a so-called traditional hot core to a non-traditional. Thus, chemical differentiation among the S-families could be pointed out in a non-traditional hot core, contrary to a so-called traditional hot core, where all the S-bearing species are thermally desorbing around the hot core.

The observations of an outflow region allowed us to understand the morphology of the region. The combinations of the observations with the modeling results not only provided the characteristics of the observed outflow, such as the shock type, the shock velocity, etc., but it also provided insight on the chemistry of the observed regions. Comparing the column densities of the observed species with the modeled ones, showed the chemical complexity of such a region, where the chemistry in the gas phase is not only affected by the current shock conditions but also by the remnants of the previous shocks in the same region.

The work performed during this thesis helped the understanding of the chemical and physical contributions of a protostellar environment. However, there is still a long way to go for fully understanding it.

We propose here several paths which could be considered to pursue this research. In the laboratory, the reactivity of H_2S has been studied only on a gold surface. The next step would be to use an icy substrate: pure ice (crystalline and amorphous) and mixed ice (e.g., CO/H_2O). The reactivity of H_2S could also be studied with the addition of an external source of energy, which would simulate the photodesorption process occurring in the ISM. Finally, H_2S was considered as the initial step for studying the reactivity of the sulphur chemistry in a controlled environment, the study can therefore be taken a few steps ahead by studying the reactivity of other key species such as CS, OCS, etc. From the observational side, the possibilities to follow up this study are great. First, sulphur inventory of the ten most luminous sources of the Cygnus-X could be performed and compared with the analyzed sources from this thesis. In such way, it will be possible to determine if the sources display similar trends regarding the sulphur chemistry. This survey could then be extended to other

star forming complexes other than Cygnus X, such as e.g., Serpens, Orion molecular cloud complexes, etc. One should target not only class 0 but also class 1 protostars to study how the sulphur chemistry varies with the evolving protostars. This study can ultimately be taken one step further by extending it to extra-galactical observations. These should not only concern gas-phase observations, which are the observations used in this research. But, a special attention should be given to the observations of ice. These would allow us to connect the expected reactions on the icy dust grains and the species observed in the gas phase. Last but not least, observations of the icy dust grains would help us to conclusively identify the main sulphur reservoir on the grains, in a protostellar environment.

Finally, from the modeling side, this study focuses on four main molecular species, CS, SO, CH_3OH and H_2CO. The natural follow up would be to increase the sample of observed molecules, with a focus on the S-bearing species, and comparing their column density with the modeled ones. Moreover, a new version of the Paris-Durham code will be available soon. This combination of observations/models could be extended to more sources, e.g., L1448, L1157-B1, IRAS04166, etc.

The research performed in this thesis is a kickoff of the understanding of the sulphur chemistry in star-forming regions. There is still a lot to discover and understand, and as Ann Druyan said "*science is nothing more than a never-ending search for the truth*".